Delft University of Technology

Document Version
Final published version

Citation (APA)
Henzel, J. (2026). *Breaking down the reverse bias breakdown of perovskite solar cells.* [Dissertation (TU Delft), Delft University of Technology]. https://doi.org/10.4233/uuid:6d40a14e-625c-4568-af9f-7abbecd6b7a0

Important note
To cite this publication, please use the final published version (if applicable).
Please check the document version above.

Copyright
In case the licence states "Dutch Copyright Act (Article 25fa)", this publication was made available Green Open Access via the TU Delft Institutional Repository pursuant to Dutch Copyright Act (Article 25fa, the Taverne amendment). This provision does not affect copyright ownership.
Unless copyright is transferred by contract or statute, it remains with the copyright holder.

Sharing and reuse
Other than for strictly personal use, it is not permitted to download, forward or distribute the text or part of it, without the consent of the author(s) and/or copyright holder(s), unless the work is under an open content license such as Creative Commons.

Takedown policy
Please contact us and provide details if you believe this document breaches copyrights.
We will remove access to the work immediately and investigate your claim.

This work is downloaded from Delft University of Technology.

Breaking down the reverse bias breakdown of perovskite solar cells

Jonathan Antonio Henzel

Breaking down the reverse bias breakdown of perovskite solar cells

Jonathan Antonio Henzel

Breaking down the reverse bias breakdown of perovskite solar cells

Dissertation

for the purpose of obtaining the degree of doctor
at Delft University of Technology
by the authority of the Rector Magnificus,
Prof.dr.ir. H. Bijl,
chair of the Board for Doctorates
to be defended publicly on
Wednesday, 24 June 2026 at 15:00

by

Jonathan Antonio HENZEL

This dissertation has been approved by the (co)promotors.

Composition of the doctoral committee:

Rector Magnificus,	chairperson
Em. prof. dr. A.W. Weeber,	Delft University of Technology, promotor
Prof. dr. ir. O. Isabella,	Delft University of Technology, promotor
Dr. L. Mazzarella,	Delft University of Technology, copromotor

Independent members:

Prof. dr. E. Garnett,	University of Amsterdam
Prof. dr. L.J.A. Koster,	University of Groningen
Dr. ir. T.J. Savenije,	Delft University of Technology
Prof. dr. ir. A.H.M. Smets,	Delft University of Technology
Prof. dr. ir. M. Popov,	Delft University of Technology, *reserve member*

Additional non-independent members:

Dr. M.J. Theelen,	TNO

Keywords: perovskite solar cells, partial shading, reverse bias, degradation, stability, breakdown
Printed by: Ridderprint
Cover by: Constance Vrijdag, Studio Ridderprint

Copyright © 2026 by J.A. Henzel

An electronic version of this dissertation is available at
https://repository.tudelft.nl.

He that breaks a thing to find out what it is has left the path of wisdom.

Gandalf in *The Lord of the Rings, 3rd Edition, The Council of Elrond, p. 259 (1994),*
J.R.R. Tolkien

Contents

Summary

Perovskite solar cells are expected to enter industrial production on a large scale in the near future. This might happen either as single-junction perovskite photovoltaic (PV) modules, or as top cells in tandem devices in combination with silicon-based bottom cells. However, before any perovskite-based PV technology can be reliably deployed outdoor, one major hurdle must be overcome: their notorious lack of stability. Under realistic operating conditions, this instability will lead to degradation of the photovoltaic performance over time.

Among the various stress factors that have been shown to degrade perovskite solar cells, reverse bias stress has emerged as a particularly critical issue. A reverse bias can occur in a module when one cell in a string of series-connected cells generates significantly less current than the other cells in that string. This typically occurs during partial shading events, where, to give an idealized example, one cell is shaded while the remaining cells are illuminated. Due to the series-connection of the cells, the shaded cell is impacted by the current that is generated by the illuminated solar cells. Two different scenarios can result from this situation:

Firstly, the reverse bias that the illuminated cells apply to the shaded cell is large enough to force it into breakdown. Then, a large reverse bias current flows through the shaded cell, which can cause rapid degradation. Nevertheless, the remaining, illuminated part of the string continues to generate a current and, as long as the shaded cells keeps conducting it, power can be extracted from the module.

In the second scenario, the maximum reverse bias that the illuminated cells can impose on the shaded cell is not large enough to cause the breakdown. The maximum bias is the sum of the open-circuit voltages of the illuminated cells. It can be insufficient for effecting breakdown when the number of cells making up the string is small or when more than one cell in a string is shaded. Then, the shaded cells act as a blocking diode and almost no current flows through the shaded cells, which also prevents current from flowing through the rest of the string, resulting in zero power output. At the same time, less degradation can be expected to occur due to the lack of current flowing through the shaded cells.

Which of these scenarios occurs depends on the reverse bias behavior of the shaded cells, as well as the overall module design. Therefore, understanding the behavior of perovskite solar cells under reverse bias is instrumental for increasing the stability of modules under partial shading conditions. For this reason, the reverse bias behavior of perovskite solar cells is as the central focus of this thesis.

A more thorough introduction to the topic and its background is given in Chapter 1.

Chapter 2 provides an overview of the current state of research. The chapter begins with a brief introduction to the operating principles of a perovskite solar cell and the functionality of the individual layers that constitute the device. This is

followed by a detailed discussion of the widely accepted mechanisms underlying the reverse bias breakdown in perovskite solar cells, along with a summary of the experimental evidence supporting this model. The chapter concludes with a review of the proposed degradation mechanisms and the observations on which they are based.

Chapter 3 gives an overview of the fabrication of the samples and introduces the key characterization techniques used throughout this experimental work.

Chapter 4 examines the "breakdown voltage" metric, which is commonly used in literature to describe the reverse bias behavior of perovskite solar cells. A closer inspection reveals a lack of standardization in regard to this metric, both in the measurement parameters and conditions, and in the definition and method of determination of the breakdown voltage. This lack of consistency limits the comparability of the results from different studies.

To address this issue, the impact of measurement parameters and conditions on the resulting metric on the basis of data from literature is discussed. This enables the proposal of a set of measurement parameters as a first step towards standardization. Furthermore, the available definitions of the breakdown voltage are compared with regard to to comparability, generality, and usefulness. The point of maximum curvature is proposed as a new definition of the metric that combines comparability with the ability to be analytically expressed. That means that it could eventually be connected to a theoretical model of the breakdown mechanism.

In Chapter 5, the breakdown voltage proves its usefulness as a link between the voltage, the reverse bias current and cell degradation. When varying the applied reverse bias and the duration of the degradation experiments, a significant inhomogeneity in the current flowing through the reverse biased cells was observed. By normalizing the applied biases with the cell-specific breakdown voltages, cell-to-cell differences in reverse bias behavior can be minimized. This normalization procedure results in a clearer relationship between current and voltage and also between the degradation rate and voltage. It reveals that both relationships are exponential, suggesting that the degradation rate is closely related to the reverse bias current. This finding is interpreted as evidence that degradation is primarily current-driven.

In Chapter 6, the breakdown mechanism itself is brought into the focus of research. Realistic partial shading events might include incomplete shading, where the affected cell still receives low-intensity illumination. This may occur through diffuse illumination when the shading object is located at some distance from the module, or due to reflected back-side illumination in case of a bifacial module. Voltage sweeps into the reverse bias regime under low-intensity illumination reveal a pronounced dependence on the voltage scan rate. At small scan rates, illumination has little effect, while the reverse bias behavior is strongly influenced at large scan rates.

Based on the role of mobile ions during breakdown and to explain the effect of illumination on the breakdown, a hypothesis is developed: Illumination has been shown to increase the conductivity of mobile ions. Since the presence of mobile ions at the interfaces of the perovskite layer is instrumental to allowing tunneling, increased conductivity leads to a reduction of the absolute value of the breakdown voltage ("less negative"). At the same time, the reverse bias current drives an electrochemical reaction that increases the breakdown voltage, possibly by neutralizing the mobile ions. The electrochemical reaction depends on the total charge that has passed through the solar cell, which, in turn, is strongly influenced by the scan rate. This dependence explains the pronounced impact of the scan rate on the apparent breakdown voltage that has been observed experimentally.

The central role of the current (and charge) is further supported by additional quasi-steady state experiments. In these experiments, a constant reverse bias current is injected for enough time to allow the solar cells to reach a quasi-steady state before illumination is added. Under these conditions, illumination significantly affects the reverse bias behavior only at low current injection levels. Furthermore, pre-conditioning a solar cell by injecting a large reverse bias current prior to a voltage sweep under illumination also suppresses the influence of light on the measured breakdown voltage. Therefore, these experiments support the hypothesis. From these observations, the conclusion is drawn that the effect of low-intensity illumination under realistic partial shading conditions is unlikely to have a significant impact on the reverse bias behavior. However, these findings also emphasize the importance of a deeper understanding of the reverse bias breakdown mechanism to ultimately address reverse bias degradation.

Chapter 7 extends the investigation of the breakdown mechanism from a different perspective. Up to this point, a solar cell has been implicitly treated as one-dimensional or spatially uniform. In this chapter, reverse bias electroluminescence (ReBEL) is introduced as a powerful mapping technique for investigating the local reverse bias behavior of perovskite solar cells.

To that end, the technique is validated: The ReBEL spectrum closely resembles the electroluminescence (EL) spectrum, confirming that the ReBEL emission originates from the perovskite layer. Comparison between ReBEL images and those obtained from steady state infrared thermography and reverse bias lock-in thermography reveals consistent spatial features. This serves as proof that the ReBEL signal can be used to image the local reverse bias current.

Subsequently, ReBEL mapping is performed at various current injection levels. At small reverse bias currents, emission is localized primarily at the cell edges and at small spots, while the rest of the device area remains dark. On the other hand, at large currents, the entire cell area emits light, while the cell edges are not present as separate features anymore. The cell area shows a significant spatial inhomogeneity of the emission rate.

Semi-quantitative analysis reveals an additional difference between the cell edges, the bright spots and the general cell area: The emission rate at the cell edges and at some of the bright spots grows strongly at small current levels, but stagnates at larger current levels. In contrast, the emission rate in the cell area continues increasing exponentially at large current levels. Therefore, the behavior of the cell area dominates the behavior of the complete cell at large current levels. From these differences, the conclusion is drawn that different breakdown mechanisms are present.

Additional experiments trace the activity at the cell edges back to the sharp geometry of the bottom electrodes. Cells with more rounded bottom electrodes show less increased emission rates at the edges at small current levels. For the spatially inhomogeneity of the emission rate in the cell area, on the other hand, no satisfactory explanation is found. Comparison with forward electroluminescence imaging hints at a possible connection to the series resistances of the top and bottom electrode. That connection, however, is inverted, with an assumed high series resistance seemingly leading to large emission rates. Possibly, the reverse bias breakdown mechanism, governing current flow, plays an as of yet unknown role here.

In Chapter 8, the thesis is brought to a close by summarizing conclusions and outlining several recommended research directions. These include the development of integrated bypass diodes, a more rigorous investigation of the breakdown mechanism including a formalism, and an extension of the research to perovskite-based tandem solar cells.

Samenvatting

Samenvatting in het Nederlands gerealiseerd met hulp van Google Translate.

Perovskiet-zonnecellen zullen naar verwachting op korte termijn grootschalig in productie worden genomen. Dit kan gebeuren als enkelvoudige perovskiet-fotovoltaïsche (PV voor fotovoltaïsch) modules, of als topcellen in tandemstructuren in combinatie met silicium-gebaseerde bodemcellen. Voordat perovskiet-gebaseerde PV-technologie echter betrouwbaar in praktijk kan worden ingezet, moet eerst een grote horde worden genomen: hun beruchte gebrek aan stabiliteit. Onder realistische omstandig-heden zal deze instabiliteit in de loop van de tijd leiden tot degradatie van de fotovoltaïsche prestaties.

Onder de verschillende stressfactoren waarvan is aangetoond dat ze perovskiet-zonnecellen aantasten, is reverse bias (negatieve spanning) stress naar voren gekomen als een bijzonder kritisch aspect. Een negatieve spanning kan in een module optreden wanneer één cel in een reeks in serie geschakelde cellen aanzienlijk minder stroom levert dan de andere cellen in die reeks. Dit gebeurt typisch tijdens gedeeltelijke beschaduwing, waar, om een geïdealiseerd voorbeeld te geven, één cel volledig beschaduwd is, terwijl de overige cellen worden belicht. Door de serieschakeling van de cellen heeft de stroom die door de belichte cellen wordt opgewekt, effect op de beschaduwde cel. Door deze beschaduwing kunnen twee mogelijke situaties ontstaan:

Ten eerste is de negatieve spanning die de belichte cellen over de beschaduwde cel aanbrengen groot genoeg om deze in doorslag ("breakdown") te dwingen. Vervolgens vloeit er een grote stroom door de beschaduwde cel, wat snelle degradatie kan veroorzaken. Toch blijft het overige, belichte deel van de string stroom genereren en, zolang de beschaduwde cel deze blijft geleiden, kan er vermogen uit de module worden gehaald.

In de tweede situtatie is de maximale negatieve spanning die de belichte cellen op de beschaduwde cel kunnen uitoefenen niet groot genoeg om doorslag te veroorzaken. De maximale spanning is de som van de open-circuitspanningen van de belichte cellen. Deze kan onvoldoende zijn om doorslag te veroorzaken wanneer het aantal cellen in de string klein is of wanneer meer dan één cel in een string beschaduwd is. De beschaduwde cellen fungeren dan als een blokkerende diode en er loopt vrijwel geen stroom door de beschaduwde cellen, wat ook voorkomt dat er stroom door de rest van de string loopt, met als gevolg een vermogensafgifte van nul. Tegelijkertijd kan er minder degradatie worden verwacht door het gebrek aan stroom door de beschaduwde cellen.

Welk van deze situaties zich voordoet, hangt af van het reverse bias gedrag van de beschaduwde cellen, evenals van het algehele moduleontwerp. Daarom is inzicht in het gedrag van perovskiet-zonnecellen onder negatieve spanningen essentieel voor het verhogen van de stabiliteit van modules onder gedeeltelijke beschaduwing. Om deze reden vormt het reverse bias gedrag van perovskiet-zonnecellen het centrale thema van dit proefschrift.

Een uitgebreidere inleiding op het onderwerp en de achtergrond ervan is te vinden in hoofdstuk 1.

Hoofdstuk 2 geeft een overzicht van de huidige stand van het onderzoek. Het hoofdstuk begint met een korte introductie van de werkingsprincipes van een perovskietzonnecel en de functionaliteit van de afzonderlijke lagen waaruit de cel is opgebouwd. Hierna volgt een gedetailleerde beschrijving van de algemeen aanvaarde mechanismen die ten grondslag liggen aan de doorslag in perovskiet-zonnecellen onder reverse bias, samen met een samenvatting van het experimentele bewijs dat dit model ondersteunt. Het hoofdstuk sluit af met een overzicht van de voorgestelde degradatiemechanismen en de waarnemingen waarop deze gebaseerd zijn.

Hoofdstuk 3 geeft een overzicht van de fabricage van de cellen en tussenproducten en introduceert de belangrijkste karakteriseringstechnieken die in dit experimentele werk zijn gebruikt.

Hoofdstuk 4 onderzoekt de "doorslagspanning"-parameter ("breakdown voltage"), die in de literatuur vaak wordt gebruikt om het gedrag van perovskiet-zonnecellen bij negatieve spanningen te beschrijven. Bij nadere inspectie blijkt er een gebrek aan standaardisatie te bestaan met betrekking tot deze meetwaarde, zowel wat betreft de meetparameters en -omstandigheden als de definitie en de methode voor het bepalen van de doorslagspanning. Dit gebrek aan consistentie beperkt de mogelijkheid tot het vergelijken van de resultaten uit verschillende onderzoeken.

Om dit probleem aan te pakken, wordt de impact van meetparameters en -omstandigheden op de resulterende metriek besproken aan de hand van gegevens uit de literatuur. Dit maakt het mogelijk om een set meetparameters voor te stellen als eerste stap naar standaardisatie. Verder worden de beschikbare definities van de doorslagspanning vergeleken met betrekking tot mogelijkheid tot vergelijken, algemeenheid en bruikbaarheid. Het punt van maximale kromming wordt voorgesteld als een nieuwe definitie van de metriek die mogelijkheid tot vergelijken combineert met de mogelijkheid om analytisch te worden uitgedrukt. Dat betekent dat het uiteindelijk gekoppeld zou kunnen worden aan een theoretisch model van het doorslagmechanisme.

In hoofdstuk 5 bewijst de doorslagspanning zijn nut als een schakel tussen de spanning, de reverse bias stroom en celdegradatie. Bij variatie van de toegepaste spanning en de duur van de degradatie-experimenten werd een significante inhomogeniteit in de stroom door de cellen met negatieve spanningen waargenomen. Door de toegepaste spanningen te normaliseren met de celspecifieke doorslagspanningen, kunnen cel-tot-cel verschillen in reverse bias gedrag worden geminimaliseerd. Deze normalisatieprocedure resulteert in een duidelijker verband tussen stroom en spanning, en ook tussen de degradatiesnelheid en de spanning. Het laat zien dat beide verbanden exponentieel zijn, wat suggereert dat de degradatiesnelheid nauw samenhangt met de stroom onder negatieve spanningen. Deze bevinding wordt geïnterpreteerd als bewijs dat degradatie voornamelijk stroomgedreven is.

In hoofdstuk 6 wordt het doorslagmechanisme zelf centraal gesteld in het onderzoek. Realistische gedeeltelijke beschaduwing kunnen onvolledige schaduw omvatten, waarbij de betreffende cel nog steeds een lage lichtintensiteit ontvangt. Dit kan optreden door diffuse belichting wanneer het schaduwobject zich op enige afstand van de module bevindt, of door gereflecteerde belichting aan de achterzijde in het geval van een bifaciale module. Spanningsmetingen in het negatieve spanningsgebied onder lage lichtintensiteit laten een uitgesproken afhankelijkheid van de snelheid van de spanningsscan zien. Bij lage snelheden heeft de belichting weinig effect, terwijl het gedrag in negatieve spanning sterk wordt beïnvloed bij hoge snelheden. Op basis van de rol van mobiele ionen tijdens de doorslag en om het effect van belichting op de doorslag te verklaren, wordt een hypothese ontwikkeld: Het is aangetoond dat belichting de geleiding van mobiele ionen verhoogt. Omdat de aanwezigheid van mobiele ionen aan de grensvlakken van de perovskietlaag essentieel is voor tunnelen, leidt een verhoogde geleiding tot een verlaging van de absolute waarde van de doorslagspanning ("minder negatief"). Tegelijkertijd drijft de stroom een elektrochemische reactie aan die de doorslagspanning verhoogt, mogelijk door de mobiele ionen te neutraliseren. De elektrochemische reactie is afhankelijk van de totale lading die door de zonnecel is gegaan, die op zijn beurt sterk wordt beïnvloed door de scansnelheid. Deze afhankelijkheid verklaart de uitgesproken invloed van de scansnelheid op de schijnbare doorslagspanning die experimenteel is waargenomen. De centrale rol van de stroom (en lading) wordt verder ondersteund door aanvullende zogenaamde quasi-stationaire experimenten. In deze experimenten wordt een constante reverse bias stroom geïnjecteerd gedurende een voldoende lange tijd om de zonnecellen een quasi-stationaire toestand te laten bereiken voordat de zonnecel wordt belicht. Onder deze omstandigheden heeft belichting alleen bij lage strominjectieniveaus een significant effect op het gedrag bij negatieve spanning. Bovendien onderdrukt het voorconditioneren van een zonnecel door het injecteren van een grote stroom bij negatieve spanning vóór een spanningsscan onder belichting ook de invloed van de belichting op de gemeten doorslagspanning. Deze experimenten ondersteunen daarom de hypothese. Uit deze waarnemingen wordt geconcludeerd dat het effect van belichting met lage intensiteit onder realistische gedeeltelijke beschaduwing waarschijnlijk geen significante invloed heeft op het gedrag onder negatieve spanning. Deze bevindingen benadrukken echter ook het belang van een dieper begrip van het doorslagmechanisme om uiteindelijk degradatie bij negatieve spanning te voorkomen.

Hoofdstuk 7 breidt het onderzoek vanuit een ander perspectief uit naar het doorslagmechanisme. Tot nu toe werd een zonnecel impliciet beschouwd als eendimensionaal of lateraal uniform. In dit hoofdstuk wordt elektroluminescentie bij negatieve spanning (in het Engels Reverse Bias ElectroLuminescence ReBEL) geïntroduceerd als een krachtige karteringstechniek voor het onderzoeken van het lokale gedrag van perovskiet-zonnecellen onder negatieve spanning. Daartoe wordt de techniek gevalideerd: Het ReBEL-spectrum vertoont een sterke gelijkenis met het elektroluminescentiespectrum (EL), wat bevestigt dat de ReBEL-emissie afkomstig is van de perovskietlaag. Vergelijking tussen ReBEL-beelden en beelden verkregen met steady-state infraroodthermografie en reverse bias lock-in thermografie onthult consistente laterale kenmerken. Dit dient als bewijs dat het ReBEL-signaal gebruikt kan worden om de lokale reverse bias stroom in beeld te brengen.

Vervolgens werd ReBEL-karakterisering uitgevoerd bij verschillende injectiestroomniveaus. Bij kleine reverse bias stromen is de genormaliseerde emissieintensiteit voornamelijk gelokaliseerd aan de celranden en op kleine plekken / spots, terwijl de rest van het zonnecel donker blijft. Bij grote stromen daarentegen zendt het gehele celoppervlak licht uit, terwijl de celranden niet langer als afzonderlijke kenmerken aanwezig zijn. Het celgebied vertoont een significante laterale inhomogeniteit van de genormaliseerde emissieintensiteit.

Semi-kwantitatieve analyse onthult een aanvullend verschil tussen de celranden, de heldere plekken en het algemene celoppervlak: De genormaliseerde emissieintensiteit aan de celranden en bij sommige van de heldere plekken neemt sterk toe bij lage stroomsterktes, maar stagneert bij hogere stroomsterktes. Daarentegen blijft de genormaliseerde emissieintensiteit over het celoppervlak exponentieel toenemen bij hoge stroomsterktes. Het gedrag over het celoppervlak domineert dus het gedrag van de gehele cel bij hoge stroomsterktes. Uit deze verschillen werd geconcludeerd dat er verschillende doorslagmechanismen aanwezig zijn.

Aanvullende experimenten bringen de activiteit aan de celranden in verband met de scherpe geometrie van de onderste elektroden. Cellen met meer afgeronde onderste elektroden vertoonen geen hogere genormaliseerde emissieintensiteit aan de randen bij lage stroomsterktes. Voor de laterale inhomogeniteit van de genormaliseerde emissieintensiteit over het celoppervlak word daarentegen geen bevredigende verklaring gevonden. Vergelijking met voorwaartse elektroluminescentiebeeldvorming suggereert een mogelijk verband met de serieweerstanden van de bovenste en onderste elektrode. Die verbinding is echter omgekeerd, waarbij een veronderstelde hoge serieweerstand kennelijk leidt tot hoge genormaliseerde emissieintensiteit. Mogelijk speelt het doorslagmechanisme, dat de stroom regelt, hier een tot nu toe onbekende rol.

In hoofdstuk 8 wordt het proefschrift afgesloten met een samenvatting van de conclusies en een overzicht van enkele aanbevolen onderzoeksrichtingen. Deze omvatten de ontwikkeling van in de module geïntegreerde bypassdiodes, een grondiger onderzoek naar het doorslagmechanisme inclusief een formalisme, en een uitbreiding van het onderzoek naar op perovskiet gebaseerde tandemzonnecellen.

Nomenclature

1. Abbreviations

AM1.5G	Air Mass 1.5G
CCD	Charge-Coupled-Device
CIGS	Copper-Indium-Gallium-Diselenide
DJV measurement	Dark Current Density-Voltage measurement
DLIT	Dark Lock-In Thermography
DMF	N,N-dimethylformamide
DR	Degradation Rate
EDX	Energy-Dispersive X-Ray Spectroscopy
EL	Electroluminescence
EQE	External Quantum Efficiency
ETL/ETM	Electron Transport Layer/Material
e^-	electron
FF	Fill Factor
FW	Forward (Sweep)
HTL/HTM	Hole Transport Layer/Material
h^+	hole
IEC	International Electrotechnical Commission
IR	Infrared
ISO	International Organization for Standardization
ISOS	International Summit on Organic and Hybrid Photovoltaics
ITO	Indium-Tin-Oxide
IV measurement	Current-Voltage measurement
JV measurement	Current Density-Voltage measurement
LCOE	Levelized-Cost-Of-Electricity
LED	Light-Emitting-Diode
light RB-JV measurement	Reverse Bias Current Density-Voltage measurement with illumination
MPP	Maximum-Power-Point
MPPT	Maximum-Power-Point-Tracking
Me	Metal
NMP	N-methyl-2-pyrrolidone
OPV	Organic Photovoltaics
PCE	Power Conversion Efficiency
PL	Photoluminescence
PSC	Perovskite Solar Cell
PTAA	poly(triaryl amine)

PV	Perovskite
PV	Photovoltaics
PoMC	Point-of-Maximum-Curvature
RB	Reverse Bias
RB-JV measurement	Reverse Bias Current Density-Voltage measurement
RT	Room Temperature
RV	Reverse (Sweep)
ReBEL	Reverse Bias Electroluminescence
sALD	spatial Atomic-Layer-Deposition
ssIR	steady state infrared (thermography)
SD	Standard Deviation
STC	Standard Test Conditions
Si	Silicon
TCO	Transparent Conductive Oxide
TL	Transport Layer
XPS	X-Ray Photoelectron Spectroscopy
2T, 4T	2-terminal, 4-terminal (tandem)

2. Symbols and Units

symbol	**description**	**units**
E	Energy	J
E_c	Conduction Band Energy	eV
E_g	Band Gap Energy	eV
E_v	Valence Band Energy	eV
ER	Emission Rate	$\mathrm{s^{-1}}$
I	Current	A
I_0	Saturation Current or Dark Current	A
I_{mpp}	Maximum-Power-Point Current	A
I_{rev}	Reverse Bias Current	A
I_{sc}	Short-Circuit Current	A
J	Current Density	$\mathrm{A\,m^{-2}}$
J_{BD}	Breakdown Current Density	$\mathrm{A\,m^{-2}}$
J_{inj}	Injected Current Density	$\mathrm{A\,m^{-2}}$
J_{mpp}	Maximum-Power-Point Current Density	$\mathrm{A\,m^{-2}}$
$J_{rev,avg}$	Average Reverse Bias Current Density	$\mathrm{A\,m^{-2}}$
J_{rev}	Reverse Bias Current Density	$\mathrm{A\,m^{-2}}$
J_{sc}	Short-Circuit Current Density	$\mathrm{A\,m^{-2}}$
k_B	Boltzmann-Constant	$\mathrm{J\,K^{-1}}$
N_{neutr}	Density of Neutralized Mobile Ions	$\mathrm{m^{-2}}$
P_{light}	Illumination Intensity relative to 1 sun	–
P_{mpp}	Maximum-Power-Point Power	W
q	(Elementary) Charge	C
Q	Charge	C

symbol	**description**	**units**
R_{sh}	Shunt Resistance	Ω
R_s	Series Resistance	Ω
T	Temperature	°C
t	time	s
t_{deg}	Degradation Time	s
V	Voltage	V
V_{appl}	Applied Voltage	V
V_{BD}	Breakdown Voltage	V
V_i	Local Diode Voltage in point i	V
V_{mpp}	Maximum-Power-Point Voltage	V
V_{oc}	Open-Circuit Voltage	V
V_{th}	Thermal Voltage	V
ΔV_{BD}	Breakdown Voltage Shift	V
ϕ_{norm}	Normalized Voltage	$-$
κ	curvature	$-$

1

Introduction

1.1. PV and perovskite PV

Worldwide, more and more electricity is generated via photovoltaics (PV). In 2024, PV systems satisfied already more than 10 % of the electricity demand of the world. [1] This electricity generation was accomplished by an installed cumulative capacity of over 2.2 TW. [1] Nearly all of this installed PV capacity consisted of systems with wafer-based silicon solar cells. [2] However, there are other PV technologies in development. Among them, perovskite solar cells are "...the emerging PV technology with the most potential for industrialization". [3]

The perovskite solar cells that will be addressed in this work use hybrid organic-inorganic, lead-halide perovskites as absorber. They are part of a group of PV technologies that are often called 'thin-film' PV technologies. That name is a hint towards the direct band gap of the eponymous materials which allows for far thinner absorber layers than in crystalline silicon.

The first implementation of these perovskites (PVKs) in photovoltaics occurred in 2009, when they were employed as dye for dye-sensitized-solar cells. [4] In the following years, constant improvements led to the emergence of a distinct solar cell technology: The perovskite solar cell (PSC) was born. Since then, the power conversion efficiencies (PCE) of lab-scale cells has gone through an unprecedented development: Since 2014, it rose from about 14 % to about 27 % in 2025. [5, 6] While further progress on up-scaling is still required, the initial phases of industrialization have already begun. First productions plants are in construction or have begun operation. [3]

At least equally promising is the progress in the development of tandem solar cells. They make use of (at least) two different absorber materials with different band gap to enhance the attainable efficiency. While several combinations of PV technologies are in development, the combination of a well-established and stable crystalline silicon bottom cell with a high-efficiency and possibly cheap perovskite top cell raises high expectations. Lab-scale perovskite/silicon tandem solar cells have already reached PCEs of around 35 %. [5] For the future, it is expected for silicon-based tandems (with perovskites) to gain a market share of 10 % by

2035. [7]

Nonetheless, some hurdles still need to be overcome before perovskite solar cells enter the market on a large scale: One remaining challenge is the limited stability. [3] The stability of PV panels is an important factor in the calculation of the levelized-cost-of-electricity (LCOE). [8] This figure-of-merit is used to judge technologies by their techno-economical competitiveness. [9] To stand on equal ground with established technologies, similar warranties on finished products will likely be required. To compete with silicon PV, guaranteeing outdoor operation of 25 to 30 years with a total degradation of less than 20 % of the initial performance would be necessary. [10]

1.2. Stability of perovskite PV

While there are many stressors that can cause degradation of perovskite solar cells, years of research have yielded solutions to some of them: The degradation due to atmospheric species (oxygen, humidity, etc.) can be relatively easily prevented by encapsulating/packaging the solar cells. [11, 12] In a similar manner, the incorporation of a down-converting layer can protect the solar cell from the detrimental influence of ultraviolet light. [13] However, there are also stressors whose influence cannot be negated. Illumination, (forward) bias or heat are such stressors that are intrinsically connected to operation. [14] Against these, intrinsic stability of the materials and interfaces constituting a perovskite solar cell is required.

Additionally, there are stressors that emerge from the way modules are designed. Module design generally favors connecting cells electrically in series. Series-connection means that one current flows through the cells while their voltages are added up. This leads to reduced resistive losses and therefore higher efficiency. However, this design also makes modules vulnerable to the danger of partial shading.

Partial shading describes a condition where a part of the module area is shaded while the remaining module area is illuminated. In a simple partial shading scenario, one cell is completely shaded while all other cells of the module are illuminated. Current is only generated by the illuminated cells, but needs to pass through all cells equally. This current can only flow through a shaded cell if this cell is operating in reverse bias.

This is schematically depicted in Figure 1.1. There, a string of series-connected solar cells (A to E) is shown. In Figure 1.1a, all cells are illuminated and generate the same current I. A simple partial shading scenario is represented in Figure 1.1b. One cell of the string (cell C) is shaded and therefore is not illuminated. It does not generate any current but the other cells of that string (cells A, B, D, and E) still do. They attempt to push their current through cell C which is operating in the dark. If cell C reaches its reverse bias breakdown, it passes the current generated by the other cells. If the reverse bias breakdown is not triggered, no current is flowing throughout the string.

In the established silicon PV technology, this reverse bias current flow occurs at

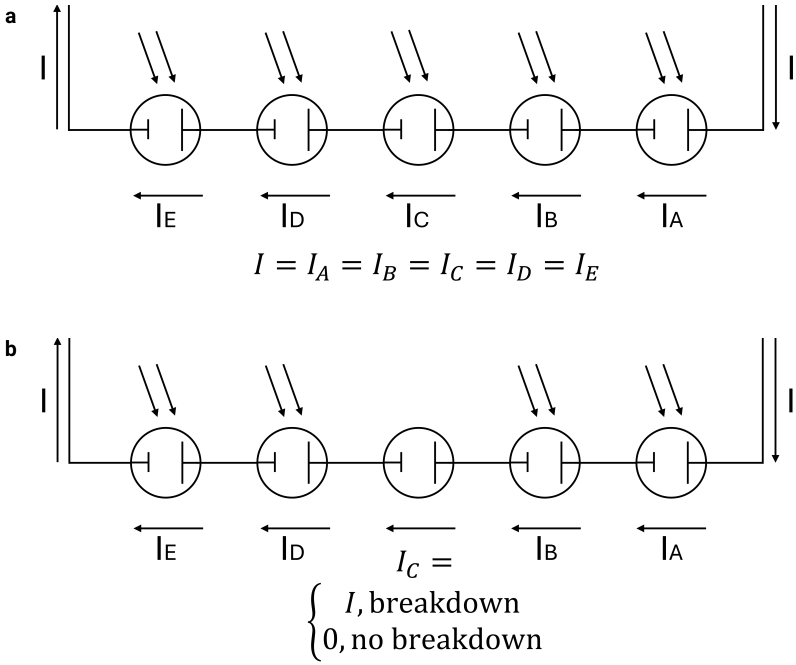

Figure 1.1. A schematic depiction of a module consisting of 5 series-connected solar cells (A to E). In normal operation without any shading, they all generate the same current I (a). However, in a partial shading scenario, one cell (here cell C) is shaded and not illuminated (b). Then, this shaded cell either passes the current of the illuminated cells (breakdown) or it does not (no breakdown). If it does not reach its breakdown, no current is flowing through the string and no power can be extracted.

very large negative voltages and with very large local current densities. The resulting Joule heating leads to the occurrence of hot spots which is a serious danger to PV modules. [15] Therefore, external bypass diodes are normally employed which are connected anti-parallel to a string of cells. These bypass diodes serve as low-resistance current pathways in case of partial shading. That way, the current does not flow through the shaded cells and cannot cause degradation. Unfortunately, this solution cannot be easily deployed in perovskite PV modules.

There are two reasons for that:
Firstly, differences in preferred module design make implementing external bypass diodes not feasible in perovskite PV. [16] The preferred module design for thin-film PV technologies in general is based on the "monolithic interconnection scheme". Such a module is displayed in Figure 1.2. One of the advantages of this design is that all the layers can be deposited on the full module area. In-between the deposition steps, the local removal of material ("scribing") creates the monolithic interconnection by connecting and disconnecting certain layers. This leads to the thin, stripe-like cells that are connected to each other in series along their whole length.

This design means that external bypass diodes could only be implemented at the edges of the module. The resulting problem is described in the work by Wolf *et al.*: [16] In the case of partial shading with one shaded cell, the current would bypass the shaded cell by flowing along the length of an illuminated cell to the edge of the module, through the bypass diode, and back along the length of another illuminated cell to the center. For current to flow such distances without significant resistive losses, highly-conductive, very thick (metal) electrodes would be required which is highly undesirable.

The second problem is related to bypass diodes but appears on cell-level:
A single bypass diode can only protect a certain number of series-connected solar cells. This number of cells is largely determined by the voltage at which a cell breaks down and lets current pass in the dark. This voltage is often called 'breakdown voltage'. The breakdown voltages that are generally reported for perovskite solar cells are significantly smaller than those of most silicon-based solar cells. [17] Instead of about -15 V for cells based on monocrystalline silicon, values of -1 V to -5 V are often reported. [17] That means that a perovskite PV module would require many more bypass diodes. More bypass diodes per module can be expected to lead to a significant increase in cost. [16]

An alternative to using bypass diodes would be to ensure that reverse bias and reverse bias current does not impact the shaded cells negatively. Unfortunately, studies have conclusively shown that reverse biases affect the PCE of perovskite solar cells quite dramatically. [18–20] Various degradation mechanisms have been identified that can occur in parallel and impact the reverse biased-solar cell in various ways. [18–20] For this reason, there have been increasingly more attempts to increase the reverse bias stability by solar cell engineering in the last years. [21–27] Increasing the breakdown voltage to make it easier to eventually use bypass diodes in modules is another direction that some researchers are following. [28–32]

However, progress is hampered by a few obstacles. One important problem is the

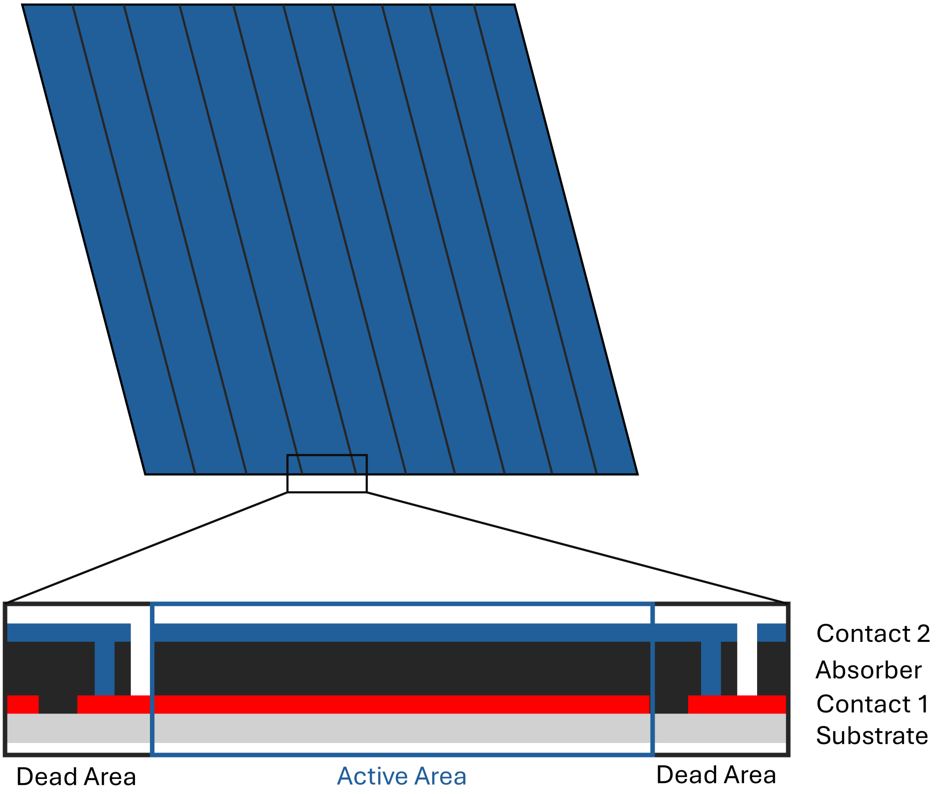

Figure 1.2. A module consists of many stripe-like cells (blue) on one substrate. These cells are defined and separated by the scribes (black). In the scribe areas (also known as dead areas), parts of the layer stack have been removed during deposition. This design with its series-connected cells is called "monolithic interconnection".

lack of standardization: While there are standards for efficiency measurements and degradation testing for cell research (ISOS protocols [33]), the metric that describes the reverse bias behavior of solar cells, the breakdown voltage, is determined in various different ways that lack comparability. This problem is aggravated by a lack of detailed knowledge about the breakdown mechanism itself and the factors influencing it.

1.3. Aim and outline

These issues lead us to the conclusion that this field of research requires a more solid basis to stand on. The overarching goal of this work is, therefore, to describe and understand the reverse bias breakdown of PSCs more thoroughly. To that end, the first aim is to introduce standards and definitions that improve the comparability of reported findings. Secondly, the research efforts are focused on the mechanisms affecting the reverse bias behavior. By contributing to these research directions, the efforts of the community to solve the problem of partial shading in perovskite PV is supported.

We begin in Chapter 2 with a look at the dominant model of the reverse bias breakdown of perovskite solar cells. Building up on that, the reverse bias degradation and the various mechanisms ascribed to it are introduced.

Chapter 3 continues by introducing the samples used in our own research and the employed methods of characterizing them.

In Chapter 4, the focus lies on the breakdown voltage as a metric that describes the reverse bias behavior of solar cells. We reveal that many different ways of measuring and determining the breakdown voltage of perovskite solar cells are used in parallel. After a discussion of the impact of measurement conditions, sets of measurement parameters are provided to improve comparability of results. Additionally, the available definitions of the breakdown voltage are compared and a new definition is proposed that combines comparability, general applicability and the possibility of analytical expression.

Chapter 5 applies the lessons learned in the previous chapter. We connect discrepancies in the relationship between applied reverse bias and reverse bias current to differences in reverse bias behavior. By relating the reverse bias to the breakdown voltage, the relationship with the current and the degradation is clarified. These relationships point towards the degradation being dominated by current-driven mechanisms.

In Chapter 6, the breakdown mechanism itself is the object of research. Adding low-intensity illumination to the measurements that are used to characterize the reverse bias behavior reveals the significant influence of slow processes within the perovskite solar cells. We identify these processes with the migration of mobile ions and electrochemical reactions and construct a model to explain the observed impact of light.

In Chapter 7, the investigation of the reverse bias behavior is extended below cell-level. By introducing reverse bias electroluminescence (ReBEL) as an imaging technique, spatial differences in reverse bias behavior within a perovskite solar cell can be detected. It is validated by comparing it to thermal imaging techniques. ReBEL imaging allows to distinguish parts of the cell area that show different behaviors, depending on the current injection level. The results imply that the reverse bias current can flow through large areas and not through localized weak spots. That means that reverse bias breakdown might not necessarily lead to hot spots.

1.4. Contribution to the field

Our main contributions to the field are listed in the following:

- Sets of measurement parameters to characterize perovskite solar cells in regards to their reverse bias behavior were provided. Additionally, a new definition of the breakdown voltage was proposed. This standardization should improve comparability and provide a point of orientation for newcomers to this field of research.

- By normalizing the reverse bias with the breakdown voltage, the relationships between reverse bias with current and degradation were revealed. This demonstrated an application of the breakdown voltage to describe differences in reverse bias behavior. It also allowed the conclusion that degradation is dominated by current-driven mechanisms.
- By adding illumination to the reverse bias breakdown process, the significant impact of ion migration and electrochemical reactions in the perovskite solar cells were shown. Based on the observed phenomena, a model of these two antagonistic mechanisms was constructed as extension of the standard breakdown model.
- Reverse bias electroluminescence imaging was introduced as new technique to characterize the local reverse bias behavior. It revealed that the reverse bias current at realistic current levels flows through the whole cell area and not through small weak points. That implies that the occurrence of hot spots might not be a necessary consequence of reverse biases in perovskite solar cells.

2

Fundamentals

This chapter aims to provide the reader with a basic understanding of the important terms and concepts used in this thesis. At the same time, it serves a similar function as a literature review by giving an overview over the state of research.

We will begin with the basic principle of a perovskite solar cell. This is followed by a introducing the reverse bias breakdown of perovskite solar cells and the widely-accepted model of its mechanism. Finally, the mechanisms that have been proposed to explain the reverse bias degradation of perovskite solar cells are described.

2.1. Basic perovskite solar cell physics

Fundamentally, a perovskite solar cell (PSC) is a solar cell which uses a perovskite as absorber layer. However, it contains several more layers even in a simple layout. The conduction and valence band energy levels of the (isolated) materials that the solar cells in this thesis consist of are displayed in Figure 2.1.

Perovskites (PVKs) are a large and diverse class of materials as the name describes only a crystal structure with the formula ABX_3. Therefore, the term is sometimes specified for the solar cell application as 'organic-inorganic halide perovskite'. This term points towards the (often organic) A-site cation (e.g. methylammonium $CH_3NH_3^+$), the inorganic B-site cation (e.g. Pb^{2+}), and the X-site halide anion (e.g. I^-).

Such a material makes up the absorber layer of a perovskite solar cell which correctly implies that there, light is absorbed. It is a direct band gap semiconductor which results in a high absorption coefficient. [34] Thus, perovskite solar cells are reckoned among the group of thin-film PV technologies where the absorber possesses a thickness of about 1 µm. When a photon is absorbed, a charge carrier-pair consisting of an electron and a hole is generated. Due to the exciton-binding energy being in the same order of magnitude as the thermal energy at room temperature, the charge carriers are separated 'automatically'. [35] Perovskites show additionally quite good electron and hole transport properties, so that both charge carriers can also be transported over distances over several hundreds of nanometers. [36, 37]

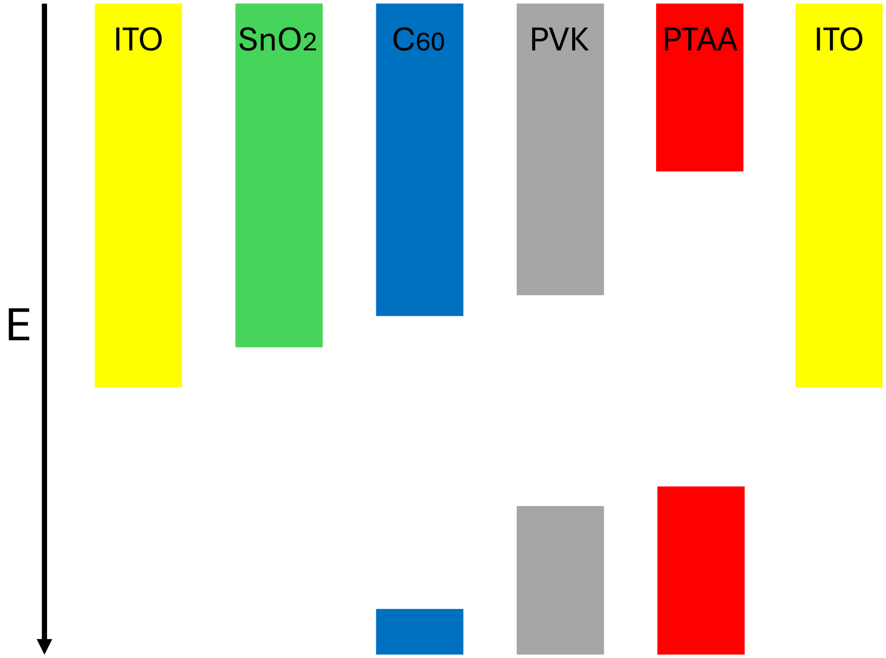

Figure 2.1. A schematic energy level diagram of the isolated materials that constitute the inverted perovskite solar cells used in this thesis. In a solar cell, the perovskite (PVK) functions as absorber, the PTAA as hole transport layer, the C_{60} as electron transport layer, SnO_2 as buffer and barrier layer and the ITO as electrodes.

Nevertheless, so-called ’charge transport layers’ are required for the selective extraction of the charge carriers from the perovskite layer. In this thesis, PTAA is the hole transport layer (HTL). It is called HTL because it blocks the passage of electrons from the perovskite to the ITO electrode on the right due to the energy level of its conduction band (see Figure 2.1, red). Thus, it only allows holes to be extracted at this side of the solar cell. Consequently, C_{60} is the electron transport layer (ETL) as it blocks the passage of holes from the PVK to the ITO electrode on he left (see Figure 2.1, blue).

SnO_2 is a buffer and barrier layer. [38] It improves the quality of the interface between the ETL and the electrode layer (ITO). It also protects the C_{60} from damage during the deposition of the ITO-layer. Finally, it prevents the penetration of humidity into the perovskite layer.

The purpose of the electrodes (ITO in Figure 2.1) is to enable the lateral transport of charge. To fulfill that purpose, their conductivity needs to be as high as possible. At the same time, at least one electrode (and for semi-transparent devices, both electrodes) should also be as transparent as possible since illumination needs to pass them in order to reach the absorber layer. These conditions are fulfilled by a group of materials called ’transparent conductive oxides’ (TCOs). Indium-doped tin oxide (ITO) is the member of that group that is most commonly used due to its excellent electrical and optical properties, as well as its stability. [39]

2.2. Reverse Bias Breakdown

In this section, a detailed overview of the state of research regarding the proposed mechanisms of the reverse bias breakdown in perovskite solar cells is provided. To ensure understandability, the definition of the term "reverse bias breakdown" should be clarified first. This is required since, even in the literature on reverse bias of perovskite solar cells, this term is filled with different meanings.

2.2.1. Nomenclature

Figure 2.2 shows IV curves with three different behaviors in reverse bias. In an ideal pn-junction, the current flowing through the device follows the ’ideal diode equation’: [40]

$$I(V) = I_0\left[\exp\left(\frac{qV}{k_B T}\right) - 1\right] \tag{2.1}$$

It follows that the current approaches the value $-I_0$ in the dark at infinitely large reverse biases (black). [40] I_0 is called *saturation current* or just *dark current*. This current is very small and is generally considered negligible for reverse bias degradation when real devices are considered. Often, the current at small (positive and negative) voltages is dominated by small ohmic shunts, instead.

Real solar cells might also develop new shunts when operating in reverse bias (red). This can lead to an abrupt increase of the reverse bias current, and a severe loss of PCE. This abrupt increase of current through shunts might be related to a

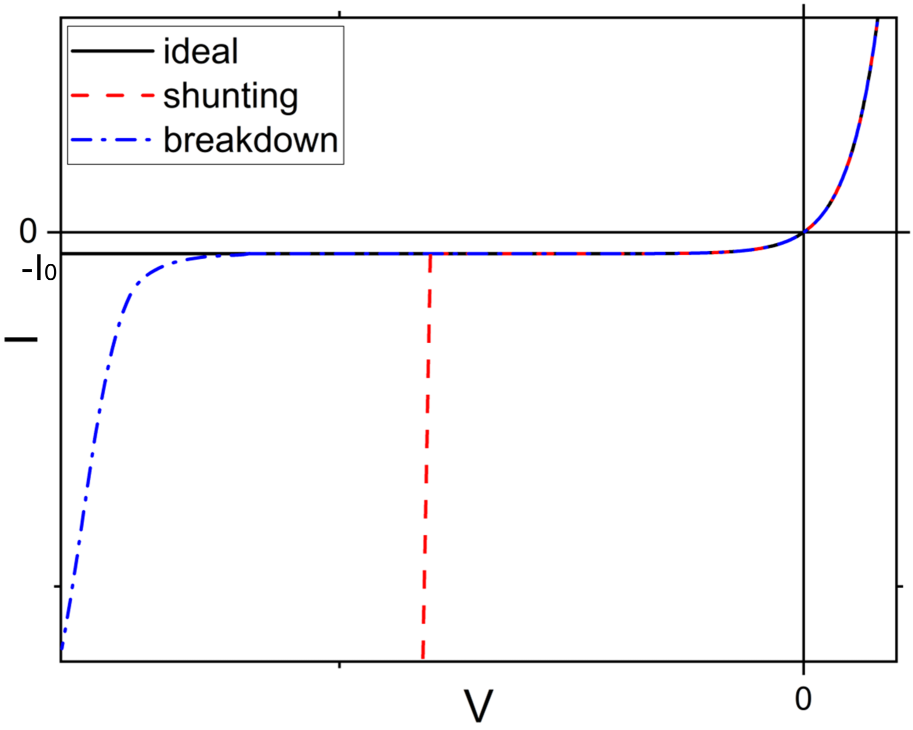

Figure 2.2. An IV curve that reaches into the negative voltage-regime with three types of reverse bias behaviors: The ideal diode approaches I_0 (black), shunting appears as an abrupt increase of the current (red), and the reverse bias breakdown as gradual increase of the current (blue).

phenomenon called ’thermal runaway’. [41] This involves a local current leading to local heating which increases the local conductivity. Increased conductivity results in more local current flow in a self-reinforcing process. This might go on until the Joule heating accompanying the high local current density leads to the decomposition of the surrounding material and severe degradation of the solar cell.

Finally, the blue curve shows the only behavior that will be called ’reverse bias breakdown’ in this work. Here, the current follows a gradual, approximately exponential increase. Most importantly, however, this breakdown in not inherently damaging to the solar cell. Instead, as long as damage due to excessive Joule heating is avoided, it is likely a reversible process (see Chapter 4 and 5).

2.2.2. Breakdown mechanism

Traditionally, the breakdown in diodes (and a solar cell can be seen as a simple diode) is effected through one of two basic mechanisms: [41]

- Avalanche Multiplication
- Tunneling

The first mechanism, avalanche multiplication, starts with a thermally-generated charge carrier in the depletion region. By the electric field (reverse bias), this charge carrier is accelerated. At higher reverse bias, the electrical field will become so strong that this charge carrier will have enough kinetic energy to create another charge carrier by collision (impact ionization). The newly-excited charge carriers can, in turn, also be accelerated and create more charge carrier pairs. This leads to a current flowing in a junction in the "wrong" direction.

The second mechanism, tunneling, allows charge carriers to flow across a junction without having sufficient energy to "cross over it". The probability for tunneling depends on the width and height of the tunneling barrier. [41] This process only plays a significant role when the barrier width, the ’tunneling distance’, is very small. Such a tunneling mechanism lies at the basis of the widely-accepted model for the reverse bias breakdown of perovskite solar cells.

This model was proposed by Bowring *et al.* and is displayed in Figure 2.3: [19] They consider a basic PSC stack with a perovskite absorber, transport layers on both sides and metal electrodes. The perovskite contains a mobile species that they identify as positively-charged iodide vacancies (V_I^+). However, the authors clarify that their model works just as well with other dominant mobile ion species, even if they are of a different charge. That clarification is necessary since it is often not clear which species is the dominant mobile ions species.

At $V = 0\,\text{V}$, in the dark and at a certain temperature (Figure 2.3a), the positively charged vacancies can diffuse through the perovskite material. Upon reaching the hole transport layer (HTL), they will accumulate in a thin layer at the perovskite/HTL interface because of the built-in electric field. At the same time, the comparatively immobile counter-ions are left behind and form a vacancy depletion region at the

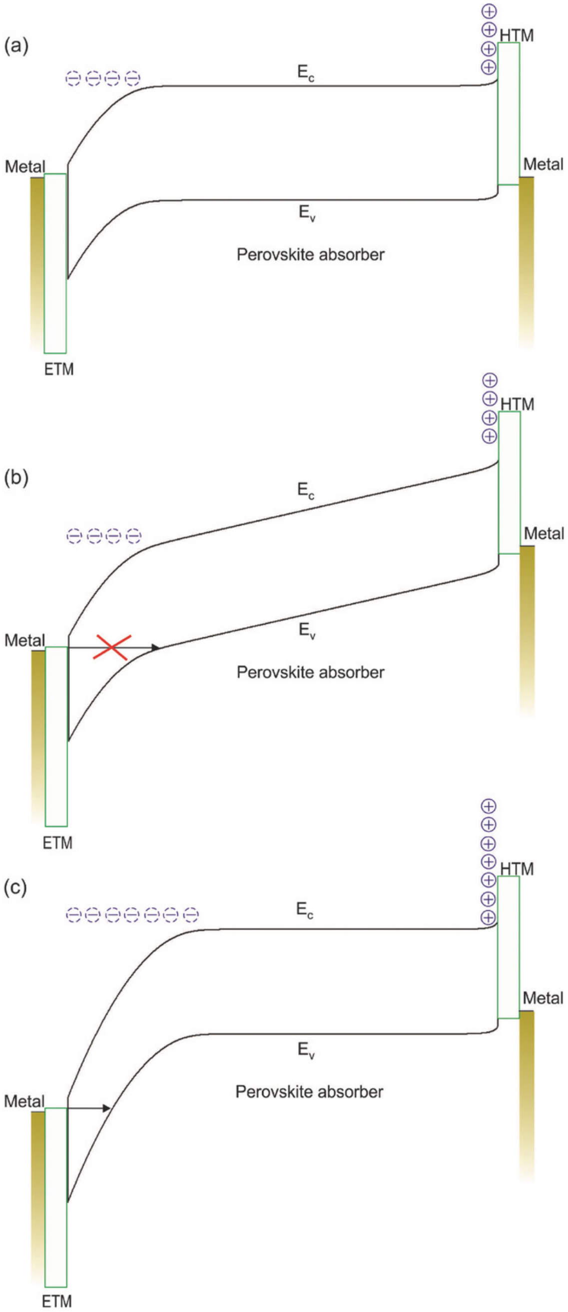

Figure 2.3. The model for the reverse bias breakdown of perovskite solar cells by Bowring *et al.* [19] In thermal equilibrium and at open-circuit in the dark ($V = 0\,\mathrm{V}$) (a), mobile vacancies have migrated to the interface, leaving behind a depletion region that bends the bands. When a reverse bias is applied, additional mobile ions begin moving towards the interfaces to screen the external field (b). When a new equilibrium is reached, the band bending can be strong enough to allow tunneling of charge carriers into the perovskite absorber (c). (with permission from [19])

electron transport layer (ETL). This accumulation of charges causes bending of the valence and conduction band. In equilibrium, the built-in field is restricted to the regions at the interfaces - mostly to the broad depletion region at the ETL - while there is no electrical field in the bulk of the perovskite absorber.

When a reverse bias is applied, the resulting electric field is added to the built-in field (Figure 2.3b). It causes additional vacancies to move towards the HTL to counteract the externally-applied field. That means that the depletion region at the ETL side of the absorber also grows. The increased accumulation of charges enhances the band bending further.

With increasing band bending, the distance between equal energy levels in the conduction band of the ETL and in the valence band of the absorber shrinks. As this distance is the width of the tunneling barrier, the probability for holes to tunnel from the ETL into the absorber rises (Figure 2.3c). Together with this probability, the reverse bias current grows. This current consists of injected holes which cross the absorber layer and recombine with electrons at the perovskite/HTL-interface.

This general model is not restricted to a specific dominant mobile ion species. Instead, it works just as well even with mobile anions instead of cations. Then, the difference is that the depletion region forms at the HTL and electrons tunnel from there into the absorber. In other words, the whole process proceeds in a mirrored way.

Indeed, the notion that mobile vacancies are the dominant mobile cation species was based on their experimental identification in methylammonium lead iodide ($MAPbI_3$). [42] However, Futscher *et al.* identified iodide (I^-, not the vacancy) and the methylammonium cation (MA^+) as mobile ion species in $MAPbI_3$. [43] In the work by Ni *et al.*, the authors argued that the dominant mobile ion species in $MAPbI_3$ are the positive and negative iodide interstitials (I_I^+, I_I^-). [29] Finally, Jacobs *et al.* investigated ion migration on double and triple cation perovskites. [44] They thought it likely that there are several mobile ion species and that their relative concentrations depend on details of the fabrication. That way, they could explain their findings that the sign of the dominant mobile ion species seems to vary between (theoretically alike) samples.

In this work, the term "mobile ions" is generally used to describe all mobile atomic species, being vacancies, interstitials, or ions.

The model of Bowring *et al.* was developed with a simplified, idealized perovskite solar cell in mind. To extend it to real materials, they added some additional considerations:

In most perovskite solar cells, the absorber is a polycrystalline material. A polycrystalline material consists of grains that are separated by grain boundaries. It has been shown that grain boundaries can serve as channels for ion migration. [45] Additionally, grain boundaries have also been connected to band bending and could therefore act as local weak spots for the breakdown mechanism. [46–48]

Finally, the reverse bias behavior has also been found to be dynamic, i.e. not a static property. Bowring *et al.* already noticed that the reverse bias current is not constant at all when a constant reverse bias voltage is applied. [19] They proposed that an electrochemical reaction augments the tunneling barrier during reverse bias current flow. One possible mechanism with this result would be the neutralization of mobile ions (i.e. reduction or oxidation). Neutralized mobile 'ions' would not contribute to the field screening anymore and weaken the band bending. This, in turn, would hinder the tunneling of holes into the absorber and decrease the reverse bias current.

Related to these findings, Wang *et al.* reported that the breakdown voltage of their devices increased with subsequent voltage sweeps into the reverse bias, naming this phenomenon 'dynamic reverse bias behavior'. [49] They argue that the mobile ions moving towards the interfaces of the perovskite absorber under reverse bias create an electric field opposite to the externally-applied reverse bias. This weakens the field that is felt by charge carriers within the perovskite layer and decreases the reverse bias current.

Other explanations for the dynamic reverse bias behavior include the formation of an insulating layer and dipole formation at an interface. [19] These could act as injection barrier for holes and thus hinder the reverse bias current flow.

2.2.3. Experimental support and alternative mechanism

What experimental findings support this mobile ion-facilitated tunneling mechanism?

Bowring *et al.* observed breakdown at voltages between $-1\,\mathrm{V}$ and $-4\,\mathrm{V}$. [19] They argued that these voltages are too low to cause the impact ionization that is necessary for avalanche breakdown. However, it is the electric field strength that is truly decisive for this mechanism, not the applied voltage. Due to the screening effect of mobile ions, the voltage could drop over only a part of the complete layer thickness of the perovskite. Then, the electric field could be far stronger in this part of the perovskite absorber than the voltage would let assume.

One criterion for distinguishing avalanche and tunneling mechanisms is the spatial variation in current density. It is often assumed that the avalanche breakdown is more localized than tunneling. [50–52] Bowring *et al.* presented infrared imaging results that show that current can flow through the whole cell area, therefore providing some more evidence for a tunneling mechanism.

The temperature-dependence of the breakdown voltage is traditionally a distinguishing feature, as well: [50] Avalanche breakdown shows a positive temperature coefficient. After all, the electric field required to accelerate charge carriers sufficiently for impact ionization depends on their mean free path between collisions. A higher temperature leads to a shorter mean free path. This means that a stronger electric field is necessary and that the breakdown voltage increases.

In contrast, tunneling has a negative temperature coefficient. [50] Increasing temperature leads to a shrinking of the band gap. A shrinking band gap means that the barrier height is decreased and thus the tunneling probability increased. Additionally, more free charge carriers are available at the band edge at higher temperatures. Therefore, a higher temperature is connected to a smaller breakdown voltage.

Additionally, in the case of perovskite solar cells, there is the effect of temperature on mobile ions to consider. Increased temperature would increase ion conductivity which could have a positive effect on the band bending due to the accumulation of mobile ions. More band bending could also result in a smaller breakdown voltage. Therefore, this is another reason why the tunneling breakdown in perovskite solar cells could show a negative temperature-coefficient.

While there is no dedicated study on the temperature-effect on the reverse bias behavior of perovskite solar cells available, some data has been published. Bowring *et al.* reported that a decrease in temperature leads to a larger breakdown voltage. [19] Tayagaki *et al.* reported that an increase in the temperature causes a decrease in the breakdown voltage. [53] Therefore, both sources show a trend that supports the previously-described breakdown model. However, preliminary experiments investigating the influence of temperature more thoroughly hint towards a more complicated relationship (see Appendix A).

More data is available that supports the crucial role of mobile ions. Ren *et al.* heated up their as-cast perovskite films in inert atmosphere for up to 20 h before proceeding with their fabrication process. The aim of this procedure was to allow for the increased volatilization of iodide, resulting in a higher concentration of iodide vacancies. With increasing heating duration, the breakdown voltage decreased, thus supporting the model. However, they did not show any experimental data supporting creation of additional mobile ions in the perovskite layer due to their heating procedure. Therefore, other effects, like improved annealing leading to bigger grains, could also play a role.

Another way of revealing the effect of mobile ions is varying the scan rate in voltage sweeps. With that in mind, Bowring *et al.* reported that a higher scan rate leads to a larger breakdown voltage. [19] They argued that the the mobility of the mobile ions could be the limiting factor at large scan rate since they are required to drift towards the interfaces in order to have an effect on the breakdown. At a larger scan rate, less mobile ions have reached the interfaces when a certain voltage is applied. Less mobile ions result is less band bending. Thus, the breakdown voltage appears larger since the tunneling barrier is wider. However, in the work by Wang *et al.*, higher scan rates led to a smaller breakdown voltage, instead. [49]

These results show that mobile ions play an important role in the reverse bias breakdown mechanism. At the same time, there seem to be factors or other mechanisms at play that are not yet sufficiently understood. Finally, it should be added that both Wang *et al.* and Auf der Maur *et al.* consider it likely that both tunneling and avalanche breakdown occur in perovskite solar cells and photodetectors. [49, 54]

2.2.4. Increasing the breakdown voltage

Based on this tunneling model, the authors of several publications investigated methods to increase the breakdown voltage. These attempts were motivated by the fact that higher breakdown voltages decrease the number of required bypass diodes in a module (as explained in Chapter 1). This is one way of dealing with the issue of partial shading and is supposed to increase the economical viability of perovskite PV. [16]

In the work by Ni *et al.*, a barrier for hole injection from the ETL into the perovskite was introduced at the perovskite/ETL side of the solar cell. [29] With such a barrier, a symmetric device with HTL layers on both sides of the perovskite layer (a ’hole-only’ device) showed lower currents at low voltages. Additionally, the degradation rate of a solar cell upon application of a small reverse bias was decreased. We interpret this stability increase as a consequence of a lower RB current at the same applied bias. This is equivalent to a higher breakdown voltage.

Wang *et al.* and Liu *et al.* worked on quasi-2-dimensional perovskite absorbers. The former improved both perovskite interfaces and reported an increase of the breakdown voltage. [30] The latter achieved increased breakdown voltages by reducing the concentration of iodide defects in their perovskite film. [32] Both defined the breakdown voltage as the voltage at which the reverse bias current suddenly, step-like increases in a voltage sweep. This might be caused by the development of shunts.

Jiang *et al.* focused on the "p-side" by modifying the HTL. [28] They argued that, even if hole injection occurs at the perovskite/ETL interface, the holes have to be extracted or recombine at the HTL for current to flow. Bertoluzzi *et al.* already argued that the process at the HTL might be the limiting factor for the reverse bias current flow. [20] To investigate this, Jiang *et al.* compared several common hole transport materials with various thicknesses and found that a thick PTAA layer provided the highest breakdown voltages.

As explanation, two possible effects were named. Firstly, a thick, polymeric HTL (e.g. PTAA) layer planarizes the rough electrode (ITO) beneath. A planar HTL, on which the perovskite absorber layer is deposited, prevents the local concentration of the electric field or reverse bias current at ’defected’ locations like ITO pyramids. Secondly, the thick, polymer layer serves as barrier against the injection of electrons from the PTAA into the perovskite. They also noted that both effects could well be responsible for the high breakdown voltages.

Additionally, they also showed that the metal electrode seems to play a role in the reverse bias breakdown. As explanation, they propose that the metal might be oxidized by injected charge carriers and then migrates into the perovskite. There it could be turned back to its metallic form which plays a role in the formation of shunts. For that reason, using a electrochemically less-reactive metal electrode yielded further increases to the breakdown voltage.

2.3. Reverse bias degradation

In the previous section, it was shown how a reverse bias leads to the breakdown of the diode behavior of a perovskite solar cell. As per our definition, the breakdown (avalanche or tunneling) itself is not detrimental. Nevertheless, in literature, it is tightly connected to a dramatic loss of the PCE in a very short time. Therefore, the mechanisms that this degradation has been ascribed to are described in the following sections.

2.3.1. Nomenclature

Just as the term ’breakdown’, the terms ’stability’ and ’degradation’ are used in various ways in this field of research. Therefore, they are shortly defined in the following. The stability describes how stable the solar cell parameters (i.e. PCE) are over time under certain conditions. Degradation means the loss in the solar cell parameters, observed when the solar cell experiences certain conditions for a certain time. However, there is reversible and irreversible degradation. A reversible loss of PCE can be (partially) recovered by a recovery treatment. This recovery treatment could involve maximum-power-point tracking, storage in the dark or other operating conditions. Irreversible degradation is the loss of PCE that remains after the recovery treatment.

While there were no standardized procedures for determining the breakdown voltage, there are protocols to draw upon for degradation experiments: The International Electrotechnical Commission (IEC) defines test sequences for "terrestrial flate-plate module materials". [55] Their purpose is to show that the modules are able to operate outdoors for a prolonged time. They, however, specifically deny that the test results are a quantitative prediction of lifetimes.

There are good reasons *not* to use these protocols for the purpose of investigating the reverse bias degradation of perovskite solar cells. One reason is that the IEC protocols are qualification tests for commercial products. They are not meant for research on solar cells. Another reason is that the reverse bias degradation of perovskite solar cells might follow different rules than the degradation of other technologies. Accelerated testing requires a thorough understanding of the degradation mechanisms. [56] It follows that tests designed for a completely different solar cell technology might not provide useful results.

The ISOS protocols were designed for research on thin-film solar cells. [33] Originally, meant for organic photovoltaic devices (OPV), they were extended to account for the idiosyncrasies of perovskite solar cells. The ISOS-V1 to V3 protocols clarify conditions under which a reverse bias degradation experiment is to be performed. They propose two electrical conditions that imitate the situations in a module with and without bypass diodes. Applying the negative open-circuit voltage ($-V_{oc}$) is related to the former situation, while the injection of the maximum-power-point current (I_{MPP}) corresponds to the latter. These protocols also define temperature and relative humidity: ambient air and room temperature (for V1). Furthermore, to account for the meta-stability of perovskite solar cells, they recommend a recovery process. This process includes storage in the dark at open circuit-conditions with periodic measurements of the performance until a saturation is reached. Also, they recommend using MPPT instead of voltage sweeps to measure in a steady state. Finally, the reporting of in-situ currents (at a fixed voltage) or in-situ voltage (at a fixed current) is requested.

Unfortunately, these protocols are rarely used in literature. For reverse bias degradation experiments, (seemingly) randomly-chosen fixed voltages are often applied. As a consequence, it is difficult to distinguish a changed breakdown voltage from a change in stability. To provide an example, picture two solar cells with breakdown voltage of $V_{BD} = -2\,\mathrm{V}$ and with $V_{BD} = -4\,\mathrm{V}$. When a reverse bias of $V = -3\,\mathrm{V}$ is applied, the first cell will let a large reverse bias current pass and show significant degradation. The second cell will let barely any current pass and will degrade far less. The conclusion would be that the cell with a larger breakdown voltage is more stable. However, if the degradation experiment involves injecting I_{MPP} to imitate the operating conditions of a shaded cell in a module without bypass diodes, then both cells would pass the same current. However, the first cell would operate at smaller reverse bias than the second voltage. Therefore, it might degrade less and suddenly the first cell appears more stable.

As additional weak spot, the degradation is often reported without detailing whether and which recovery process has been performed prior to the post-degradation measurement of the solar cell parameters. This might lead to the comparison of reversible with irreversible degradation.

Experiments that do not follow the ISOS protocols (or other detailedly-described protocols) are valuable when it comes to research into mechanisms, of course. However, to compare and report degradation, following the ISOS standards seems to be the best practice.

2.3.2. Mechanisms of reverse bias degradation

Various degradation mechanisms have been proposed to occur in perovskite solar cells. They are schematically represented in Figure 2.4:

- Shunt formation (1, 2)
- Halide incorporation into ETL (3)
- Oxidation of halides (4)
- Undefined interfacial process (5)
- Phase segregation (6)

In the following, the mechanisms are described in more detail and a look at the (experimental) results that support them is taken.

Shunt formation

The formation of shunts is the most serious of the degradation mechanisms in perovskite solar cells. Shunting leads to irreversible and drastic decrease of the PCE.

Its frequentness and seriousness can be gathered from the fact that it is considered as a breakdown mechanism in several publications. As consequence, the observation that shunt formation occurs at larger voltages in a voltage sweep is sometimes understood as a sign of increased stability against reverse bias degradation. Additionally, it is a hurdle for research on reverse bias stability since shunting hides other information about the solar cell. Accordingly, the mechanism of shunt formation is investigated in several publications.

There are two different schools of thought. On one hand, the formation of shunts might be related to metal filaments forming in the perovskite layer (Figure 2.4: 1). On the other hand, shunting might also occur at pinholes in the perovskite layer.

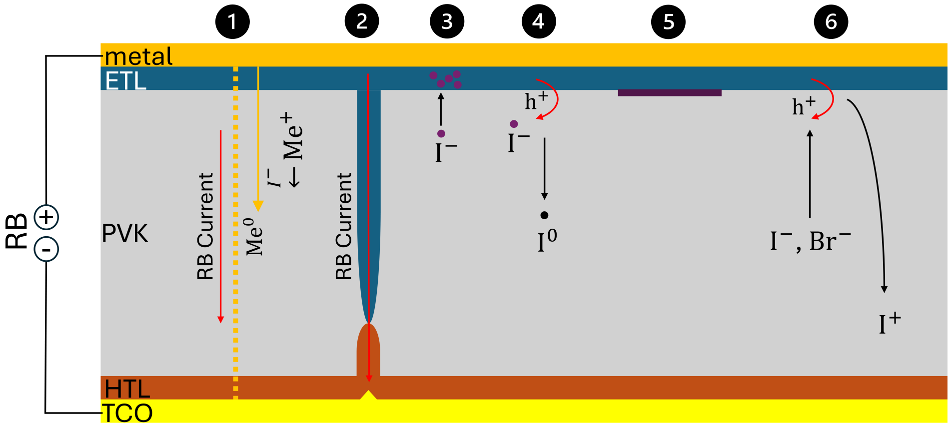

Figure 2.4. A schematic representation of a perovskite solar cell in reverse bias with six different degradation mechanisms: 1 and 2 show ways of shunt formation: either by way of metal migrating into the perovskite and the creation of a filament, or at pinholes in the absorber where ETL and HTL are in contact, forming a thin pn junction. 3 shows the migration of iodide (I^-) towards and into the ETL. 4 shows the tunneling of holes (h^+) into the perovskite and their oxidation of iodide (I^-) to iodine (I^0) which acts as recombination center. 5 shows a barrier at an interface. 6 shows halide phase segregation with the halide anions (I^-, Br^-) moving towards the ETL, iodide (I^-) being oxidized there to its cation form (I^+) which then moves towards the HTL.

There, the transport layers are (nearly) in contact with each other and form diode-like shunts which can breakdown and turn into ohmic shunts ((Figure 2.4: 2)).

The fact that shunting occurs in perovskite solar cell when a reverse bias is applied has already been reported by Bowring *et al.* [19] They did not only present the linear JV curves of shunted solar cells but also used infrared imaging to see the localization of current. They also found that this shunting happens more often, but not only, in cells with metal electrodes.

Razera *et al.* reported similar observations using dark lock-in thermography for imaging. [18] They proposed two different mechanisms to explain shunt formation at metal electrodes and at ITO electrodes. Inspired by corresponding reports for perovskite memristors and reports about metal migration at forward biases, they proposed the formation of metal filaments in the absorber layer. However, for metal-free devices a different explanation was required. Therefore, the authors proposed that the loss of iodide due to outgassing or the local accumulation of ions might lead to the destabilization of the perovskite, resulting in the formation of metallic lead. Metallic lead in the perovskite layer could then act as shunt.

Especially the latter model was further developed by connecting it to reduction/oxidation reactions of halides:
According to Li *et al.*, iodide (I^-) drifts towards the ETL and is there oxidized to its neutral form (I^0) by injected holes. [31] Iodine can then react with metallic copper (Cu^0) of the electrode, resulting in the formation of the copper cation (Cu^+). This cation is driven by the electric field into the perovskite layer and is there reduced

again to metallic copper (Cu^0) which can create local weak spots for current flow.

Jiang *et al.* proposed a slightly different model with iodide reacting with metallic silver of the electrode. [28] Silver could also be oxidized by injected holes to its cation (Ag^+). In the perovskite layer, the silver cation could then be reduced again to metallic silver. Additionally, the lead cation (Pb^{2+}) could be reduced to metallic lead (Pb^0), leading to degradation and shunting.

In contrast, the work by Johnson *et al.* attempts to shift the paradigm completely. They argue that the shunts that often appear in perovskite solar cells under reverse bias form at pre-existing defects in the absorber layer. At these pinholes, the transport layers (ETL, HTL) are in direct contact with each other, locally behaving like a pn junction. These pn junctions with thicknesses of around $20\,\mathrm{nm}$ could allow avalanche breakdown at small reverse biases.

They showed that these pn junctions normally act as non-ohmic shunts with limited impact on the PCE in operation. However, when a realistic current flows through such a small shunt in reverse bias, it can heat up the metal electrode to its melting point. This molten metal is then responsible for the destructive shunting by creating a contact between the opposite electrodes.

Halide incorporation into ETL

When the solar cells do not shunt, other degradation mechanisms can be observed instead. One of them is the halide incorporation into the organic electron transport layer (Figure 2.4: 3).

This was observed by Razera *et al.* via energy-dispersive x-ray spectroscopy (EDX) chemical mapping. [18] From a comparison of the iodine signals before and after reverse bias degradation, it could be seen that iodine has moved into the C_{60} layer. In its anion form, it might p-dope the ETL (or compensate the n-doping) and reduce conductivity of the transport layer. The occurrence of s-shapes in the JV curves after reverse biasing was explained with this iodide incorporation into the ETL. S-shapes are generally signs of a barrier for charge transport or extraction. [57]

Further support for this model came from the work by Gould *et al.*: [58] They investigated the changes in the bands using cross-sectional Kelvin probe force microscopy. Their results showed a shift of the work function of the C_{60} that increased with the duration of the reverse biasing. They ascribed this change in band energetics to the presence of iodide or iodine at the ETL.

Finally, Ren *et al.* incorporated a layer at the the perovskite/ETL interface whose purpose was the capturing and confining of iodide. [21] They used x-ray photoelectron spectroscopy (XPS) to confirm the presence of iodine on the peeled-off metal electrode. Only the solar cells without the above-mentioned additional layer showed significantly increased iodine signals after reverse biasing.

Oxidation of halides

Bertoluzzi *et al.* built up on the breakdown mechanism that was summarized above (see section 2.2.2) to propose an additional degradation mechanism. [20] They argue that the injection of holes at the ETL and the injection barrier for electrons at the HTL lead to a far higher concentration of holes than electrons in most of the absorber. Especially in the region where the band are nearly flat, outside of the depletion region, their model implies an accumulation of holes. This accumulation of holes can lead to the oxidation of halide anions, notably iodide (Figure 2.4: 4).

The resulting halogens act as centers for non-radiative recombination and reduce the open-circuit voltage (V_{oc}) and the short-circuit current density (J_{sc}) of a solar cell in operation. This degradation mechanism is, however, reversible as upon illumination or operation in forward bias, the concentration of electrons and holes are approximately equal. Then, the neutral halogens would be reduced back to their anion form. Only when neutral iodine forms gaseous I_2 and effuses from the device, an irrecoverable aspect of the mechanism is present.

Their simulations were able to reproduce most of the degradation that they observed in their devices. Only the significant fill factor losses due to a series resistance (R_s) increase could not be explained. This increased R_s was explained by undefined interface processes. Experimental support for this model might come from an observation by Tayagaki *et al.*: [53] They observed after partial shading degradation that the shaded cell showed a reduced electroluminescence intensity and ascribed this to an increase in non-radiative recombination.

Undefined interfacial process

The undefined interfacial processes (Figure 2.4: 5) that were previously mentioned have been proposed in the work by Bowring *et al.*: [19] They observed the increase of the breakdown voltage and a decrease in V_{oc} and ascribed both to one process. Their experimental results implied a dependence on the current and therefore they concluded that a electrochemical reaction might be responsible. One option might be the neutralization of mobile ions near an interface. Other propositions involve the formation of an insulating layer or dipole formation at an interface.

More experimental proof of interfacial processes are available in the work by Aninat *et al.*: [59] They performed partial shading experiments on mini-modules. After degradation, they observed a stronger photoluminescence (PL) signal in short-circuit but a drastically weakened electroluminescence (EL) signal. They interpreted these findings as a sign of a barrier at a perovskite/transport layer interface. This barrier would then hinder the extraction of charge carriers in PL and the injection of charge carriers in EL.

Phase segregation

Halide phase segregation in double-halide perovskites during reverse biasing was first reported by Razera *et al.* ((Figure 2.4: 6)): [18]
They identified iodide-rich (near the HTL) and bromide-rich (near the ETL) regions in the absorber after reverse biasing, using EDX. Additionally, photoluminescence spectra showed a red shift from the HTL side and a blue shift from the ETL side, corresponding to the same demixing of halides. They also found that the reverse bias current has to play a role since the changes to the PL spectrum could only be observed when a reverse bias current had flowed through the solar cell.

As a consequence, they connected their findings to the model for photoinduced halide segregation, reported by Hoke *et al.* [60] There, the presence of excess free carriers are necessary for the effect to occur. Reverse bias current flow could be responsible for these charge carriers.

A more detailed explanation was supplied by Kerner *et al.* [61] They argue that halide ions (e.g. I^- and Br^-) drift under the electric field towards the ETL where hole injection occurs. Only iodide is oxidized there due to its more advantageous oxidation potential in comparison to bromide. Thus, Br^- accumulates at the ETL while I^- reacts to its neutral form (I^0) or even its cationic form (I^+). These iodine forms consequently drift or diffuse in the opposite direction towards the HTL. This leads to the observed halide phase segregation.

Critical requirement for this mechanism is that, in reverse bias, there are far more holes present in the absorber than electrons. This has been shown by Bertoluzzi *et al.* and underlies their model on halide oxidation. [20]

2.3.3. Increasing stability

Based on these degradation mechanisms, methods to improve the stability are proposed. In most cases, the destructive shunting of perovskite solar cells under reverse bias is the target of these mitigation attempts:

Several authors introduced interlayers or barrier/buffer layers between the perovskite and the metal electrode. [21, 25, 26] The goal of these modifications was to prevent the migration of halide ions or metal ions towards the metal electrodes or into the absorber, respectively. In other publications, the material of the electrode is exchanged for a less reactive alternative: Jiang *et al.* exchanged silver for gold electrodes and Bogachuk *et al.* presented highly stable mesoporous cells with carbon electrodes and without organic ETL. [23, 28] Bogachuk *et al.* also used a perovskite with only one cation and one halide to prevent phase segregation. [23]

Following their alternative model for the formation of shunts, Johnson *et al.* showed higher stability on smaller cells since the probability of macroscopic defects is lowered. Additionally, they recommend clean deposition processes for the perovskite to reduce the occurrence of pinholes as weak spots and uniform deposition for the transport layers. That way, the transport layers do not come into contact with each other even if pinholes are present in the absorber layer. This should decrease the chance of the formation of shunts.

For the other proposed degradation mechanisms, no counter has yet been proposed.

While these solutions demonstrate the degradation mechanisms, their direct applicability in the commercial production of perovskite PV modules is doubtful (e.g. gold electrodes) or will require more optimization (carbon electrodes). The use of a perovskite with only one cation and one halide even removes one of the unique advantages of the technology and is therefore not practical. Clearly, more research is required to find ways to improve the stability of perovskite solar cells under reverse biases.

3

Experimental

3.1. Fabrication and Sample Design

In the following section, a basic description of our samples will be provided. They differ from chapter to chapter only in small details. The detailed fabrication procedures can be found in the appendices of each corresponding chapter.

Our samples were small, lab-scale perovskite solar cells with cell areas of $0.16\,\mathrm{cm}^2$ or $0.20\,\mathrm{cm}^2$. Their layer structure is displayed in Figure 3.1a with approximate thicknesses. As transparent conductive oxides (TCOs) have been used for both bottom and top electrode (in this case indium-tin oxide (ITO)), the cells are semi-transparent. The main reason for using semi-transparent cells is that the metal electrodes of opaque cells plays an important role in quick degradation by shunting when operating under reverse bias. A more detailed discussion of the degradation mechanisms and the role of metal can be found in Chapter 2. The hole transport layer PTAA and the perovskite layer were deposited by spin coating. The electron transport layer C_{60} was thermally evaporated, SnO_2 was deposited via spatial atomic layer deposition (sALD), and both ITO electrodes were sputtered. The gold grids were thermally evaporated.

The substrate design used in this work places four cells on each substrate. This is displayed in Figure 3.1b. The cell area is defined by the overlap between the orthogonal bottom and top ITO stripes.

3.2. Characterization

The characterization of these samples plays an important role in our experimental research. For that reason, some of the standard techniques that were employed in our work are introduced. Generally, however, the details of measurements and unique additional experiments are provided in the chapters or the corresponding appendices.

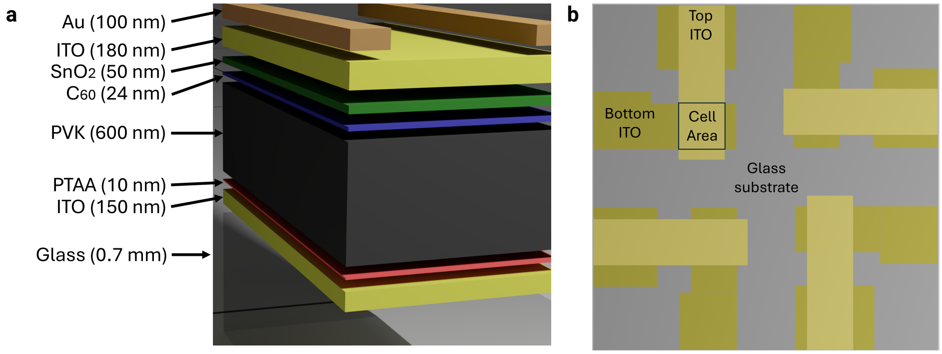

Figure 3.1. The samples used in this work are depicted schematically as a cross-section of the perovskite solar cells (a) and a substrate with four cells in a top-view to demonstrate how the overlap of the electrodes defines the cell area (b).

3.2.1. JV measurements and MPPT

One of the most basic characterization techniques employed on solar cells is the *JV measurement*. Its main purpose is to ascertain the power conversion efficiency (PCE), together with several other solar cell parameters. To that end, certain standard measurement conditions have been defined to ensure widespread comparability of the results; the standard test conditions (STC) according to ISO 9845-1: The incident power and approximate spectrum of the illumination are fixed as $1000\ \mathrm{W\,m^{-2}}$ and the AM1.5G spectrum, respectively. The temperature of the solar cell should be kept at 25 °C. Since the temperature of our cells under illumination during measurements was generally not measured, compliance with this requirement is not guaranteed.

In this work, a dual light source solar simulator (WACOM, class AAA) together with a Keithley 2400 source meter was used. The voltage sweeps were performed with a scan rate of about $0.1\ \mathrm{Vs^{-1}}$, starting from 1.2 V and ending at either -0.5 V or -0.2 V for the reverse (RV) sweep. Immediately afterwards, the forward sweep was performed within the same voltage range but the opposite direction. The four cells on one substrate were characterized sequentially from cell 1 to cell 4 under constant illumination of all cells. Cooling was provided by blowing dry air over the sample surface. Generally, the sets of JV measurements were repeated to serve as pre-conditioning treatment in order to ensure the measuring of stable parameters.

In the field of perovskite solar cells, it is standard practice to use an illumination mask. This is a plate of opaque material (e.g. metal) with a (square) hole that lies between the light source and the substrate. Its purpose is to define the illuminated area clearly and to reduce the impact of the edges of the cell area on the measurement. This is achieved by choosing a size for the illuminated area that is smaller than the cell area. In this case, an illuminated area of $0.09\ \mathrm{cm^2}$ was used with cell areas of at least $0.16\ \mathrm{cm^2}$. This results in a "JV curve" of which an example is displayed in Figure 3.2.

The solar cell parameters that are determined that way include the open-circuit voltage (V_{oc}), the short-circuit current density (J_{sc}), the fill factor (FF), and the max-

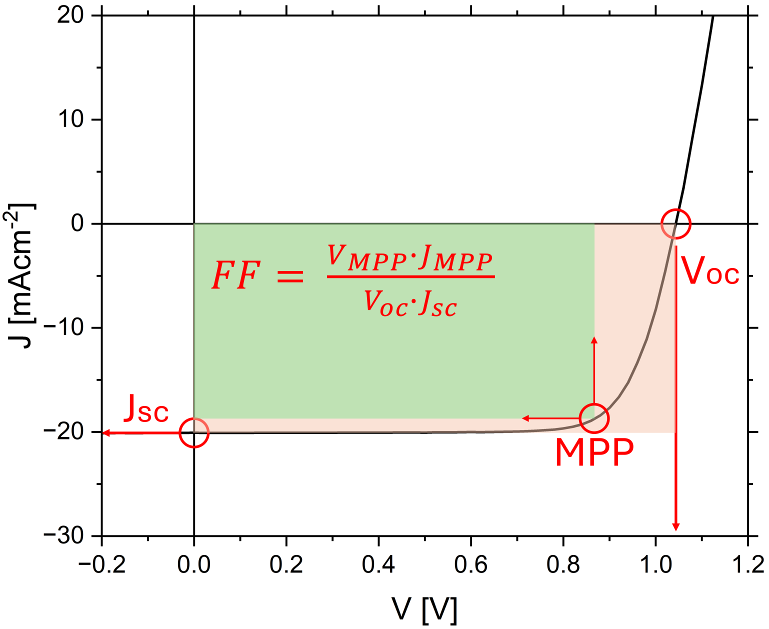

Figure 3.2. A JV curve with solar cell parameters.

imum extracted power (P_{MPP}). The power conversion efficiency (PCE) is calculated by comparing the P_{MPP} to the power input via illumination ($P_{illumination}$):

$$PCE = \frac{P_{MPP}}{P_{illumination}} = \frac{V_{MPP} \cdot J_{MPP}}{P_{illumination}} = \frac{V_{OC} \cdot J_{SC} \cdot FF}{P_{illumination}} \tag{3.1}$$

Not only, but especially for perovskite solar cells, this measurement and the interpretation of its results are complicated by the so-called *JV hysteresis* phenomenon. It has been first identified in a work by Snaith *et al.* in 2014. [62] Here, it describes the impact that the sweep direction has on the JV curve. That means that a reverse (RV) sweep from V_{OC} to J_{SC} results in different solar cell parameters than a forward (FW) sweep from J_{SC} to V_{OC}. In most cases, the RV sweep returns a higher PCE than the FW sweep. This impact of the sweep direction is additionally modulated by the scan rate of the voltage scan. [63, 64]

The origin of this phenomenon has been the subject of research that has been on-going for years (e.g. [62, 65, 66]). It is generally assumed that mobile ions are the main reason behind the occurrence of JV hysteresis. [65–70]

Following Tress *et al.*, the impact of mobile ions can be explained by their interaction with the external electric fields during RV and FW sweep: [71]
A RV sweep begins at a voltage $V \geq V_{OC}$ and proceeds towards $V \leq 0$ V, while a FW sweep returns from $V \leq 0$ V to a voltage $V \geq V_{OC}$. Therefore, the solar cells operates with a pre-bias of a high voltage during the RV sweep and with a pre-bias of a slightly negative or absent bias during the FW sweep. An absent or negative voltage causes

mobile ions to accumulate at the interfaces. There, they screen the external electric which hinders charge collection. That leads to a lower PCE during the FW sweep. In contrast, the mobile ions move away from the interfaces towards the bulk of the absorber layer upon high voltages. That, consequently, leads to improved charge collection compared to the first case. It follows that the JV measurement during a RV sweep shows a higher PCE than during a FW sweep.

The impact of the voltage scan rate then emerges from the limited ability of the mobile ions to 'react' to the changing external electric field: [63, 64, 72] The mobility of the mobile ions is the limiting factor. It has been found that the hysteresis is absent at both very large and very small scan rates. At very large scan rates, mobile ions can be assumed to be static during a voltage scan. At very small scan rates, the mobile ions are able to reach a new equilibrium at every measurement point. Therefore, at these extrema, the inadvertent pre-bias treatments do not affect the solar cell operation. No hysteresis is present. On the other hand, at scan rates between the two extrema, hysteresis can be observed.

This phenomenon, and the resulting lack of confidence in JV measurements, forced the community to search for solutions or work-arounds: One consists of extended reporting of measurement results and parameters. For instance, it is widespread standard practice to report the results of both RV and FW sweep.

Another solution is to measure the PCE in a steady state that corresponds closer to outdoor operation with an absence of fast changes to the operating point. This is called "maximum-power-point-tracking" (MPPT). As the name implies, the cell is operating in the maximum-power-point, so at V_{MPP} and J_{MPP}, and changes to this operating point are tracked actively. This is realized by incrementally changing the voltage and measuring the change in extracted power. If the power has increased, a new MPPT has been found; if not, the previous voltage is applied again.

The disadvantages of this technique lie in its longer duration and its more demanding measurement apparatus. In return, the absence of a voltage sweep means that hysteresis cannot occur and the resulting PCE is more realistically describing the performance in operation. Together, JV measurements and MPPT form the most basic characterization techniques that are performed on perovskite solar cells.

3.2.2. Reverse Bias (RB-)JV measurements

The purpose of the RB-JV measurement is to investigate the behavior of the solar cell in reverse bias. It is a voltage sweep with a range that extends into the reverse bias regime. As it is supposed to imitate a partial shading event, it is generally performed in the dark. Often, a metric called "Breakdown Voltage" (V_{BD}) is determined from the RB-JV curve, aiming to describe the reverse bias behavior with a single number. However, in contrast to JV measurements, neither the measurement conditions nor the method of determining this metric are standardized. As a result, the measurement conditions vary among published RB-JV measurements and various different definitions of the V_{BD} are used in parallel. This problem will be discussed in more detail in Chapter 4.

The setup used in this study for RB-JV measurements consisted of an electromagnetically shielded box for sample placement and contacting, and an Autolab

PGSTAT30, controlled by the software NOVA 2.1.4 from Metrohm as voltage/current-source.

Generally, RB-JV measurements used a voltage range of 1.0 V to -8.0 V, or until a current cut-off was reached (RV sweep) and back to 1.0 V (FW sweep). This current cut-off differs from chapter-to-chapter from around $0.3I_{sc}$ to $0.5I_{sc}$, and to I_{sc}. The choice of the current-cutoff significantly influences the degradation experienced by the samples during the measurement and was therefore adjusted to expected sample stability. This is also discussed in more detail in Chapter 4.

3.2.3. Imaging Techniques

Often, solar cells with contacts on both sides are considered to be 1-dimensional or as one spatially homogeneous device. One example can be found in the JV measurements: From the current flowing through the solar cell and the approximate cell area, a current density is determined. This assumes that the current density within the cell area is homogeneous. Another example is the usual equivalent circuit where one diode and some resistances are used to model the behavior of a solar cell. Once again, this is based on the underlying assumption that the diode behavior of the solar cell is constant across the cell area.

This works well for small devices where gradients in material properties and series resistance are negligible. However, when the resistance of the electrodes increases or when local material properties rise in importance, a more realistic perspective is advantageous. That is where imaging techniques gain prominence that allow the creation of a 2-dimensional map of a solar cell property. One such imaging technique is electroluminescence (EL) imaging.

In order to take an electroluminescence image, a current is injected into a solar cell. The resulting charge carriers in the device can recombine via different mechanisms. For one of these recombination mechanism, a electron and a hole recombine radiatively, meaning that their energy ($E = E_g$) is released in the form of a photon. This photon can be detected by a camera. As recombination and emission of a photon is the reciprocal process to the "normal" process of absorption of a photon and creation of a pair of charge carriers, both are closely connected.

The EL signal ϕ_i detected at a position i can be described the following way: [73]

$$\phi_i(E) = C_i \cdot \exp\left(\frac{qV_i}{V_{th}}\right) \tag{3.2}$$

Here, C_i is a constant that depends on the geometry of the setup, properties of the camera and recombination in the sample.V_i is the local diode voltage, and V_{th} is the thermal voltage. It is important to note that V_i is generally *not* equal to the externally applied voltage. Instead, it is modified by series resistance losses across the electrodes.

A schematic EL measurement is depicted in Figure 3.3a where a gradient of V_i leads to a gradient in EL signal ϕ_i. To determine the local diode voltage and indirectly image the local series resistance, several methods have been developed. One such

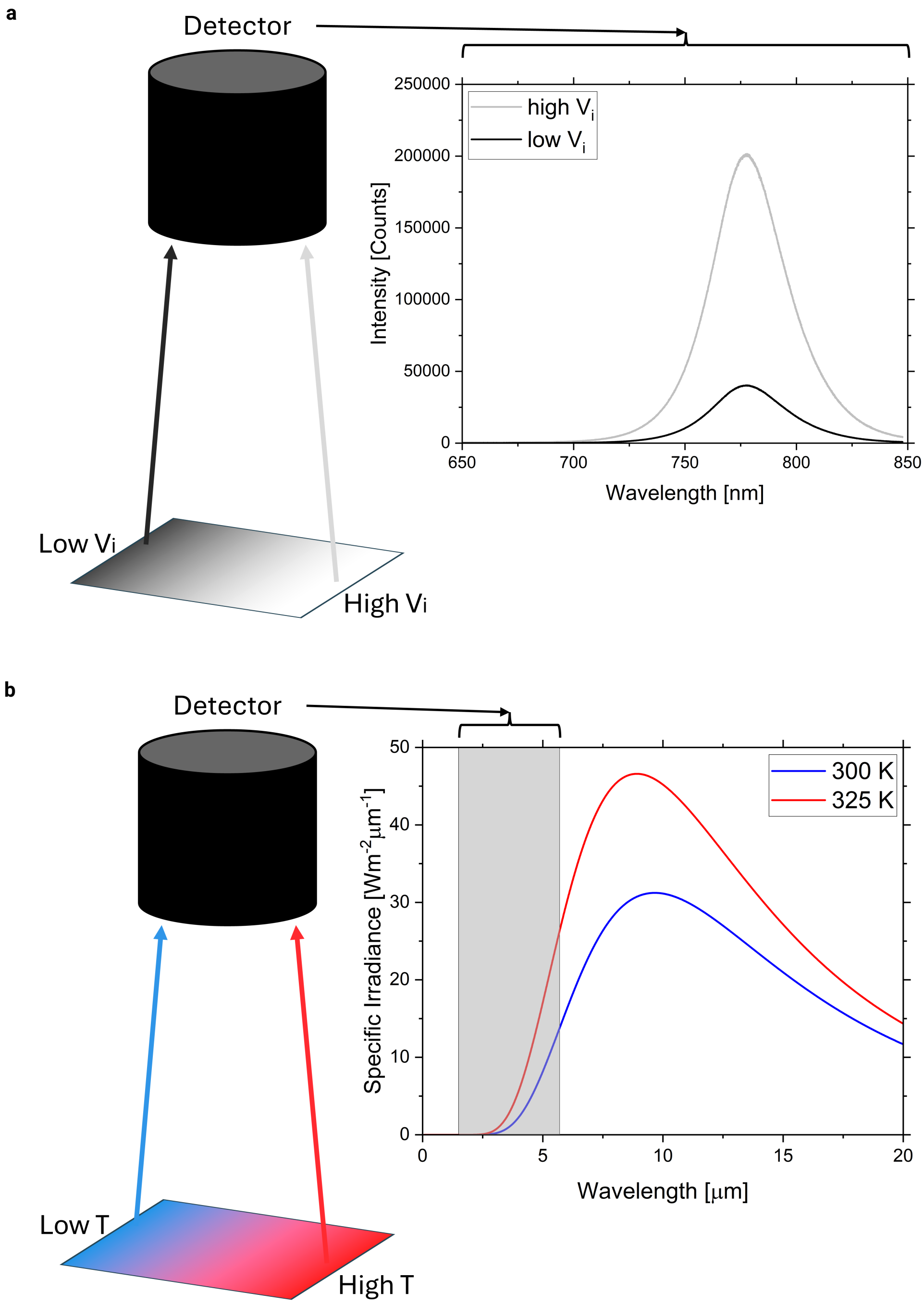

Figure 3.3. The basic principles of the imaging techniques: electroluminescence (a), thermography (b).

method has been published by Haunschild *et al.* and is described in detail in Chapter 7. [74]

In this work, the setup used for electroluminescence imaging was a GreatEyes system with a GE 1024 1024 BI MID camera (Si-CCD) and a Keithley 2400 as current-voltage-source. The software controlling the system and for the basic data processing was GreatEyes LumiSolarCell 7.0 SR in combination with a Python script.

Imaging of solar cells is not only possible by making use of electroluminescence. Imaging techniques based on thermography are another option. Two such techniques will be shortly introduced here. They are steady-state infrared imaging (ssIR) and its more advanced derivative the Lock-In thermography (LIT).

Fundamentally, both make use of the property of matter of a certain temperature to emit light. This is the black body radiation which is, for non-ideal objects, modified by a factor called emissivity. Generally, however, the spectrum or the irradiance at certain energies depends mostly on the temperature. That makes it possible to image the temperature, or at least temperature distributions, on surfaces by detecting the local emission of photons in the infrared (IR). This is displayed in Figure 3.3b where a temperature gradient leads to a gradient in IR emission intensity. Imaging temperature differences in solar cells is attractive since any internal current flow heats up the surrounding area due to Joule heating. That means that imaging the surface temperature of a solar cell enables us to investigate where the current flows.

The main difference between ssIR and LIT lies in the way the observed temperature differences are caused. Steady-state infrared thermography is also called 'passive' since it involves recording the surface temperature in a steady-state. We can observe the temperature distribution on the surface in normal operation (in-situ), or any other desired state. The only demand is that that current flow is present to cause significant local heating. Due to the (normally) low-power operation of a solar cell and the limited sensitivity of thermocameras, this is a serious limitation. A second problem of ssIR is the spatial dissipation of locally generated heat. The signal of a localized heat source is spread into the surrounding area which limits the available spatial resolution.

Both limitations are partially overcome by adding the Lock-In principle to the technique. That means that the sample is not passively observed anymore but actively excited by injecting a current periodically. In other words, the current source is rhythmically switched on and off and in that way, a wave-like temperature signal with a defined (Lock-In) frequency is created. The camera records the surface temperature with another frequency than the Lock-In frequency. The resulting images are averaged over several periods and weighted with the Lock-In frequency. That results in the removal of signal noise that does not follow the wave-function of the excitation. Even if statistical noise approximately follows the Lock-In frequency, it averages to zero due to the integration over several periods. Additionally, the spatial resolution is increased since the thermal waves radiating out from local heat source are also related to the Lock-In frequency. This improvement, however, depends on the chosen Lock-In frequency.

That brings us to the main disadvantage of the Lock-In technique: The modulated, square-wave excitation is not at all a natural state of operation for a solar cell. Additionally, the slow processes in perovskite solar cells that can take many seconds (e.g. ion migration) cannot be resolved with faster Lock-In frequencies. That means that the measurement is restricted to relatively large Lock-In frequencies which reduces the advantage in spatial resolution. And even then, the state in which the solar cell operates during the excitation is not well-defined.

All three imaging techniques are used to image the reverse bias behavior of perovskite solar cells in Chapter 7. The strengths and weaknesses of each technique are shown there on the basis of experimental results.

The thermocamera used for both ssIR and DLIT in this work was a InfraTec ImageIR 8300 (InSb-camera). For the ssIR imaging, an Autolab PGSTAT30 with the software NOVA 2.1.4 served as current-voltage-source. The camera control and basic data processing was performed by the software IRBIS 3.1 Professional. For the DLIT imaging, a TDK-Lambda was the voltage source, instead. The software IRBIS active online 1.1.154 controlled source and camera and did the basic data processing.

4

Determining the reverse bias breakdown voltage

The degradation of perovskite solar cells due to reverse biases is one of the remaining challenges hindering the commercialization of the technology. To overcome this challenge, a thorough understanding of and control over the breakdown voltage is crucial. A prerequisite for this is that the community 'speaks the same language', i.e. that the breakdown voltages that are reported are comparable. A review of literature data shows that the impact of measurement parameters is often unknown and seems to depend strongly on sample properties. It follows that standardization is the only way to reach comparability. Here, a set of measurement parameters to fill this gap is proposed. As additionally various definitions of a 'breakdown voltage' are used in parallel without any way of relating them to each other, this metric and its determination need to be considered as well. After a thorough discussion of the available definitions, using the point of maximum curvature is introduced. Its main advantage is the possible connection to an analytical description of the breakdown mechanism. In this way, a starting point for scientists new to the field of reverse bias stability is provided and the ground for a broader discussion in the community is prepared.

This chapter is based on: J. Henzel *et al.*. 'Determining the Reverse Bias Breakdown Voltage of Perovskite Solar Cells'. In: Solar RRL. 10.3 (2026), p. e202500875. DOI: 10.1002/solr.202500875.

4.1. Introduction

Concerns about the stability of perovskite solar cells (PSC) and modules is considered one of the remaining hurdles for the commercialization of this technology. [14, 75] There are various stressors that have been reported to cause degradation in perovskite solar cells, e.g. light [76, 77], temperature [78], atmosphere [79, 80], and bias [19, 81]. The existing IEC standards were designed to test the silicon-based field panels and have been shown to reflect the stability of thin-film photovoltaic technologies insufficiently. [82] Therefore, the ISOS (International Summit on Organic Photovoltaic Stability) protocols were designed which define experimental conditions that can be used to investigate the impact of these stressors and combination of stressors on perovskite solar cells in a comparable way. [33]

The ISOS-V-1 to ISOS-V-3 protocols deal with electrical bias stability which includes the degradation caused by reverse biases. [33] In a module, reverse biases can occur when the series-connected cells in a string do not generate the same current. This can be caused by partial shading, when a part of the module area is shaded while the remaining part of the module is illuminated.

A simplified, standardized partial shading event has been described in the work by Dongaonkar: [83] One cell of a module is completely shaded and does not generate any current while the remaining cells are illuminated. Due to the series-connection, this one shaded cell has to pass the current of the current-generating cells. That is only possible when this cell operates at a negative voltage, i.e. at a reverse bias.

It has been shown that reverse bias (on cells) and partial shading (on modules) can lead to significant and fast degradation of the power conversion efficiency (PCE) in PSCs. [18, 19, 59] An overview over the mechanisms involved in breakdown and degradation can be found in the work by Wang *et al.* [17] Interestingly, it seems that the degradation rate scales with the *reverse bias current* and not the reverse bias itself. [84, 85] It follows that - in order to avoid degradation in modules - the reverse bias current needs to be limited as much as possible during partial shading events.

Silicon photovoltaics (PV) manufacturers employ bypass diodes for this purpose. They are added anti-parallel to strings of cells in order to offer a low-resistance current path in case of a reverse bias. However, this solution does not work for modules based on PSCs and other thin-film PV technologies.

One reason is the monolithic interconnection strategy with its long, narrow cells that is preferably employed in thin-film PV technologies. That leads to problems with the use of external bypass diodes (for more information, see [16]). Another problem lies in the difference in *breakdown voltage* between silicon solar cells and PSCs. The breakdown voltage (V_{BD}) is a metric that describes the voltage at which a reverse bias current flows. A higher V_{BD} means that one bypass diode can protect a 'longer' string, so more series-connected cells. [16, 18] A smaller number of bypass diodes per module leads to lower manufacturing costs. Typical breakdown voltages in crystalline-silicon solar cells are reported to be -15 V. [86] In contrast, often-mentioned values for perovskite solar cells are -1 V to -5 V. [87] Recently, there have been, however, also reports of higher breakdown voltages. [21, 28, 30, 31]

As the breakdown voltage is a decisive parameter for the reverse bias stability, significant effort has been put into investigating the breakdown voltage mechanism of perovskite solar cells or into manipulating it towards larger ("more negative") voltages. [21, 28, 30, 31, 53, 84] However, a well-defined measurement procedure and analysis method - as for the certified PCEs of perovskite solar cells - is missing for the breakdown voltage. Hence, how the breakdown voltage is measured differs from publication to publication and information about procedures and parameters is often lacking. Additionally, various definitions of the breakdown voltage and thus methods to analyze the measured data are in use.

As the influence of measurement parameters is generally unknown and the relationships between the different metrics that are called breakdown voltages are unclear, the published breakdown voltages cannot be directly compared with each other. That hampers the efforts to find more generally applicable methods of controlling the breakdown voltage. It also means that we cannot compare different designs and layer stacks.

In this publication, we discuss how to characterize the reverse bias behavior of perovskite solar cells. To that end, we take a look at the measurement parameters and conditions playing a role in reverse bias voltage sweeps and their impact on the measurement result. Furthermore, we consider the pros and cons of various breakdown voltage definitions and demonstrate the superiority of using the point of maximum curvature for that purpose.

4.2. How is the breakdown voltage measured? - Definitions and implications

In the following, we will use the term ’reverse bias (RB) breakdown’ for the reversible increase of the current that occurs when a voltage sweep into the RB regime is performed. Here, the current follows an approximately exponential dependence on the voltage and originates from a tunneling/Zener or, possibly, an avalanche breakdown mechanism. The breakdown itself is not damaging to the solar cell, but the reverse bias and reverse bias current lead to a gradual degradation of the solar cell parameters.

This breakdown is depicted in Figure 4.1a as reverse bias current density-voltage (RB-JV) curve with reverse (RV) and forward (FW) sweep (for details of the measurement procedure, see appendix B, Table B.1). The RV sweep starts in the positive voltage regime and ends in the negative. The FW sweep returns from a negative voltage to the positive voltage regime. To judge the impact on the efficiency, the (standard) JV curves from measurements before and after this RB-JV sweep are shown as inset (find measurement details in appendix B, Table B.2). It should be noted that the word ’breakdown’ points at the breakdown of the diode which is not intrinsically damaging to the solar cell. The solar cell does not necessarily ’break down’ in the sense of losing its functionality.

This reversible behavior stands in sharp contrast to the ’thermal breakdown’ that is depicted in Figure 4.1b (for measurement details, see appendix B, Table B.1). Here, a sudden, very steep increase of the current to $\approx 1400\,\mathrm{mA\,cm^{-2}}$ is observed. Its effect on the sample is destructive as it is likely accompanied by the formation of shunts. There might also be a component of thermal runaway where localized

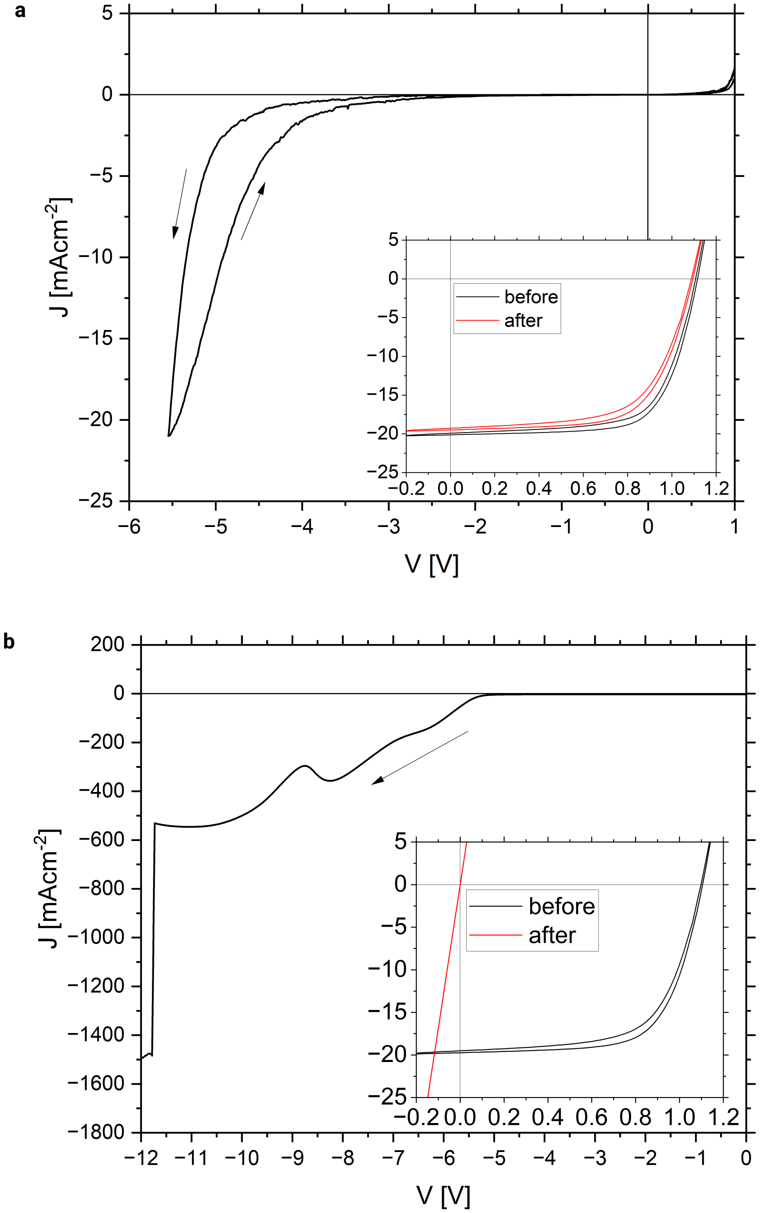

Figure 4.1. Comparing the reversible 'reverse bias breakdown' (a) and the irreversible 'thermal breakdown' (b). The insets show standard JV curves from measurements before (black) and after (red) the RB-JV measurements. A detailed description of the measurement parameters used for the RB-JV measurements can be found in the appendix B, Table B.1. The parameters of the JV measurements in the insets can be found in appendix B, Table B.2.

heating due to localized current flow leads to a locally-increased conductivity with the two effects escalating towards the destruction of the sample. The inset shows the (standard) JV curves before and after this RB-JV measurement and clearly illustrates the destructive effect of this thermal breakdown: Shunts dominate the cell behavior and the PCE is reduced to nearly 0 % (find measurement details in appendix B, Table B.2).

Furthermore, we will generally talk about absolute breakdown (BD) voltage values. Therefore, a 'larger breakdown voltage' is one that is more negative. Additionally, we will use the abbreviation 'JV measurement' for the standard voltage sweep whose purpose it is to measure the PCE of solar cells. When the voltage range is extended to more negative voltages in order to investigate the reverse bias behavior, we will refer to it as 'RB-JV measurement'.

4.2.1. Procedures and parameters in literature

With these initial definitions out of the way, we can start discussing how the breakdown voltage is measured. Normally, researchers perform a voltage sweep while measuring the current, similar to the JV measurement that is performed in order to determine the efficiency and other standard solar cell parameters. When it comes to performing a RB-JV sweep, there are several measurement parameters to decide on:

- Upper Limit (often the starting voltage of the RV sweep)
- Lower Limit (either the end voltage of the RV sweep or a current cutoff)
- Scan Rate
- Sweep Direction (Hysteresis measurement)
- External Factors: Illumination, Temperature, Atmosphere

What can we find in literature on PSCs in regards to these parameters? We have summarized the ranges that can be found in literature in Table 4.1. A table showing the detailed parameters can be found among the data underlying this article (see the Data Availability statement of the publication that this chapter is based on). It should be noted that the values mentioned there are partially assumptions based on the parameters used for standard JV measurements in the same publication or the limits of data that are displayed in graphs. Additionally, they are partially from measurements of the V_{BD} and partially from experiments on the reverse bias behavior.

The extremely wide range used for these parameters is clearly visible and demonstrates why we consider it important to discuss their impact on the measurement result.

4.2.2. Literature survey: Impact of measurement parameters

Could these measurement parameters have an impact on the measurement results? Furthermore, are there practical considerations to take into account when deciding on

Parameter	Range
Upper Limit	0 V to 2 V
Lower Limit: Voltage	-0.2 V to -20 V
Lower Limit: Current Density	$-1\,\mathrm{mA\,cm^{-2}}$ to $-1000\,\mathrm{mA\,cm^{-2}}$
Scan Rate	$0.02\,\mathrm{V\,s^{-1}}$ to $10\,\mathrm{V\,s^{-1}}$
Sweep Direction	mostly only RV; sometimes RV + FW
Illumination	often unreported; darkness, 0.02 suns to 0.25 suns
Temperature	mostly unreported; -19 °C to 45 °C
Atmosphere	mostly unreported; ambient, at controlled relative humidity 35 %, in N_2

Table 4.1. Main measurement parameters of RB-JV measurements and the range of values that can be found in PSC literature.

a set of parameters to use? We endeavor to answer these questions in the following sections.

As comparing the reverse bias behavior of PSCs from different publications is difficult, we rely on articles in which the comparison of measurement parameters is attempted. The motivation for these experiments is often increasing realism of measurements or investigating the breakdown mechanism.

However, a fundamental problem, when it comes to determining the impact of measurement parameters on results, lies in the limited stability of the PSCs: Any voltage sweep into the reverse bias regime changes the sample, if only temporarily. In a recent publication by Wang *et al.*, the dynamic reverse bias behavior, i.e. changes of the reverse bias behavior due to RB-JV measurements, is discussed in detail. [49] It is likely that the movement of mobile ions is the origin of this phenomenon. Often, the changes are completely reversible and the solar cell returns to its original state after some hours of storage in darkness. This still makes the simple comparison of two different measurement settings (e.g. two different voltage scan rates) tedious. Ways around this problem, e.g. repeating measurements to estimate the effect of successive voltage sweeps, bring their own problems with them. This might be one of the reasons why information on the impact of some measurement parameters is sparse. Therefore, the quantitative results should be considered with the appropriate care.

Voltage scan rate

The voltage scan rate has been shown to have an impact on the results of standard JV measurements on PSCs. Both the PCE (and thus the other solar cell parameters) and the hysteresis are dependent on the scan rate. The presence of mobile ions is named as one of the origins of this effect. [63, 64, 70]

According to the widely-accepted mechanism of the reverse bias breakdown in PSCs, mobile ions also play an important role there. [19, 20] Under the influence of a reverse bias, they accumulate at an interface and cause band bending. This facilitates the tunneling of charge carriers into the perovskite and thus the flow of a reverse bias current. Therefore, it stands to reason that the scan rate has an impact on the reverse bias behavior.

The influence of the voltage scan rate has been investigated in several publications: Bowring *et al.* compared the RB-JV measurements with scan rates of $10\,\mathrm{V\,s^{-1}}$ and $0.1\,\mathrm{V\,s^{-1}}$. [19] They reported that a higher scan rate leads to a higher breakdown voltage. Their explanation was based on the idea that the mobile ions do not reach steady states faster than the voltage is changed. In their case, the RB-JV curve shifted by approximately $0.1\,\mathrm{V}$.

In contrast, Wang *et al.* reported a lower breakdown voltage at higher scan rates, comparing $1\,\mathrm{V\,s^{-1}}$, $0.5\,\mathrm{V\,s^{-1}}$, and $0.1\,\mathrm{V\,s^{-1}}$. [49] This contrasting result might be explained by the difference in solar cell layer stack: Wang *et al.* investigated the behavior of ETL-free PSCs while Bowring *et al.* used a more traditional p-i-n layout.

In Henzel *et al.*, scan rates of $5\,\mathrm{V\,s^{-1}}$, $2\,\mathrm{V\,s^{-1}}$, $1\,\mathrm{V\,s^{-1}}$, $0.5\,\mathrm{V\,s^{-1}}$, and $0.1\,\mathrm{V\,s^{-1}}$ were compared. [88] However, it was concluded that the effect of performing several (15) successive measurements (shifting the RB-JV curves by about $0.5\,\mathrm{V}$) was interfering with any conclusions regarding the impact of only the scan rate.

A more significant impact of the scan rate was reported for the combination of reverse bias and low-intensity illumination by Henzel *et al.* [88]. There, choosing different scan rates lead to qualitatively different RB-JV curves with strongly diverging behavior in the large- and small-RB-current regime. They explained their observations with an activation of mobile ions by the illumination.

Beyond the effect on the measurement result, there is also the effect on the sample itself to consider. PSCs with limited stability might degrade already during RB-JV measurements. After all, they are operating in reverse bias during the measurement. As degradation was shown to be a function of RB current and time, a lower scan rate can be expected to lead to more degradation. [84]

Some of the available data suggests that the impact of the scan rate on the RB behavior (and therefore a V_{BD}) is small. However, it is doubtful whether any general validity regarding the magnitude of the impact of the scan rate can be claimed. It is likely that this magnitude depends on the properties of the mobile ions (e.g. mobility). These properties, in turn, depend on the perovskite formulation and the macroscopic structure (e.g. grain boundaries as channels for ion migration). [22, 45, 89] Therefore, the choice of the voltage scan rate should be carefully considered when measuring the V_{BD} via a RB-JV measurement.

Sweep direction and hysteresis

The influence of the sweep direction is connected to the issue of reverse bias hysteresis as this term describes a difference between a reverse (RV) and the forward (FW) sweep. As per the definition, the reverse sweep starts at a positive voltage and proceeds towards a negative voltage while the forward sweep starts at a negative voltage and proceeds towards a positive voltage.

The "normal" hysteresis phenomenon in standard JV measurements has attracted great interest and research effort since its initial description in 2014. [62] The general consensus is that the occurrence of hysteresis in JV measurements is caused by mobile ions and interface defects. [70]

In contrast, the hysteresis phenomenon in RB-JV measurements is rarely reported and barely investigated. Specifically, it remains unclear what the "true" breakdown voltage is and, indeed, whether there is one. Regarding the origin of the reverse bias hysteresis, there is no clarity yet: Assuming that there exist similarities to "normal" hysteresis, it is likely that the same solar cell properties (i.e. mobile ion conductivity and interface defects) play a decisive role. However, to the best of our knowledge, no publication has mentioned any correlation between (standard) hysteresis and reverse bias hysteresis. Another origin of reverse bias hysteresis could involve the storing and discharge of charges (discussed in the work by Henzel *et al.* [88]). Furthermore, mechanisms that change the breakdown voltage while the cell is operating in reverse bias on a similar time scale as the voltage sweep could have an impact appearing as hysteresis. However, it should be noted that no detailed research on the origin of reverse bias hysteresis is published.

Wang *et al.* showed RB-JV curves where the difference between RV and FW sweeps amounted to about 0.4 V. [49] Henzel *et al.* also reported both RV and FW sweeps that were showing hysteresis. [84] The difference between the sweeps was most significant in the low-current regime (at RB currents below $-5\,\mathrm{mA\,cm^{-2}}$). The difference between RV and FW sweeps was between 0.2 V and 0.7 V. [84] In the work by Aninat *et al.*, RB-JV measurements with hysteresis were shown as well. [59] However, they continued their voltage sweep until reaching a current density of $-20\,\mathrm{mA\,cm^{-2}}$ and used the voltage there as the breakdown voltage. Therefore, the issue of hysteresis does not appear in their breakdown voltages. Finally, Tayagaki *et al.* measured RB-JV hysteresis at low current densities ($\leq 1\,\mathrm{mA\,cm^{-2}}$) and at various temperatures. [53] Henzel *et al.* additionally reported hysteresis in another publication. [88] Again, differences between RV and FW sweeps between 0.2 V and 0.7 V were visible.

It seems that the effect of the sweep direction on the V_{BD} varies in the few examples where both sweep directions have been reported. The work by Henzel *et al.* proposes a way of dealing with small differences between RV and FW sweep. [84] They use the mean of the two breakdown voltages. The results of both sweep directions should be reported in any case. When hysteresis becomes more significant, however, using a mean might not be good practice anymore. Then, steady state measurements, as equivalent to MPPT, could be utilized to determine a breakdown voltage. Alternatively, a different voltage scan rate might yield a smaller hysteresis.

Lower limit of the voltage sweep

In literature, a large variety of lower voltages or current limits are employed (see Table 4.1). This variety is caused by the different metrics that are supposed to be measured. If $V_{BD} = V(J = -1\,\mathrm{mA\,cm^{-2}})$, then it is more than sufficient to use a current density limit of $-5\,\mathrm{mA\,cm^{-2}}$. On the other hand, if $V_{BD} = V(J = J_{sc}) \approx V(-20\,\mathrm{mA\,cm^{-2}})$, then the before-mentioned limit would not be sufficient. Finally, if the desired metric is the voltage where the thermal breakdown occurs, then even higher current limits and voltages are required.

Can the choice of the lower limit have an impact on the measurement result?

Logically speaking, there can be no impact on the initial RV sweep. After all, for the current density at $V = -1\,\mathrm{V}$ in a RV sweep, it does not matter whether the sweep ends at $V = -4\,\mathrm{V}$ or $V = -5\,\mathrm{V}$. However, the FW sweep and any successive measurements might well be influenced by the choice of the lower limit.

Any effect of the lower limit would be connected to degradation or at least changes to V_{BD} due to operation in RB during the measurement. The idea that operation in RB might affect the reverse bias behavior itself has already been formulated by Bowring *et al.* [19] They proposed an electrochemical reaction at an interface that is driven by the reverse bias current. Additional evidence of the effect can be found in the publication of Wang *et al.* where the effect of successive RB-JV measurements is shown in great detail. [49] They argue, however, that the mobile ions accumulating an the interfaces can also lead to an increasing breakdown voltage. More support can be found in the publication by Henzel *et al.* on the impact of illumination on the reverse bias behavior. [88]

Therefore, we expect that the RV sweep has an impact on the subsequent FW sweep. The magnitude of this impact is likely dependent on the lower limit since it affects both the RB current and the time spent in RB during the RV sweep. Therefore, the choice of a lower limit should take the stability of the sample into account and which changes to the sample are acceptable.

Illumination

There are at least two reasons for wanting to add illumination to an experiment on the reverse bias behavior: One is the desire to increase the realism in RB-JV measurements and imitate actual operating conditions more closely. Measurements in the dark imitate the simple partial shading event where a cell of a module is completely shaded. Adding illumination tries to extend this scenario to partial shading events where only a part of a cell is shaded or where still a low illumination intensity reaches the cell. A more detailed motivation can be found in Henzel *et al.* [88] Another reason could lie in an investigation of the reverse bias breakdown mechanism itself by disturbing the breakdown mechanism in a controlled way.

The effect of illumination on the reverse bias behavior has been judged as significant by Wang *et al.* who found that the breakdown voltage is strongly reduced by the addition of illumination intensities of about $25\,\mathrm{mW\,cm^{-2}}$. [49] As explanation, they proposed that light promotes the generation of mobile ions.

In contrast, Jiang *et al.* reported that the reverse bias behavior and V_{BD} of their PSCs was barely influenced by the addition of $10\,\mathrm{mW\,cm^{-2}}$. [28] A more thorough investigation of the impact of illumination has been published by Henzel *et al.* [88] They tested the effect of different colors of illumination and the effect of illumination in combination with various voltage scan rates. The range of the illumination intensity used in their experiments was between $2\,\mathrm{mW\,cm^{-2}}$ to $30\,\mathrm{mW\,cm^{-2}}$. They found that the light of different wavelengths leads to qualitatively similar results and that the impact of illumination strongly depends on the scan rate. At large scan rates, illumination had a dramatic effect on the V_{BD} values of their cells, while it was insignificant at small scan rates. [88] Finally, they also reported the effect of illumination on quasi-steady state experiments where a fixed current was being injected before illumination was switched on. They proposed an explanation involving the effect of illumination on mobile ions but also an electrochemical reaction that counteracts the effect of the light at small scan rates. [88]

This effect of illumination was assumed to be related to intrinsic properties of the perovskite layer and therefore generally valid for all perovskite solar cells. However, the strength of the effect and its dependence on the scan rate might depend on the properties and materials of the perovskite solar cells. It is clear, however, that the illumination intensity during RB-JV measurements should be controlled and reported.

Temperature

The temperature of the sample can be of interest for two reasons: Firstly, in order to take a further step towards realism and imitate the outdoor situation at increased temperatures. [28] Secondly, as a way to show the dependence on temperature as evidence for the influence of mobile ions that is suggested by the widely-accepted breakdown mechanism. [19]

At a scan rate of $0.1\,\mathrm{V\,s^{-1}}$, the temperature difference between room temperature (RT) and $-19\,°\mathrm{C}$ seemed to cause a difference of approximately $0.4\,\mathrm{V}$ in the small-RB-current regime. [19] Jiang *et al.* did not find a significant difference between the V_{BD} values at RT and $45\,°\mathrm{C}$. [28] Tayagaki *et al.* reported that the RB current increased at lower reverse biases when the RB-JV measurements were performed at higher temperatures. [53] That means that the V_{BD} decreased with increasing temperature which corroborates the above-mentioned results of Bowring *et al.* Both explained this temperature-dependence with the effect of temperature on the conductivity of mobile ions. Their conductivity, i.e. mobility and/or concentration, influences how they react to external electric fields.

It seems that the temperature can have an influence on V_{BD} via its effect on mobile ions. Thus, the temperature should also be taken into account as a measurement parameter.

Other parameters

There are two measurement parameters left over that were mentioned in the list at the beginning of this section: One is the upper (voltage) limit of the voltage sweep.

To the best of our knowledge, there is no data available on this parameter having an impact on the reverse bias behavior. Xu *et al.* explained, however, that they pre-treated their cells at $0\,\mathrm{V}$ for $1\,\mathrm{min}$ and then started the RB-JV measurements at $0\,\mathrm{V}$ with the intention of avoiding "capacitative charging effects". [90] That implies that starting the voltage sweep at a positive voltage is an inadvertent pre-biasing. Unfortunately, we have not seen any data on the effect of positive voltage pre-biasing on the reverse bias behavior. Pre-biasing with a negative voltage, on the other hand, has been shown to have an effect in the work by Henzel *et al.* [88] There, it helped bringing the RB behavior of fast voltage sweeps under illumination closer to the behavior of slow voltage sweeps.

The second missing parameter is the atmosphere in which the RB-JV measurement is performed. This atmosphere is nearly exclusively ’ambient’ in the available literature. This could be a problem for two reasons: Firstly, degradation due to ambient atmosphere might occur on a timescale that is similar to the process of performing the RB-JV measurements. Secondly, direct interactions between the reverse bias behavior and components of the atmosphere, e.g. water, might influence the reverse bias behavior. We are not aware of any publications discussing any of these issues. Therefore, we cannot make a statement about the possible impact they might have. However, it is clear that the parameter ’atmosphere’ includes information about eventual encapsulation/packaging.

We have seen that a lot is unclear about the impact of measurement parameters and conditions on the resulting V_{BD}. For several parameters, there is some information available. However, even in these cases, the properties of the PSCs are likely to affect the impact of the measurement parameters. That means that there is no ’general V_{BD}’, there are only breakdown voltages according to the methods of determining them. That makes it difficult to compare V_{BD} values from different sources.

One solution to that issue is for everyone to use the same measurement parameters. To that end, we will propose two sets of parameters and conditions; one for stable cells and one for less stable cells.

4.2.3. Recommendations towards standardized measurements

We have discussed the relevant measurement parameters that impact a RB-JV measurement and its results. To that end, we showed the wide range of parameters that has been employed in measurements and experiments regarding the reverse bias behavior of perovskite solar cells. Subsequently, we presented data from literature on the impact of these parameters on the measurement results. It seems that the impact often depends on the perovskite solar cell properties. This makes it difficult to define a general ’best practice’. Nevertheless, we will propose a set of parameters that can be used as a starting point. Generally, however, reporting the detailed measurement parameters and conditions helps the most.

Two sets of recommended measurement parameters are presented in Table 4.2. Since literature showed that there is a wide spread in reverse bias stability, we decided to provide recommendations for ’stable’ and ’less stable’ samples. Here, ’stable’ cells are those that do not degrade significantly during one RV-JV sweep. Providing a set for less stable cells should enable similar experiments on a wider range of PSCs and thus increase inclusivity. A measurement without significant impact on the solar cell performance could also gain entrance into the group of ’standard measurements’, like IV or EQE measurements. This would greatly help this field of research.

Our argumentation for this choice of measurement parameters is the following: By using an upper limit of 1.0 V, we incorporate a dark JV measurement and therefore information about the state of the solar cell. That way, changes to the cell due to the RB-JV measurement are tracked ’automatically’. Additionally, a certain recovery

Parameter	Recommendation (stable cells)	Recommendation (less stable cells)
Upper Limit	$1.0\,\mathrm{V}$	$1.0\,\mathrm{V}$
Lower Limit	J_{sc}	$0.5J_{sc}$
Scan Rate	$0.1\,\mathrm{V\,s^{-1}}$ to $0.2\,\mathrm{V\,s^{-1}}$	$1.0\,\mathrm{V\,s^{-1}}$
Hysteresis	RV and FW sweep	RV and FW sweep
External Conditions	darkness, RT, ambient atmosphere	darkness, RT, ambient atmosphere

Table 4.2. Recommended measurement parameters for the characterization of the reverse bias behavior of PSCs.

occurs during the operation in the positive voltage regime at the end of the RB-JV measurement.

Using a lower limit of J_{sc} provides information about the whole ’realistic’ range of operating conditions of a cell in a module. If less impact on the cell is desired, the Lower Limit can also be limited to $0.5J_{sc}$. That way, the measurement still provides information about the large RB current density regime.

When it comes to the Scan Rate, a compromise between two opposed considerations has to be found. On the one hand, a smaller scan rate means that the cell spends more time operating in RB and therefore experiences more degradation. On the other hand, it has been shown that slow processes occur in PSCs in reverse bias and that it can take a long time to reach an equilibrium upon applying a new bias. Therefore, a small scan rate is necessary to allow the cell to reach a steady state for each measurement point. A scan rate of $0.2\,\mathrm{V\,s^{-1}}$ for stable cells was chosen because it is a typical scan rate for JV measurements on PSCs. For less stable cells, using $1.0\,\mathrm{V\,s^{-1}}$ reduces the total charge flowing through the cell and the time spent in RB drastically, and therefore limits degradation.

Hysteresis is a well-known phenomenon in JV measurements on PSCs. As the sweep direction can have an impact on the measurement results, it is standard procedure to perform and report both RV and FW sweep and their respective results. As a hysteresis phenomenon has been shown to occur in RB-JV measurements, RV and FW sweeps should also be performed and reported here. The fact that barely anything is known about the RB hysteresis and its connection to ’normal’ hysteresis increases the importance further.

Finally, when it comes to the External Conditions, we decided to keep things simple: RB-JV measurements should be performed in complete darkness. This standardized measurement should model the simple and idealized partial shading event of one cell of a module being completely shaded. They can be performed without special temperature control at room temperature (RT). Regarding the atmosphere, we have not seen any data on an impact of oxygen, humidity, etc. on RB-JV measurements. Therefore, as long as the PSCs are stable enough to be characterized in ambient atmosphere via JV measurements, we assume that they are not being significantly changed within the time frame of a RB-JV measurement

Despite pre-conditioning being a relatively common procedure in the perovskite community and in other solar cell technologies, we have decided not to include any such treatment in this list beyond our choice of positive voltage upper limit. The main reason is that it does not seem to be a common procedure to do so in the publications on RB on PSCs. If the impact of an RB-JV measurement on the reverse bias behavior causes concern, we recommend performing two RB-JV measurements in order to gain an estimation of their effect.

4.2.4. Steady state measurements

At the end of this section, we would like to comment on a completely different way of determining a breakdown voltage: Measuring the reverse bias behavior in a (quasi-) steady state by applying a constant voltage or injecting a constant current. This procedure could be called the functional equivalent of the maximum-power-point tracking (MPPT). This experiment has been reported in few publications. [18, 19, 84, 88] There, the experiment was not performed to determine a breakdown voltage and compare it with the breakdown voltage from a voltage sweep. Instead, the impact of time operating in RB was the target of these experiments.

One reason for this might be that these cases showed that either there does not seem to be a steady state, i.e. the voltage or current continues to change in time without stabilizing. In any case, it seems to take some time (several 10 s) to even approximately stabilize when large current densities are injected. This is shown in the data from the work of Henzel *et al.* (see appendix D, Figure D.12). [88] That means that even if a steady state is reached, significant degradation is to be expected due to the long time spent operating in reverse bias. For these reasons, we do not follow up on this method here.

4.3. Defining a breakdown voltage

After having discussed how to perform RB-JV measurements, we will turn our attention to the following step: How do we get from the raw data of a current (density)-voltage curve to a meaningful metric that describes the reverse bias behavior? In literature, there are various breakdown voltage definitions available. The problem with that is illustrated in Figure 4.2a. Different voltages, often describing different parts of the RB-JV curve, are all called V_{BD}. One of the reasons for this large variety lies in the different purposes these breakdown voltages are supposed to fulfill. Three possible purposes are listed in the following:

- Comparability:

The V_{BD} should allow the comparison of PSCs of different batches, with different perovskite formulations, layer stacks, and cell layouts in regards to their reverse bias behavior.

- Describing real operating conditions:

The V_{BD} should make a statement about the solar cell behavior as part of a module during a realistic partial shading event. Hence, this breakdown voltage provides information for the design of modules.

- Compatibility with theoretical descriptions:

The V_{BD} should be defined in a way that can be described analytically/mathematically. In that way, a theoretical description of the breakdown mechanism could be connected to empirical values of V_{BD}.

Additionally, we require that definitions of the breakdown voltage fulfill some basic requirements: Firstly, the V_{BD} should be clearly, unambiguously defined, so that it describes one voltage (and not a range of voltages) for each sweep direction. Secondly, the V_{BD} should describe the reverse bias behavior and should not be unduly influenced by other factors. We will later see that RB-JV curves exist where small or short-lived shunts ("irregularities") affect (only) the low-RB-current density regime. Since they do not seem to have a significant impact on the high-RB-current density regime, they should also not dominate the metric describing it.

In the following, we will present the breakdown voltage definitions that have been used in publications on the RB behavior of perovskite solar cells. More definitions can be found when looking at publications about other solar cell technologies, e.g. for CIGS in Puttnins *et al.* and Szaniawski *et al.* [51, 91] Here, we will, however, confine ourself to those used in the perovskite PV technology and, in the process, propose one additional definition. Furthermore, we will discuss the definitions in regards to the above-mentioned purposes and requirements.

4.3.1. Definitions in Literature

When categorizing the breakdown voltage definitions that we will discuss, three groups appear:

- Graphical Definitions
  - Graphical Onset (see Figure 4.2b: blue)
  - Thermal Breakdown/Shunting (see Figure 4.2c)
- Fixed Current Density (see Figure 4.2b: red)
  - $V(J = -1.0\,\mathrm{mA\,cm^{-2}})$
  - $V(J = -10.0\,\mathrm{mA\,cm^{-2}})$
  - $V(J = J_{sc} \approx -20\,\mathrm{mA\,cm^{-2}})$
- Advanced Analysis Techniques
  - Linear Fit (see Figure 4.2b: magenta)
  - Point of Maximum Curvature

In the following, we will describe them in more detail and discuss their strength and weaknesses.

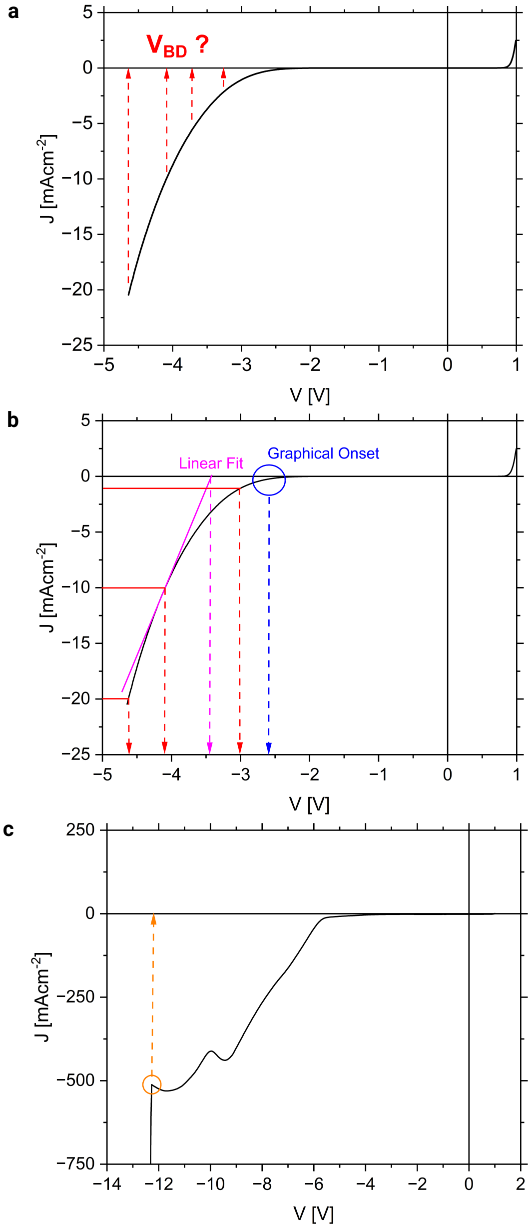

Figure 4.2. Defining a breakdown voltage: The topic of this section is illustrated (a): What is the breakdown voltage (V_{BD})? Various definitions of V_{BD} that have been used in publications on PSCs (b): The onset of the RB current density (blue), three versions of a definitions based on fixed current densities (red), and a definition based on a linear fit of the high-RB-current density regime (magenta). An additional definition based on the sudden current density increase caused by the solar cell shunting (c).

Graphical Definitions

Both graphical definitions have in common that the breakdown voltage is marked by a change in the current density that is visible in a graph.

The definition using the onset of the current density (J) was employed in only one publication. [23] It involves plotting the RB-JV curve and then proclaiming the voltage where the current (density) visually increases as V_{BD}. While it is easy to (manually) determine from graphical depictions of RB-JV measurement results, it suffers from a serious problem: It is not well defined.

As is shown in Figure 4.3, the voltage that seems to correspond to the onset of J, depends on the graphical depiction. In Figure 4.3a - c, the same curve is depicted but progressively more 'zoomed in'. Even though we used axis ranges that ensure that the depicted parts of the curve use most of the graph area (thus, a 'realistic' way of presenting the data), V_{BD} seems to shift towards lower voltages. We expect the same to happen when different lower limits (end voltage or current density cutoff) are used for the RB-JV measurements. Even when the same axis ranges are used, this 'onset' describes rather a voltage range than a specific point on the curve. This vagueness not only causes problems for comparing exact values but also makes it difficult to determine it automatically from RB-JV measurement data.

Due to these fundamental issues, it does not seem to be fit for any of the above-mentioned purposes.

The second definition using a graphical depiction was employed by several authors. [21, 26, 30–32] This breakdown voltage is characterized by a sudden, drastic increase of the current density (see Figure 4.2c). Based on the assumed mechanism behind this current density increase, it was called 'thermal breakdown (voltage)' in one publication and described as 'voltage at which the current spikes suddenly and permanent damage occurs'. [26] We assume this description points at the thermal runaway effect, a feedback loop between localized current flow leading to local Joule heating which increases the local conductivity and therefore leads to increased current flow. It is connected to shunt formation and *not* to the (Zener or avalanche) diode breakdown, i.e. the reversible reverse bias breakdown.

As before, a thusly-defined breakdown voltage is easy to determine, not only manually/graphically but also in an automated way. The characteristic current spike can easily be detected by an algorithm. At the same time, its nature as current spike means that it describes a single point on the RB-JV curve and is therefore well-defined. Therefore, it does allow the comparison of different solar cells.

It is, however, important to note that current spikes can occur in the small-RB-current regime (i.e. $J \leq -5\ \mathrm{mA\,cm^{-2}}$) without significant effect on the reverse bias behavior at larger current densities (see for example Figure 4.4, red curve with peak). Therefore, a RB-JV measurement with a very large lower limit should be used for determining the thermal breakdown voltage to ensure that the characteristic current spike does lead to the destruction of the solar cell. Since it causes catastrophic damage in the sample, it is a measurement that cannot be reproduced on the same sample and is therefore also not useful as one characterization method among others. Additionally, it also does not allow any statement about the hysteresis as a damaging RV sweep cannot be followed by a FW sweep.

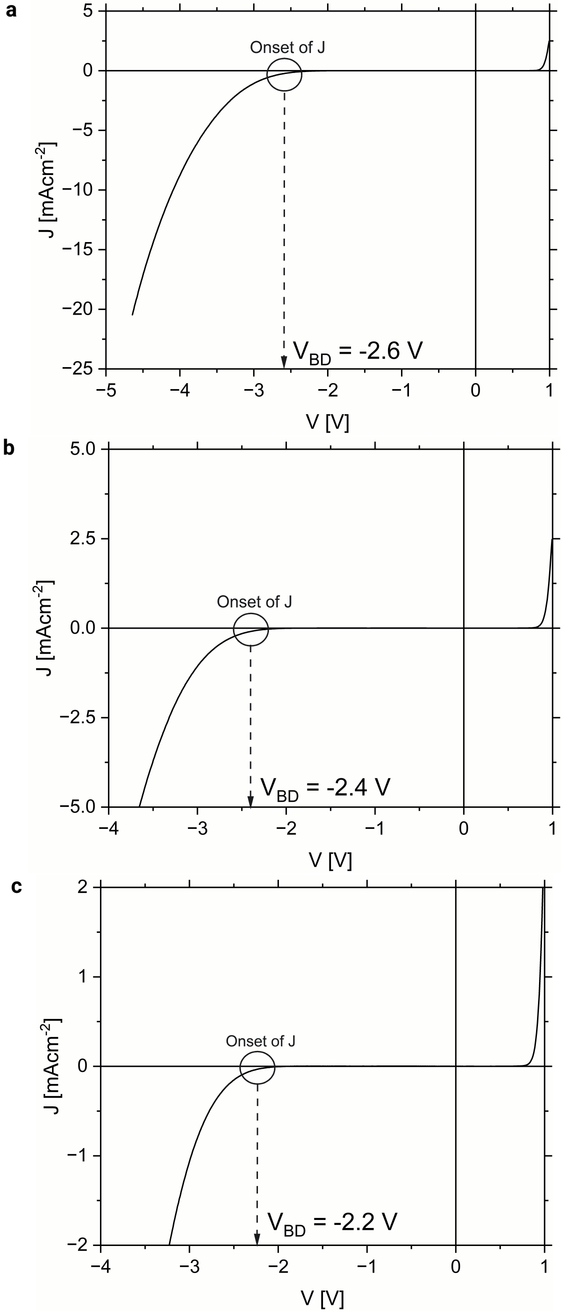

Figure 4.3. Using the graphical onset of the current density as definition of V_{BD}. The axis ranges is changed between the three graphs to show that they influence the breakdown voltage (a-c).

Furthermore, it is questionable whether the thermal breakdown voltage is a meaningful metric to describe reverse bias stability: Does it indicate a reverse bias threshold with smaller reverse biases being safe for the PSCs? Data from one of the publication using this definition answers that question: Even only successive RB-JV measurements to -5 V performed on samples with thermal V_{BD} values of -7.6 V showed complete degradation after a few cycles. [26]

Does it describe a realistic degradation mode? In a module without bypass diodes, the largest RB current density that flows through a shaded cell is J_{mpp} if the cell operates beyond its breakdown. Any voltage with a current density above J_{sc} would therefore be unrealistic. The voltage, at which the thermal breakdown occurs, depends, of course, on the solar cell, but in the case depicted in Figure 4.2c, this spike occurs beyond $-500\,\mathrm{mA\,cm^{-2}}$, so at about $25 \times J_{sc}$.

Finally, as long as the mechanism of the thermal breakdown is not clear, any connection to the generally-accepted RB breakdown mechanism (tunneling [19]) is not possible. Additionally, if local shunting is the main process leading to thermal breakdown, the V_{BD} is likely determined by weak spots, e.g. particles and other inhomogeneities and not material or interface properties.

To summarize, while the thermal breakdown voltage allows for the easy comparison of PSCs, it is not clear whether the underlying cell property that is compared is decisive for the reverse bias stability. Combined with the practical limitations caused by being a destructive measurement, it does not seem to be a good fit for any of the above-mentioned purposes.

Fixed Current Density

Breakdown voltage definitions based on a fixed current density are present in various publications. Here, the breakdown voltage is the voltage where the fixed current density J_{BD} is reached: $V_{BD} = V(J = J_{BD})$. The most commonly used version ($J_{BD} = -1.0\,\mathrm{mA\,cm^{-2}}$) was proposed by Bowring *et al.* and subsequently adopted by several other authors. [18, 19, 49, 58, 84] Bowring *et al.* described their choice of J_{BD} themselves as "arbitrary".

Another publication preferred $J_{BD} = -20.0\,\mathrm{mA\,cm^{-2}}$ for being close to J_{sc} and therefore the maximum current that their devices were capable of generating. [59] This current density is the theoretical maximum that a shaded cell would need to pass in a partial shading event on a module without bypass diodes.

Finally, Henzel *et al.* chose a compromise, using $J_{BD} = -10.0\,\mathrm{mA\,cm^{-2}} \approx 0.5 J_{sc}$. [88] As their experiments included up to 75 RB-JV measurements per cell, they desired to limit degradation and therefore endeavored to decrease the lower limit of their measurements. At the same time, they wanted to prevent their V_{BD} from being influenced too much by the low-RB-current density regime.

These three versions of this definition are shown in Figure 4.2b as red, dashed lines and red arrows.

All of them have in common that their corresponding V_{BD} values are very easy to determine, also in an automated way. In principle, these V_{BD} values are also unambiguously-defined; at least when the RB-JV curve does not show any of the irregularities that are shown in Figure 4.4: There, three RB-JV curves are presented. One is close to ideal (black), one shows a peak before the actual breakdown, i.e. a short-lived, sudden increase of the current density (red). That might be caused by a newly-formed or newly-activated shunt which heals immediately again. This is a rarely-occurring phenomenon with an unclear origin though we expect a connection to small imperfections in the solar cell area. The last curve shows a pre-breakdown, i.e. an irregular early breakdown that leads to a significant RB current even before the actual, exponential breakdown occurs (blue curve in Figure 4.4). This phenomenon was caused by the addition of blue, low-intensity illumination on RB-JV measurements with small scan rates (e.g. $0.1\,\mathrm{V\,s^{-1}}$). The data shown here stems from the publication by Henzel *et al.* (see Chapter 6) [88] We use these RB-JV curves to demonstrate how breakdown voltage definitions based on fixed current densities deal with ideal and non-ideal RB-JV results.

In Figure 4.4a, the three RB-JV curves are shown with the addition of a horizontal line that marks $J_{BD} = -1.0\,\mathrm{mA\,cm^{-2}}$. Filled circles and empty circles mark the breakdown voltages of RV sweep and FW sweep, respectively. For the ideal RB-JV curve, the two V_{BD} values also convey information about the RB hysteresis. For the RB-JV curve with the peak, one red circle marks the peak since it crosses J_{BD} while the empty circle is placed at the actual V_{BD} values of the RV and FW sweeps. The blue circles mark very different V_{BD} values; one dominated by the pre-breakdown, the other by the ’real’ breakdown.

Thus, we have seen that using $J_{BD} = -1.0\,\mathrm{mA\,cm^{-2}}$ does work well for ideal RB-JV curves. However, whenever there are irregularities present that affect the low-RB-current regime, they can significantly influence the determined V_{BD} values. As can be seen in the same graph, the same irregularities do not significantly impact the high-RB-current regime. Additionally, the irregularities are not present at all in the FW sweep. That calls into question whether the V_{BD} values that use $J_{BD} = -1\,\mathrm{mA\,cm^{-2}}$ represent the reverse bias behavior accurately.

When we take a look at Figure 4.4b and c, we see how the definitions using $J_{BD} = -10.0\,\mathrm{mA\,cm^{-2}}$ and $J_{BD} = -20.0\,\mathrm{mA\,cm^{-2}}$ fare with the same RB-JV curves. Their advantage of not being unduly influenced by the RB behavior in the low-RB-current behavior is clearly visible.

In return, while determining these V_{BD} values at $0.5J_{sc}$ and J_{sc}, (irreversible) degradation is likelier to occur. Jiang *et al.* found that their PSCs experienced irreversible degradation when passing J_{mpp} (which is still smaller than J_{sc}). Cells that had to pass smaller current densities ($\leq -1\,\mathrm{mA\,cm^{-2}}$) showed irreversible or reversible degradation. [28] That fits with the conclusion of Henzel *et al.* that degradation is current-driven. [84] In the light of these observations, using $J_{BD} = -10.0\,\mathrm{mA\,cm^{-2}}$ seems to be a compromise that enables measuring V_{BD} without degrading the samples while still conserving the meaning of the metric as representing the large-RB-current regime. This approach suffices for comparing cells, at least.

To summarize, all the definitions using a fixed current density possess the advantage of easy determination. However, $J_{BD} = -1.0\,\mathrm{mA\,cm^{-2}}$ and $J_{BD} = -10.0\,\mathrm{mA\,cm^{-2}}$ are completely arbitrary values. Therefore, the V_{BD} values determined using them as fixed current densities do not have any meaning in the sense of describing the

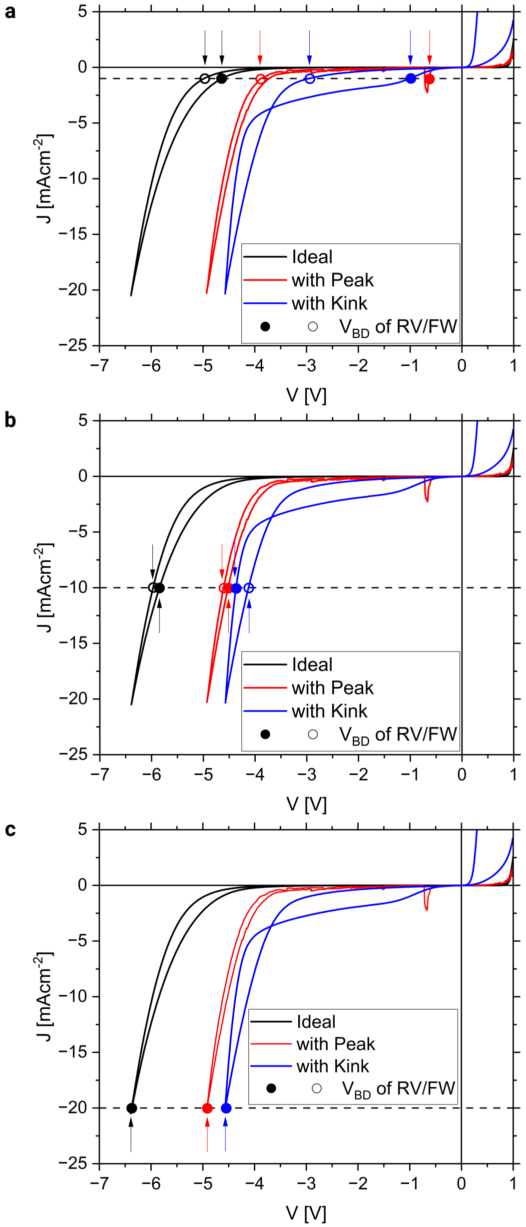

Figure 4.4. Three breakdown voltage definitions based on fixed current densities are compared with the aid of three representative RB-JV curves (black, red, blue): $J_{BD} = -1.0\,\mathrm{mA\,cm^{-2}}$ (a), $J_{BD} = -10.0\,\mathrm{mA\,cm^{-2}}$ (b), $J_{BD} = -20.0\,\mathrm{mA\,cm^{-2}}$ (c). The V_{BD} values are marked with circles and arrows. Detailed measurement parameters can be found in the appendix B, Table B.3.

state of operation or physics. Only $V_{BD} = V(J = J_{sc})$ stands out as it can be connected to the worst case scenario in a module without bypass diodes. Finally, using a high J_{BD} as fixed current density negates the impact of irregularities in the low-RB-current regime on the metric. On the other hand, the deleterious effects of RB-JV measurements (degradation to destruction) increase with a larger lower limit.

A Linear Fit

Another publication proposed a breakdown voltage definition that requires a sightly more advanced analysis procedure. [28] They performed a linear fitting in the current density range of $-5\ \mathrm{mA\,cm^{-2}}$ to $-15\ \mathrm{mA\,cm^{-2}}$. The V_{BD} is then the voltage where the linear fit function crosses the x-axis. The intention behind that procedure was generating V_{BD}-values for the two types of RB-JV curves they observed: Most showed a gradual increase of the RB current with increasing reverse bias, but some showed a sudden increase.

We imitated that analysis procedure, using a script that performs a linear fit on the RB-JV curve in the above-mentioned current density-range. We executed this procedure on the same three representative RB-JV curves that we introduced in Figure 4.4. The results of this analysis are shown in Figure 4.5. The measurement results are always split into reverse sweep (black) and forward sweep (red). The linear fit functions corresponding to RV and FW sweep are plotted in the same graph as black and red dashed lines, respectively, with the corresponding V_{BD} values marked by black and red dots.

In Figure 4.5a and b, we can see that the described approach of the linear fit works well with ideal curves and curves with a peak in the low-RB-current density regime since this method only uses the data beyond $-5\ \mathrm{mA\,cm^{-2}}$. It is, therefore, not influenced by irregularities in the low-RB-current regime.

Only when the irregularities have an impact on the curve within the fitting region, the resulting quality of the fit decreases and does not mirror the high-RB-current regime as well. This is visible in Figure 4.5c where the pre-breakdown behavior has a significant impact on the RV sweep at current densities up to $-10\ \mathrm{mA\,cm^{-2}}$. To improve this, the fitting region would have to be restricted to a regime of larger current densities. Therefore, this definition is generally able to deliver a V_{BD} that can be used to compare solar cells.

However, while ignoring differences in breakdown mechanisms with possibly very different consequences for the cells might be helpful for a quantitative investigation, it might be disadvantageous as long as the breakdown mechanisms are not understood in detail. Additionally, the V_{BD} resulting from this definition is an arbitrary number that does not have a technical or physical meaning and lacks an analytical description. So, it might be useful for comparison but does not allow any further conclusions. Finally, in order to use the whole current density range ($-5\ \mathrm{mA\,cm^{-2}}$ to $-15\ \mathrm{mA\,cm^{-2}}$, as proposed by the authors, and include information about hysteresis, a voltage sweep to at least $-20\ \mathrm{mA\,cm^{-2}}$ seems to be necessary, with all the disadvantageous effects previously mentioned.

With that, we have discussed the various definitions of the breakdown voltage

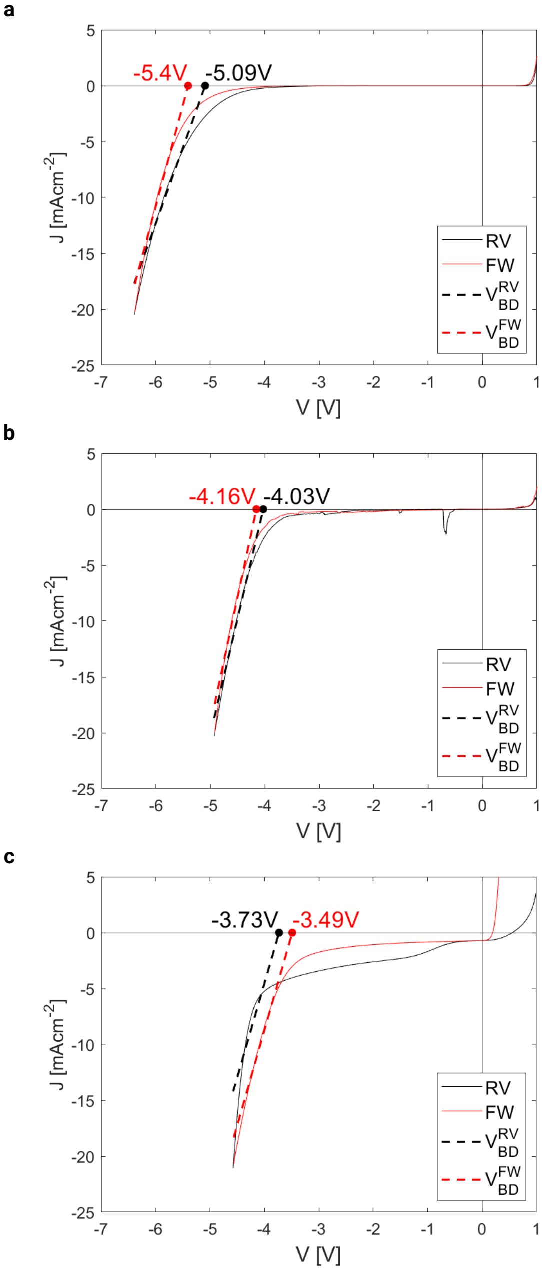

Figure 4.5. The linear fit method proposed in [28] is executed on three representative RB-JV curves to test the impact of the low-RB-current density regime (a-c). The resulting V_{BD} values are marked with circles.

that have been previously used to describe the reverse bias behavior of PSCs. Our basic requirements included being well-defined and not-unduly-influenced by the behavior in the low-RB-current regime. These needs were met by a few definitions: Those based on a fixed current density of $-10\,\mathrm{mA\,cm^{-2}}$ and $-20\,\mathrm{mA\,cm^{-2}}$ and the linear fit method.

Of these, only one is not just an arbitrary number and therefore useful for more than only comparison: The definition of the fixed current density of $-20\,\mathrm{mA\,cm^{-2}}$ can be connected to a partial shading scenario of a module without bypass diodes.

4.3.2. Proposing an additional definition

After having presented all the breakdown voltage definitions present in literature on PSCs, we would like to propose an additional definition. In 1971, Mahadevan *et al.* published a list with definitions that had been used to describe the reverse bias breakdown of semiconductor p-n junctions. [50] One of the entries is annotated with the assessment: "tedious though capable of analytical formulation and of universal applicability". Especially the aspect of the analytical formulation has attracted our interest since that implies the possibility of connecting the V_{BD} to theoretical descriptions of the breakdown mechanism. This property is notably missing among the previously described definitions. The criterion, i.e. the definition, that is described here, is the point of maximum curvature (PoMC) in the RB-JV curve.

While the point of maximum curvature is, in principle, well- and unambiguously-defined, the practical execution of its determination leaves room for variance. Therefore, we will add some additional constraints to our definition:

- Definition of the curvature κ
- Method of derivation
- Fit function

We use the following definition of the curvature: [92]

$$\kappa = \frac{|\ddot{J}|}{(1+\dot{J}^2)^{\frac{3}{2}}}, \tag{4.1}$$

with J being the current density, $\dot{J}$ its first derivative with respect to the voltage, and $\ddot{J}$ its second derivative with respect to the voltage.

Regarding the method of derivation, there are two different options. One is to perform numerical differentiations. This option suffers from two disadvantages: The previously shown irregularities would disturb the numerical differentiations. The peak shown in Figure 4.4, would lead to massive, local curvatures. Additionally, even slight non-ideal behavior of the RB-JV curve makes the use of a smoothing algorithm necessary. This introduces additional variance to the result and complexity to the procedure.

The second option is to perform curve fitting on the data to approach it with a function and then calculate the derivatives and the PoMC of this fit function. This stands and falls with the quality of the fit, i.e. how well the analytical expression mirrors the measured RB-JV data. We have not found an expression with physical background (e.g. describing Fowler-Nordheim tunneling) that has been confirmed to describe the results of our RB-JV measurements well. As developing a physical model is beyond the scope of this publication, we choose a purely empirical approach. For the sake of keeping this procedure simple, we will use a simplified relationship between current density (J) and applied bias (V): We choose a single-term exponential function with only empirical coefficients a, b, c:

$$J = a \cdot e^{b \cdot V} + c \tag{4.2}$$

This function can describe most of our RB-JV curves reasonably well (see appendix B, Figure B.1). However, our interest lies in determining a point of maximum curvature as accurately as possible. Therefore, we use a two-step process to increase the accuracy of the fit around the expected point of maximum curvature. This method of restricting the data range used for fitting seems to be the most generally applicable.

1. Fit of complete RB-JV curve ($V \leq 0\,\mathrm{V}$)
2. Calculation of PoMC (intermediate)
3. Fit of data around PoMC (final)
4. Calculation of PoMC (final)

More details of the procedure can be found in the Supporting Information (B Note B.3.1).

The result of this procedure is shown in Figure 4.6. There, the RV and FW sweeps of RB-JV measurements are displayed as black and red solid lines, respectively. The fit functions are plotted within their range as blue, respectively, magenta dashed lines. Blue and a magenta symbols mark the resulting points of maximum curvature. Again, we are using three RB-JV curves as examples. One is ideal (Figure 4.6a), one shows a peak (Figure 4.6b), and the third shows the pre-breakdown behavior in the RV sweep (Figure 4.6c). We see that, for the ideal curve (a) and the curve with a peak (b), the fit functions follow the data very well in the assigned data ranges. The breakdown voltage values of the RV and FW sweeps also reflect the hysteresis in the corresponding data well. When it comes to the curve with kink (c), the FW sweep is described very well, too. However, the RV sweep with the significant kink carries this method in its present state to its limit. Nonetheless, it is still possible to extract a V_{BD}-value.

Here, it is necessary to mention that the point of maximum curvature is *not* the ’knee’ of an exponential curve. In fact, what is described as ’knee’ is an illusion of the linear plotting, depends on the choice of axes, and is not related to a special point of the curve. [93] This statement is demonstrated in the appendix B, Figure B.2 where we plot the same exponential function with very different axes and see that the ’knee’ appears at wildly different values of x. In contrast, the point of maximum curvature describes a unique point of the curve that is well-defined and which is *not* dependent on the axes of the graph.

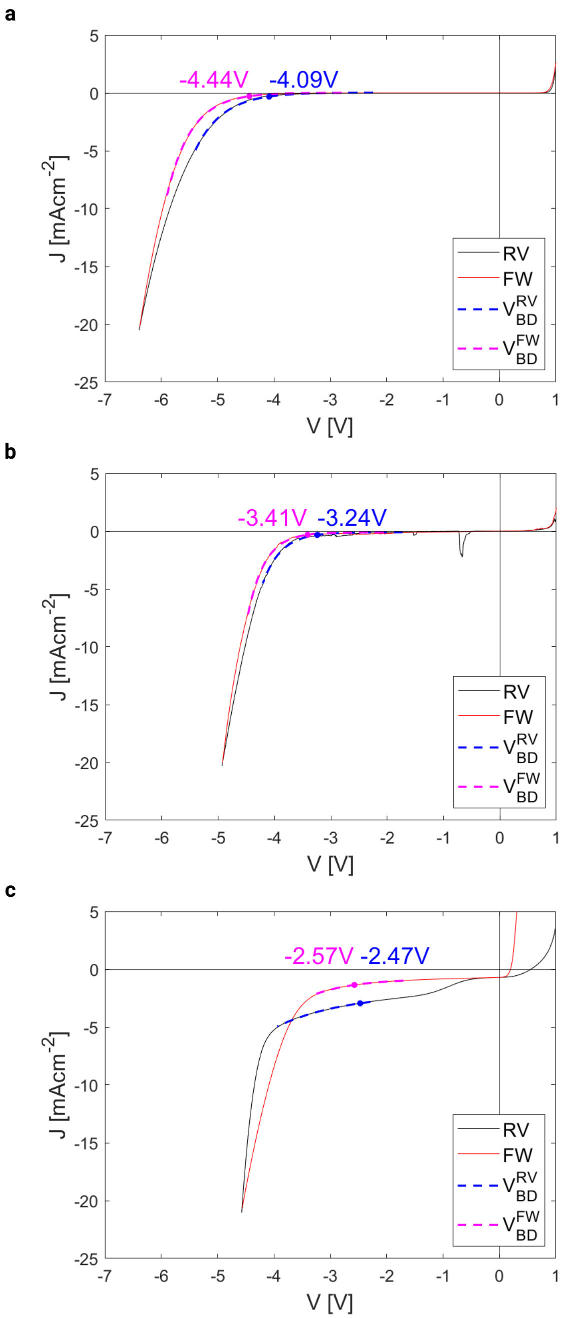

Figure 4.6. The newly proposed definition using the power of maximum curvature is tested on the three representative RB-JV curves (a-c). The resulting V_{BD} values are marked by circles.

Thus, we have successfully extracted the points of maximum curvature for use as breakdown voltages from the three example RB-JV measurements. This V_{BD} has the unique advantage of being analytically-expressible, so that it can be potentially connected to a theoretical description of the breakdown mechanism. Due to fitting a function to it, this method is also mostly independent of possible irregularities in the low-RB-current regime.

Also, the demand of comparability is fulfilled since this method of analyzing RB-JV curves should result in very similar V_{BD}-values as long as the quality of the fit is acceptable. Thus, even using different fit functions should not lead to very different breakdown voltages. Nonetheless, it surely is good practice to report the detailed procedure, if not the whole analysis script.

There are, however, also downsides to this definition of the breakdown voltage: Firstly, this V_{BD} does not have a meaning that is intuitively accessible. It can be analytically expressed but the voltage is not related to a specific operating point of the solar cell. Secondly, the analysis is comparatively complex which could serve as hurdle for users. Finally, there is one area where the most important improvement can be made: Extending or modifying the fit in connection with an accompanying physical model, could allow more detailed investigations into the parameters influencing the reverse bias breakdown of perovskite solar cells. However, especially for the case of illumination (shown in Figure 4.6c), developing a well-fitting model that allows for quantitative predictions is challenging. [88]

4.3.3. Comparing the breakdown voltages

After having discussed various ways of measuring and determining the breakdown voltage, we will demonstrate the impact of using different breakdown voltage definitions. To that end, we will first compare the V_{BD} values of the three representative RB-JV curves that result from the different described definitions. These V_{BD} values are listed in Table 4.3.

V_{BD}-Definition	Ideal (RV/FW) [V]	with Peak (RV/FW) [V]	with Illumination (RV/FW) [V]
FixedJ: $J_{BD} = -1\,\mathrm{mA\,cm^{-2}}$	-4.63 / -4.98	-0.63 / -3.88	-1.00 / -2.93
FixedJ: $J_{BD} = -10\,\mathrm{mA\,cm^{-2}}$	-5.83 / -5.98	-4.51 / -4.60	-4.35 / -4.11
FixedJ: $J_{BD} = -20\,\mathrm{mA\,cm^{-2}}$	-6.37 / -6.37	-4.91 / -4.91	-4.56 / -4.56
Linear Fit	-5.09 / -5.40	-4.03 / -4.16	-3.49 / -3.73
PoMC	-4.09 / -4.44	-3.24 / -3.41	-2.47 / -2.57

Table 4.3. The V_{BD} values of the three representative RB-JV measurements, as determined by the various different definitions.

Furthermore, we compare the results of RB-JV measurements performed on a batch of semi-transparent, p-i-n perovskite solar cells. Details of fabrication of the PSCs can be found in the Supporting Information (Appendix B, Note 2). The detailed measurement parameters are shown in Table 4.4. We largely followed the recommendations for less stable cells but used a lower limit of J_{sc} to make the comparison with breakdown voltages of the fixed current densities possible. Additionally, we performed two RB-JV measurements on each cell to estimate the effect of the measurement itself. The data shown here is from the second measurement.

Parameter	Measurement conditions Figure 4.7
Upper Limit	1 V
Lower Limit: Current Density	J_{sc}
Scan Rate	$1.0\,\mathrm{V\,s^{-1}}$
Hysteresis	RV and FW sweep
External Conditions	darkness, RT, ambient atmosphere
Additional Note	second RB-JV measurement

Table 4.4. Measurement parameters used during the RB-JV measurements whose results are shown Figure 4.7.

In Figure 4.7, the breakdown voltages of a batch of 60 PSCs are displayed. In Figure 4.7a, the three definitions based on fixed current densities are shown, in Figure 4.7b, the V_{BD} values of the linear fit method, and in Figure 4.7c, the corresponding result using the point of maximum curvature (PoMC).

The black diamonds mark the data points determined from RV sweeps while the white squares come from the FW sweeps. The green box shows the standard deviation around the mean of the values from the RV sweeps and the gray boxes the corresponding information for the FW sweeps. The horizontal lines with attached labels mark the medians. The distribution of the data points on the x-axis does not have a meaning in any of the box plots of Figure 4.7.

We observe how the breakdown voltage definitions compare when the analysis is performed on many RB-JV curves. The medians of the V_{BD} values of the RV sweeps vary between -5.7 V and -3.9 V. The standard deviation (SD) differs slightly between 0.3 V for the PoMC method to 0.5 V for the fixed current density method using $J_{BD} = -20.0\,\mathrm{mA\,cm^{-2}}$. In the appendix B, Figure B.3, we show example data points and how they change between the definitions.

With that, we have shown the significant differences in the magnitude of V_{BD} that can be caused by using different definitions. At the same time, it seems that the standard deviation of the RB behavior is relatively independent of analysis method. This serves as validation for the proposed V_{BD}-definition and proof that it can be used to describe the reverse bias behavior of perovskite solar cells as long as a reversible breakdown occurs. This should be valid for all perovskite solar cell variants, so not only p-i-n layer stacks, but also n-i-p as long as the immediate formations of shunts can be prevented.

4.4. Conclusions

The information at which voltage perovskite solar cells break down and pass current in reverse bias is of utmost importance for both the research on the breakdown mechanism and for dealing with the underlying issue of partial shading. However, standards for characterizing PSCs in regard to their reverse bias behavior are missing.

This study showed how measurement parameters and conditions vary among publications on the topic. At the same time, data on the impact of measurement parameters on the result are sparse, with sometimes contrary observations reported. A significant dependence on sample-specific properties is presumed. Additionally, the method of defining and determining the breakdown voltage also varies wildly in available literature, without any information about the relationship between different breakdown voltage definitions available.

That suggests that standardization is the only way to comparability. To that end, we proposed detailed sets of measurement parameters and conditions that can serve as starting point for newcomers to the field and as input for a discussion in the community. Additionally, a new definition of the breakdown voltage is proposed: Using the point of maximum curvature provides a comparable breakdown voltage that can be analytically expressed. Therefore, it can prospectively be connected to theoretical descriptions of the breakdown voltage mechanism.

That touches on one important gap in our understanding of the reverse bias behavior of perovskite solar cells: A detailed formulation of the breakdown mechanism that incorporates the unique properties of perovskites would be of great help to refine both the measurement procedure and the method of determining a breakdown voltage.

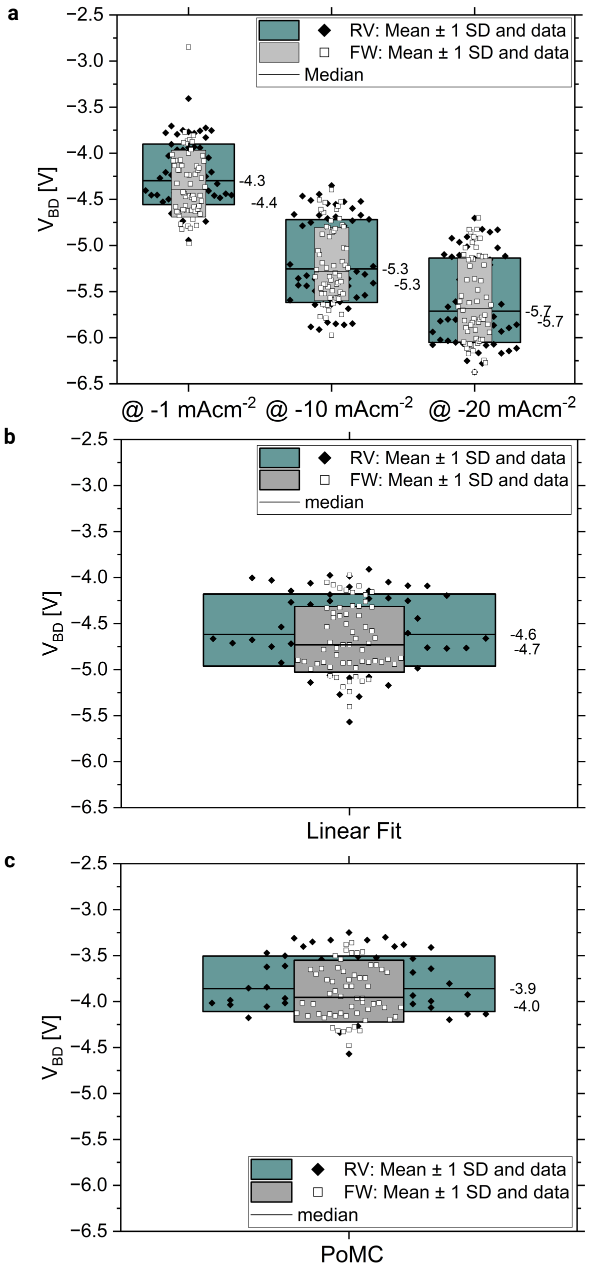

Figure 4.7. The breakdown voltages of a batch of 60 PSCs, determined using five different definitions are compared: Three version based on fixed current densities (a), the linear fit method from the work from [28] (b), and the method using the PoMC (c). The detailed measurement parameters are listed in Table 4.4.

5

The impact of the current on reverse bias degradation

Non-equal current generation in the cells of a photovoltaic module, e.g. due to partial shading, leads to the occurrence of a reverse bias. This quickly causes a significant efficiency loss in perovskite solar cells. Here, a quantitative investigation of reverse bias degradation is reported. Various small reverse biases (negative voltages) were applied for different durations and the change of the efficiency measured. The effects of cell-to-cell differences are softened by normalizing the applied voltage with the breakdown voltage. Possibly exponential dependencies of the current and the degradation rate on the voltage are revealed and serve as proof that degradation is current-driven.

This chapter is based on: J. Henzel *et al.*. 'Impact of the Current on Reverse Bias Degradation of Perovskite Solar Cells'. In: ACS Applied Energy Materials. 6.22, p. 11429-11432 (2023). DOI: 10.1021/acsaem.3c02273.

5.1. Introduction

The topic of partial shading and reverse bias stability has only recently begun to attract specific interest in the perovskite community. [14] Progress towards commercialization of the technology is one main driver behind the increased effort dedicated to the issue of stability in general of which research into the reverse bias behavior is a part. Reverse biases hold a special status as stressors that cannot be mitigated by packaging but need to be researched on cell level. [14] But despite the relevance, also for silicon-perovskite tandem solar cells, [16, 94, 95] the field of reverse bias degradation does not receive much attention and detailed mechanisms are still unclear or require validation.

Reverse biases occur when cells in a module generate very different currents. Then, the series-connection of the cells forces an under-performing cell to pass the current of the other cells. This is only possible if this cell operates at a negative voltage, a reverse bias. Possible reason for the non-equal current generation are partial shading, local differences in aging, and manufacturing defects. [14]

In perovskite solar cell, significant loss of the power conversion efficiency (PCE) has been observed following instances of reverse bias. Important phenomenological studies have been published by Bowring *et al.* and Razera *et al.* whose observations are the basis upon which most discussed degradation mechanisms are built. [18, 19] An overview over the present state of research is given in Chapter 2.

In several publications, the role of the current in reverse bias degradation mechanisms has been addressed. Bowring *et al.* suggested an electrochemical reaction at an interface to explain a decrease of the reverse bias current over time under a constant reverse bias. [19] Such an electrochemical reaction would be driven by the reverse bias current. Razera *et al.* investigated the effects of a voltage below and beyond the breakdown voltage on halide phase segregation. [18] They found different effects that seemed to depend on the amount of charge that had passed the cell. Bertoluzzi *et al.* presented a degradation mechanism involving the electrochemical reaction of halides that is directly dependent on the reverse bias current flowing through the cell. [20] Furthermore, Ni *et al.* added a hole blocking layer and reported slower degradation, possibly due to reduced reverse bias current injection. [29]

On the other hand, there are also degradation mechanisms which can be considered voltage-driven: One example is the migration of iodide into the organic electron transport layer – as proposed by Razera *et al.* and further investigated by Gould *et al.* [18, 58] The same could be true for the formation of local shunts due to migration of metal ions or destabilizing accumulation of ions. [18, 96] It is unclear which degradation mechanisms dominate the observed loss of PCE.

We contribute a quantitative investigation that considers the integrated impact of all occurring degradation mechanisms. We found significant cell-to-cell differences in the breakdown voltage and in the reverse bias current and degradation. Using the breakdown voltage as cell-specific descriptor of the reverse bias behavior, we succeed in partially compensating for these differences. In this way, we reveal exponential relationships of reverse bias current and of the degradation rate with the normalized voltage. This can serve as proof that degradation is mostly current-driven.

5.2. Experimental

Our samples are planar perovskite solar cells in the p-i-n configuration with the following layer stack: glass/ITO/PTAA/perovskite/C_{60}/SnO_2/ITO. The absorber was a triple-cation, double-halide perovskite $Cs_{0.05}MA_{0.15}FA_{0.8}PbI_{2.7}Br_{0.3}$ with a band gap of about 1.6 eV. It was deposited by spin-coating with gas-quenching from a DMF:NMP-solution.

Four cells with areas of $0.16\,\mathrm{cm}^2$ were fabricated on each glass substrate. The power conversion efficiencies (PCEs) of the best 20 cells chosen from 9 different substrates used in the following experiments were determined as $15.6\,\% \pm 0.1\,\%$ by maximum-power-point-tracking (MPPT). Further details of the fabrication process can be found in the appendix (B). Parts of it were based on Bracesco *et al.* [97] and Glowienka *et al.* [98].

The experimental procedure to investigate reverse bias degradation can be separated into an initial characterization, a degradation step, and a final characterization. The characterization steps consisted of voltage sweeps under illumination (JV measurements), dark JV measurements (DJV measurements), dark JV measurements with an extended voltage range to investigate the reverse bias response (RB-JV measurements), and MPPT. During JV measurements and MPPT, the samples were cooled with dry air. During the degradation step, a constant negative voltage (V_{appl}) was applied to a cell for a duration t_{deg} in the dark under ambient conditions at room temperature while the reverse bias current (I_{rev}) was monitored. With the cell area, we calculated a reverse bias current density J_{rev}. Among the samples, V_{appl} was varied between -1.0 V and -4.0 V and t_{deg} between 15 min and 60 min; in one case it was extended to 990 min. Further details can be found in the appendix (B).

5.3. Results and discussion

We use the breakdown voltage (V_{BD}) as a metric to describe the reverse bias behavior of a cell. This metric is defined as the point of maximum curvature of the RB-JV curve and is extracted as is described in Chapter 4. An example demonstrating this method is displayed in Figure 5.1.

As we observe hysteretic behavior of the current density in the negative voltage regime, the mean of the breakdown voltages from the forward and reverse sweeps is used in the following. The cells used in this work showed breakdown voltages between -2.9 V and -4.7 V.

During degradation experiments, a reverse bias current density (J_{rev}) flows through the solar cells. In this chapter, we use the absolute of the current for the reverse bias current. We calculate the mean of this current density and use the resulting average current density ($J_{rev,avg}$) as figure-of-merit to compare the current flows of the different cells.

$J_{rev,avg}$ in dependence of the applied voltage is displayed in Figure 5.2a. We observe an increase of $J_{rev,avg}$ with V_{appl} as can be expected from the RB-JV measurements. However, a significant spread at large and at small (see inset) reverse biases is visible. We can explain the spread at small negative voltages with the existence of local shunts that form the dominating reverse bias current pathway far

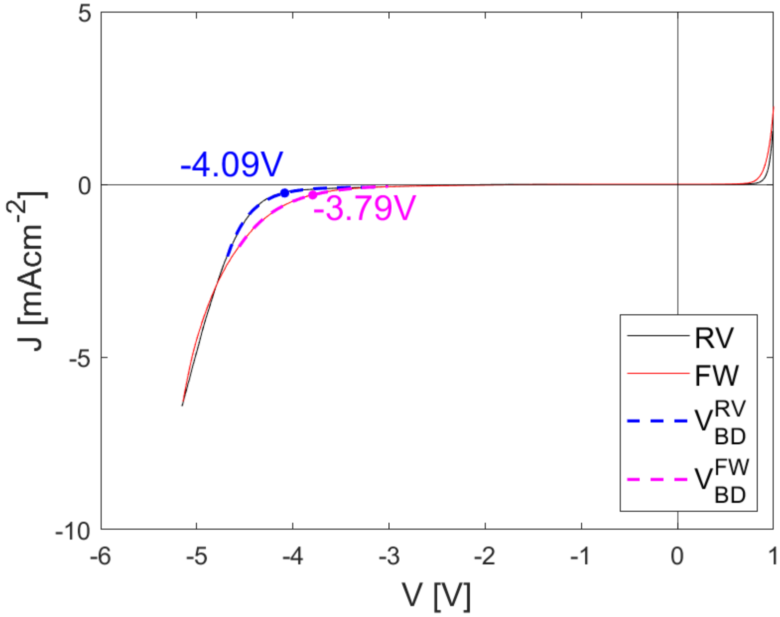

Figure 5.1. The results of RB-JV measurements on a perovskite solar cell, consisting of the reverse (RV: black) and forward sweep (FW: red). The breakdown voltages are marked by blue (RV) and pink (FW) dots. As demonstration of the method of determination, the exponential fit of the selected data range is shown (dashed-blue for RV and dashed-pink for FW). This data range is used for the calculation of the point of maximum curvature.

below the reverse bias breakdown. Regarding the spread at large negative voltages, we hypothesize that the cell-to-cell differences of the breakdown voltage are responsible. After all, a cell with a small breakdown voltage (e.g. $V_{BD} = -2$ V) will experience a large reverse bias current when -3 V are applied. At the same reverse bias, a cell with a larger breakdown voltage (e.g. $V_{BD} = -4$ V) will let barely any current pass.

We attempt to correct for the differences in reverse bias behavior by putting the applied voltage in a relation to the cell-specific breakdown voltage: We obtain the normalized voltage (Φ_{norm}) by dividing V_{appl} by V_{BD}:

$$\Phi_{norm} = \frac{V_{appl}}{V_{BD}}$$

If our hypothesis is correct, we should see a reduced spread when plotting $J_{rev,avg}$ against Φ_{norm}.

This is depicted in Figure 5.2b. We find that the current values ($J_{rev,avg}$) of $V = -4.0$ V are now spread out along different values of Φ_{norm}. The same is true for the other applied voltages. With a larger normalized voltage generally corresponding to a larger current, a clearer relationship between current and voltage is visible. This relationship can be approximated by an exponential function. Such a function is

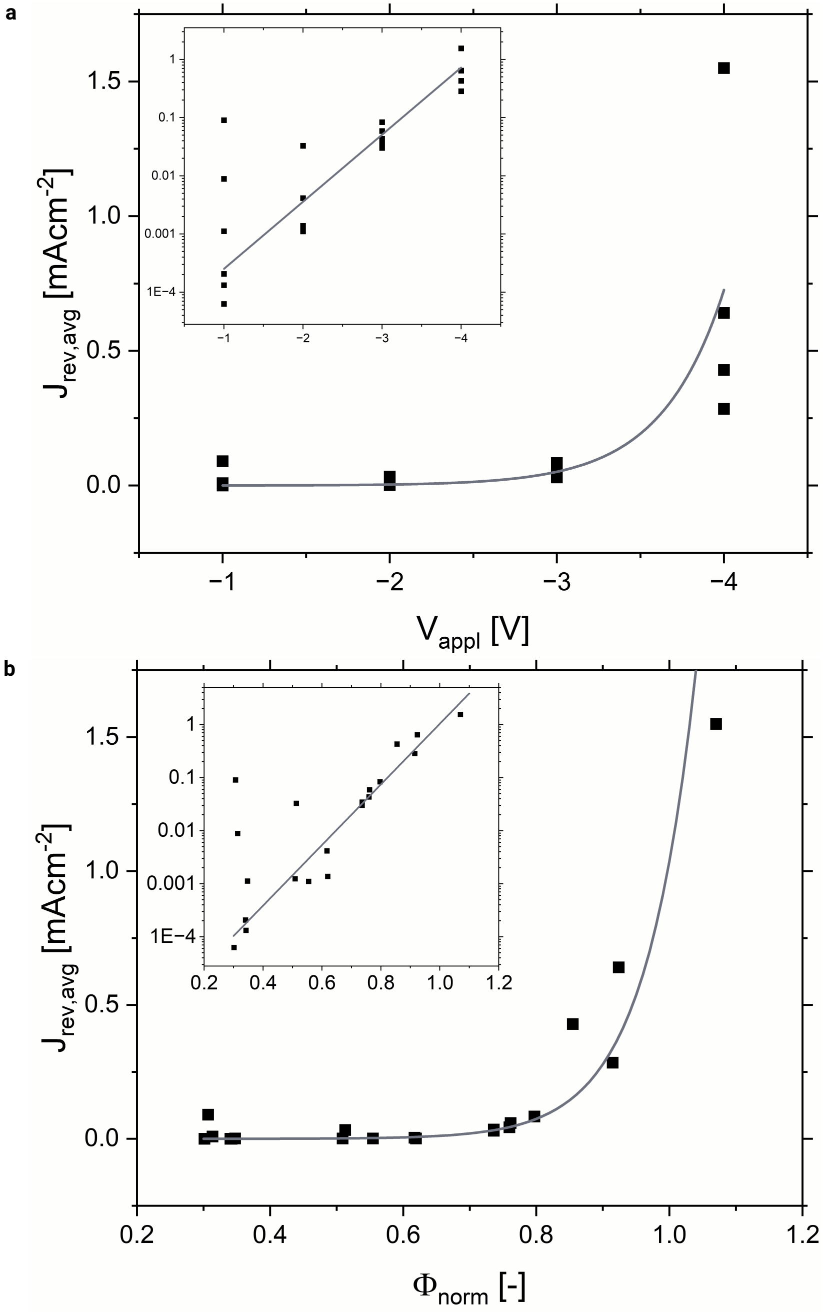

Figure 5.2. The average reverse bias current densities $J_{rev,avg}$ flowing through perovskite solar cells during the degradation step, plotted against the applied voltage V_{appl} (a) and the normalized voltage Φ_{norm} (b). The insets show the same on semi-logarithmic scales. Exponential functions are inserted as guide to the eye.

inserted into Figure 5.2b as guide to the eye.

In the inset of Figure 5.2b, the same data points are depicted on a semi-logarithmic scale. There, it is clearly visible that the spread at small voltages is still present. That implies that the current flow, that is dominating in this regime, is not related to the breakdown voltage. That fits to our previous explanation of this current being shunt-dominated.

The largest voltages that we applied correspond to normalized voltages around 1.1. This explains the relatively small average current densities which remained smaller than $1.6\,\mathrm{mA\,cm^{-2}}$. These degradation conditions were chosen to prevent excessive Joule heating to hide other degradation mechanisms. However, in a simple partial shading event of a perovskite module, we expect a current density that is more than ten times larger ($J_{MPP} \approx 18\,\mathrm{mA\,cm^{-2}}$).

It should be added that the current density was not constant during the degradation. On the contrary, we observed time-dependent changes to the current density that exceeded an order of magnitude. This is shown in the appendix (C). One example is a cell that we applied $-4.0\,\mathrm{V}$ to: The reverse bias current density began at $0.1\,\mathrm{mA\,cm^{-2}}$ in the first second and peaked at $2.8\,\mathrm{mA\,cm^{-2}}$ after about $300\,\mathrm{s}$. That shows that the breakdown voltage is a highly dynamic quantity and implies that there are complex processes at hand that might not be displayed completed in a voltage sweep.

Despite these small average current densities, we observed already significant loss of the PCE. Using efficiencies from illuminated JV measurements performed directly before and after the degradation step, we calculate a (linear) degradation rate DR by dividing the relative PCE loss by the duration of the degradation t_{deg}. This DR is plotted against V_{appl} on a linear scale and in the inset on a semi-logarithmic scale in Figure 5.3a.

We observe a spread that is especially apparent at large reverse biases as was observed in $J_{rev,avg}$. A significant spread at small voltages, however, is not visible here. Small shunts do not seem to greatly impact the degradation rate, despite their impact on $J_{rev,avg}$. If we apply our method of normalizing the applied voltage, we obtain Figure 5.3b. This reduces the spread at large reverse biases. An exponential function is inserted as a guide to the eye. This shows that the relationship between DR and Φ_{norm} could be approximated by an exponential function.

The relationship between degradation rate and normalized voltage allows for conclusions regarding the dominating degradation mechanism. In case of a field-driven mechanism, DR should be proportional to the normalized voltage. That is clearly not the case. Instead, a superlinear behavior that is possibly exponential has been observed for DR. Together with the likewise possibly exponential dependence of the current and the proposed degradation mechanisms in literature, this leads us to the conclusion that degradation is current-driven.

On the other hand, a voltage-driven process could be accompanied by a current showing a voltage-dependence similar to our $J_{rev,avg}$. Garcia-Batlle *et al.* found on monocrystalline perovskites that the ionic current caused by positive voltages can show a superlinear dependence on the voltage. [99] They, however, also noted that the mobility of holes and electrons is ≈ 7 - 9 orders of magnitude larger than of ions.

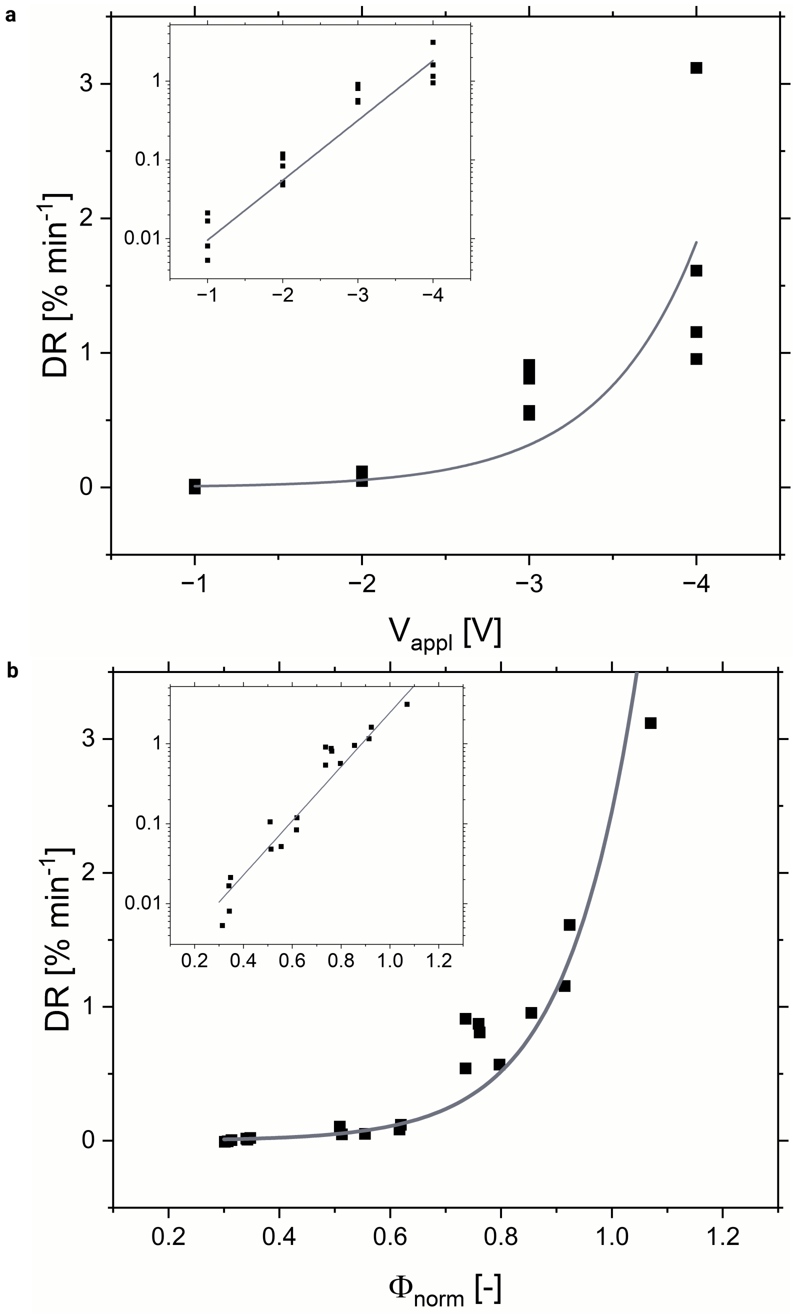

Figure 5.3. The degradation rate (*DR*) is plotted against the applied voltage (V_{appl}) (a) normalized voltage (Φ_{norm}) (b). The insets show the semi-logarithmic depiction. Exponential functions are inserted as guides to the eye.

Therefore, the magnitude of the electronic current far outshines the ionic current. A similar conclusion had also been drawn for the reverse bias current. [19]

5.4. Conclusion

The goal of this work was to connect the reverse bias with the current and the degradation rate quantitatively. To that end, we applied various reverse biases for various durations to perovskite solar cells and monitored current and efficiency. Our results show that differences in the reverse bias behavior within a batch can lead to a large spread in current and degradation rate. By using the breakdown voltage, determined from voltage sweeps, we successfully corrected for these cell-to-cell differences. That proves that the breakdown voltage can describe the reverse bias behavior of perovskite solar cells in steady state degradation.

The correction of the cell-to-cell differences revealed relationships between RB current and degradation rate with the voltage. In both cases, these relationships were superlinear and possibly exponential. That implies that the dominant degradation mechanisms are not field-, but current-driven. This condition matches several proposed degradation mechanism that involve electrochemical reactions in the bulk and at interfaces. Therefore, further research is required to assess which mechanism is responsible for the bulk of the observed degradation.

6

The impact of low-intensity illumination on the reverse bias behavior

In realistic partial shading scenarios, the impact of low-intensity illumination needs to be considered. However, there is barely any research available and the published results are contradictory. Here, it is shown that the reverse bias behavior of perovskite solar cells under low-intensity illumination strongly depends on the voltage scan rate. As explanation, a hypothesis is developed and experimentally verified that is based on two antagonistic mechanisms: On the one hand, illumination affects the conductivity of mobile ions, decreasing the breakdown voltage. On the other hand, an electrochemical reaction, caused by the reverse bias current, increases the breakdown voltage. Since the two mechanisms occur on slightly different time scales, it depends on the voltage scan rate which mechanism dominates. These findings emphasize that more detailed research into the mechanism occurring in reverse bias and the factors affecting the reverse bias breakdown is still necessary. Firstly, a deeper understanding would be helpful for investigating the effect of realistic, non-ideal partial shading scenarios on perovskite modules. Secondly, knowing how cell properties and external factors influence the breakdown voltage is necessary for developing an integrated model for the breakdown mechanism.

This chapter is based on: J. Henzel *et al.*. 'The impact of low-intensity illumination on the reverse bias behavior of perovskite solar cells'. Journal of Materials Chemistry A. 13.37 (2025), p. 31755-31769. DOI: 10.1039/D5TA04100G.

6.1. Introduction

The power conversion efficiencies (PCEs) of perovskite solar cells (PSCs) are leaping from record to record. With small-area cells having reached around 27 % efficiency, and even perovskite minimodules with around 24 % being revealed, [6, 100] it seems that the commercial breakthrough is only a question of time. However, there are still some hurdles that need to be overcome first. One important challenge is the stability.

Just like with the efficiency, the bar is set by the dominating silicon (Si) PV technology where panels generally come with a warranty of 25 - 30 years, guaranteeing that during this time, degradation remains below 0.4 % - 0.6 % per year. [10] Therefore, accelerated lifetime testing is required, where unrealistically harsh conditions are used to imitate the effects of long-term outdoor exposure. Here, challenges lie in only accelerating those degradation pathways relevant to outdoor exposure and in the need to translate the results of indoor tests into predictions of outdoor lifetime of modules. While these challenges pose questions yet to be answered in full, there exists a framework of defined testing conditions whose purpose it is to improve the comparability of stability experiments on (among other technologies) perovskite solar cells: [33] The authors of the ISOS protocols (International Summit on Organic Photovoltaic Stability) name various stressors that can be expected to occur under operating conditions and cause changes in perovskite solar cells. [33] One such stressor is the occurrence of reverse biases (RB).

Reverse biases are an especially serious problem in monolithically interconnected modules which is the preferred module design for thin-film PV technologies. Such a module consists of narrow but long, stripe-like cells which are electrically-connected in series. That means that one and the same current is flowing through all cells. This monolithic interconnection provides advantages but leads to problems when current is *not* generated homogeneously across the module area. This can occur, for instance, due to disparate aging or partial shading. [14]

During a typically considered partial shading event, a part of a module, e.g. one cell, is completely shaded. This scenario has been named ’asymmetric’ partial shading by Dongaonkar *et al.* [83] There, all cells but one are fully illuminated while the one shaded cell operates in darkness and does not generate any current. Since the shaded cell is series-connected to the illuminated cells, the shaded cell has to pass the current generated by them. That leads to the accumulation of charge carriers at the interfaces and the build-up of an electric field. This electric field is oriented in the opposite direction to the electric fields in the illuminated cells. Therefore, the voltage dropping over the shaded cell is negative. This voltage is called ’reverse bias’.

This reverse bias grows, until either the shaded cell passes the current generated by the other cells, or the maximum voltage that the illuminated cells can generate is reached. This maximum reverse bias is the sum of the open-circuit voltages (V_{OC}) of the illuminated cells. In this case, no current flows through the cells of that module and no power can be extracted. In the other, more realistic case, however, the shaded cell breaks down, the current is passed and the module continues to generate power at the price of the shaded cell operating in reverse bias, therefore dissipating power.

There are several publications available that investigate the effect of partial shading on perovskite modules: A detailed discussion of the effects of partial shading and possible methods of mitigation (bypass diodes, module design, cell geometries), including their problems, can be found in Wolf *et al.* [16] Experimental results of partial shading experiments on perovskite (mini-)modules have been presented by Bogachuk *et al.*, Yang *et al.*, Tayagaki *et al.*, and Aninat *et al.* [23, 53, 59, 101] Additionally, inspiration can be found in the research that has already been performed on other thin-film PV technologies: When it comes to module design or interconnection strategies, or considerations of realistic partial shading scenarios, lessons from research on CIGS modules can come handy. [83, 102, 103]

Nonetheless, the impact of reverse bias on a single solar cell was the focus of most publications at present. Instead of investigating the effects of a partial shading event on a perovskite module, a reverse bias is directly applied to a single perovskite solar cell in the dark. This allows the investigation of the effects of reverse biases without being hindered by the problems of fabricating modules with enough cells to force a shaded cell into breakdown while maintaining a device quality that is relevant for degradation experiments. This method of applying reverse biases to single cells has been successful in demonstrating the devastating impact that this degradation mode has on perovskite solar cells and in investigating the degradation pathways that serve to quickly decrease the PCE. The phenomenological works of Razera *et al.* [18] and of Bowring *et al.* [19] form the basis of all research in this field. A more general overview can be found in Wang *et al.* [17]

An important point is that it seems that degradation is driven by the reverse bias *current* and not by the reverse bias itself. [84, 85] It follows that the reverse bias breakdown has to be avoided in order to limit the reverse bias current and therefore retard degradation. In modules, that necessitates the use of bypass diodes that provide low-resistance current paths above a certain voltage threshold. One question is how to integrate bypass diodes into the modules: The problems related to this question are illustrated and discussed in Bowring *et al.* [19] and Wolf *et al.* [16] Another hurdle to overcome is the cost effectiveness which is directly related to the number of bypass diodes required. The number of bypass diodes is, in turn, related to the breakdown voltage of the perovskite solar cells that are to be protected. [16] A larger (i.e. a "more negative") breakdown voltage reduces the number of bypass diodes needed. Accordingly, significant effort has been focused on manipulating the breakdown voltage towards larger values by introducing additives or additional layers to the perovskite solar cell layer stack. [22, 24, 28–31]

An important aspect that has only very recently received attention is the interaction between reverse biases and illumination. At the first glance, adding illumination to a phenomenon that occurs during a partial shading event (as defined above) might seem less relevant. There are, however, two scenarios during which the impact of illumination might be important:

1. Perfect shading, that is, complete darkness in the shaded area, is probably quite rare in real operating conditions. Whenever the object that is casting the shadow is located at a distance from the module, some diffuse illumination will still reach the 'shaded' module area. Additionally, when considering the trend towards bifaciality, even perfect shading from one side might not prevent

diffuse illumination from the other side.

2. Partial shading might not follow a simple pattern as posited for the simplified asymmetric shading case where one or more cells of a module are completely shaded. [83] A more realistic scenario expects the ’realistic’ shading case (named by Dongaonkar *et al.*) where only a part of a cell area is shaded while the remaining area is illuminated. [83] This illumination can be of low-intensity as in the first scenario.

In CIGS solar cells, it was shown that illumination causes a significant reduction of the breakdown voltage. [51, 104] This effect would mean for the first scenario of incomplete but spatially-homogeneous shading that the effective V_{BD} would be smaller than measurements in the dark show. This would have implications for the number of bypass diodes required. Following the second scenario of incomplete and inhomogeneous shading, local, low-intensity illumination would lead to a locally smaller V_{BD}. If a part of a cell that operates in reverse bias has a smaller V_{BD}, we expect most of the reverse bias current to flow there. This locally concentrated reverse bias current would lead to locally increased degradation. Aninat *at al.* recently proposed this explanation for locally increased partial shading degradation observed in a perovskite module. [59]
Nevertheless, there have been only few publications that mention the interaction of reverse bias with illumination in PSCs: Jiang *et al.* observed that an illumination intensity of 0.1 suns did only have a negligible effect on the breakdown voltage. [28] Wang *et al.*, on the other hand, found that the breakdown voltage changes drastically upon adding low-intensity illumination. [49] They considered an illumination wavelength-dependent mechanism as in CIGS but also emphasized the possible importance of mobile defects.

In all these publications, the topic of reverse bias under illumination has only been treated peripherally. That means that a detailed investigation with a proposed mechanism is still missing. The qualitatively different observations regarding the impact of illumination on the breakdown voltage in the presented literature serve as proof that there is a phenomenon worth investigating. Together with the possibly great relevance of this topic for the partial shading stability of PSCs, this discrepancy serves as motivation for us to take a more detailed look at the interaction of reverse biases with illumination.

In this publication, we present an investigation of the interaction between reverse bias and illumination in perovskite solar cells. We varied various experimental parameters (scan rate, illumination intensity, illumination wavelength) and built up on our results by developing a mechanism to explain the observed phenomena. Finally, we designed and executed experiments to test our hypothesis.

6.2. The effects of illumination on the reverse bias behavior in voltage sweeps

6.2.1. The voltage sweep experiment

Our samples are p-i-n structured, semi-transparent perovskite solar cells with a triple-cation (Cs^+, MA^+, FA^+), double-halide (Br^-, I^-) absorber composition. The layer stack consists of glass/ITO/PTAA/PVK/C_{60}/SnO_2/ITO. Details about fabrication and the results of the initial characterization can be found in the appendix D. The detailed measurement parameters used throughout this publication if not mentioned differently are available there as well.

There are three parameters whose impact on the breakdown voltage we want to investigate: The illumination intensity, the wavelength of the illumination, and the voltage scan rate. While the former two parameters also play a role in the mechanism described for CIGS, [51] varying the scan rate reveals the impact of mobile ions and other slow processes unique to PSCs. [63]

To that end, we executed an experimental procedure that is schematically depicted in Figure 6.1. This experiment consisted of JV measurements with a voltage range that is extended into the reverse bias regime. We always performed both a reverse (RV) sweep (from 1.0 V to -8.0 V or to the current cutoff at -20.0 mA cm^{-2}) and a forward (FW) sweep (from -8.0 V or the current cutoff to 1.0 V). These *RB-JV measurements* were executed using five different voltage scan rates (between 5.0 V s^{-1} and 0.1 V s^{-1}). For every voltage scan rate, we performed eight dark RB-JV measurements and seven light RB-JV measurements (Figure 6.1a). We call such a set of 15 RB-JV measurements a "group".

The dark and light RB-JV measurements were alternated in order to use the latest dark measurement as baseline for the following light measurement (see Figure 6.1b and c). That way, we were able to correct for changes to the cell due to previous measurements. A set of a dark and corresponding light RB-JV measurement is called a "pair".

The illumination intensity (expressed as a ratio $P_{light} = \frac{J_{sc}^{light}}{J_{sc}^{1sun}}$) was successively increased from light measurement to light measurement. As light source, we used a blue (455 nm), green (530 nm) or far red (735 nm) LED. The purpose of using different wavelengths were the resulting different absorption profiles which might reveal information about the role of the interfaces between the absorber and the transport layers.

Figure 6.1d shows how we analyzed the data: We corrected for the photo-generated current by subtracting J_{sc}: $J_{RB} = J - J_{sc}$. The breakdown voltage V_{BD} is defined using a fixed current density: $V_{BD} = V@-10.0$ mA cm^{-2}. In general, we will describe the absolute value of the breakdown voltage. Therefore, a "larger V_{BD}" means a more negative breakdown voltage. The difference between the V_{BD} under illumination and the V_{BD} in the dark is defined as the breakdown voltage shift ΔV_{BD}.

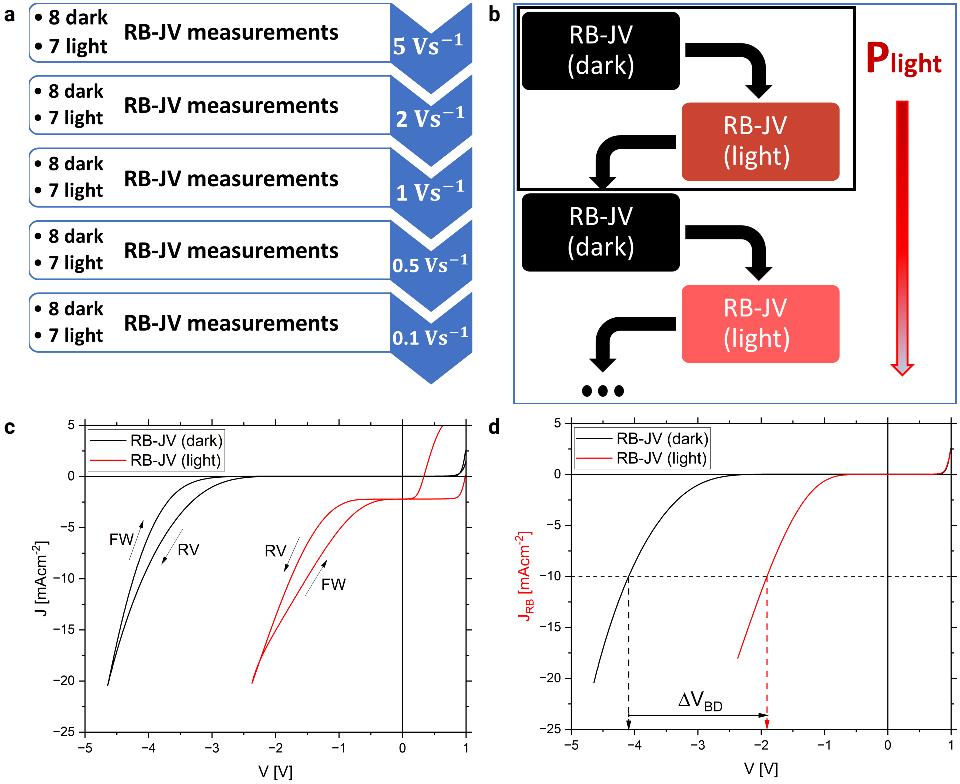

Figure 6.1. The experimental procedure and analysis: The five groups of reverse bias (RB-) JV measurements that each consist of eight dark and seven light RB-JV measurements are shown (a). Within each group of measurements, one voltage scan rate was used. The first four RB-JV measurements of a group (b). Dark and light RB-JV measurements were alternated and the illumination intensity P_{light} was increased light RB-JV-to-light RB-JV. One such pair of one dark (black) and one light (red) RB-JV measurement (c). Each pair consists of a reverse (RV) sweep and a forward (FW) sweep. The analysis of the gathered data (d).

6.2.2. Initial results

Figure 6.2 shows representative results from this experiment, using a blue LED as light source. Only the RV sweeps are displayed. The FW sweeps and results from other cells can be found in the appendix D.

Figure 6.2a displays the measurement results of a group of RB-JV measurements, using the voltage scan rate $5.0\,\mathrm{V\,s^{-1}}$. The curves are corrected for the photo-generated current as described previously. The eight RB-JV measurements in the dark ("dark" RB-JV) are displayed as black curves and the seven RB-JV curves under illumination ("light" RB-JV) in various shades of red. The lightness of the color corresponds to the illumination intensity P_{light}, so that the darkest red curve belongs to the light RB-JV measurement with the smallest P_{light}. The horizontal, dashed line marks the current density selected to define V_{BD}.

Looking at the black curves, we see that most of them are nearly lying on top of each other. That means that also V_{BD} is nearly constant among them. Only one curve, corresponding to the first measurement, lies separate. Even then, however, the spread is smaller than 0.5 V (see appendix D). Contrary to the dark RB-JV curves, the light RB-JV curves (in red) do not lie on top of each other. Instead, we observe that they shift towards smaller voltages with increasing P_{light} (dark red to orange). Therefore, the V_{BD}'s under illumination move to smaller voltages. The difference between dark and light RB-JV curves grows and therefore ΔV_{BD} increases.

In Figure 6.2b, another group of RB-JV measurements from the same experiment is displayed. Here, the scan rate was $0.1\,\mathrm{V\,s^{-1}}$. Again, the black curves are the results from measurements in the dark while the red curves correspond to the measurements with increasing illumination intensity.

Looking at the dark RB-JV measurements first, we see that the black curves mostly overlap, again. One curve (corresponding to the first measurement) lies partially separate from the others. However, near the horizontal, dashed line, all black curves are close to each other, so that the spread of V_{BD} is small. If we turn our attention to the light RB-JV curves (in red), we observe that the (absolute) current density begins to increase at a very small voltage ($V \approx -1$ V, marked by blue arrow). With increasing reverse bias, the current density proceeds to increase only slowly, however. This is a new phenomenon that we call 'pre-breakdown' (blue bracket). At a voltage $V \approx -4$ V, the current density suddenly increases steeply. Here, the actual breakdown occurs. This happens for all light RB-JV curves at nearly the same voltage. This means that V_{BD} is nearly the same for all light RB-JV measurements with this scan rate. As the difference between the dark and light RB-JV curves at $-10.0\,\mathrm{mA\,cm^{-2}}$ is minimal, ΔV_{BD} is small.

We now proceed to comparing Figure 6.2a and b, i.e. the results from measuring with $5.0\,\mathrm{V\,s^{-1}}$ and $0.1\,\mathrm{V\,s^{-1}}$:
When looking at the dark RB-JV curves first, we see a rather similar behavior. In both cases, the spread of V_{BD} is small, with the first measurement as outlier. Also, the V_{BD} of both groups lie around $V \approx -4.5$ V and not much more than 0.5 V apart from each other (see appendix D). We conclude that the scan rate (within the selected range) has only a limited impact on V_{BD} in the dark.

Comparing the light RB-JV curves shows significant differences:

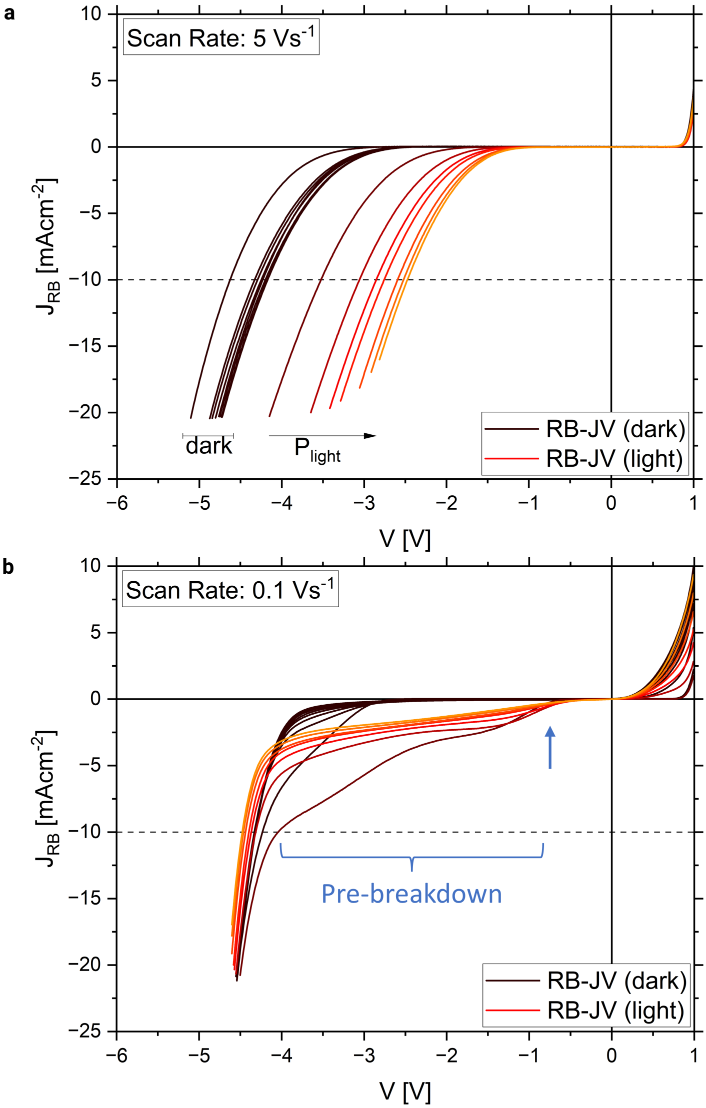

Figure 6.2. Representative results of the experiment using a blue LED: The $J_{RB} = J - J_{sc}$ of the reverse (RV) sweeps with a scan rate of $5.0\,\mathrm{V\,s^{-1}}$ (a). The dark JV curves are shown in black, the light JV curves in various shades of red. The lightness of the color corresponds to the illumination intensity. A dashed, horizontal line marks the current density used for defining V_{BD}. The results for a scan rate of $0.1\,\mathrm{V\,s^{-1}}$ in the same way (b). A blue arrow marks the aborted early breakdown and a blue bracket the pre-breakdown of the RB-JV measurements under illumination.

At $5.0\,\mathrm{V\,s^{-1}}$ (a), the light RB-JV curves and their V_{BD}'s shift significantly with P_{light}. In contrast, at $0.1\,\mathrm{V\,s^{-1}}$ (b), the V_{BD} is nearly unaffected by illumination. An additional difference is visible in the low current density regime ($J_{RB} \leq -3\,\mathrm{mA\,cm^{-2}}$). At $5.0\,\mathrm{V\,s^{-1}}$ (Figure 6.2a), the light RB-JV curves look like dark RB-JV curves that have been shifted to smaller voltages. In contrast, the light RB-JV curves at $0.1\,\mathrm{V\,s^{-1}}$ (Figure 6.2b) show the pre-breakdown and therefore completely different behavior than the corresponding dark RB-JV curves.

Finally, we take a look at the positive voltage region: In Figure 6.2a, all the dark and light RB-JV curves lie on top of each other. It seems that neither the successive measurements nor the illumination has a lasting impact on the behavior in the positive voltage region. That is different at $0.1\,\mathrm{V\,s^{-1}}$ in Figure 6.2b. There, we observe for both the dark and the light RB-JV curves, that the current density begins to increase at smaller positive voltages with every RB-JV measurement. As these are the RV sweeps that start at $1.0\,\mathrm{V}$, it seems that the solar cells do not return to their initial state in between the measurements.

The corresponding results obtained from the FW sweeps are attached to the appendix D as they show qualitatively the same behavior. Only at the smallest scan rate of $0.1\,\mathrm{V\,s^{-1}}$, a significant difference can be observed: The 'pre-breakdown' is completely absent in the forward sweeps (see also Figure

The observations in regards to the V_{BD} values are summarized for all investigated voltage scan rates and illumination wavelengths in Figure 6.3 by means of comparing the breakdown voltages. To that end, the breakdown voltage shift (ΔV_{BD}), i.e. the difference between the V_{BD} in the dark and in the corresponding light RB-JV measurement, is plotted against the illumination intensity.

Figure 6.3a shows results from the same cell as was shown in Figure 6.2 on which blue illumination was used. We see two very different types of behavior:
ΔV_{BD} is very small when using a scan rate of $0.1\,\mathrm{V\,s^{-1}}$ (black squares). In contrast, all other scan rates lead to ΔV_{BD}'s that range from $1.0\,\mathrm{V}$ to $2.5\,\mathrm{V}$ (orange, blue, green, and red symbols). These are the results from using scan rates $\geq 0.5\,\mathrm{V\,s^{-1}}$. Additionally, a dependence on P_{light} is visible for these scan rates as well: At low illumination intensities, ΔV_{BD} increases steeply, but that increase levels off at $P_{light} \approx 0.05$. This might point to a logarithmic dependence (see semi-logarithmic plot in the appendix D.

Figure 6.3b and c show the results from experiments with different illumination wavelengths (green and far red) on other cells. It is clear that nearly the same behavior is observed as in Figure 6.3a. The differences that are visible (especially in regards to $0.5\,\mathrm{V\,s^{-1}}$, Figure 6.3b) fall within the cell-to-cell variation and do not seem to be connected to the illumination wavelength (see the results from more cells in the appendix D. We consider $0.5\,\mathrm{V\,s^{-1}}$ a boundary case where it varies from cell-to-cell whether it resembles the "fast" or the "slow" voltage sweeps. The fact that the observed phenomenon does not depend on the wavelength of the illumination means that it does not depend on the absorption depth. That leads us to the conclusion that the mechanism responsible for the impact of illumination can occur in the whole perovskite layer.

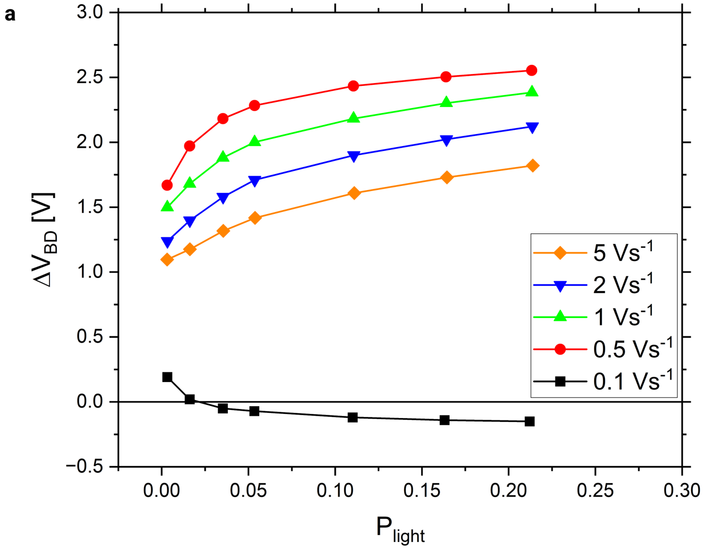

Blue LED

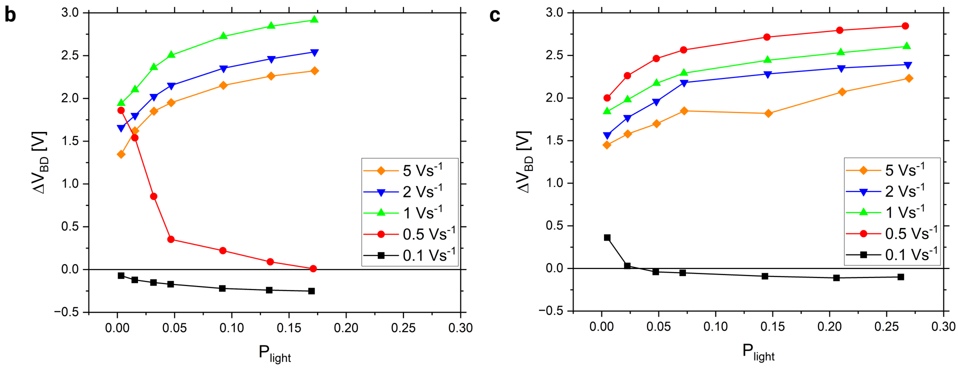

Green LED

Far Red LED

Figure 6.3. Summary of the results of the experiments: The breakdown voltage shift (ΔV_{BD}), i.e. the difference in V_{BD} between the dark and the light RB-JV curves, is shown as function of the illumination intensity P_{light}. The results from blue illumination (a), from green illumination (b) and far red illumination (c).

6.2.3. Comparison with literature and open questions

Summarizing our observations, we can classify our results in two groups:
When using a small voltage scan rate (e.g. $0.1\,\mathrm{V\,s^{-1}}$), we observe the 'pre-breakdown' phenomenon but barely any change to the breakdown voltage. Indeed, V_{BD} even seems to be slightly larger under illumination than in darkness. In contrast, the results when using a larger voltage scan rate ($\geq 1.0\,\mathrm{V\,s^{-1}}$) *do* show a significant change of the breakdown voltage. Here, the breakdown seems to occur at a far smaller voltage under illumination than in darkness. The magnitude of that shift shows a

clear dependence on the scan rate and the illumination intensity. The scan rate $0.5\,\mathrm{V\,s^{-1}}$ seems to lie in the middle between the two cases. Generally, we did not observe any qualitative impact of the wavelength of the illumination in either case.

These results fit in with the observations in literature described above: Jiang *et al.* used a voltage scan rate of $0.35\,\mathrm{V\,s^{-1}}$ for reverse bias measurements with illumination and did not observe a significant impact of illumination. [28] The closest scan rate we used are $0.1\,\mathrm{V\,s^{-1}}$ and $0.5\,\mathrm{V\,s^{-1}}$. The former did never show a significant impact of illumination, while for the latter, the results varied from cell to cell. We explain this with possible variations in material parameters, like mobile ion concentration, caused by details of the fabrication procedure. However, the lack of 'pre-breakdown' in their results is a more significant difference. Later, we will show that this difference could be the result of pre-conditioning of the cells before the measurement.

Wang *et al.* presented a significant impact of illumination on V_{BD}. [49] Therefore, our observations seem to confirm the results of Wang *et al.*, although a direct comparison is difficult due to differences in sample structure and experiment design.

So, while there is an overlap between our observations and results reported in literature, there remain open questions:

- Why does illumination greatly influence the breakdown voltage when using high voltage scan rates?
- How can we explain the dependence of this breakdown voltage shift on scan rate and illumination intensity?
- What causes the 'pre-breakdown' phenomenon and why is the effect of illumination absent or even inverted at small scan rates?

In the following section, we develop a hypothesis that is able to explain the observed phenomena.

6.3. A detailed explanation

6.3.1. Developing a hypothesis on the effects of light and scan rate

Before we start formulating our hypothesis, we will give a short introduction to the generally-accepted reverse bias breakdown mechanism in perovskite solar cells that was proposed by Bowring *et al.*: [19]

This model posits that the breakdown mechanism is based on tunneling facilitated by the accumulation of mobile ions at the interfaces. Already without an external voltage, the built-in field leads to ion migration towards the interfaces until the bulk of the absorber is screened and most of the voltage drops near the interfaces. When a reverse bias is applied, additional mobile ions begin moving towards the interfaces until the external field is also screened. This accumulation of charged species leads to additional band bending which reduces the width of the tunneling barrier, thus increasing the probability for a tunneling event. [19]

A very simplified schematic of this breakdown mechanism is displayed in Figure 6.4a. There, a certain concentration of mobile ions (red-filled circles) is present in the absorber of a PSC in darkness. Upon the application of a reverse bias ($-V$) and with enough time (Δt), these mobile ions drift towards an interface with a transport layer (TL1). When they reach it, a reverse bias current (J_{RB}) begins to flow (red arrow).

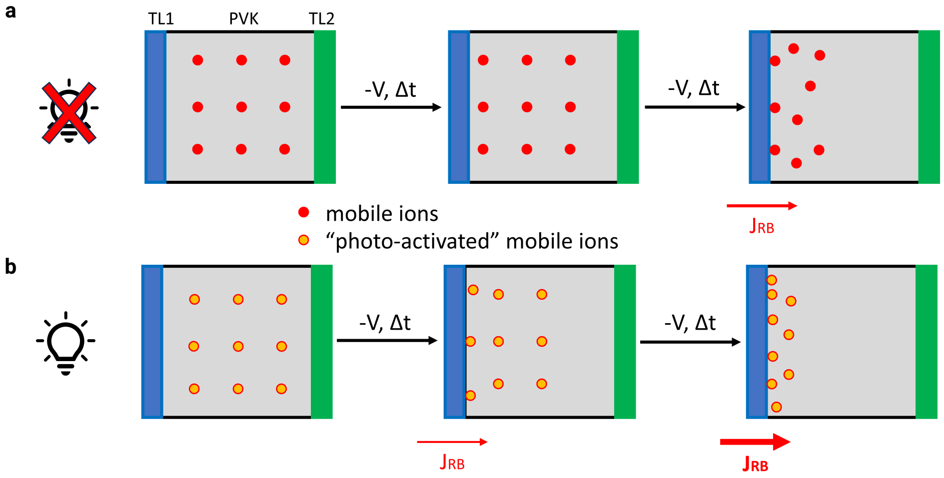

Figure 6.4. A schematic representation of the reverse bias breakdown mechanism in the dark (a) and under illumination (b). The effect of illumination is here presented as an increase of the mobility of the mobile ions by "photo-activation". A simplified schematic of a PSC with transport layers (TL1, TL2) and perovskite absorber (PVK) is depicted. The red-filled circles represent the mobile ions that are present in the dark while the orange-filled circles with red edge represent the photo-activated mobile ions with a higher mobility. When a reverse bias is applied ($-V$), both species move towards an interface which takes time (Δt). When they reach the interface, they contribute to the reverse bias breakdown mechanism and allow tunneling. That increases the reverse bias current (J_{RB}), depending on the number of mobile ions at the interface. Its magnitude is expressed as thickness of the red arrow.

In the publication of Bowring *et al.*, several factors are mentioned that add to the complexity of this mechanism: [19]
Firstly, perovskite absorbers are generally polycrystalline materials with grains separated by grain boundaries. It is well-known that grain boundaries form channels for ion migration. [22, 45, 89] Secondly, there might be additional energy states within the tunneling barrier, opening the door for a trap-assisted tunneling mechanism. Additional factors could be macroscopic defects that are practically unavoidable in large-scale layer deposition and the impact of the electrodes on the electric field. [19, 44, 96] It should also be mentioned that there are also publications that discuss a possible role of an avalanche breakdown mechanism in perovskite devices. [49, 54] Finally, it was reported that the breakdown voltage is not a static property but changes during the application of a reverse bias: The breakdown voltage changes in time due to the slow migration of mobile ions. Additionally, the reverse bias current might itself cause an electrochemical reaction enhancing the tunneling barrier. [19] An enhanced tunneling barrier leads to a lower probability for tunneling and thus a

decrease of the reverse bias current.

To develop our hypothesis, we can draw inspiration from possibly related phenomena in PSCs: A phenomenon where the voltage scan rate has a significant impact on JV measurements under illumination is the JV hysteresis. There, the voltage sweep direction influences the results, i.e. the measured power conversion efficiency. [62] The general consensus on the origin of this hysteresis points toward the migration of mobile ion species and non-radiative recombination at interfaces. [70] Le Corre *et al.* demonstrated the impact of a wide range of voltage scan rates on the magnitude of hysteresis experimentally and connected their results to ion mobility by way of simulation. [63] They argued that a voltage scan at a very large scan rate (e.g. $1000\,\mathrm{V\,s^{-1}}$) negates the impact of mobile ions as they cannot react to the changing bias. On the other hand, at very small scan rates (e.g. $0.01\,\mathrm{V\,s^{-1}}$), the solar cell approaches steady-state as the mobile ions have enough time to reach a new equilibrium in between the measurement points. [63] In between these extrema, JV measurements show hysteresis.

The scan rate where hysteresis reaches a peak in magnitude depends mostly on the diffusion coefficient of the mobile ions. [63] Their experiments were performed on solar cells considered to be "hysteresis-free" as they did not show significant hysteresis at a typical scan rates of about $0.1\,\mathrm{V\,s^{-1}}$. [63] That matches our cells (see appendix D). We can therefore assume that the impact of the scan rate must be connected to the ability of the mobile ions to react to the changing electric field during voltages sweeps. This ability depends on the mobility and concentration of the mobile ions and on how much time they have to reach a new equilibrium (Δt in Figure 6.4a).

The impact of illumination on the mobile ions could come about indirectly via the temperature or directly. In the following, we will first investigate the possible effect of a temperature increase due to illumination.

Temperature could play a role since it has an effect on the mobile ions and on the reverse bias behavior. It has been reported in two publications that higher temperatures lead to smaller breakdown voltages. [19, 53] This has been linked to quicker mobile ion movement. [19] As the voltage scan rate determines how long a cell is exposed to illumination, we could expect higher temperatures at smaller scan rates. This should lead to smaller V_{BD} values.

To get an idea about the temperature changes we can expect, we used an infrared (IR) camera to track the surface temperature of a PSC. After a few seconds without illumination, we switched on a blue LED, set to an intensity equivalent to $P_{light} = 0.25$. As this illumination intensity is among the upper limit of what we used during the voltage sweep experiments, this gives us also the upper limit of temperature increase. The detailed results can be found in the appendix D. They show that even after 3 minutes of constant illumination (approximately the duration of a complete voltage sweep at $0.1\,\mathrm{V\,s^{-1}}$), the temperature has only increased by about 3 K.

Therefore, the temperature cannot be expected to play a significant role, especially at smaller illumination intensities than $P_{light} = 0.25$. Since most of the ΔV_{BD} is, however, already visible at illumination intensities $P_{light} \leq 0.05$, another factor seems to be responsible for affecting the mobile ions.

The temperature could, however, be playing a role in the differences in ΔV_{BD} of the fast voltage sweeps ($\geq 0.5\,\mathrm{V\,s^{-1}}$). There, we observe larger ΔV_{BD} values with smaller scan rates (see Figure 6.3). That could be explained by higher temperatures due to longer scan durations. However, there is evidence against this temperature effect playing an important role here, as well: The difference between the ΔV_{BD} of the different scan rates stay constant for all illumination intensities. This observation argues against an impact of the temperature increase due to illumination. Therefore, we conclude that the illumination influences the mobile ions via a different mechanism than the temperature.

The impact of illumination on the mobile ions has been an object of research, based on the observation that the capacitance of solar cells at small frequencies increases significantly upon addition of illumination. [105] As origin of this observation, a reduction of the activation energy of mobile ions and the additional creation of defects were discussed. [106, 107] However, conclusive answers even to fundamental questions regarding mobile ions species or mechanisms of ion migration or interaction with illumination are missing.

Recently, Schiller *et al.* showed that the capacity-increase is caused by the photo-induced electronic currents being modulated by mobile ions and can therefore be explained without a change to ion mobility or ion concentration. [108] However, they still found evidence of a photo-conductive effect, meaning that illumination does indeed impact the ion conductivity. They did not specify whether it is the concentration or the mobility of the mobile ions that is affected by light. Developing a mechanism of interaction between light and ions was beyond the scope of their publication. [108] They did, however, argue that any interaction between illumination and mobile ions has to be mediated by photo-generated charge carriers. [108]

With that, we can incorporate the effect of illumination:
Light increases the conductivity of mobile ions, i.e. the concentration and/or mobility. These, in turn, affect the reverse bias behavior of perovskite solar cells. This is displayed in Figure 6.4b. There, the effect of illumination is depicted as the photo-activation of mobile ions which increases their mobility. The mobility affects how fast the mobile ions move under a certain reverse bias ($-V$): Due to the higher mobility under illumination, the photo-activated mobile ions reach the interface earlier than in darkness. More ions at the interface leads to stronger band bending and therefore a higher tunneling current. Thus, J_{RB} is larger under illumination. This is shown in Figure 6.4b as a thicker red arrow than in a. We should note that similar considerations are valid for the case of an increased concentration of mobile ions.

These considerations are sufficient to formulate answers to the first two of our questions:
Illumination leads to an increase of the conductivity of the mobile ions. Therefore, it takes less time under reverse bias until the accumulation of mobile ions at the interface is significant. This accumulation leads to a larger reverse bias current.

We can translate that explanation to a fast voltage sweep: When the voltage sweep crosses a minimum reverse bias threshold, the mobile ions begin to move towards the interfaces. While they are moving, the sweep continues and the reverse bias increases and accelerates them further. At some time Δt, the mobile ions reach the interface and reverse bias current begins to flow. The voltage that is applied at this time (Δt) appears as the breakdown voltage. A higher mobility (e.g. due to illumination) means that the mobile ions are faster. As they are faster, they reach the interface earlier, i.e. Δt is smaller. As Δt is smaller, the observed breakdown voltage appears smaller. In the same way, an increased concentration means that, after the same Δt, a larger number of mobile ions has reached the interface. This means that a significant J_{RB} begins flowing earlier which again appears as a smaller V_{BD}.

The same argumentation also holds for the dependence of ΔV_{BD} on the scan rate: We observed that, under illumination, ΔV_{BD} increases with smaller scan rate (see Figure 6.3). This observation complies with our argumentation because the smaller scan rates give the mobile ions more time to react to the applied bias, i.e. "reach the interface". Δt is the same as before, but the voltage sweep is slower. That means that the voltage sweep has not progressed as far when the the mobile ions reach the interface. That appears as a smaller breakdown voltage. Since the impact of scan rate on the dark V_{BD} is nearly negligible, the difference between dark and light V_{BD} increases and therefore ΔV_{BD} increases as well.

Finally, the illumination intensity was also observed to play a role. At low intensities, ΔV_{BD} increases steeply, but at higher intensities, the increase levels off (see Figure 6.3). That means that additional photons have less of an effect at already higher illumination intensities (higher being here around 0.05 suns). The same observation was made for CIGS solar cells. [51] There, they connected this illumination intensity-dependence to the excess charge carrier density. The same might be true for PSCs, as the interaction between mobile ions and light likely works via photo-generated charge carriers in the absorber. [108]

Thus, we successfully formulated explanations for our observations during fast voltage sweeps. They are based on the illumination affecting mobile ions and the accumulation of mobile ions at the interface affecting the breakdown voltage. The voltage scan rate affects the breakdown voltage only indirectly by determining which voltage is applied when enough mobile ions have arrived at the interfaces and have triggered the reverse bias breakdown. Instead, time (Δt) seems to be the decisive parameter.

However, our hypothesis in its current state does not explain the fundamentally different results at small scan rates ($0.1\,\mathrm{V\,s^{-1}}$). We would expect even smaller breakdown voltages than when we are using higher scan rates. Instead, we observe the pre-breakdown phenomenon, but barely any effect of illumination on the breakdown voltage. Therefore, we need to add an additional component to our hypothesis.

Like the reverse bias breakdown mechanism, this one was originally put forward in the publication of Bowring *et al.* [19] They observed an increase of the breakdown voltage over time while applying a constant reverse bias and proposed an electrochemical reaction at an interface as explanation. [19] This electrochemical reaction is expected to enhance the tunneling barrier and consequently increase the breakdown voltage, or decrease the reverse bias current. We follow one of the authors' proposals in regards to the mechanism and will assume in the following that this electrochemical reaction is the neutralization of mobile ions by charge carriers that constitute the reverse bias current. For the sake of comprehensibility, we will call them *neutralized mobile "ions"*, even though they are, of course, not ions anymore after being neutralized. Neutralized mobile ions do not cause band bending which means that the electrochemical reaction leads to the tunneling barrier increasing in width. This reduces the probability of tunneling and decreases the reverse bias current.

The reaction rate of an electrochemical reaction is proportional to the current (I). [109] That means for our case, that the number of neutralized mobile ions N_{neut} at a time Δt is determined by the charge Q that has flowed through the device until Δt:

$$N_{neut} \propto \int_{t=0}^{\Delta t} I\,dt = \int_{t=0}^{\Delta t} \frac{Q}{t}\,dt \tag{6.1}$$

This is the point where the voltage scan rate comes into play: During a measurement with a smaller scan rate, it takes more time for the cell to reach V_{BD} and the cell operates in the reverse bias regime for longer (Δt is larger). Therefore, during this longer time, more charge is flowing through the cell and more mobile ions are neutralized. It follows that there are less mobile ions present at the interface and band bending is less pronounced. Thus, V_{BD} appears to be larger.

In contrast, when using a larger scan rate, the time that the solar cell spends in reverse bias is shorter. Therefore, the effect of the electrochemical reaction is less strong and the V_{BD} appears to be smaller. Again, it is the time (Δt) that is the decisive parameter. The difference between a sweep with $1.0\,\mathrm{V\,s^{-1}}$ and $0.1\,\mathrm{V\,s^{-1}}$ regarding the charge flowing through the cell is shown in the appendix D.

With that in mind, we have found a mechanism that has the potential to counteract the effect of illumination on the reverse bias breakdown. One increases and one decreases the breakdown voltage. In reality, both mechanisms are interdependent and act in parallel. This is schematically displayed in Figure 6.5.

There, a simplified PSC is depicted with transport layers (TL1, TL2) and the perovskite absorber PVK. Under illumination, photo-activated mobile ions are present with a high mobility. Under the influence of the reverse bias ($-V$), they drift towards an interface. After some time (Δt), the first mobile ions reach the interface and contribute to the reverse bias breakdown mechanism. A current (J_{RB}) starts to flow (red arrow).

This reverse bias current leads to the neutralization of some mobile ions. They turn into black-filled circles with a red edge. These do not affect the reverse bias breakdown anymore. Thus, this neutralization compensates for the additionally arriving mobile ions. As many mobile ions are neutralized as newly arrived at the interface. Therefore, the current does not increases (the a red arrow is as thin as before).

In a voltage sweep, the slowly increasing reverse bias increases the number of arriving mobile ions faster than they are neutralized. We observe a slow increase of the current. Therefore, there must be a limiting factor to the neutralization reaction. That also explains why we observe the normal, exponential breakdown at a high reverse bias. At some point, it seems that the accumulation of mobile ions surpasses the neutralization reaction. Then, the near-balance between the two antagonistic mechanisms is broken.

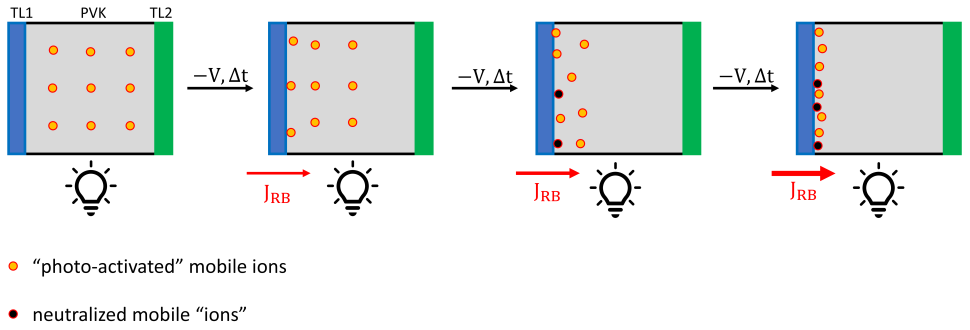

Figure 6.5. A schematic representation of the two counteracting mechanisms: A simplified PSC is depicted with transport layers (TL1, TL2) and the absorber layer (PVK). Within the absorber, the photo-activated mobile ions are depicted as orange-filled circles with red edge. Under the reverse bias ($-V$) and in time (Δt), they move towards the interfaces. There, the mobile ions contribute to the breakdown mechanism and allow reverse bias current (J_{RB}) to flow (red arrow). However, the reverse bias current neutralizes some of the photo-generated mobile ions (they turn into black-filled circles with a red edge). After neutralization, they do not affect the reverse bias breakdown anymore. Therefore, this neutralization slows the increase of J_{RB} down.

6.3.2. Applying the hypothesis

This combined hypothesis, consisting now of two counteracting mechanisms, can explain our remaining observations concerning the light RB-JV measurements with a smaller scan rate ($0.1\,\mathrm{V\,s^{-1}}$). In the following, we will take a closer look at the RB-JV curve of such a measurement and apply our hypothesis to explain the relevant observations. This light RB-JV curve (corrected for the photo-generated current) is displayed in Figure 6.6. There, we have defined five different regions that we will discuss in more detail:

Region A (marked in red) contains the pre-breakdown that is only present in the RV sweep. Until this point ($V \approx -1\,\mathrm{V}$), only the first component of our hypothesis (the standard reverse bias breakdown mechanism including the effect of illumination) is playing a role. An early breakdown like in the RB-JV curves with high scan rates begins to appear. Here, the reverse bias current starts to increase, i.e. charge carriers are flowing. These charge carriers exert their influence via the second component of our hypothesis (the electrochemical reaction) and partially counteract the effect of the reverse bias: A part of the mobile ions arriving at the interface is neutralized and therefore does not contribute to the band bending. The early exponential breakdown is aborted.

In region B (marked in green), a near-balance between the two antagonistic mechanisms is established. It seems that the increase of the voltage barely has an additional impact on the number of mobile ions at the interface. Most of the newly arriving mobile ions are neutralized, so that the reverse bias current increases only slightly.

In region C (marked in blue), the exponential breakdown finally occurs. It seems that the breakdown mechanism gains supremacy over the inhibiting mechanism

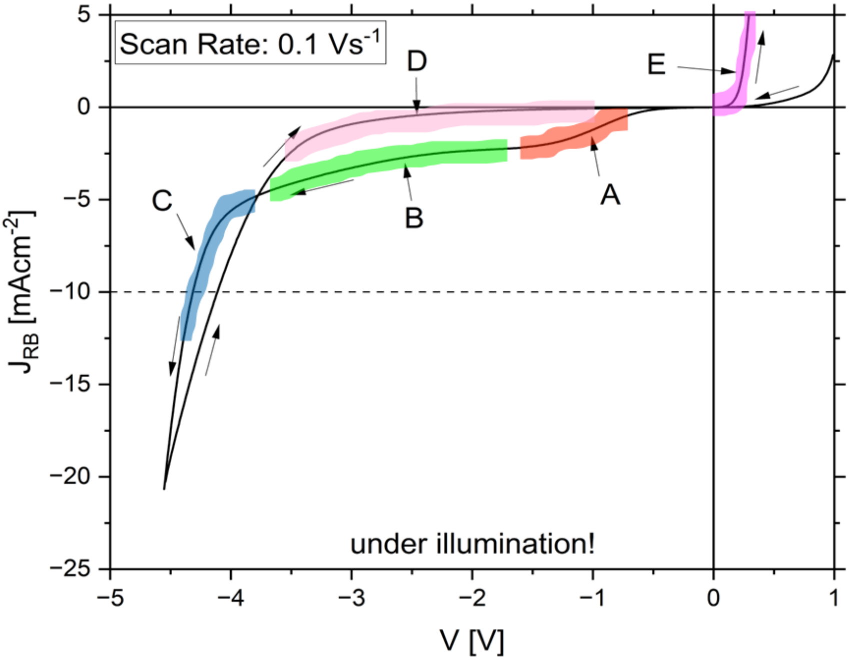

Figure 6.6. A single light RB-JV curve after correction for the photo-generated current from a voltage sweep experiment with a scan rate of $0.1\,\mathrm{V\,s^{-1}}$. Both RV and FW sweeps are shown. Five regions of interest are marked in color. A shows the aborted early breakdown, B the period of near constancy of the current density, and C the actual reverse bias breakdown. D highlights that the 'pre-breakdown' is not present in the FW sweep, and E shows the drastically changed behavior in the positive voltage region of the FW sweep.

at a similar voltage as in the dark. A possible reason for this change could be that illumination activates a second species of mobile ions with a higher mobility than the (original) species that is present in the dark. Then, the onset of region C would mark the voltage where the original ion species begins to play the dominant role in the reverse bias breakdown again.

Region D (marked in pink) highlights the low-current density regime of the FW sweep where the 'pre-breakdown' behavior is *not* visible. In this part of the measurement, the reverse bias is slowly decreasing. That means that the driving force behind the reverse bias breakdown diminishes. However, as long as the cell is still operating in reverse bias and there is still reverse bias current flowing, there is no impetus for turning the neutralized mobile ions back into their original states (e.g. reducing them). Thus, the state that leads to the pre-breakdown does not recur in the FW sweep. Instead, it looks very similar to the sweeps in the dark. To formulate it in a simpler way: The RV sweep looks at the cell before and during a 'reverse bias current treatment' (the sweep itself). The reverse bias current during this 'treatment' increases V_{BD}. The FW sweep, on the other hand, looks at the cell after the application of this 'reverse bias current treatment', when the V_{BD} has already been increased. Thus, the 'pre-breakdown phenomenon' is not present.

Finally, region E (marked in violet) shows the behavior of the cell in the positive voltage region in the FW sweep. It might be interpreted as a discharge of charge that has been stored in the cell. This might be connected to the re-ionization of previously neutralized mobile ions.

Thus, we have demonstrated that our hypothesis can explain the observed phenomena. In order to strengthen our case, however, we have performed additional experiments designed to test the hypothesis. They will be presented in the following section.

6.4. Testing the hypothesis

We have developed a hypothesis and applied it to explain the previously described phenomena. It is based on two antagonistic mechanisms:
Firstly, illumination affects the conductivity of mobile ions. These mobile ions play a decisive role in the reverse bias breakdown. Secondly, the charge flowing through the solar cell in reverse bias leads to a increase of V_{BD} and therefore limits the RB current. The scan rate is involved by determining the time that mobile ions have to react to the voltage. Additionally, the scan rate also determines how long the solar cell remains in reverse bias and through that, how much charge flows through it. The time (Δt) is a core element of our hypothesis.

6.4.1. Experiment 1: The effect of illumination in (quasi-) steady state

In order to test our hypothesis, we have designed an experiment that allows us to investigate the effect of illumination on the reverse bias behavior outside of voltage sweeps. In that way, the effect of time, independent of voltage scan rate, should be more obvious. The experimental procedure is schematically displayed in Figure 6.7a.

We inject a fixed current density J_{inj} into the solar cell in the dark and measure the voltage $V(t)$. We wait until the voltage has stabilized and the cell has reached a quasi-steady state. Then, we add illumination with a blue LED. According to our previous results, the wavelength of the illumination does not have a significant impact. We show that this is also true for the (quasi-) Steady State experiment in the appendix D. The illumination intensity is chosen such that $P_{light} \sim 0.1 J_{inj}$. In that way, the solar cell continues to operate in a similar reverse bias regime as in the dark. We continue measuring the voltage with the light switched on.

We performed this experiment on various cells, using two different values for J_{inj}. A measurement with a current density of $J_{inj} = -10.0\,\mathrm{mA\,cm^{-2}}$ allows the investigation of the breakdown voltage as this current density was used for defining V_{BD} in the voltage sweeps. The illumination intensity (following $P_{light} \sim 0.1 J_{inj}$) corresponds to $P_{light} \approx 0.05$ in the RB-JV measurements. A representative voltage curve is displayed in Figure 6.7b.

The second value is $J_{inj} = -1.0\,\mathrm{mA\,cm^{-2}}$. Here the illumination intensity (following $P_{light} \sim 0.1 J_{inj}$) is equivalent to $P_{light} \approx 0.005$. The idea behind this choice is that voltage and current density are smaller which should slow the processes driven by either of them. Additionally, it is the current density regime where the pre-breakdown phenomenon is visible in the voltage sweeps with a small scan rate. The results of this version of the quasi-steady state experiment are displayed in Figure 6.7c. The same experiments using different cells showed qualitatively the same results. These results are presented in the appendix D.

We will first look at the results in Figure 6.7b:
The first observation is that the voltage increases in the first second and then decreases again over an initial period of 20 s. The voltage in the first few seconds is around -5 V, which fits the breakdown voltages observed during the voltage sweeps in the dark quite well. After 40 s, the voltage seems to stabilize at a slightly smaller voltage ($V \approx -4.3$ V). Here, we switched on the LED.

After the addition of illumination, we observe that the voltage decreases but only by $\Delta V \approx 0.05$ V. This decrease lasts for less than 1 ms (measurement period), then another process leads to an increase of the voltage by $\Delta V \approx 0.15$ V over a period of $t \approx 2$ s. Afterwards, other processes are taking over which are hard to distinguish from the processes generally occurring within the cells during reverse bias.

Focusing on the second version of this experiment in Figure 6.7c with $J_{inj} = -1.0\,\mathrm{mA\,cm^{-2}}$, we observe the (quasi-)stabilization of the voltage after $t \approx 60$ s at a voltage of $V \approx -3.5$ V. Upon addition of illumination, the voltage decreases drastically to $V \approx -2$ V within $t \approx 5$ s. Over the following 70 s, the voltage slowly increases again until it reaches the voltage it showed before we added illumination.

The behavior of the solar cell in the first seconds in the dark is probably heavily influenced by the history of the solar cell and possibly by the sudden injection of a reverse bias current (capacitative effects). This undefined behavior was the reason for waiting for the voltage to stabilize before adding illumination. Therefore, discussing this effect in more detail is beyond the scope of this publication.

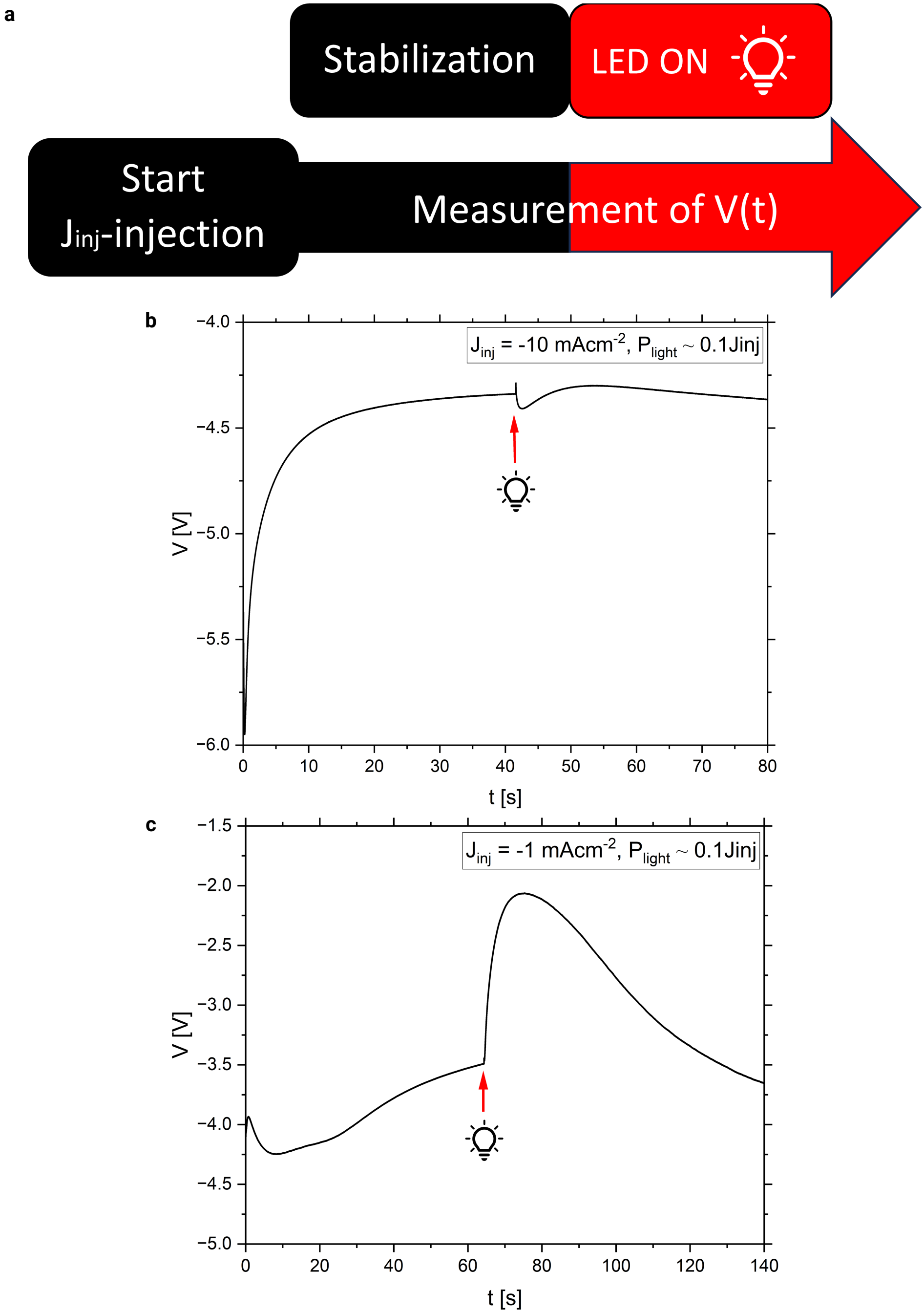

Figure 6.7. A schematic of the procedure (a) and representative results (b, c) of the quasi-steady state experiment with two different injected current densities J_{inj}.

More interesting for us is the reaction to the addition of illumination: In Figure 6.7b at $J_{inj} = -10.0\,\mathrm{mA\,cm^{-2}}$, we observe a very fast reaction in the form of a small voltage decrease and then a slower voltage increase. However, both voltage changes are barely significant if compared to the voltage applied as they amount to only a few percent. Therefore, it seems that the addition of illumination barely has an impact on V_{BD} at this current density level. At $J_{inj} = -1.0\,\mathrm{mA\,cm^{-2}}$, we observe the opposite: The voltage shifts significantly and then very slowly returns to the initial value. Do these results fit to the previous experiments?

If a voltage sweep is slow enough, the solar cells should reach a quasi-steady state in between the measurement points. Therefore, we will compare the results from the quasi-steady state experiment with the results from the voltage sweeps with a smallest employed scan rate $0.1\,\mathrm{V\,s^{-1}}$. There, we had observed only a very slight change of V_{BD} (see Figure 6.3, black squares). That corresponds to a very slight change of the voltage at $J_{RB} = -10.0\,\mathrm{mA\,cm^{-2}}$. In the quasi-steady state experiment at $J_{RB} = -10.0\,\mathrm{mA\,cm^{-2}}$, we also have not seen a significant voltage shift upon addition of illumination (Figure 6.7b). Thus, the results from slow voltage sweeps and from quasi-steady state measurement are in agreement in regards to the impact of illumination on V_{BD}.

In the low current density regime ($\leq -3\,\mathrm{mA\,cm^{-2}}$), we had observed the pre-breakdown behavior in the slow voltage sweeps (see Figure 6.2c and Figure 6.6). This phenomenon was only present in the RV sweep and not in the FW sweep. In the quasi-steady state experiment, we should see results equivalent to the RV and FW sweeps clearly separated in time. That is exactly what Figure 6.7c shows: The initial decrease of the voltage upon addition of illumination corresponds to the pre-breakdown phenomenon. There, we observed a significant difference between dark and light RB-JV at this low current density level, too. With further flow of charge through the solar cell, this voltage decrease slowly vanishes and a state close to the dark is regained. That corresponds to the results of the FW sweep where we barely saw a difference between the dark and light RB-JV curves.

With these additional experiments, we have confirmed the important role that time is playing in the processes surrounding the interaction of illumination and reverse bias. In the low current density-regime, we have observed significant and slow changes to the voltage over timescales ranging from $1\,\mathrm{s}$ to $100\,\mathrm{s}$. These findings do not only confirm our hypothesis of time being the decisive factor, but also support our explanation for the pre-breakdown phenomenon specifically: The difference between RV and FW sweep lies in the amount of charge that has flowed through the cell which is determined by the time the cell has spent in reverse bias. In the high current density-regime, we observed only insignificant changes to the voltage due to illumination, thus affirming the corresponding observations regarding V_{BD} from the slow voltage sweeps.

6.4.2. Experiment 2: Voltage sweeps after a pre-conditioning step

While the experiments in the previous section already provided experimental support for our hypothesis, a more direct confirmation is desirable: Thus, we performed the experimental procedure is displayed in Figure 6.8a-c. This shows a modified version of the previously presented voltage sweep experiment. It consists of a group of RB-JV measurements with a scan rate of $1.0\,\mathrm{V\,s^{-1}}$. As before, eight measurements are performed in darkness and seven in various states of illumination. Dark and light JV measurements are alternated. However, this time, a pre-conditioning step before the first JV measurements is added to the procedure. We pre-condition the solar cell by injecting a current density of $-10.0\,\mathrm{mA\,cm^{-2}}$ for $60\,\mathrm{s}$ in the dark. Additionally, we start and end the RB-JV measurements at $V = 0\,\mathrm{V}$ in order to prevent recovery while the cell is forward biased.

The idea behind this experiment is the following:

Previously, we argued that the RB-JV measurements with a small scan rate (e.g. $0.1\,\mathrm{V\,s^{-1}}$) do not show a significant impact of illumination on V_{BD} because a large amount of charge is flowing through the cell during the measurement. This augments the tunneling barrier and therefore V_{BD} (see Figure 6.5). The same is not true for the JV measurements with a higher scan rate (e.g. $1\,\mathrm{V\,s^{-1}}$), because the higher scan rate means a faster sweep and less time spent in reverse bias. Therefore, less charge flows through the cell and so, the effect of illumination that decreases V_{BD} dominates (see Figure 6.4).

During this experiment, the pre-conditioning should bring the cell into a state where V_{BD} has already been increased. By avoiding positive biases during the voltage sweeps, we prevent the cell from recovering between the RB-JV measurements. Therefore, we expect to see a very limited impact of illumination on V_{BD} despite using a high voltage scan rate. Representative measurement results are presented in Figure 6.8c,d.

In Figure 6.8d, the RB-JV curves are shown. The dark RB-JV curves are plotted as black lines, the light RB-JV curves in shades of red. Both RV and FW sweeps are shown.

We see that the black curves are nearly lying on top of each other as we had observed in previous experiments. This time, however, the red curves are also nearly inseparable and shifted slightly to larger voltages in comparison with the black curves. These results bear a strong resemblance to the previous results from measurements with $0.1\,\mathrm{V\,s^{-1}}$ (compare Figure 6.2b). In contrast to those, however, there is barely any difference between RV and FW sweep visible. In other words, the 'pre-breakdown' phenomenon is missing.

In Figure 6.8e, the ΔV_{BD} values calculated from RV and from FW sweeps are plotted against the illumination intensity. For comparison, results from a previous experiment without pre-conditioning are added to the graph. For the case with pre-conditioning, we see that $\Delta V_{BD} \approx 0\,\mathrm{V}$ for all illumination intensities. Again, a strong resemblance to the previous results with a small scan rate of $0.1\,\mathrm{V\,s^{-1}}$ is observed. The contrast to the measurement results with the same scan rate but without pre-conditioning (in light green triangles) is striking.

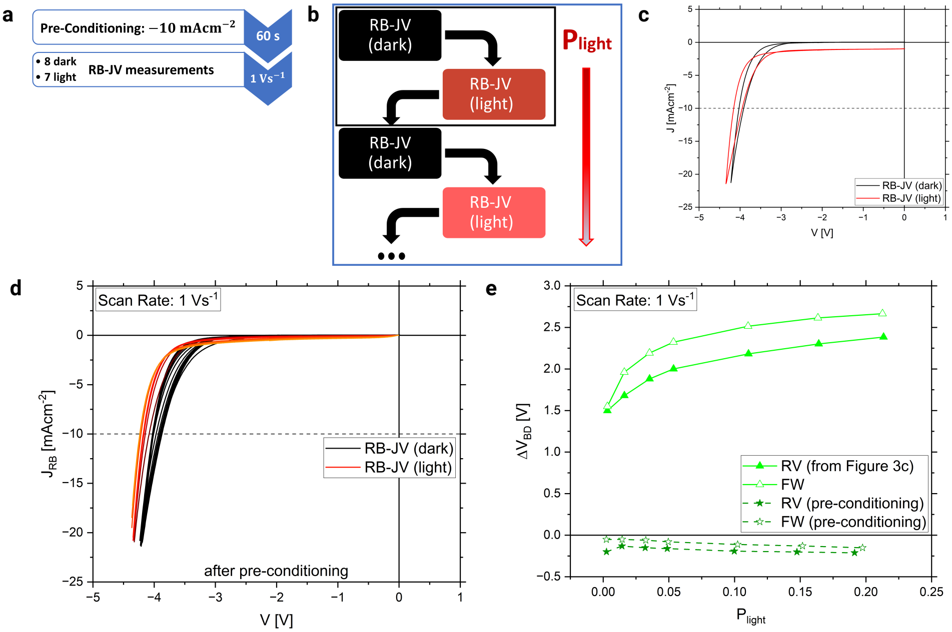

Figure 6.8. A schematic of the procedure (a-c) and representative results (d, e) of the pre-conditioning experiment.

These results show that the behavior of our PSCs during voltage sweeps is indeed influenced by the reverse bias current before or during the measurement. That supports our hypothesis that the main difference between small and high scan rates lies in the amount of charge that flows through the solar cell. The absence of a pre-breakdown after pre-conditioning fits to our explanation of this phenomenon, too: We explained it with the electrochemical reaction occurring during the voltage sweep and increasing V_{BD}. Here, that process has already occurred during the pre-conditioning and is therefore not visible in the voltage sweep. Therefore, we speculate that a pre-conditioning or an equivalent history of the solar cells could be a reason for the lack of the pre-breakdown phenomenon in the RB-JV curves with illumination in the work by Jiang *et al.* [28] However, this could also be explained by different ion mobility or concentration in their solar cells.

With that, we have shown two additional experiments that corroborate our hypothesis. As both the migration of mobile ions and the electrochemical reactions in the reverse bias regime are likely general, intrinsic phenomena that are not restricted to specific perovskite formulations or device designs, it should be also valid for different PSCs than the ones investigated in this study. Especially the results of JV measurements, however, depend strongly on the concentration or mobility of the mobile ions. These properties can vary strongly with the perovskite formulation employed and even the details of fabrication. Therefore, the scan rates necessary to observe the phenomena described in this study and time scales on which they occur, might differ. Additionally, the transport layers also seem to play an important role in the reverse bias breakdown mechanism and as a likely place for the electrochemical reaction to occur. Therefore, variations in transport layer material and device architecture might not modify the impact of illumination directly but the V_{BD} in the dark and the electrochemical reaction. Finally, there are open questions regarding the electrochemical reaction and the limiting factors to it. Investigating them in more detail was beyond the scope of this publication and was relegated to a future study.

6.5. Conclusions

The lack of stability against partial shading-induced degradation is one of the hurdles that the perovskite PV technology needs to overcome before commercialization. Solving this issue will require research effort on module and on cell level. One of the key details of the latter is the reverse bias breakdown. However, despite its importance, the mechanism of the reverse bias breakdown and its interplay with important perovskite solar cell properties (e.g. ion conductivity) or external factors (e.g. illumination, temperature) has not yet been investigated in detail.

In this publication, we observed that the reverse bias behavior under low-intensity illumination shows a strong dependence on the voltage scan rate. To explain this new phenomenon, we developed and tested a hypothesis based on two antagonistic mechanisms:

On one hand, illumination increases the ion conductivity (mobility and/or concentration) which leads to smaller breakdown voltages than in the dark. On the other hand, an electrochemical reaction driven by the reverse bias current leads to an increase of the breakdown voltage. The scan rate determines how long the solar cell spends under reverse bias conditions and therefore how much time the mechanisms have to take effect. While the first mechanism is dominant in fast voltage scans, the second mechanism supersedes it at small voltage scan rates.

These results allow for a statement regarding the impact on modules in realistic partial shading scenarios: Assuming that changes to illumination and shading of modules in outdoor applications are slow, we expect that the behavior in the quasi-steady state experiments represents what might occur in modules. Then, our results imply that low-intensity illumination does not have a significant impact on the breakdown voltage. Therefore, if a module is protected against the simplified partial shading scenario with one cell shaded completely, then spatially inhomogeneous partial shading or incomplete partial shading should not pose a problem.

Our findings also emphasize that more basic research on the behavior of perovskite solar cells in reverse bias is required: Even well-known effects (i.e. of illumination on the conductivity of mobile ions) can lead to surprising results when combined with the rarely-regarded conditions in the reverse bias regime. While the hysteresis phenomenon and its dependence on the voltage scan rate has attracted much interest in the research community, the equivalent phenomenon in reverse bias has not yet been investigated in detail at all and is in most publications on the reverse bias behavior not even reported. And despite the temperature coefficient of the breakdown voltage being one of the decisive properties distinguishing avalanche from tunneling breakdown, a detailed investigation of the temperature-dependence of the V_{BD} in perovskite solar cells is still missing.

Investigating these fundamental relationships is necessary to understand the mechanisms underlying the reverse bias behavior of perovskite solar cells. However, additional to research on cells, actual partial shading investigations on perovskite modules should be intensified. We expect that the different sizes of cells in modules and the scribes play a role in the partial shading stability as well. Only with such a thorough understanding, we will be able to integrate highly stable cell technology with intelligent module design to achieve the partial shading stability that is necessary for the commercialization of the perovskite PV technology.

7

Luminescent imaging of the reverse bias behavior using ReBEL

Partial shading remains a critical challenge for perovskite photovoltaics, as shaded cells in otherwise illuminated modules operate in reverse bias, which can accelerate degradation. In other solar cell technologies, reverse bias electroluminescence (ReBEL) imaging has been successfully employed to investigate the reverse bias breakdown mechanism. Here, ReBEL imaging is proposed as technique for imaging the local reverse bias current flow on perovskite solar cells. To that end, the ReBEL signal is affirmed to originate from radiative recombination in the absorber layer. ReBEL imaging is compared to established thermal current imaging techniques and reveals superior sensitivity and spatial resolution while showing similar features in the investigated samples. Further experiments reveal a dependence on the reverse bias current: The spatial distribution of the ReBEL signal differs significantly between small and large current injection levels. This could point towards two different breakdown mechanisms. These results show that, despite some open questions, ReBEL imaging could help understand the reverse bias behavior of perovskite solar cells better..

This chapter is based on a manuscript submitted to Small Science.

7.1. Introduction

The degradation caused by partial shading has been described as one of the major hurdles that are slowing down the introduction of perovskite photovoltaics (PV) into the market. [14] Such a partial shading event occurs when a part of a module area is shaded while the remaining module area is illuminated. Since modules typically consist of series-connected cells, inhomogeneous photocurrent generation among the cells is undesirable.

In a simple partial shading scenario, only one of the cells is completely shaded and therefore, does not generate any current. However, this shaded cell still needs to pass the current generated by the illuminated cells. This requires it to operate at a negative voltage, i.e. the reverse bias (RB). In perovskite solar cells (PSCs), applying a reverse bias can quickly lead to dramatic degradation of the power conversion efficiency (PCE). [18, 19, 84]

Accordingly, significant research activity has been carried out on cell-level, both in manipulating the breakdown voltage (a key metric for the design of modules), [28] and in understanding the breakdown and degradation mechanisms. [17, 21, 88]

Research on (mini-)modules is also available: Aninat *et al.* performed partial shading experiments on perovskite modules and observed pronounced degradation restricted to parts of the shaded cell. [59] Their interpretation attributes this effect to spatial variations in the breakdown voltage, leading to locally-increased reverse bias current densities. These elevated current densities, in turn, induced increased degradation. Their findings demonstrate the importance of uniform reverse bias breakdown for partial shading stability since large local current densities can lead to significant local degradation. Nevertheless, to the best of our knowledge, a detailed investigation of the spatial (in)homogeneity of the reverse bias behavior of cells has not yet been reported.

In many studies on cell-level, perovskite solar cells are assumed to be spatially homogeneous or 1-dimensional in regards to the reverse bias behavior. Thermography-based imaging techniques are occasionally used but typically only to show the presence of shunts. Examples are the publications by Bowring *et al.*, Najafi *et al.*, Bogachuk *et al.*, and Li *et al.* who used steady-state thermography (ssIR). [19, 23, 96, 110] In the work of Razera *et al.*, the authors employed reverse bias dark lock-in thermography (RB-DLIT). [18]

In other solar cell technologies (i.e. silicon- and CIGS-based), reverse bias electroluminescence (ReBEL) imaging is a technique that has been used to great effect to investigate the local reverse bias behavior. [51, 111]

The goal of this publication is to investigate the application of ReBEL imaging as a tool for investigating the local reverse bias behavior of perovskite solar cells. To that end, we show that PSCs exhibit electroluminescence when reverse biases are applied. We compare ReBEL to RB-DLIT and ssIR imaging. Finally, the relationship between local ReBEL emission rate and applied reverse bias is examined. In that way, signs of two different breakdown mechanisms are and the influence of the sample design are revealed. These results show that ReBEL imaging can be used as a supplement or alternative to thermal imaging techniques.

7.2. Experimental

In this work, we study semitransparent perovskite solar cells in a p-i-n configuration. The cell area is 0.20 cm^2 and the perovskite is a triple cation, double halide formulation ($Cs_{0.05}MA_{0.15}FA_{0.8}PbI_{2.7}Br_{0.3}$) with a band gap of around 1.6 eV. The complete layer stack and the solar cell design are shown in Figure 7.1a and b. On each glass substrate, four isolated solar cells are fabricated that are rotated by 90° to each other. The details of the fabrication process are described in the appendix E, Note 1.

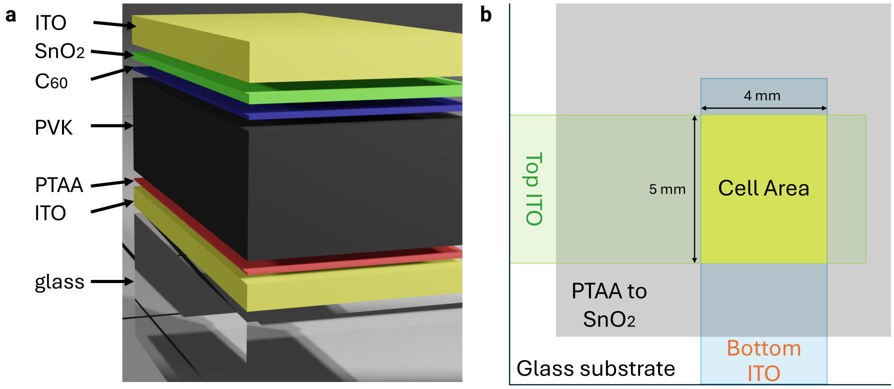

Figure 7.1. A cross-section of the perovskite solar cells (a) and a top-view of the cell design (b). For further information on the layers, see appendix E.

The results of the initial characterization, consisting of JV measurements and maximum-power-point-tracking (MPPT), are presented in the appendix E, Note 2. The median efficiency of the batch of 56 cells was 15.5 % for the forward sweep and 15.3 % for the reverse sweep. This is caused by a low fill factor (median 70.8 % and 69.6 % for the forward and reverse sweep respectively) due to large resistive losses in the top electrode. We forwent metal electrodes or even metal fingers that could have decreased these losses since they disturb the imaging techniques that are the focus of this publication. Additionally, the presence of metal electrodes have been convincingly related to shunting under reverse bias.

Before proceeding with describing the experiments, we clarify our nomenclature: The current (I) measured under illumination is negative. The approximate short-circuit current of our cells is $I_{sc} = -4$ mA, the corresponding current density is $J_{sc} = -20$ mA cm^{-2}. Under reverse bias, the injected current flows in the same direction, and so is negative as well (e.g. $I = I_{sc} = -4.0$ mA). In contrast, the current that is injected during (forward) electroluminescence measurements is positive, e.g. $I = -I_{sc} = 4.0$ mA.

The basic principle of EL and ReBEL measurements is displayed in Figure 7.2a. For spectrally-resolved EL and ReBEL measurements, we use a Renishaw Raman system to make use of its microscope and its cooled camera. The sample is excited using a Keithley source/measure unit as current source. We measure from 630 nm to 850 nm. For the EL measurement ($I = 4.0$ mA), we accumulate signals for 10 s. For the ReBEL spectrum ($I = -4.0$ mA), we integrate over 100 s in total. The software Wire 3.4 by Renishaw is used to control the system.

To acquire a ReBEL image, we inject a reverse bias current (I) for a time (t) while a camera (greateyes LumiSolarCell system with a 16-bit Si-CCD) detects light emission from the "n-side" of the sample. The local light emission is integrated over t and depicted as an image. Before and after this integration time, the current source (Keithley 2400) is switched off. The reverse bias that is applied to the sample during the integration time is logged with a frequency of approximately 100 Hz.

The core experiment of this publication is the ReBEL sweep. Its procedure and important parameters are shown in Figure 7.2b and in Table 7.1.

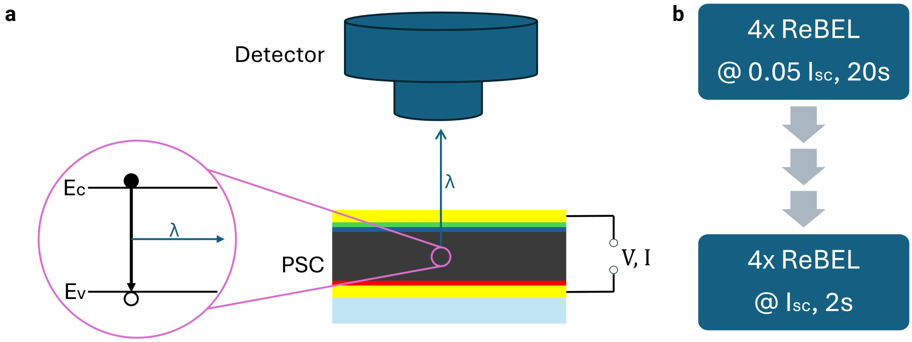

Figure 7.2. The basic principle of EL and ReBEL measurements (a) and the experimental procedure of the ReBEL sweep (b).

I/I_{sc}	0.05	0.10	0.15	0.25	0.375	0.50	0.625	0.75	0.875	1.0
I [mA]	-0.2	-0.4	-0.6	-1.0	-1.5	-2.0	-2.5	-3.0	-3.5	-4.0
J [mAcm^{-2}]	-1.0	-2.0	-3.0	-5.0	-7.5	-10.0	-12.5	-15.0	-17.5	-20.0
t [s]	20	10	8	4	3	2	2	2	2	2

Table 7.1. Important measurement settings of a ReBEL sweep.

We acquire a sequence of ReBEL images, starting at small RB currents and proceed towards larger RB currents. During this sweep, t is regularly adjusted to provide a signal strength above the camera noise level while not overloading the CCD. In order to account for the meta-stability of PSCs under reverse bias, we repeat the image-taking at every I-level four times. That provides us with information about the changes caused by the reverse bias during the measurement and allows the sample to reach a quasi steady-state. In the following analysis, only the fourth images taken at each current level are shown. A more detailed reasoning behind our experimental procedure can be found in the appendix E, Note 3.

For analyzing the resulting ReBEL images, we proceed as follows: As the voltage is not constant when a fixed reverse bias current is injected, we calculate a mean voltage from the voltages logged during the recording of a ReBEL image. This is shown in appendix E, Note 4. The emission intensity is divided by the integration time to receive an emission rate ER. To gain information about the local behavior, small parts of the observed area are chosen and a mean local ER calculated: ER_{avg}. In the ReBEL images depicted below, these areas are marked with blue rectangles.

Additionally, we imitate the ReBEL-sweep with two other imaging techniques: Firstly, we perform ssIR thermography. We inject currents for a certain time and record images with a frequency of 5.0 Hz, using a InSb camera of InfraTec. The time set at a constant current is consistent with the ReBEL integration times at the corresponding current level. The local heating is displayed after subtracting a baseline-image that was acquired before the current injection started.

Secondly, we employ RB-DLIT. There, we apply *voltages*, starting at small reverse biases and proceeding towards larger reverse biases. For every applied bias, we take an image with a measurement duration of 30 s, a pulse-duty factor of 0.5, a frame rate of 100 Hz, 200 frames per second and a Lock-In Frequency of 0.5 Hz. For DLIT, being a lock-in technique, the voltage is switched on and off with the Lock-In Frequency to create a wave-like disturbance. By filtering out the parts of the measured signal that do not follow this wave-form and averaging over many images, the spatial resolution can be improved. The same camera as for the ssIR thermography is used.

7.3. Introducing ReBEL as imaging technique

7.3.1. Do perovskite solar cells exhibit ReBEL behavior?

The most basic requirement for ReBEL imaging is that perovskite solar cells show electroluminescence when reverse biases are applied. To test that, we performed spectrally-resolved measurements at $-I_{sc}$ (EL) and at I_{sc} (ReBEL).

The EL spectrum shows a strong signal with a peak centered at $\lambda \approx 778$ nm. The ReBEL spectrum is depicted after smoothing and a baseline-correction. The original data can be found in the appendix E, Note 5. It shows a peak centered at the same wavelength as the EL spectrum ($\lambda \approx 778$ nm). This wavelength corresponds to the band gap of the perovskite of $E_g \approx 1.6$ eV.

While the wavelength-dependence of EL and ReBEL is alike, the intensity of emission shows a difference of several orders of magnitude. This is likely related to the direction of the current. In both situations, the same (absolute) current is flowing through the device. However, in EL, the diode is operating in the ’right’ direction while the diode is forced into breaking down in the ’wrong’ direction in ReBEL. It is not surprising that less radiative recombination occurs in the ReBEL case.

These results confirm that perovskite solar cells emit photons when operating in reverse bias. As the peak corresponds to the band gap, the emission seems to occur in the perovskite layer with radiative recombination via the band gap. This matches the observations of Puttnins *et al.* for CIGS solar cells. [51] They also found that the spectra of EL and ReBEL coincide. They explained that phenomenon with a second diode that is inversely, serially-connected to the "main diode". In contrast, the spectrum for ReBEL in multicrystalline silicon solar cells is more complex and the result of several mechanisms occurring in parallel. [112, 113]

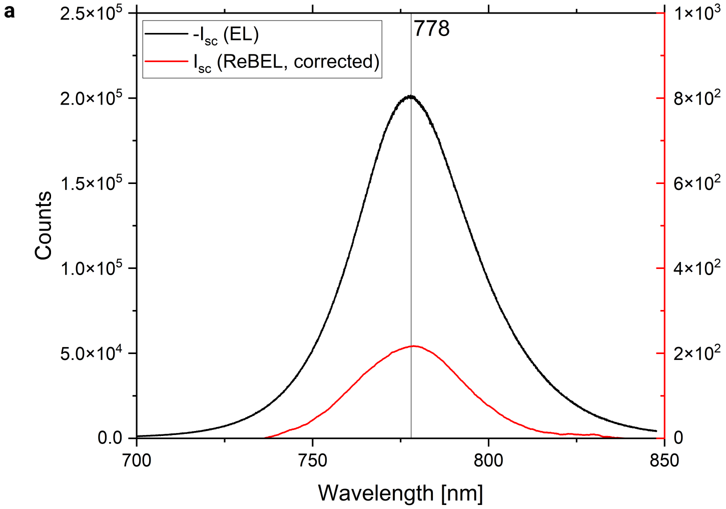

Figure 7.3. The emission spectra of EL ($-I_{SC}$) in black and ReBEL (I_{SC}) in red. The ReBEL spectrum has been smoothed and baseline-corrected.

To the best of our knowledge, this is the first time that the ReBEL spectrum of a perovskite solar cells is reported. The detailed mechanism of photon emission underlying ReBEL (beyond it being radiative recombination in the perovskite layer) remains material for future research. However, the similarity to the EL spectrum could be indicative of a similar mechanism occurring in reverse bias and of similar laws being applicable.

7.3.2. Can ReBEL imaging be used to characterize the reverse bias behavior?

After having shown that the perovskite solar cells used in this study emit light when reverse biased, the next step consists of testing whether we can use this photon emission to image the local reverse bias behavior. To that end, we compare images gained from ReBEL to images gained via more established thermal imaging techniques: steady-state infrared thermography (ssIR) and reverse bias lock-in thermography (RB-DLIT).

These thermal imaging methods map the surface temperature distribution of the sample. There are various mechanisms leading to heat generation in solar cells in the dark, e.g. Joule heating and thermalization of (injected) hot carriers. [114] Generally, the locally dissipated power is measured which depends on the local voltage and local current density.

ssIR imaging can be performed at a constant current, however, often suffers from the effects of effects of lateral heat transport. This leads to a ’smearing’ of the signal and reduced resolution and sensitivity. [114] Using lock-in techniques (e.g. RB-DLIT) is a way of improving both by applying a periodic excitation (e.g. a current). The lock-in principle reduces noise and increases resolution. [114] However, as perovskite solar cells react only slowly to changing electrical conditions, RB-DLIT images with high lock-in frequencies might not be representative of the behavior at steady-state. Therefore, relatively large lock-in frequencies are employed in this experiment, which limits the advantages usually resulting from a lock-in imaging technique.

We recorded several ReBEL images at various reverse bias current levels, then several RB-DLIT images at various reverse biases, and finally several ssIR images at various reverse bias current levels on the same sample. On each current or voltage level, only one image was taken (contrasting the ReBEL sweep that is described in 7.2 Experimental). We started with small reverse bias currents and reverse biases and proceeded towards larger values. Results of this experiment are presented in Figure 7.4. Similar results from other samples can be found in the below-mentioned data repository (see Data Availability).

The top row (Figure 7.4a - c) shows contour plots from all three imaging techniques at a small RB current. In this state, only a small reverse bias current is passing through the cell. The RB-DLIT image at this voltage (-5.5 V) was chosen due to its similarity to the ReBEL image as we could not measure the current during the RB-DLIT measurement.

The bottom row (Figure 7.4d - f) shows the corresponding images at a large RB current. In this state, a substantial current is going through the cell and it operates past its breakdown. In the case of ReBEL and ssIR at I_{sc}, in the case of RB-DLIT at -6.0 V.

In all images, the emission intensity (for ReBEL) or the temperature increase (ΔT) (for ssIR, RB-DLIT) are depicted in logarithmic color scales. The x- and y-axes represent the spatial extent of the samples. Since the camera used for the ReBEL-sweep is a different one than for ssIR and RB-DLIT, the resolutions are different. Therefore, the number of pixels that measure the width and height of the cell are different, as well. The images were scaled to approximate each other in size.

We start by describing the images at a small RB current (Figure 7.4a-c). The ReBEL image (Figure 7.4a) shows a cell area that is largely dark. Only bright vertical stripes at the edge of the cell area and a multitude of small bright spots are visible. The corresponding RB-DLIT image (Figure 7.4b) shows warm vertical edges. Especially the left edge and the bottom corner are bright and this apparent activity is extended into the cell area. Additionally, there are a few warm spots visible in the cell area. Finally, the ssIR image (Figure 7.4c) shows a very slight heating in the whole cell area. Additionally, the left edge of the cell seems warmer than the middle part of the cell area and the right edge colder.

When comparing these images, some observations stand out: The ReBEL image and the RB-DLIT image agree relatively well with each other. Both show bright edges, a cell area that is not very active, as well as some bright spots in that area. The ReBEL image shows far more bright spots which can partially be assigned to bright spots in the RB-DLIT image. Additionally, the distinction between edge and cell area is clearer in the ReBEL image than in RB-DLIT. In contrast, the ssIR image just shows a slight uniform heating up of the whole cell area. The warmer and colder edges are a measurement artifact as is shown in appendix E, Note 6.

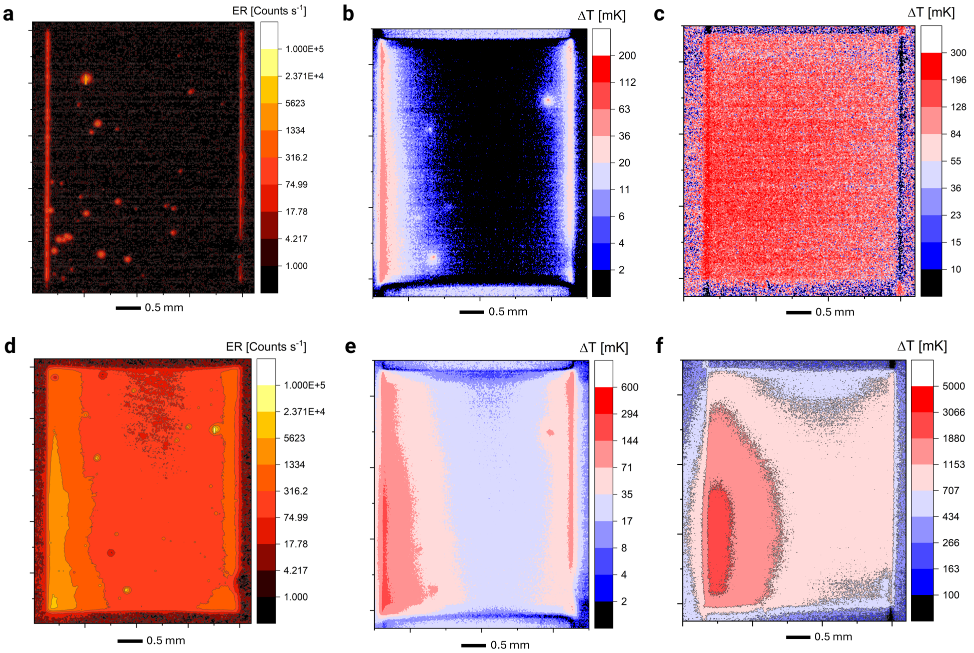

Figure 7.4. ReBEL images at $0.05 I_{SC}$ (a) and at I_{SC} (d), respectively. RB-DLIT images at -5.5 V (b) and at -6.0 V (e), and ssIR images at $0.05 I_{SC}$ (c) and at I_{SC} (f). ReBEL and RB-DLIT show largely the same features while ssIR only agrees with the other techniques at a large current. However, the details are clearest in the ReBEL images, and the least visible in ssIR.

Proceeding to the images at large RB currents (Figure 7.4d-f), we see in the ReBEL image (d) that large parts of the cell area are lighting up, even if most of the intensity comes from the regions near the edges and the bottom left corner. Some bright spots in the cell area are still present. They do not seem to have an impact on the surrounding area. The corresponding RB-DLIT image (Figure 7.4e) shows a strong signal along the vertical edges on the left and right of the cell area. Especially the left edge and the cell area near it are bright. Additionally, some bright spots are visible. In the ssIR image (Figure 7.4f), we see the bottom left corner heating up strongly which extends into the surrounding area, even outside of the cell. Furthermore, the remaining cell area seems to heat up relatively homogeneously. Only the bottom right corner and the top center are slightly cooler. Generally, the area outside of the cell area appears to have heated up on all sides of the cell.

When comparing the techniques at large RB current, we make the following observations: All three techniques show that the cell area is now active as well, even if only at a low level. They all also show that the bottom left corner is especially active. Additionally, in ReBEL and RB-DLIT, the top center is clearly less active than the bottom center. This is less obvious in the ssIR image. The edges are not visible anymore in ReBEL, but are still present in RB-DLIT. In ssIR, they have not been visible even at small RB currents and are still not present. The remaining bright spots, that are visible in ReBEL and RB-DLIT, correspond to each other according to their location. However, there are more and weaker bright spots visible in ReBEL, while ssIR does not show any bright spots.

To summarize our observations, the ReBEL and RB-DLIT images show largely similar features. The slight differences that are present could be explained by the current-defined state of the ReBEL images and the voltage-defined state of the RB-DLIT image not corresponding to each other perfectly. The presence of more bright spots in the ReBEL images might be explained, in part, by a higher sensitivity and resolution. Also, changes to the sample due to the ReBEL measurements could have occurred that altered the local behavior at bright spots in the RB-DLIT measurements.

On the other hand, the ssIR images show far less details that could be compared to the images resulting from the other techniques. At least, at a large reverse bias current, the warming in the bottom left corner corresponds to similarly increased activity in the ReBEL and the RB-DLIT images. That could imply that the sensitivity and resolution of the technique is simply too low to display the features that can be observed in the other images.

Our conclusion of the results of this comparison of imaging techniques is that ReBEL imaging in this current/voltage regime seems to reveal the same qualitative information as thermal imaging (especially RB-DLIT) via a different mechanism. That means, from ReBEL imaging, we can at least draw tentative and qualitative conclusions about the local reverse bias current densities and reverse bias (breakdown) behavior. At the same time, ReBEL imaging shows advantages in sensitivity and resolution. However, for more reliable quantitative results, e.g. local JV curves, the mechanism of ReBEL needs to be clarified in more detail.

7.4. Using ReBEL to investigate the local RB behavior

After having presented results that imply that ReBEL can be used to image the reverse bias behavior of perovskite solar cells, the next step is to show, using our cells as an example, what ReBEL imaging can reveal. To that end, we have performed the ReBEL sweep experiment (described in 7.2 Experimental) on our solar cells and will discuss the results in detail in the following.

7.4.1. Qualitative analysis

In Figure 7.5, the results of a ReBEL sweep are presented. For each current injection level, the fourth ReBEL image is shown as it is the most stabilized. The emission rate is displayed with a logarithmic color scale. Similar results from other cells and the complete data (e.g. the images 1-3 for each current injection level) can be found in the data repository that is described in Data Availability.

At the smallest injection current ($I = 0.05 I_{sc}$), the only visible intensity is emitted from the two thin stripes at the side edges of the cell area and a few bright spots in the cell area. The general area of the cell is dark.

When the reverse bias current is increased, the edges increase in brightness and more bright spots appear at first. However, at a certain current ($I = 0.15 I_{sc}$), the cell

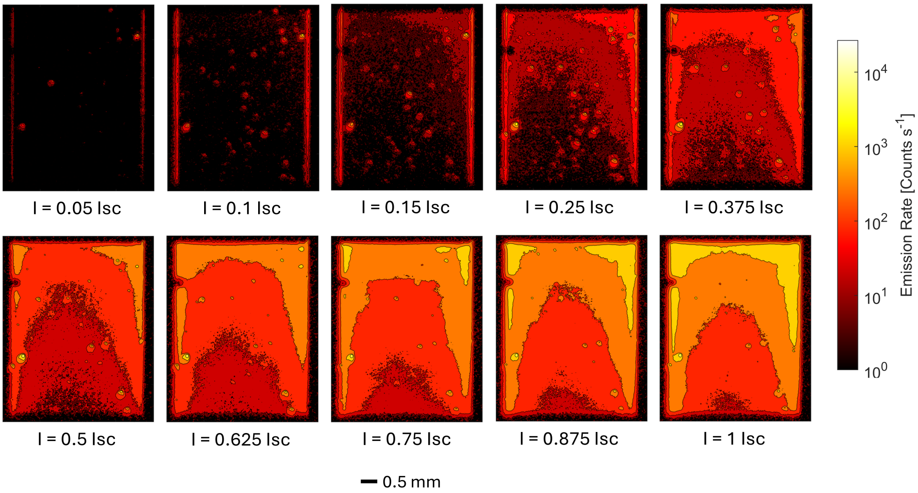

Figure 7.5. The results of a ReBEL sweep experiment. For each current injection level, the fourth image is shown. The emission rate is displayed on a logarithmic color scale.

area itself begins lighting up as well, in parallel and apparently independent of the bright spots. This begins in the top right corner.

Already at $I = 0.375 I_{SC}$, the whole cell area is active. At the same time, many bright spots are still distinct from the surrounding area. In contrast, the edges of the cell are barely distinguishable from the cell area anymore.

With larger reverse bias currents, the cell area gets brighter. A gradient of the emission rate remains clearly visible. Clearly, the ReBEL activity is higher at the top of the cell than at the bottom. It is possibly also slightly higher on the right side than on the left side. Finally, the cell area near the side edges also is brighter than the center of the cell area.

At the same time, most bright spots do not significantly increase in brightness and are therefore "swallowed" by the surrounding area when it reaches a similar order of magnitude of the emission rate. Some especially bright spots, however, remain visible even at the largest injected current level. The edges are not visible at all anymore at larger reverse bias currents. Their former position is taken up by a liminal area between the bright cell area and the ReBEL-inactive area outside of it.

These observations agree with those shown in subsection 7.3.2 where we compared the imaging techniques. It should be noted that the orientation of the cell here is rotated by $180°$.

These results reveal a significant difference between the appearance at small currents and large currents. At small reverse bias currents, the cell edges and bright spots are mainly responsible for the ReBEL emission. The general cell area is largely ReBEL-inactive. On the other hand, at large currents, the cell area dominates the ReBEL emission, even if it is spatially not homogeneous. Here, the cell edges and most of the bright spots are not distinguishable from the cell area anymore. If we interpret ReBEL emission as a sign of local reverse bias current flow (as discussed in subsection 7.3.2), this difference could indicate the presence of two different reverse bias breakdown mechanisms.

7.4.2. Semi-quantitative analysis

The ReBEL sweep experiment allows the extraction of semi-quantitative information by relating the local emission rate to the applied reverse bias. This is shown in Figure 7.6 by examples for the cell area, the cell edges, and a bright spot. Their average emission rates are displayed semi-logarithmically against the reverse bias. Other examples for the cell area, the edges and bright spots can be found in the appendix E, Note 7. In the graph in Figure 7.6c, the emission rate of the total area is used as comparison. To ease that, its average emission rate is multiplied by the factor 10^{-4}.

It is clearly visible that different relationships between emission rate and applied reverse bias are present. The bright spot shows the highest emission rates, yet seems to reach saturation at large reverse biases. The average emission rate at the cell edges increases strongly at small reverse biases but reaches a point of saturation at $V = -5.8$ V. At large reverse biases, its emission rate seems to increase again. However, that is an artifact as the edge is not distinguishable from the cell area anymore at these reverse biases.

The part of the cell area used as example here, shows very small emission rates at small reverse biases as was already visible in Figure 7.5. From the third data point at $V = -5.8$ V, the behavior changes suddenly, corresponding to the cell area beginning to light up in the third image of Figure 7.5. At larger reverse biases, a nearly linear increase of the average emission rate is visible, corresponding to an exponential relationship with the reverse bias. In general, the behavior of the total area is most closely mirrored by the spot in the cell area. That proves that, while bright spots are present even at large currents, the behavior of the cell is dominated by the cell area.

Both the spatial distribution of the ReBEL emission rate in Figure 7.5 and the semi-quantitative analysis of the local ReBEL emission rate point to the same conclusion: Significant differences in behavior separate the cell edges (and bright spots) from the cell area. This points either at two different mechanisms of ReBEL emission or at two different breakdown mechanisms. However, as the thermal imaging techniques showed similar features, we tentatively conclude that two different breakdown mechanism are occurring at different current injection levels. Additionally, we can at least provide more detailed information on the bright edges and the inhomogeneity of the emission rate in the cell area. The bright spots are more difficult to pin down as they do not show a single behavior. They will have to be the focus of a future publication.

7.4.3. Bright edges

The feature that we call 'bright edge' is only clearly visible at small reverse bias currents ($I \leq 0.375 I_{sc}$). It describes two vertical stripes at the left and right edges of the cell area with increased ReBEL emission rates. At larger reverse bias currents, they are not distinguishable anymore from the brighter cell area.

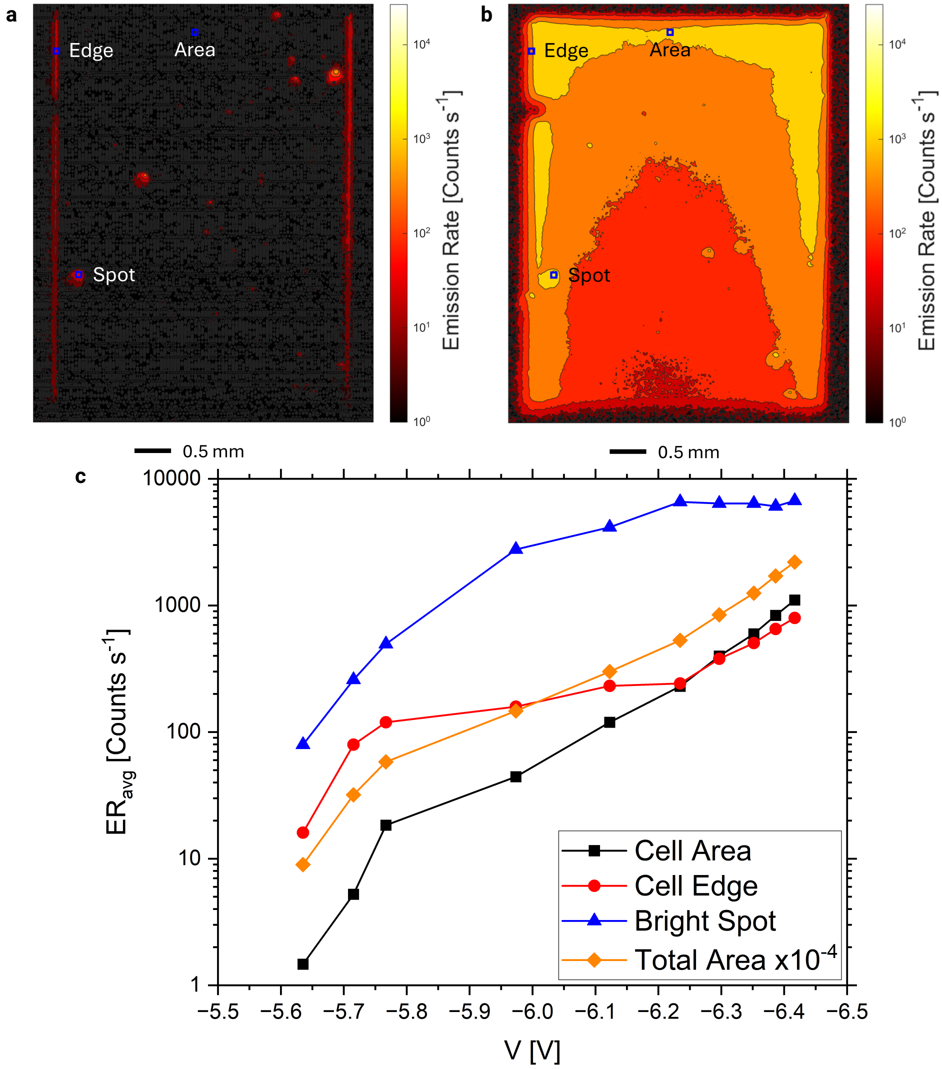

Figure 7.6. The areas that were used as examples for the semi-quantitative analysis are marked as blue squares in a small (a) and large (b) current ReBEL image. The average emission rates of these areas and the average total emission rate are plotted semi-logarithmically (c). The ER_{avg} of the total area is multiplied by 10^{-4} to make the comparison easier.

Their location is the key information for explaining their origin. The orientation of the cell in Figure 7.5 and Figure 7.6 corresponds to the schematic of the cell design that is displayed in Figure 7.1. That means that the location of the bright edges matches the location of the edges of the bottom ITO electrode.

The bottom ITO electrode has a thickness of ca. 150 nm. Its overlap with the top electrode defines the cell area. It is fabricated by full-area ITO sputtering, followed by a photolithography process to pattern the layer. On this scale, photolithography leads to a step-like edge as is shown by stylus profiling results in the appendix E, Note 8.

This situation is displayed in Figure 7.7a in the top schematic. To test whether the step-like step geometry of the ITO electrode is really responsible for the observed bright edges, we fabricated solar cells with more rounded bottom ITO electrodes. This is displayed in Figure 7.7a in the bottom schematic. The relevant profiling results can be found in the appendix E, Note 8.

A resultant ReBEL image, taken at a small reverse bias current $I = 0.05I_{sc}$ is shown in Figure 7.7b. There, no bright edges are visible. Instead, parts of the cell area are already showing ReBEL emission. The black horizontal stripe is part of a metal electrode on top of the top ITO electrode. This confirms that the geometry of the bottom ITO is responsible for the occurrence of the bright edges.

For the mechanism of how the step-like ITO edge is connected to locally increased ReBEL emission, several possible options are available:
The layer on top of the ITO electrode is the PTAA hole transport layer which has an approximate thickness of only 10 nm. At these step-like edges, this could lead to insufficient coverage or, at least, a locally very thin PTAA layer. Insufficient coverage of the ITO electrode by a hole transport layer has been connected to small breakdown voltages on cell level in a recent publication. [28] Here, a local breakdown voltage that is smaller than the breakdown voltage of the general area could be present and could explain the increased ReBEL emission rates at smaller reverse biases than the cell area.

Other explanations could involve the formation of non-ohmic shunts at the edges due to direct contact between electrode and perovskite. Another alternative might be a local increase of the electric field strength due to the sharp geometry of the ITO electrode. However, ascertaining the exact mechanism is the work of a future publication.

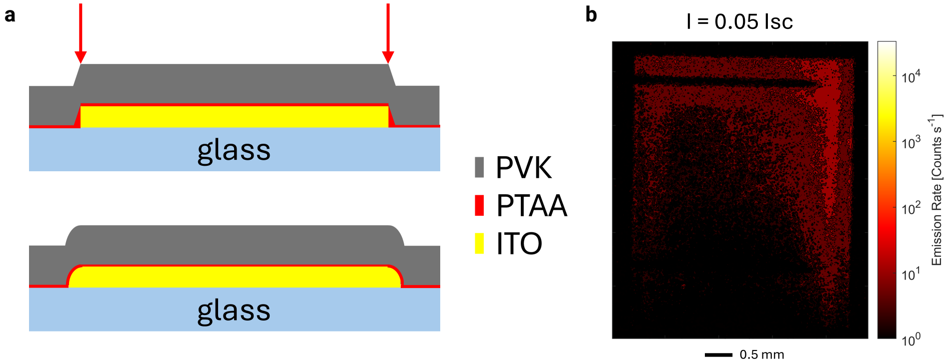

Figure 7.7. Schematics showing the step-like edges (top) and the rounded edges (bottom) of the bottom ITO electrode with the glass substrate, hole transport layer PTAA, and the perovskite layer (a). A ReBEL image of a solar cell with rounded bottom ITO edges at a small reverse bias current (b).

7.4.4. Cell area

The inhomogeneity of the ReBEL emission in the cell area is the second observation that we would like to discuss in more detail. In Figure 7.5, the cell area begins lighting up at $I = 0.15 I_{sc}$ in the top right corner. With increasing reverse bias current, additional parts of the cell area also begin emitting ReBEL, seemingly spreading from the top to the bottom. This vertical gradient (small emission rates at the bottom and large emission rates at the top) remains present at all larger current injection levels. Additionally, a smaller horizontal gradient (larger emission rates to the right than to the left) might be visible additionally. Furthermore, it seems that the cell area near the cell edges to the sides is more active than the center of the cell area. At the largest reverse bias current ($I = I_{sc}$), a difference of several orders of magnitude of the emission rate is visible between different parts of the cell area.

Previously, we argued that ReBEL likely follows similar laws as (forward) EL. This was based on the observation of the same emission spectrum (Figure 7.3). The near-linear relationship of the logarithm of the emission rate with the reverse bias at large reverse biases (Figure 7.6c) also fits the exponential dependence described for EL. [74] Therefore, we compare the previously presented results of ReBEL imaging with results of EL imaging.

The results of EL imaging at a small current ($I = -0.1 I_{sc}$) and a large current ($I = -I_{sc}$) are displayed in Figure 7.8. The EL intensity is shown on a linear color scale. The measurement was performed before the ReBEL sweep on the same cell as the ReBEL sweep of Figure 7.5. Therefore, the cell is oriented (like in the ReBEL images) as displayed in Figure 7.1b.

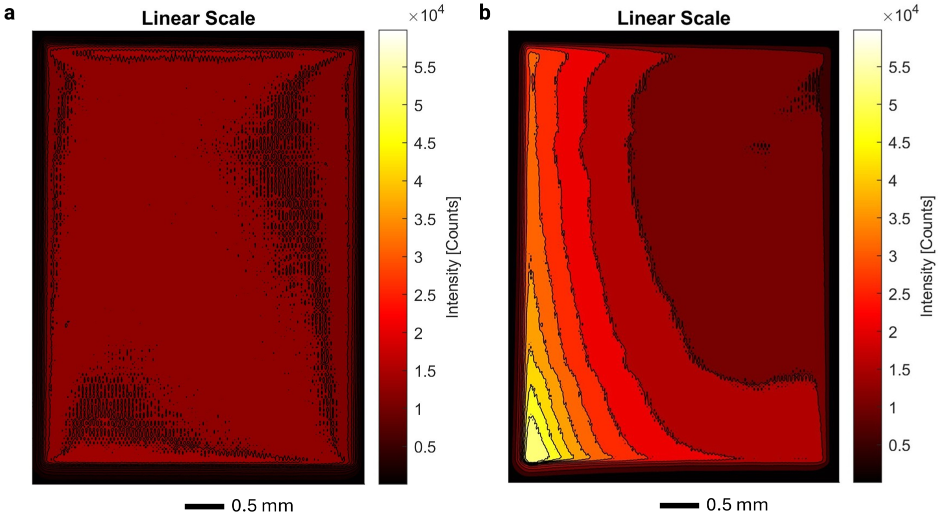

Figure 7.8. Results of EL imaging measurements at a small current $I = -0.1 I_{sc}$ (a) and a large current $I = -I_{sc}$ (b). The emission intensity is shown on a linear color scale. The orientation of the cell agrees with the orientation of the ReBEL images in Figure 7.5 and the schematic cell design in Figure 7.1b.

According to the laws governing EL (as described in Haunschild *et al.* [74]), the electroluminescence intensity is highly sensitive to differences in local series resistance. Due to the exponential dependence of the intensity on the local diode voltage, the impact of the series resistance is especially visible at large current injection levels. It stands to reason that the intensity gradients visible in Figure 7.8b are caused by the series resistance of the electrodes.

Two separate intensity gradients are visible: One very steep gradient is oriented vertically from the top to the bottom of the cell. Another, slightly less steep gradient is oriented orthogonally from the right to the left of the cell. These gradients match well with the orientation of the bottom and the top ITO electrodes, respectively, and therefore correspond to the local series resistance.

A comparison with the ReBEL images in Figure 7.5 at the corresponding absolute current injection levels reveals certain similarities and differences: The vertical gradient of the emission rate is clearly visible in ReBEL as well. The horizontal gradient is less clearly present at the largest current level but is more obvious at smaller injection levels. However, the gradients in the ReBEL images are inverted in relation to the gradients visible in EL. In EL, the intensity decreases from the bottom to the top; in ReBEL, the emission rate increases dramatically in the same direction. Finally, in the ReBEL images, the center of the cell area shows smaller emission rates than the edges to the sides of the cell area. This observation does not have a parallel in the EL images.

At this point, we do not have an explanation for the inverted vertical and horizontal gradients of the emission rate in ReBEL. It is very likely that these gradients are connected to the electrodes somehow as their orientation fits very well. However, as per our understanding, the direction of the current should not influence the impact of the series resistance of the ITO electrodes. That is a question that we have to leave open for a future investigation.

The brighter side edges of the cell area could be connected to the same bottom ITO geometry as the ’bright edges’ at small current injection levels. Then, this effect would be stretched on both sides towards the center of the cell area. An argument against this is the observation in Figure 7.6b where the blue square, marking the position of the bright edge, can be seen to be just outside of the yellow area with the largest emission rate. Therefore, the increased emission rate at small currents and the increased emission rate at large currents at the edge are present at slightly different locations. That could mean that two different mechanisms occur near the edge: The first occurs just outside the cell area at small currents, while the second one occurs just inside the cell area at large currents.

Alternatively, lateral ion migration at the borders of the cell area as shown in the publication by Jacobs *et al.* could serve as a partial explanation. [44] Lateral ion migration would increase the concentration of mobile ions near (all) the edges of the cell area and therefore decrease the local breakdown voltage, leading to increased local ReBEL emission rates. The main argument against this hypothesis is that it does not explain why we do not see increased local emission rates near the bottom edge of the cell area. As for the inverted gradients of the emission rate, we do not have a satisfactory explanation for the observed phenomena and thus can only propose this initial speculation.

Experiments on solar cells with a different electrode design (e.g. with metal grids to decrease series resistance) could help answering these questions. Unfortunately, these additions were beyond the scope of this study and are relegated to future investigations.

In this section, we have qualitatively and semi-quantitatively analyzed the results of a ReBEL sweep. We observed that, in the investigated samples, the bright edges and bright spots dominate the ReBEL emission at small reverse bias currents, while the general cell area dominates at large reverse bias currents. Investigating the cell area, the cell edges and a bright spot semi-quantitatively, we found that these features differ in their relationship between the local emission rate and the reverse bias. That means that we observe either two different mechanisms of ReBEL emission or of reverse bias breakdown in our solar cells.

More detailed investigations of the bright edges revealed that they are connected to the step-like edges of the bottom ITO electrode. When these sharp electrodes are exchanged for more rounded electrodes, the bright edges are not present anymore in ReBEL imaging. The exact mechanism, e.g. local non-ohmic shunts or a locally smaller breakdown voltage, remains unclear, however.

Finally, the inhomogeneity of the emission rate in the cell area at large reverse bias currents was discussed. A comparison with EL imaging showed that the effects of the series resistance of the electrodes seem to be present in ReBEL, however inverted. Additionally, an effect of the edges to the side of the cell area seems to increase the emission rates locally. Both for explanations of the inversion of the effects of series resistance and of the effect of the edges at large currents, we have to refer to future research.

7.5. Conclusions

The aim of this study was to test whether ReBEL imaging could be used to investigate the reverse bias behavior of perovskite solar cells. To that end, we showed on our solar cells that ReBEL emission is generated in the perovskite layer when reverse biases are applied. A comparison between ReBEL imaging and more established thermal imaging methods revealed that ReBEL seems to show largely the same information with increased resolution and sensitivity. That finding informed our tentative interpretation of ReBEL intensity as a sign of local current flow. Varying the injected reverse bias current revealed significant differences between different current injection levels in our cells. At small currents, the cell edges and localized spots dominated the cell behavior, while at large currents, the whole cell area was active, however, spatially inhomogeneous. Our analysis pointed towards two different mechanisms of the reverse bias breakdown. Further investigation ascribed the bright edges to the geometry of the bottom ITO electrodes of our solar cells. The inhomogeneity of the ReBEL emission in the cell area seems to have an inverted connection to the series resistance of the electrodes and the cell edges. However, a satisfying explanation could not be provided in this study.

Thus, our results show that the imaging of the reverse bias behavior of perovskite via ReBEL is possible and that it promises advantages over thermal imaging techniques. However, a more detailed understanding of its correct interpretation and the factors influencing it is required. Additionally, the influence of properties that are specific to our cells (e.g. cell layout, perovskite composition and fabrication) is not yet clear and needs to be investigated before the generalization of our interpretations is safely possible.

8

Conclusions & Outlook

8.1. Conclusions

Protecting perovskite modules against degradation caused by partial shading remains a key hurdle that needs to be overcome in order to facilitate large-scale commercialization of perovskite PV. During an idealized partial shading event, one solar cell in a string of series-connected solar cells is completely shaded (so, in the dark), while the remaining illuminated cells force their photocurrent through the shaded cell. To pass a current in the dark, the shaded cell operates in the reverse bias regime. Such an operating condition has been shown to trigger rapid performance degradation in perovskite solar cells.

Fundamentally, two possible ways to address this problem exist.
The first strategy consists of the integration of bypass diodes. Their purpose is to provide an alternative pathway during a partial shading event, preventing reverse bias current to flow through the shaded cell and preventing degradation. However, the monolithic interconnection scheme, the preferred thin-film PV module design, complicates the integration of external bypass diodes, that is commonly used in crystalline silicon PV. Additionally, many perovskite solar cells exhibit breakdown voltages that are smaller than usually observed in crystalline silicon solar cells. That means that a perovskite module would require the integration of numerous bypass diodes which would impact design and production complexity, and the overall commercial viability of such a product.

The second possible solution is to allow the reverse bias current to flow through the shaded cell, but to prevent it from causing degradation. For this to be feasible, the formation of hot spots must be avoided. Hot spots are highly-localized weak spots for reverse bias current. Local high current densities can trigger degradation of the surrounding area due to severe Joule heating. However, some proposed degradation mechanisms suggest that even de-localized reverse bias current flow might be detrimental for perovskite solar cells.

To further develop these solution approaches, a deeper understanding of the physico-chemical processes occurring under reverse bias within perovskite solar cells is required. In that context, this thesis is focused on the reverse bias breakdown as the mechanism that enables current to flow in the dark under the influence of a reverse bias. The main conclusions of this research are listed in the following.

Determining a Breakdown Voltage

Firstly, as described in Chapter 4, the disparity of methods for measuring and calculating a breakdown voltage of perovskite solar cells in literature revealed a need for standardization. After discussing the impact of the measurement parameters on the apparent reverse bias behavior, sets of measurement parameters for solar cells were proposed. Additionally, a methodology for determining the breakdown voltage from the resulting experimental data was introduced. This methodology uses the point of maximum curvature as the breakdown voltage. This turns the breakdown voltage into a widely applicable figure-of-merit, which can be expressed analytically. The intentions were to increase the comparability of reported results and emphasizing the importance of detailed reporting of measurement conditions and definitions.

However, the limitations of this methodology of determining the breakdown voltage have also become clear: A theory-based formalism that describes the reverse bias breakdown is missing. Therefore, our method depends on an empirical approximation of the reverse bias behavior. When this empirical approximation fails, the resulting breakdown voltage might not be a meaningful metric anymore. In this case, other definitions of the breakdown voltage might be superior.

The Role of the Current on the Reverse Bias Degradation

Secondly, as described in Chapter 5, cell-to-cell differences of the breakdown voltage have consequences for the comparability of the results of reverse bias degradation experiments. When a fixed reverse bias is applied, the resulting current and degradation rate depend on the breakdown voltage of the cell. Consequently, degradation experiments using a fixed reverse bias are not directly comparable unless further information about the reverse bias behavior is reported, i.e. the breakdown voltage. Normalizing the applied reverse bias with the breakdown voltage can compensate for the differences of the breakdown voltage and restore comparability across samples. Additionally, similar dependencies have been observed for current and degradation rate. This observation suggests that the dominating degradation mechanism is current-driven. That would imply that limiting the flow of current through the cell in reverse bias is crucial for preventing degradation.

However, the degradation studied in this work was not exclusively irreversible degradation. On the contrary, reversible and irreversible degradation modes were not distinguished, even though most of the degradation turned out to be recoverable by performing JV measurements, MPPT, and storage in the dark. Thus, while the core statement of current-driven degradation remains correct, research on actual (irreversible) degradation should incorporate a recovery procedure.

The Impact of Illumination on the Reverse Bias Behavior

Thirdly, as presented in Chapter 6, the widely-accepted mechanism explaining the reverse bias behavior of perovskite solar cells was extended to incorporate the effects of low-intensity illumination. The observations were explained by a mechanism consisting of two antagonistic processes that occur on slightly different time scales. On the one hand, light increases the ion conductivity which consists of the concentration and mobility of the mobile ions. Mobile ions drift towards the interfaces of the perovskite layer where they contribute to band bending and facilitate tunneling. Therefore, a higher conductivity appears as a smaller breakdown voltage. On the other hand, this breakdown is retarded by an electrochemical reaction driven by the reverse bias current itself. The reverse bias current consists of holes being injected into the perovskite layer that might neutralize mobile halide anions, and thus nullify their effect on the tunneling barrier.

This analysis identifies ion conductivity as a decisive parameter controlling the reverse bias breakdown. The findings also imply that in realistic (i.e. slow and mostly steady state) partial shading events, imperfect shading or indirect illumination do not substantially alter the breakdown voltage.

However, while the antagonistic processes and their different time scales were confirmed by quasi-steady state experiments, a direct investigation of the mobile ions in regard to species or a quantitative analysis was not included and requires additional research. Furthermore, it was assumed that the interaction of light with the mobile ions was related to intrinsic material properties, and that therefore the qualitative conclusions were valid for all perovskite solar cells. However, this assumption was not tested by comparative experiments on solar cells with other perovskite formulations.

Imaging the Reverse Bias Behavior via ReBEL

Fourthly, in Chapter 7, a new technique for imaging the reverse bias breakdown in perovskite solar cells was introduced. Reverse bias electroluminescence (ReBEL) imaging can reveal the spatial distribution of the reverse bias current with a higher resolution and better sensitivity than thermal imaging techniques. Using ReBEL, it was shown that different breakdown mechanisms are active at different current injection levels. At small reverse bias currents, the current flowed predominantly through localized defects and along cell edges. At large currents, the entire cell area underwent breakdown, albeit with a spatially-inhomogeneous current density distribution. Here, the emission rate followed an exponential dependence on the reverse bias, dominating the behavior of the whole cell at large current levels. While the increased activity at the cell edges could be traced back to the geometry of the bottom electrode, the spatial inhomogeneity of the emission over the cell area, remained a mystery. A possible connection to the series resistance of the electrodes was found, however, a complete understanding is still missing.

This work advances understanding of the breakdown mechanism in perovskite solar cells, but also highlights several open challenges. A comprehensive understanding of the reverse bias processes is still missing. Finally, the knowledge about mechanism must also be implemented in actual devices to mitigate partial shading-induced degradation. Possible research directions emerging from this work are outlined in the following section.

8.2. Outlook

In the previous section, the two fundamental approaches to mitigating partial shading events were presented. The first is the incorporation of bypass diodes which prevent the flow of current through the shaded cells during a partial shading event. The second allows the current to flow through the shaded cells but ensures that it does not cause (irreversible) degradation. Both approaches pose specific technical problems and challenges, some of which will be discussed in the following section.

Bypass diodes

As previously described, the monolithic interconnection scheme typical for thin-film modules complicates the use of external bypass diodes. Placing diodes only at the edges of the module would force the current to travel the entire length of the stripe-like cells to reach the bypass diodes. This design would require highly conductive electrodes, and therefore thick metal grid lines.

A more promising, alternative solution is the integration of bypass diodes directly into the monolithic interconnection. Instead of adding external electrical components to a module, integrated bypass diodes would be fabricated as part of the sequential deposition/scribing process of monolithically-interconnected PV modules. In the ideal case, the process modifications needed for the integration of bypass diodes should remain compatible with large area deposition that is one of the major characteristics for thin-film PV module manufacturing. Additional challenges include avoiding a substantial reduction of efficiency and preventing new degradation pathways.

A patent filed in 2002 by Armstrong *et al.* describes the step-by-step manufacturing route for monolithically-interconnected thin-film PV modules with integrated bypass diodes. [115] Another proposed design based on alternating normal and inverted perovskite solar cells can be found in the recent work by Boschloo *et al.* [116] These solutions could, in principle, enable the inclusion of one bypass diodes for each cell, offering the best possible protection against reverse bias currents.

Despite these promising proposals, no publications have demonstrated integrated bypass diodes in perovskite modules to date. Therefore, optimizing fabrication procedures for perovskite (mini-)modules with integrated bypass diodes represents a highly relevant topic for future research.

An alternative approach is forgoing the module design with monolithic interconnections and adopting instead a wafer-like design that could easily accommodate the implementation of external bypass diodes. This solution would also be compatible with two-terminal perovskite/silicon tandem modules which will discussed in more detail below. Optimizing the fabrication process for this design presents another viable research direction.

Non-degrading breakdown

The second way of mitigating partial shading degradation in modules requires as small breakdown voltages as possible, combined with a spatially uniform breakdown behavior. This strategy was implemented in monocrystalline silicon modules, enabling a drastic reduction in bypass diode usage compared to conventional silicon modules. [117] Additionally, this approach reduces power loss and reduces the risk of catastrophic failure in case of bypass diode failure.

While perovskite solar cells naturally exhibit small breakdown voltages, and ReBEL imaging in this work has demonstrated that non-localized reverse bias current flow is achievable, there is another critical requirement: The reverse bias current that flows through the cell must not cause degradation. While a small breakdown voltage leads to a low dissipated power, there are degradation mechanisms described in perovskite solar cells that do not depend on power but only on the reverse bias current. This presents two research challenges to be overcome before this strategy can be applied in perovskite modules:

- Firstly, achieving a spatially-uniform, non-damaging reverse bias breakdown for large scale modules.
- Secondly, identifying and mitigating degradation mechanisms that do not depend on power but on current.

Addressing both challenges requires further research dedicated to reverse bias breakdown processes and degradation mechanisms in perovskite solar cells.

Breakdown mechanism

In order to pursue the solution of bypass diodes in modules, a better control over the reverse bias breakdown of perovskite solar cells is essential. A larger breakdown voltage would reduce the number of bypass diodes required per module. A smaller number of bypass diodes is likely advantageous for limiting their detrimental effects on efficiency, stability, and cost-effectiveness. Such control over the breakdown voltage can only be achieved by improving the understanding of the underlying mechanism.

Chapter 4, Chapter 6, and Chapter 7 highlighted the limitations of the breakdown model: While there is a simplified qualitative model available, the effects of important factors, i.e. temperature, illumination, remain insufficiently understood. Furthermore, a quantitative model, i.e. a formalism, for the breakdown is missing completely. Some publications employ the Fowler-Nordheim tunneling model to illustrate the dependence of the current on the width and height of the tunneling barrier, but rigorous testing of its applicability is missing. [19, 49] Moreover, the available models are one-dimensional and do not capture the possible effects of spatial inhomogeneity.

One additional property of the breakdown in perovskite solar cells that has not yet been incorporated in any breakdown model is its dependence on time. This dynamic reverse bias behavior might consist of several components:

- Ion migration on similar time scales as a voltage sweep might modify the tunneling barrier due to band bending and might change the internal electric field due to screening.
- Electrochemical reaction driven by the reverse bias current might modify the tunneling barrier by neutralizing mobile ions or other reactions at an interface.

These phenomena are unique to perovskite solar cells and thus require systematic investigation before they can be incorporated into an extended model of the reverse bias breakdown mechanism.

Extension to tandem architectures

A topic that receives more and more attention in the general field of perovskite research concerns tandem solar cells. Tandem solar cells make use of more than one absorber material to increase the achievable efficiency. They are most commonly fabricated either as 2-terminal (2T) and 4-terminal (4T) devices.

In 2T tandems, the two subcells are connected in series, typically by depositing them in a monolithic fashion with only a thin recombination layer in-between. In this case, the subcell that generates less current limits the current output of the other subcell. In 4T tandem solar cells, the subcells are optically but not electrically connected. Therefore, each subcells can be treated as a separate single junction solar cell with independent electrical contacts.

While there are various possible combinations of absorber materials possible and under investigation, most promising is the perovskite/silicon tandem solar cell. Accordingly, some research on their reverse bias stability has been published already. [87, 90] These investigations generally focus on the 2T design as it is the goal to use the superior stability of the silicon subcell to protect the perovskite subcell. In contrast, the subcells of a 4T tandem can be considered as two single junction solar cells in regard to reverse bias stability.

The results on the reverse bias stability of 2T silicon/perovskite tandem solar cells are promising. It seems that - when certain conditions are met - the combination of silicon with perovskite leads to a substantially increased reverse bias breakdown voltage. Together with the wafer-based cell design of the silicon subcells, this means that the standard, bypass diodes-based protection against partial shading degradation of silicon-based modules can be simply translated to 2T silicon/perovskite tandem modules.

The previously-mentioned conditions that need to be fulfilled mostly concern the silicon subcell: [87] A high breakdown voltage and a high shunt resistance are crucial since the protection depends on preventing current flow. Additionally, optical optimization is also necessary to ensure that the tandem cell remains bottom-cell-limited even when the light spectrum shifts to high infrared contents. These conditions will need to be brought in line with the requirements for maximizing power output.

It should be noted that the protective effect of the silicon subcell only works when the perovskite subcell does not develop shunts at very small reverse biases. Therefore, the perovskite subcell also requires some optimization. Furthermore, the tandem solar cells, that have been investigated in regard to their reverse bias stability, are exclusively based on silicon heterojunction bottom cells. Other silicon solar cells designs should also be considered for investigations into their compatibility with perovskite solar cells. Furthermore, analogous investigations should be performed for other tandem technologies, like perovskite/perovskite tandems.

References

[1] IEA. *Snapshot of global PV markets 2025*. Tech. rep. 2025. URL: http://www.iea-pvps.org/fileadmin/dam/public/report/technical/PVPS_report_-_A_Snapshot_of_Global_PV_-_1992-2014.pdf.

[2] D. S. Philipps and W. Warmuth. *Photovoltaics Report*. Tech. rep. Fraunhofer ISE, May 2025. URL: https://www.ise.fraunhofer.de/en/publications/studies/photovoltaics-report.html (visited on 23/02/2026).

[3] S. K. Kurinec, ed. *Emerging photovoltaic materials*. Wiley, Dec. 2025. DOI: 10.1002/9781119407690.

[4] A. Kojima, K. Teshima, Y. Shirai and T. Miyasaka. 'Organometal Halide Perovskites as Visible-Light Sensitizers for Photovoltaic Cells'. In: *Journal of the American Chemical Society* 131.17 (May 2009), pp. 6050–6051. DOI: 10.1021/ja809598r.

[5] M. A. Green, E. D. Dunlop, M. Yoshita, N. Kopidakis, K. Bothe, G. Siefer, X. Hao and J. Y. Jiang. 'Solar Cell Efficiency Tables (Version 66)'. In: *Progress in Photovoltaics: Research and Applications* 33.7 (July 2025), pp. 795–810. DOI: 10.1002/pip.3919.

[6] NREL. *Best Research-Cell Efficiencies*. 2025. URL: https://www.nrel.gov/pv/cell-efficiency.

[7] M. Fischer, M. Woodhouse, T. Brammer and P. Baliozian. *International technology roadmap for photovoltaic (ITRPV) 2024 results 16th edition*. 2025. URL: https://www.vdma.org/international-technology-roadmap-photovoltaic.

[8] I. M. Peters and P. Sinha. 'Value of stability in photovoltaic life cycles'. In: *2021 IEEE 48th Photovoltaic Specialists Conference (PVSC)*. Fort Lauderdale, FL, USA: IEEE, June 2021, pp. 0416–0419. DOI: 10.1109/PVSC43889.2021.9518480.

[9] Z. Li, Y. Zhao, X. Wang, Y. Sun, Z. Zhao, Y. Li, H. Zhou and Q. Chen. 'Cost Analysis of Perovskite Tandem Photovoltaics'. In: *Joule* 2.8 (Aug. 2018), pp. 1559–1572. DOI: 10.1016/j.joule.2018.05.001.

[10] P.-H. Hsi and J. C. P. Shieh. 'How Credible Is the 25-Year Photovoltaic (PV) Performance Warranty?—A Techno-Financial Evaluation and Implications for the Sustainable Development of the PV Industry'. In: *Sustainability* 16.9 (May 2024), p. 3880. DOI: 10.3390/su16093880.

[11] L. Shi, M. P. Bucknall, T. L. Young, M. Zhang, L. Hu, J. Bing, D. S. Lee, J. Kim, T. Wu, N. Takamure, D. R. McKenzie, S. Huang, M. A. Green and A. W. Y. Ho-Baillie. 'Gas chromatography–mass spectrometry analyses of encapsulated stable perovskite solar cells'. In: *Science* 368.6497 (June 2020), eaba2412. DOI: 10.1126/science.aba2412.

[12] G. Grancini, C. Roldán-Carmona, I. Zimmermann, E. Mosconi, X. Lee, D. Martineau, S. Narbey, F. Oswald, F. De Angelis, M. Graetzel and M. K. Nazeeruddin. 'One-Year stable perovskite solar cells by 2D/3D interface engineering'. In: *Nature Communications* 8.1 (June 2017), p. 15684. DOI: 10.1038/ncomms15684.

[13] F. Bella, G. Griffini, J.-P. Correa-Baena, G. Saracco, M. Grätzel, A. Hagfeldt, S. Turri and C. Gerbaldi. 'Improving efficiency and stability of perovskite solar cells with photocurable fluoropolymers'. In: *Science* 354.6309 (Oct. 2016), pp. 203–206. DOI: 10.1126/science.aah4046.

[14] D. Lan and M. A. Green. 'Combatting temperature and reverse-bias challenges facing perovskite solar cells'. In: *Joule* 6.8 (Aug. 2022), pp. 1782–1797. DOI: 10.1016/j.joule.2022.06.014.

[15] D. C. Jordan, T. J. Silverman, J. H. Wohlgemuth, S. R. Kurtz and K. T. VanSant. 'Photovoltaic failure and degradation modes'. In: *Progress in Photovoltaics: Research and Applications* 25.4 (Apr. 2017), pp. 318–326. DOI: 10.1002/pip.2866.

[16] E. J. Wolf, I. E. Gould, L. B. Bliss, J. J. Berry and M. D. McGehee. 'Designing Modules to Prevent Reverse Bias Degradation in Perovskite Solar Cells when Partial Shading Occurs'. In: *Solar RRL* 6.3 (Mar. 2022), p. 2100239. DOI: 10.1002/solr.202100239.

[17] C. Wang, L. Huang, Y. Zhou, Y. Guo, K. Liang, T. Wang, X. Liu, J. Zhang, Z. Hu and Y. Zhu. 'Perovskite Solar Cells in the Shadow: Understanding the Mechanism of Reverse-Bias Behavior toward Suppressed Reverse-Bias Breakdown and Reverse-Bias Induced Degradation'. In: *Advanced Energy Materials* 13.9 (Mar. 2023), p. 2203596. DOI: 10.1002/aenm.202203596.

[18] R. A. Z. Razera, D. A. Jacobs, F. Fu, P. Fiala, M. Dussouillez, F. Sahli, T. C. J. Yang, L. Ding, A. Walter, A. F. Feil, H. I. Boudinov, S. Nicolay, C. Ballif and Q. Jeangros. 'Instability of p–i–n perovskite solar cells under reverse bias'. In: *Journal of Materials Chemistry A* 8.1 (2020), pp. 242–250. DOI: 10.1039/C9TA12032G.

[19] A. R. Bowring, L. Bertoluzzi, B. C. O'Regan and M. D. McGehee. 'Reverse Bias Behavior of Halide Perovskite Solar Cells'. In: *Advanced Energy Materials* 8.8 (Mar. 2018), p. 1702365. DOI: 10.1002/aenm.201702365.

[20] L. Bertoluzzi, J. B. Patel, K. A. Bush, C. C. Boyd, R. A. Kerner, B. C. O'Regan and M. D. McGehee. 'Incorporating Electrochemical Halide Oxidation into Drift-Diffusion Models to Explain Performance Losses in Perovskite Solar Cells under Prolonged Reverse Bias'. In: *Advanced Energy Materials* 11.10 (Mar. 2021), p. 2002614. DOI: 10.1002/aenm.202002614.

[21] X. Ren, J. Wang, Y. Lin, Y. Wang, H. Xie, H. Huang, B. Yang, Y. Yan, Y. Gao, J. He, J. Huang and Y. Yuan. ‘Mobile iodides capture for highly photolysis- and reverse-bias-stable perovskite solar cells’. In: *Nature Materials* 23.6 (June 2024), pp. 810–817. DOI: 10.1038/s41563-024-01876-2.

[22] Y. Ma, Y. Cheng, X. Xu, M. Li, C. Zhang, S. H. Cheung, Z. Zeng, D. Shen, Y.-M. Xie, K. L. Chiu, F. Lin, S. K. So, C.-S. Lee and S.-W. Tsang. ‘Suppressing Ion Migration across Perovskite Grain Boundaries by Polymer Additives’. In: *Advanced Functional Materials* 31.3 (Jan. 2021), p. 2006802. DOI: 10.1002/adfm.202006802.

[23] D. Bogachuk, K. Saddedine, D. Martineau, S. Narbey, A. Verma, P. Gebhardt, J. P. Herterich, N. Glissmann, S. Zouhair, J. Markert, I. E. Gould, M. D. McGehee, U. Würfel, A. Hinsch and L. Wagner. ‘Perovskite Photovoltaic Devices with Carbon-Based Electrodes Withstanding Reverse-Bias Voltages up to –9 V and Surpassing IEC 61215:2016 International Standard’. In: *Solar RRL* 6.3 (Mar. 2022), p. 2100527. DOI: 10.1002/solr.202100527.

[24] X. Guo, N. Li, Y. Xu, J. Zhao, F. Cui, Y. Chen, X. Du, Q. Song, G. Zhang, X. Cheng, X. Tao and Z. Chen. ‘Mitigating Surface Deficiencies of Perovskite Single Crystals Enables Efficient Solar Cells with Enhanced Moisture and Reverse-Bias Stability’. In: *Advanced Functional Materials* 33.22 (May 2023), p. 2213995. DOI: 10.1002/adfm.202213995.

[25] C. Jiang, J. Zhou, H. Li, L. Tan, M. Li, W. Tress, L. Ding, M. Grätzel and C. Yi. ‘Double Layer Composite Electrode Strategy for Efficient Perovskite Solar Cells with Excellent Reverse-Bias Stability’. In: *Nano-Micro Letters* 15.1 (Dec. 2023), p. 12. DOI: 10.1007/s40820-022-00985-4.

[26] L. Lanzetta, L. Huerta Hernandez, B. Vishal, H. Xu, A. Sharma, S. De Wolf and D. Baran. ‘Tin–Lead Perovskite Solar Cells with Enhanced Reverse Bias Stability’. In: *ACS Energy Letters* 10.5 (May 2025), pp. 2093–2095. DOI: 10.1021/acsenergylett.5c00727.

[27] L. Zhan, S. Zhang, Z. Li, W. Li, H. Zhang, J. He, X. Ji, S. Liu, F. Yu, S. Wang, Z. Ning, Z. Li, M. Stolterfoht, L. Han, W.-H. Zhu, Y. Xu and Y. Wu. ‘Anchorable Polymers Enabling Ultra-Thin and Robust Hole-Transporting Layers for High-Efficiency Inverted Perovskite Solar Cells’. In: *Angewandte Chemie International Edition* 64.12 (Mar. 2025), e202422571. DOI: 10.1002/anie.202422571.

[28] F. Jiang, Y. Shi, T. R. Rana, D. Morales, I. E. Gould, D. P. McCarthy, J. A. Smith, M. G. Christoforo, M. Y. Yaman, F. Mandani, T. Terlier, H. Contreras, S. Barlow, A. D. Mohite, H. J. Snaith, S. R. Marder, J. D. MacKenzie, M. D. McGehee and D. S. Ginger. ‘Improved reverse bias stability in p–i–n perovskite solar cells with optimized hole transport materials and less reactive electrodes’. In: *Nature Energy* 9.10 (Aug. 2024), pp. 1275–1284. DOI: 10.1038/s41560-024-01600-z.

[29] Z. Ni, H. Jiao, C. Fei, H. Gu, S. Xu, Z. Yu, G. Yang, Y. Deng, Q. Jiang, Y. Liu, Y. Yan and J. Huang. ‘Evolution of defects during the degradation of metal halide perovskite solar cells under reverse bias and illumination’. In: *Nature Energy* 7.1 (Dec. 2021), pp. 65–73. DOI: 10.1038/s41560-021-00949-9.

[30] J. Wang, G. Nie, W. Huang, Y. Guo, Y. Li, Z. Yang, Y. Chen, K. Ding, Y. Yang, W. Wang, L.-M. Kuang, K. Yang, D. Tang and Y. Zhai. 'Reconstruction and Solidification of Dion–Jacobson Perovskite Top and Buried Interfaces for Efficient and Stable Solar Cells'. In: *Nano Letters* 24.38 (Sept. 2024), pp. 11873–11881. DOI: 10.1021/acs.nanolett.4c03013.

[31] N. Li, Z. Shi, C. Fei, H. Jiao, M. Li, H. Gu, S. P. Harvey, Y. Dong, M. C. Beard and J. Huang. 'Barrier reinforcement for enhanced perovskite solar cell stability under reverse bias'. In: *Nature Energy* 9.10 (July 2024), pp. 1264–1274. DOI: 10.1038/s41560-024-01579-7.

[32] N. Liu, Q. Zou, Y. Li, G. Li, Y. Chen, R. Liang, S. Liu, S. Lu, W. Wang, B. Ji, L. Ke, G. Nie, H. Zhou, B. Liu, Y. Zhai, Y. Guo and J. Wang. 'Halogen Bonding Enable Improved Performance and Stability of Dion–Jacobson Perovskite Solar Cells'. In: *Angewandte Chemie International Edition* 64.27 (July 2025), e202500131. DOI: 10.1002/anie.202500131.

[33] M. V. Khenkin, E. A. Katz, A. Abate, G. Bardizza, J. J. Berry, C. Brabec, F. Brunetti, V. Bulović, Q. Burlingame, A. Di Carlo, R. Cheacharoen, Y.-B. Cheng, A. Colsmann, S. Cros, K. Domanski, M. Dusza, C. J. Fell, S. R. Forrest, Y. Galagan, D. Di Girolamo, M. Grätzel, A. Hagfeldt, E. Von Hauff, H. Hoppe, J. Kettle, H. Köbler, M. S. Leite, S. Liu, Y.-L. Loo, J. M. Luther, C.-Q. Ma, M. Madsen, M. Manceau, M. Matheron, M. McGehee, R. Meitzner, M. K. Nazeeruddin, A. F. Nogueira, Ç. Odabaşı, A. Osherov, N.-G. Park, M. O. Reese, F. De Rossi, M. Saliba, U. S. Schubert, H. J. Snaith, S. D. Stranks, W. Tress, P. A. Troshin, V. Turkovic, S. Veenstra, I. Visoly-Fisher, A. Walsh, T. Watson, H. Xie, R. Yıldırım, S. M. Zakeeruddin, K. Zhu and M. Lira-Cantu. 'Consensus statement for stability assessment and reporting for perovskite photovoltaics based on ISOS procedures'. In: *Nature Energy* 5.1 (Jan. 2020), pp. 35–49. DOI: 10.1038/s41560-019-0529-5.

[34] T. Baikie, Y. Fang, J. M. Kadro, M. Schreyer, F. Wei, S. G. Mhaisalkar, M. Graetzel and T. J. White. 'Synthesis and crystal chemistry of the hybrid perovskite (CH3NH3)PbI3 for solid-state sensitised solar cell applications'. In: *Journal of Materials Chemistry A* 1.18 (Apr. 2013), pp. 5628–5641. DOI: 10.1039/C3TA10518K.

[35] C. S. J. Ponseca, T. J. Savenije, M. Abdellah, K. Zheng, A. Yartsev, T. Pascher, T. Harlang, P. Chabera, T. Pullerits, A. Stepanov, J.-P. Wolf and V. Sundström. 'Organometal Halide Perovskite Solar Cell Materials Rationalized: Ultrafast Charge Generation, High and Microsecond-Long Balanced Mobilities, and Slow Recombination'. In: *Journal of the American Chemical Society* 136.14 (Apr. 2014), pp. 5189–5192. DOI: 10.1021/ja412583t.

[36] L. Etgar, P. Gao, Z. Xue, Q. Peng, A. K. Chandiran, B. Liu, M. K. Nazeeruddin and M. Grätzel. 'Mesoscopic CH3NH3PbI3/TiO2 Heterojunction Solar Cells'. In: *Journal of the American Chemical Society* 134.42 (Oct. 2012), pp. 17396–17399. DOI: 10.1021/ja307789s.

[37] M. M. Lee, J. Teuscher, T. Miyasaka, T. N. Murakami and H. J. Snaith. ‘Efficient Hybrid Solar Cells Based on Meso-Superstructured Organometal Halide Perovskites’. In: *Science* 338.6107 (Nov. 2012), pp. 643–647. DOI: 10.1126/science.1228604.

[38] A. Lan, H. Lu, B. Huang, F. Chen, Z. Chen, J. Wang, L. Li and H. Do. ‘Toward Commercial-Scale Perovskite Solar Cells: The Role of ALD-SnO_2 Buffer Layers in Performance and Stability’. In: *ACS Applied Materials & Interfaces* 16.47 (Nov. 2024), pp. 64825–64833. DOI: 10.1021/acsami.4c14954.

[39] M. A. Riza, M. A. Ibrahim, U. C. Ahamefula, M. A. Mat Teridi, N. Ahmad Ludin, S. Sepeai and K. Sopian. ‘Prospects and challenges of perovskite type transparent conductive oxides in photovoltaic applications. Part I – Material developments’. In: *Solar Energy* 137 (Nov. 2016), pp. 371–378. DOI: 10.1016/j.solener.2016.08.042.

[40] A. Smets, K. Jager, O. Isabella and R. van Swaaij. *Solar Energy*. Cambridge, England: UIT Cambridge, 2016. ISBN: 978-1-906860-32-5.

[41] S. Sze and K. K. Ng. *Physics of Semiconductor Devices*. 3rd ed. Chichester, England: Wiley, Oct. 2006. DOI: 10.1002/0470068329.

[42] A. Senocrate, I. Moudrakovski, G. Y. Kim, T.-Y. Yang, G. Gregori, M. Grätzel and J. Maier. ‘The Nature of Ion Conduction in Methylammonium Lead Iodide: A Multimethod Approach’. In: *Angewandte Chemie International Edition* 56.27 (June 2017), pp. 7755–7759. DOI: 10.1002/anie.201701724.

[43] M. H. Futscher, J. M. Lee, L. McGovern, L. A. Muscarella, T. Wang, M. I. Haider, A. Fakharuddin, L. Schmidt-Mende and B. Ehrler. ‘Quantification of ion migration in CH_3 NH_3 PbI_3 perovskite solar cells by transient capacitance measurements’. In: *Materials Horizons* 6.7 (2019), pp. 1497–1503. DOI: 10.1039/C9MH00445A.

[44] D. A. Jacobs, C. M. Wolff, X.-Y. Chin, K. Artuk, C. Ballif and Q. Jeangros. ‘Lateral ion migration accelerates degradation in halide perovskite devices’. In: *Energy & Environmental Science* 15.12 (2022), pp. 5324–5339. DOI: 10.1039/D2EE02330J.

[45] Y. Shao, Y. Fang, T. Li, Q. Wang, Q. Dong, Y. Deng, Y. Yuan, H. Wei, M. Wang, A. Gruverman, J. Shield and J. Huang. ‘Grain boundary dominated ion migration in polycrystalline organic–inorganic halide perovskite films’. In: *Energy & Environmental Science* 9.5 (2016), pp. 1752–1759. DOI: 10.1039/C6EE00413J.

[46] Y. Wang, Z. Hu, C. Gao, C. Yang, J. Zhang and Y. Zhu. ‘Comprehensive Elucidation of Grain Boundary Behavior in All-Inorganic Halide Perovskites by Scanning Probe Microscopy’. In: *Advanced Materials Interfaces* 7.7 (Apr. 2020), p. 1901521. DOI: 10.1002/admi.201901521.

[47] N. Adhikari, A. Dubey, D. Khatiwada, A. F. Mitul, Q. Wang, S. Venkatesan, A. Iefanova, J. Zai, X. Qian, M. Kumar and Q. Qiao. ‘Interfacial Study To Suppress Charge Carrier Recombination for High Efficiency Perovskite Solar Cells’. In: *ACS Applied Materials & Interfaces* 7.48 (Dec. 2015), pp. 26445–26454. DOI: 10.1021/acsami.5b09797.

[48] J.-J. Li, J.-Y. Ma, Q.-Q. Ge, J.-S. Hu, D. Wang and L.-J. Wan. ‘Microscopic Investigation of Grain Boundaries in Organolead Halide Perovskite Solar Cells’. In: *ACS Applied Materials & Interfaces* 7.51 (Dec. 2015), pp. 28518–28523. DOI: 10.1021/acsami.5b09801.

[49] C. Wang, L. Huang, Y. Guo, S. Liu, J. Huang, X. Liu, J. Zhang, Z. Hu, K. Liu and Y. Zhu. ‘Abnormal Dynamic Reverse Bias Behavior and Variable Reverse Breakdown Voltage of ETL-free Perovskite Solar Cells’. In: *Solar RRL* 7.20 (Oct. 2023), p. 2300456. DOI: 10.1002/solr.202300456.

[50] S. Mahadevan, S. M. Hardas and G. Suryan. ‘Electrical breakdown in semiconductors’. In: *Physica Status Solidi (a)* 8.2 (Dec. 1971), pp. 335–374. DOI: 10.1002/pssa.2210080202.

[51] S. Puttnins, S. Jander, A. Wehrmann, G. Benndorf, M. Stölzel, A. Müller, H. Von Wenckstern, F. Daume, A. Rahm and M. Grundmann. ‘Breakdown characteristics of flexible Cu(In,Ga)Se2 solar cells’. In: *Solar Energy Materials and Solar Cells* 120 (Jan. 2014), pp. 506–511. DOI: 10.1016/j.solmat.2013.09.031.

[52] D. Lausch, K. Petter, H. V. Wenckstern and M. Grundmann. ‘Correlation of pre-breakdown sites and bulk defects in multicrystalline silicon solar cells’. In: *physica status solidi (RRL) – Rapid Research Letters* 3.2-3 (Mar. 2009), pp. 70–72. DOI: 10.1002/pssr.200802264.

[53] T. Tayagaki, H. Kobayashi, K. Yamamoto, T. N. Murakami and M. Yoshita. ‘Effects of partial shading and temperature-dependent reverse bias behaviour on degradation in perovskite photovoltaic modules’. In: *Solar Energy Materials and Solar Cells* 279 (Jan. 2025), p. 113229. DOI: 10.1016/j.solmat.2024.113229.

[54] M. Auf Der Maur, F. Matteocci, A. Di Carlo and M. Testa. ‘Reverse bias breakdown and photocurrent gain in CH3NH3PbBr3 films’. In: *Applied Physics Letters* 120.11 (Mar. 2022), p. 113505. DOI: 10.1063/5.0082425.

[55] IEC. *IEC 61215*. URL: https://webstore.iec.ch/en/publication/61345.

[56] W. Q. Meeker and L. A. Escobar. ‘Pitfalls of Accelerated Testing’. In: *IEEE Transactions on Reliability* 47.2 (1998), pp. 114–118.

[57] R. Saive. ‘S-Shaped Current–Voltage Characteristics in Solar Cells: A Review’. In: *IEEE Journal of Photovoltaics* 9.6 (Nov. 2019), pp. 1477–1484. DOI: 10.1109/JPHOTOV.2019.2930409.

[58] I. E. Gould, C. Xiao, J. B. Patel and M. D. McGehee. ‘In-Operando Characterization of P-I-N Perovskite Solar Cells Under Reverse Bias’. In: *2021 IEEE 48th Photovoltaic Specialists Conference (PVSC)*. Fort Lauderdale, FL, USA: IEEE, June 2021, pp. 1365–1367. DOI: 10.1109/PVSC43889.2021.9518723.

[59] R. Aninat, K. Bakker, **J. Henzel**, V. Zardetto, I. Dogan, V. Gevaerts, S. Veenstra and M. Theelen. ‘Mapping the Partial Shading Degradation in a Monolithically Integrated Perovskite Module’. In: *Progress in Photovoltaics: Research and Applications* 34.1 (Jan. 2026), pp. 60–68. DOI: 10.1002/pip.3881.

[60] E. T. Hoke, D. J. Slotcavage, E. R. Dohner, A. R. Bowring, H. I. Karunadasa and M. D. McGehee. 'Reversible photo-induced trap formation in mixed-halide hybrid perovskites for photovoltaics'. In: *Chemical Science* 6.1 (2015), pp. 613–617. DOI: 10.1039/C4SC03141E.

[61] R. A. Kerner, Z. Xu, B. W. Larson and B. P. Rand. 'The role of halide oxidation in perovskite halide phase separation'. In: *Joule* 5.9 (Sept. 2021), pp. 2273–2295. DOI: 10.1016/j.joule.2021.07.011.

[62] H. J. Snaith, A. Abate, J. M. Ball, G. E. Eperon, T. Leijtens, N. K. Noel, S. D. Stranks, J. T.-W. Wang, K. Wojciechowski and W. Zhang. 'Anomalous Hysteresis in Perovskite Solar Cells'. In: *The Journal of Physical Chemistry Letters* 5.9 (May 2014), pp. 1511–1515. DOI: 10.1021/jz500113x.

[63] V. M. Le Corre, J. Diekmann, F. Peña-Camargo, J. Thiesbrummel, N. Tokmoldin, E. Gutierrez-Partida, K. P. Peters, L. Perdigón-Toro, M. H. Futscher, F. Lang, J. Warby, H. J. Snaith, D. Neher and M. Stolterfoht. 'Quantification of Efficiency Losses Due to Mobile Ions in Perovskite Solar Cells via Fast Hysteresis Measurements'. In: *Solar RRL* 6.4 (Apr. 2022), p. 2100772. DOI: 10.1002/solr.202100772.

[64] J. Thiesbrummel, S. Shah, E. Gutierrez-Partida, F. Zu, F. Peña-Camargo, S. Zeiske, J. Diekmann, F. Ye, K. P. Peters, K. O. Brinkmann, P. Caprioglio, A. Dasgupta, S. Seo, F. A. Adeleye, J. Warby, Q. Jeangros, F. Lang, S. Zhang, S. Albrecht, T. Riedl, A. Armin, D. Neher, N. Koch, Y. Wu, V. M. Le Corre, H. Snaith and M. Stolterfoht. 'Ion-induced field screening as a dominant factor in perovskite solar cell operational stability'. In: *Nature Energy* 9.6 (Mar. 2024), pp. 664–676. DOI: 10.1038/s41560-024-01487-w.

[65] W. Veurman, J. Kern, L. Pflüger, H. Wagner-Mohnsen, M. Müller, P. P. Altermatt, Z. Lou, M. Stolterfoht, F. Haase, S. Kajari-Schröder and R. Peibst. 'Deciphering hysteresis in perovskite solar cells: Insights from device simulations distinguishing shallow traps from mobile ions'. In: *Solar Energy* 284 (Dec. 2024), p. 113037. DOI: 10.1016/j.solener.2024.113037.

[66] J. Bisquert. 'Hysteresis, Impedance, and Transients Effects in Halide Perovskite Solar Cells and Memory Devices Analysis by Neuron-Style Models'. In: *Advanced Energy Materials* 14.26 (July 2024), p. 2400442. DOI: 10.1002/aenm.202400442.

[67] S. Tammireddy, M. N. Lintangpradipto, O. Telschow, M. H. Futscher, B. Ehrler, O. M. Bakr, Y. Vaynzof and C. Deibel. 'Hysteresis and Its Correlation to Ionic Defects in Perovskite Solar Cells'. In: *The Journal of Physical Chemistry Letters* 15.5 (Feb. 2024), pp. 1363–1372. DOI: 10.1021/acs.jpclett.3c03146.

[68] S. Tang, J. Yan, L. Chen, W. Zhang and L. Tan. 'Circuit modeling and analysis of hysteresis effect of perovskite photovoltaic cells'. In: *Solar Energy Materials and Solar Cells* 278 (Dec. 2024), p. 113182. DOI: 10.1016/j.solmat.2024.113182.

[69] S. A. L. Weber, I. M. Hermes, S.-H. Turren-Cruz, C. Gort, V. W. Bergmann, L. Gilson, A. Hagfeldt, M. Graetzel, W. Tress and R. Berger. ‘How the formation of interfacial charge causes hysteresis in perovskite solar cells’. In: *Energy & Environmental Science* 11.9 (2018), pp. 2404–2413. doi: 10.1039/C8EE01447G.

[70] D. A. Jacobs, Y. Wu, H. Shen, C. Barugkin, F. J. Beck, T. P. White, K. Weber and K. R. Catchpole. ‘Hysteresis phenomena in perovskite solar cells: the many and varied effects of ionic accumulation’. In: *Physical Chemistry Chemical Physics* 19.4 (2017), pp. 3094–3103. doi: 10.1039/C6CP06989D.

[71] W. Tress, J. P. Correa Baena, M. Saliba, A. Abate and M. Graetzel. ‘Inverted Current–Voltage Hysteresis in Mixed Perovskite Solar Cells: Polarization, Energy Barriers, and Defect Recombination’. In: *Advanced Energy Materials* 6.19 (Oct. 2016), p. 1600396. doi: 10.1002/aenm.201600396.

[72] N. E. Courtier, J. M. Cave, J. M. Foster, A. B. Walker and G. Richardson. ‘How transport layer properties affect perovskite solar cell performance: insights from a coupled charge transport/ion migration model’. In: *Energy & Environmental Science* 12.1 (2019), pp. 396–409. doi: 10.1039/C8EE01576G.

[73] D. Abou-Ras, T. Kirchartz and U. Rau, eds. *Advanced characterization techniques for thin film solar cells*. 2nd, exten. Weinheim: Wiley-VCH Verlag, 2016. isbn: 978-3-527-69902-5.

[74] J. Haunschild, M. Glatthaar, M. Kasemann, S. Rein and E. R. Weber. ‘Fast series resistance imaging for silicon solar cells using electroluminescence’. In: *physica status solidi (RRL) – Rapid Research Letters* 3.7-8 (Oct. 2009), pp. 227–229. doi: 10.1002/pssr.200903175.

[75] Y. Rong, Y. Hu, A. Mei, H. Tan, M. I. Saidaminov, S. I. Seok, M. D. McGehee, E. H. Sargent and H. Han. ‘Challenges for commercializing perovskite solar cells’. In: *Science* 361.6408 (Sept. 2018), eaat8235. doi: 10.1126/science.aat8235.

[76] F. Lang, O. Shargaieva, V. V. Brus, H. C. Neitzert, J. Rappich and N. H. Nickel. ‘Influence of Radiation on the Properties and the Stability of Hybrid Perovskites’. In: *Advanced Materials* 30.3 (Jan. 2018), p. 1702905. doi: 10.1002/adma.201702905.

[77] S.-W. Lee, S. Kim, S. Bae, K. Cho, T. Chung, L. E. Mundt, S. Lee, S. Park, H. Park, M. C. Schubert, S. W. Glunz, Y. Ko, Y. Jun, Y. Kang, H.-S. Lee and D. Kim. ‘UV Degradation and Recovery of Perovskite Solar Cells’. In: *Scientific Reports* 6.1 (Dec. 2016), p. 38150. doi: 10.1038/srep38150.

[78] J. A. Schwenzer, L. Rakocevic, R. Gehlhaar, T. Abzieher, S. Gharibzadeh, S. Moghadamzadeh, A. Quintilla, B. S. Richards, U. Lemmer and U. W. Paetzold. ‘Temperature Variation-Induced Performance Decline of Perovskite Solar Cells’. In: *ACS Applied Materials & Interfaces* 10.19 (May 2018), pp. 16390–16399. doi: 10.1021/acsami.8b01033.

[79] J. Yang, B. D. Siempelkamp, D. Liu and T. L. Kelly. ‘Investigation of CH_3 NH_3 PbI_3 Degradation Rates and Mechanisms in Controlled Humidity Environments Using *in Situ* Techniques’. In: *ACS Nano* 9.2 (Feb. 2015), pp. 1955–1963. doi: 10.1021/nn506864k.

[80] D. Bryant, N. Aristidou, S. Pont, I. Sanchez-Molina, T. Chotchunangatchaval, S. Wheeler, J. R. Durrant and S. A. Haque. 'Light and oxygen induced degradation limits the operational stability of methylammonium lead triiodide perovskite solar cells'. In: *Energy & Environmental Science* 9.5 (2016), pp. 1655–1660. DOI: 10.1039/C6EE00409A.

[81] M. V. Khenkin, A. K. M., E. A. Katz and I. Visoly-Fisher. 'Bias-dependent degradation of various solar cells: lessons for stability of perovskite photovoltaics'. In: *Energy & Environmental Science* 12.2 (2019), pp. 550–558. DOI: 10.1039/C8EE03475C.

[82] K. Domanski, E. A. Alharbi, A. Hagfeldt, M. Grätzel and W. Tress. 'Systematic investigation of the impact of operation conditions on the degradation behaviour of perovskite solar cells'. In: *Nat. Energy* 3.1 (2018), pp. 61–67. DOI: 10.1038/s41560-017-0060-5.

[83] S. Dongaonkar and M. A. Alam. 'Geometrical design of thin film PV modules for improved shade tolerance and performance'. In: *Progress in Photovoltaics: Research and Applications* 20.1 (Mar. 2013). ISBN: 1099-159X tex.arxivid: 1303.4604, pp. 6–11. DOI: 10.1002/pip.

[84] **J. Henzel**, K. Bakker, M. Najafi, V. Zardetto, S. Veenstra, O. Isabella, L. Mazzarella, A. Weeber and M. Theelen. 'Impact of the Current on Reverse Bias Degradation of Perovskite Solar Cells'. In: *ACS Applied Energy Materials* 6.22 (Nov. 2023), pp. 11429–11432. DOI: 10.1021/acsaem.3c02273.

[85] L. J. Geerligs, M. Najafi, N. J. Bakker, D. Zhang, A. J. Carr, N. J. J. Dekker, J. Luiken, G. Coletti and S. C. Veenstra. 'Reverse-bias studies of semitransparent perovskite cells , and model evaluation of 4T tandem module designs'. In: *TandemPV workshop*. 2022.

[86] B. B. Pannebakker, A. C. De Waal and W. G. Van Sark. 'Photovoltaics in the shade: one bypass diode per solar cell revisited: Photovoltaics in the shade'. In: *Progress in Photovoltaics: Research and Applications* 25.10 (Oct. 2017), pp. 836–849. DOI: 10.1002/pip.2898.

[87] D. Di Girolamo, O. Dupré, G. Giuliano, J. Veirman, G. Bengasi, M. Foti and C. Gerardi. 'Silicon / Perovskite Tandem Solar Cells with Reverse Bias Stability down to -40 V. Unveiling the Role of Electrical and Optical Design'. In: *Advanced Science* 11.31 (Aug. 2024), p. 2401175. DOI: 10.1002/advs.202401175.

[88] **J. Henzel**, K. Bakker, S. Veenstra, O. Isabella, L. Mazzarella, A. Weeber and M. Theelen. 'The impact of low-intensity illumination on the reverse bias behavior of perovskite solar cells'. In: *Journal of Materials Chemistry A* 13.37 (2025), pp. 31755–31769. DOI: 10.1039/D5TA04100G.

[89] J. S. Yun, J. Seidel, J. Kim, A. M. Soufiani, S. Huang, J. Lau, N. J. Jeon, S. I. Seok, M. A. Green and A. Ho-Baillie. 'Critical Role of Grain Boundaries for Ion Migration in Formamidinium and Methylammonium Lead Halide Perovskite Solar Cells'. In: *Advanced Energy Materials* 6.13 (July 2016), p. 1600330. DOI: 10.1002/aenm.201600330.

[90] Z. Xu, H. Bristow, M. Babics, B. Vishal, E. Aydin, R. Azmi, E. Ugur, B. K. Yildirim, J. Liu, R. A. Kerner, S. De Wolf and B. P. Rand. ‘Reverse-bias resilience of monolithic perovskite/silicon tandem solar cells’. In: *Joule* 7.9 (Sept. 2023), pp. 1992–2002. DOI: 10.1016/j.joule.2023.07.017.

[91] P. Szaniawski, P. Zabierowski, J. Olsson, U. Zimmermann and M. Edoff. ‘Advancing the Understanding of Reverse Breakdown in Cu(In,Ga)Se_2 Solar Cells’. In: *IEEE Journal of Photovoltaics* 7.4 (July 2017), pp. 1136–1142. DOI: 10.1109/JPHOTOV.2017.2699860.

[92] R. G. Mortimer. *Mathematics for Physical Chemistry*. 3rd ed. London: Elsevier Science & Technology, 2005. ISBN: 978-0-12-508347-8.

[93] G. Pu. *The Inflection Point of the Exponential Function*. 2024. URL: https://georgerpu.github.io/blog/2024/exp-inflection-point/.

[94] J. Qian, M. Ernst, D. Walter, M. A. Mahmud, P. Hacke, K. Weber, M. Al-Jassim and A. Blakers. ‘Destructive reverse bias pinning in perovskite/silicon tandem solar modules caused by perovskite hysteresis under dynamic shading’. In: *Sustainable Energy & Fuels* 4.8 (2020), pp. 4067–4075. DOI: 10.1039/C9SE01246J.

[95] L. Duan, D. Walter, N. Chang, J. Bullock, D. Kang, S. P. Phang, K. Weber, T. White, D. Macdonald, K. Catchpole and H. Shen. ‘Stability challenges for the commercialization of perovskite–silicon tandem solar cells’. In: *Nature Reviews Materials* 8.4 (Jan. 2023), pp. 261–281. DOI: 10.1038/s41578-022-00521-1.

[96] W. Li, K. Huang, J. Chang, C. Hu, C. Long, H. Zhang, X. Maldague, B. Liu, J. Meng, Y. Duan and J. Yang. ‘Sparkling hot spots in perovskite solar cells under reverse bias’. In: *ChemPhysMater* 1.1 (Jan. 2022), pp. 71–76. DOI: 10.1016/j.chphma.2021.10.001.

[97] A. E. A. Bracesco, C. H. Burgess, A. Todinova, V. Zardetto, D. Koushik, W. M. M. (Kessels, I. Dogan, C. H. L. Weijtens, S. Veenstra, R. Andriessen and M. Creatore. ‘The chemistry and energetics of the interface between metal halide perovskite and atomic layer deposited metal oxides’. In: *Journal of Vacuum Science & Technology A* 38.6 (Dec. 2020), p. 063206. DOI: 10.1116/6.0000447.

[98] D. Głowienka, D. Zhang, F. Di Giacomo, M. Najafi, S. Veenstra, J. Szmytkowski and Y. Galagan. ‘Role of surface recombination in perovskite solar cells at the interface of HTL/CH3NH3PbI3’. In: *Nano Energy* 67 (Jan. 2020), p. 104186. DOI: 10.1016/j.nanoen.2019.104186.

[99] M. García-Batlle, J. Mayén Guillén, M. Chapran, O. Baussens, J. Zaccaro, J.-M. Verilhac, E. Gros-Daillon, A. Guerrero, O. Almora and G. Garcia-Belmonte. ‘Coupling between Ion Drift and Kinetics of Electronic Current Transients in $MAPbBr_3$ Single Crystals’. In: *ACS Energy Letters* 7.3 (Mar. 2022), pp. 946–951. DOI: 10.1021/acsenergylett.1c02578.

[100] M. A. Green, E. D. Dunlop, M. Yoshita, N. Kopidakis, K. Bothe, G. Siefer, X. Hao and J. Y. Jiang. ‘Solar Cell Efficiency Tables (Version 67)’. In: *Progress in Photovoltaics: Research and Applications* 34.4 (2026), pp. 482–496. DOI: https://doi.org/10.1002/pip.70068.

[101] Y. Yang, C. Liu, Y. Ding, B. Ding, J. Xu, A. Liu, J. Yu, L. Grater, H. Zhu, S. S. Hadke, V. K. Sangwan, A. S. R. Bati, X. Hu, J. Li, S. M. Park, M. C. Hersam, B. Chen, M. K. Nazeeruddin, M. G. Kanatzidis and E. H. Sargent. ‘A thermotropic liquid crystal enables efficient and stable perovskite solar modules’. In: *Nature Energy* 9.3 (Jan. 2024), pp. 316–323. DOI: 10.1038/s41560-023-01444-z.

[102] K. Bakker, A. Weeber and M. Theelen. ‘Reliability implications of partial shading on CIGS photovoltaic devices: A literature review’. In: *Journal of Materials Research* 34.24 (Dec. 2019), pp. 3977–3987. DOI: 10.1557/jmr.2019.373.

[103] T. J. Silverman, M. G. Deceglie, X. Sun, R. L. Garris, M. A. Alam, C. Deline and S. Kurtz. ‘Thermal and Electrical Effects of Partial Shade in Monolithic Thin-Film Photovoltaic Modules’. In: *IEEE Journal of Photovoltaics* 5.6 (Nov. 2015), pp. 1742–1747. DOI: 10.1109/JPHOTOV.2015.2478071.

[104] P. Szaniawski, J. Lindahl, T. Törndahl, U. Zimmermann and M. Edoff. ‘Light-enhanced reverse breakdown in Cu(In,Ga)Se2 solar cells’. In: *Thin Solid Films* 535 (May 2013), pp. 326–330. DOI: 10.1016/j.tsf.2012.09.022.

[105] E. J. Juarez-Perez, R. S. Sanchez, L. Badia, G. Garcia-Belmonte, Y. S. Kang, I. Mora-Sero and J. Bisquert. ‘Photoinduced Giant Dielectric Constant in Lead Halide Perovskite Solar Cells’. In: *The Journal of Physical Chemistry Letters* 5.13 (July 2014), pp. 2390–2394. DOI: 10.1021/jz5011169.

[106] J. Xing, Q. Wang, Q. Dong, Y. Yuan, Y. Fang and J. Huang. ‘Ultrafast ion migration in hybrid perovskite polycrystalline thin films under light and suppression in single crystals’. In: *Physical Chemistry Chemical Physics* 18.44 (2016), pp. 30484–30490. DOI: 10.1039/C6CP06496E.

[107] Y. Zhao, W. Zhou, Z. Han, D. Yu and Q. Zhao. ‘Effects of ion migration and improvement strategies for the operational stability of perovskite solar cells’. In: *Physical Chemistry Chemical Physics* 23.1 (2021), pp. 94–106. DOI: 10.1039/D0CP04418K.

[108] A. Schiller, S. Jenatsch, B. Blülle, M. A. Torre Cachafeiro, F. Ebadi, N. Kabir, M. Othman, C. M. Wolff, A. Hessler-Wyser, C. Ballif, W. Tress and B. Ruhstaller. ‘Assessing the Influence of Illumination on Ion Conductivity in Perovskite Solar Cells’. In: *The Journal of Physical Chemistry Letters* 15.45 (Nov. 2024), pp. 11252–11258. DOI: 10.1021/acs.jpclett.4c02403.

[109] M. Faraday. ‘VI. Experimental researches in electricity.-seventh series’. In: *Philosophical Transactions of the Royal Society of London* 124 (Dec. 1834), pp. 77–122. DOI: 10.1098/rstl.1834.0008.

[110] L. Najafi, S. Bellani, L. Gabatel, M. I. Zappia, A. Di Carlo and F. Bonaccorso. ‘Reverse-Bias and Temperature Behaviors of Perovskite Solar Cells at Extended Voltage Range’. In: *ACS Applied Energy Materials* 5.2 (Feb. 2022), pp. 1378–1384. DOI: 10.1021/acsaem.1c03206.

[111] O. Breitenstein, J. Bauer, K. Bothe, D. Hinken, J. Müller, W. Kwapil, M. C. Schubert and W. Warta. ‘Can luminescence imaging replace lock-in thermography on solar cells?’ In: *IEEE Journal of Photovoltaics* 1.2 (Oct. 2011), pp. 159–167. DOI: 10.1109/JPHOTOV.2011.2169394.

[112] K. Bothe, K. Ramspeck, D. Hinken, C. Schinke, J. Schmidt, S. Herlufsen, R. Brendel, J. Bauer, J.-M. Wagner, N. Zakharov and O. Breitenstein. ‘Luminescence emission from forward- and reverse-biased multicrystalline silicon solar cells’. In: *Journal of Applied Physics* 106.10 (Nov. 2009), p. 104510. DOI: 10.1063/1.3256199.

[113] O. Breitenstein, J. Bauer, K. Bothe, W. Kwapil, D. Lausch, U. Rau, J. Schmidt, M. Schneemann, M. C. Schubert, J.-M. Wagner and W. Warta. ‘Understanding junction breakdown in multicrystalline solar cells’. In: *Journal of Applied Physics* 109.7 (Apr. 2011), p. 071101. DOI: 10.1063/1.3562200.

[114] O. Breitenstein, W. Warta and M. C. Schubert. *Lock-in Thermography: Basics and Use for Evaluating Electronic Devices and Materials*. Vol. 10. Springer Series in Advanced Microelectronics. Cham: Springer International Publishing, 2018. DOI: 10.1007/978-3-319-99825-1.

[115] J. H. Armstrong, S. Wiedeman and L. M. Woods. *Monolithically integrated diodes in thin-film photovoltaic devices*. 2004. URL: https://patents.google.com/patent/US6690041B2/en.

[116] G. Boschloo. ‘Can Alternative Module Design Help to Overcome Stability Problems of Perovskite Photovoltaics?’ In: *ACS Energy Letters* 8.2 (Feb. 2023), pp. 1147–1151. DOI: 10.1021/acsenergylett.2c02841.

[117] D. D. Smith, P. J. Cousins, A. Masad, S. Westerberg, M. Defensor, R. Ilaw, T. Dennis, R. Daquin, N. Bergstrom, A. Leygo, X. Zhu, B. Meyers, B. Bourne, M. Shields and D. Rose. ‘SunPower’s Maxeon Gen III solar cell: High efficiency and energy yield’. In: *2013 IEEE 39th Photovoltaic Specialists Conference (PVSC)*. Tampa, FL, USA: IEEE, June 2013, pp. 0908–0913. DOI: 10.1109/PVSC.2013.6744291.

A

Additional data

A.1. Preliminary results on the breakdown mechanism

As described in Chapter 2, the temperature-dependence of the breakdown voltage is a property that is often connected to the breakdown mechanism. For ’traditional’ semiconductor pn-junctions, it is considered the distinguishing criterion that separates avalanche breakdown and tunneling breakdown.

The literature data available on the temperature-dependence of the reverse bias breakdown of perovskite solar cells is sparse. Therefore, a simple experiment was performed to test the relationship of the V_{BD} with the temperature. While RB-JV measurements are regularly performed, the temperature is decreased and then, when a minimum was reached, increased again. The results are depicted in Figure A.1. They show that the effect of temperature on the breakdown mechanism is not as simple as assumed. There seem to be at least two different effects present.

Additionally, the impact of the scan rate was investigated. For that purpose, RB-JV measurements with various different voltage scan rates were performed, starting at very large scan rates. The results are depicted in Figure A.2: The results can be separated into two groups with different behavior. It is not clear where this difference stems from as the samples are technically alike.

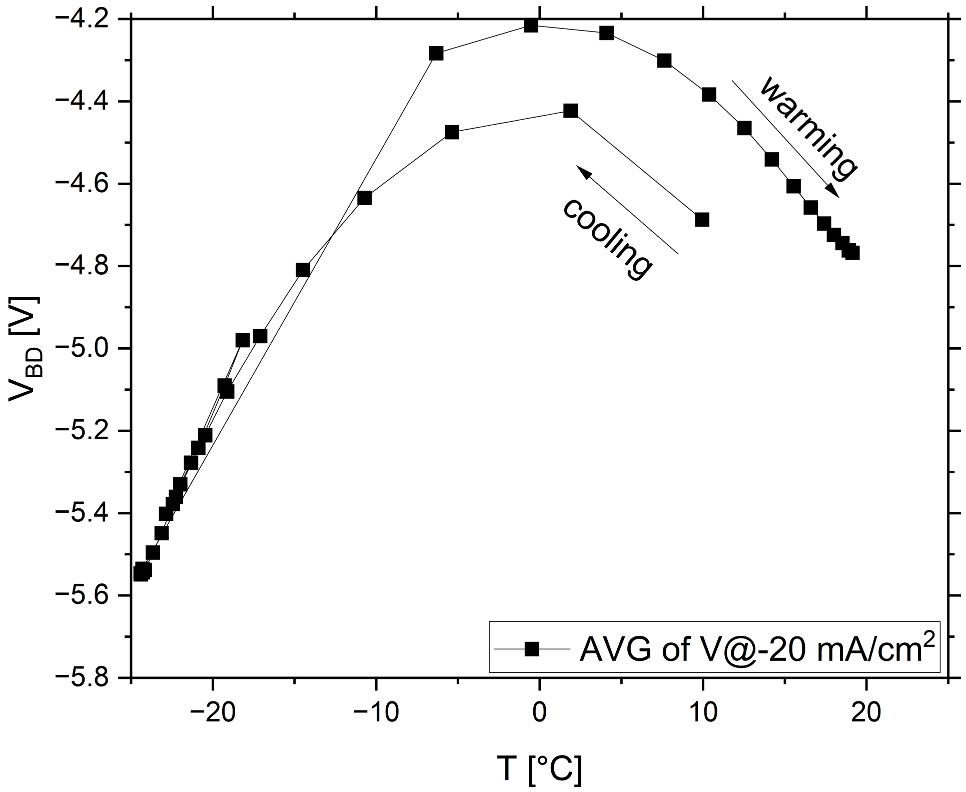

Figure A.1. Results of an experiment to investigate the temperature-dependence of the breakdown voltage of perovskite solar cells. The temperature of a solar cell was decreased and then increased again while RB-JV measurements were performed. From the measurement results, breakdown voltages were determined. Here, the mean of the voltages at $J_{BD} = -20.0\,\mathrm{mA\,cm^{-2}}$ of the reverse and the forward sweep is used as V_{BD}.

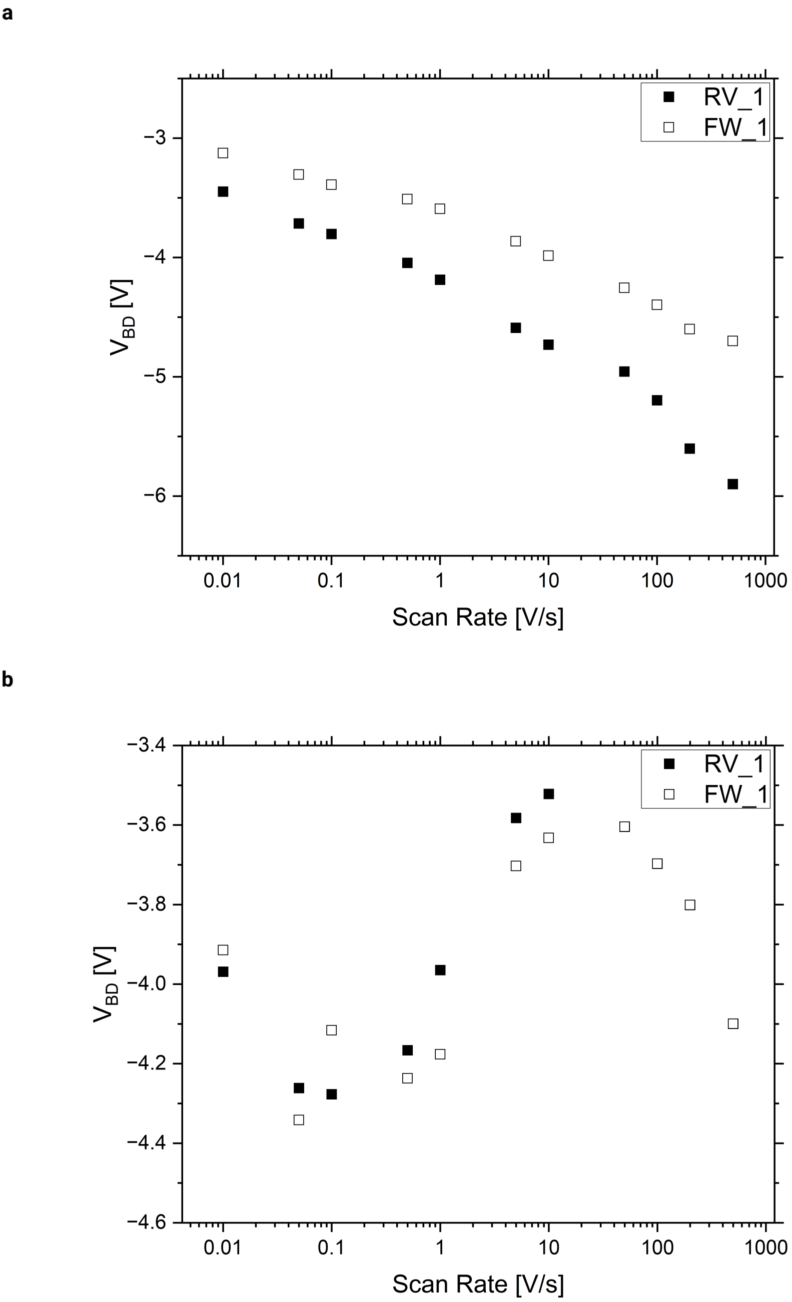

Figure A.2. The breakdown voltage (V_{BD}) is dependent on the voltage scan rate. Two different relationships have been found which are depicted in (a) and (b).

B

Supporting Information for determining the breakdown voltage V_{BD}

B.1. Tables

In Table B.1, the detailed measurement parameters of the RB-JV measurements of the curves in Figure 4.1 of the main text are displayed.

Parameter	Data of Figure 1a	Data of Figure 1b
Upper Limit	$1.0\,\mathrm{V}$	$1.0\,\mathrm{V}$
Lower Limit	$-J_{sc}$	$-15.0\,\mathrm{V}$
Scan Rate	$0.1\,\mathrm{Vs}^{-1}$	$0.1\,\mathrm{Vs}^{-1}$
Hysteresis	RV and FW sweep	RV sweep
Temperature	room temperature (uncontrolled)	room temperature (uncontrolled)
Illumination	darkness	darkness
Atmosphere	ambient air	ambient air

Table B.1. Measurement parameters used during the RB-JV measurements whose results are shown Figure 4.1 in the main text.

In Table B.2, the detailed measurement parameters of the (standard) JV measurements of the curves in Figure 4.1 of the main text are displayed.

Parameter	Data of Figure 1a (inset)	Data of Figure 1b (inset)
Upper Limit	$1.2\,\mathrm{V}$	$1.2\,\mathrm{V}$
Lower Limit	$-0.2\,\mathrm{V}$	$-0.2\,\mathrm{V}$
Scan Rate	$\approx 0.1\,\mathrm{Vs}^{-1}$	$\approx 0.1\,\mathrm{Vs}^{-1}$
Hysteresis	RV and FW sweep	RV and FW sweep
Temperature	cooling via dry air	cooling via dry air
Illumination	1 sun @ AM1.5G	1 sun @ AM1.5G
Atmosphere	ambient air	ambient air

Table B.2. Measurement parameters used during the (standard) JV measurements whose results are shown Figure 4.1 (insets) in the main text.

In Table B.3, the detailed measurement parameters of the three representative RB-JV measurements in Figure 4.4, 4.5, and 4.6 of the main text are displayed.

Parameter	Ideal	with Peak	with Kink
Upper Limit	$1.0\,\mathrm{V}$	$1.0\,\mathrm{V}$	$1.0\,\mathrm{V}$
Lower Limit	$-J_{sc}$	$-J_{sc}$	$-J_{sc}$
Scan Rate	$1.0\,\mathrm{Vs}^{-1}$	$1.0\,\mathrm{Vs}^{-1}$	$0.1\,\mathrm{Vs}^{-1}$
Hysteresis	RV+FW	RV+FW	RV+FW
Temperature	RT (uncontrolled)	RT (uncontrolled)	RT (uncontrolled)
Illumination	darkness	darkness	$\approx 3.5\,\mathrm{mWcm}^{-2}$ (blue LED)
Atmosphere	ambient air	ambient air	ambient air
Notes	second RB-JV	second RB-JV	sixth RB-JV

Table B.3. Measurement parameters used during the RB-JV measurements whose results are shown Figure 4.4, 4.5, and 4.6 in the main text.

B.2. Figures

In Figure B.1, we show the imperfect result of fitting a RB-JV curve with a simple exponential function. This is an intermediate result of the process of determining the power-of-maximum-curvature (PoMC). The intermediate PoMC values are also marked. The fit function diverges slightly from the data in the region around the intermediate PoMC. That is the reason we chose the two-step procedure that is used to determine the final PoMC in the main text.

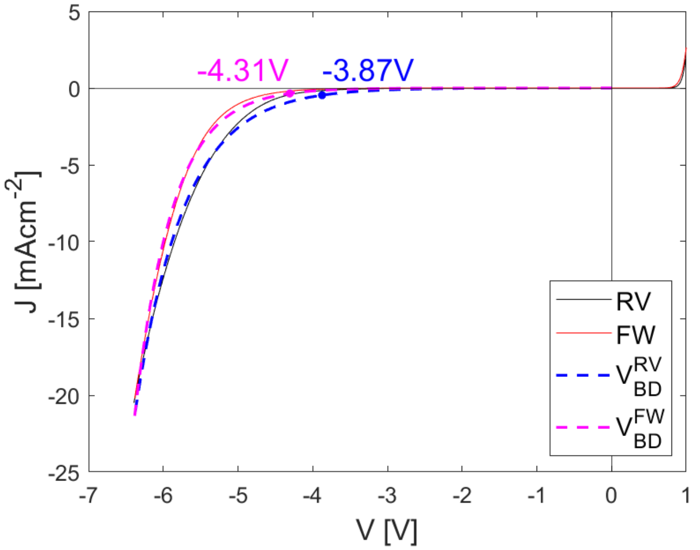

Figure B.1. A RB-JV measurement and the results of fitting the data with exponential functions. The intermediate PoMC values resulting from these fit functions are marked.

To demonstrate that the 'knee' of an exponential function does not describe a well-defined x-value, we show one exponential function ($f(x) = exp(100x)$) in Figure B.2a-c with different axes. It is clear that the x-value that seems to mark the 'knee' changes greatly from $x_{knee} \approx 6.5$ in a to $x_{knee} \approx 0.07$ in c.

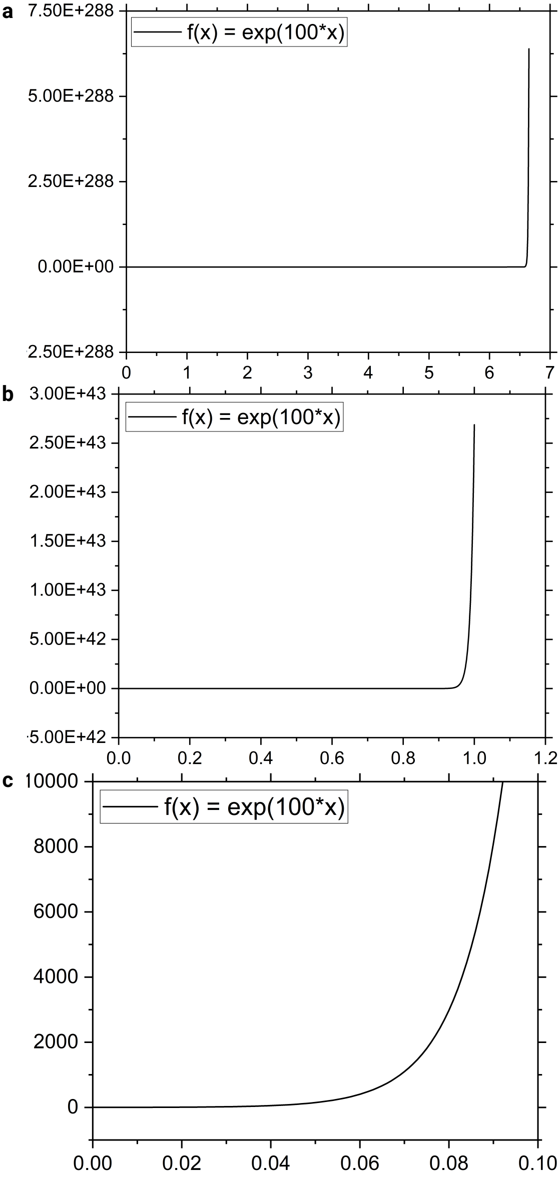

Figure B.2. One exponential function displayed in graphs with different axes.

In Figure B.3, we show the comparison of the breakdown voltages of 60 PSCs as determined by several different definitions. Here, the V_{BD}-values of three cells are colored to show how single data points change.

The colored data points show that a RB-JV curve that leads to a lower- or higher-than-average V_{BD} generally does so with all three definitions. Only the red data points show a different behavior. They show very small V_{BD} values, even outliers, at $-1.0\,\mathrm{mAcm^{-2}}$ in Figure B.3a. At the two other variants of the definitions using a fixed current density, that is not the case. That implies that their low-RB-current density regime is different from other solar cells of that batch, but their high-RB-current density regime is not. When looking at the results of the Linear Fit method and the PoMC method, the red data points do not stand out. That implies that these analysis methods are not significantly influenced by unusual behavior in the low-RB-current density regime.

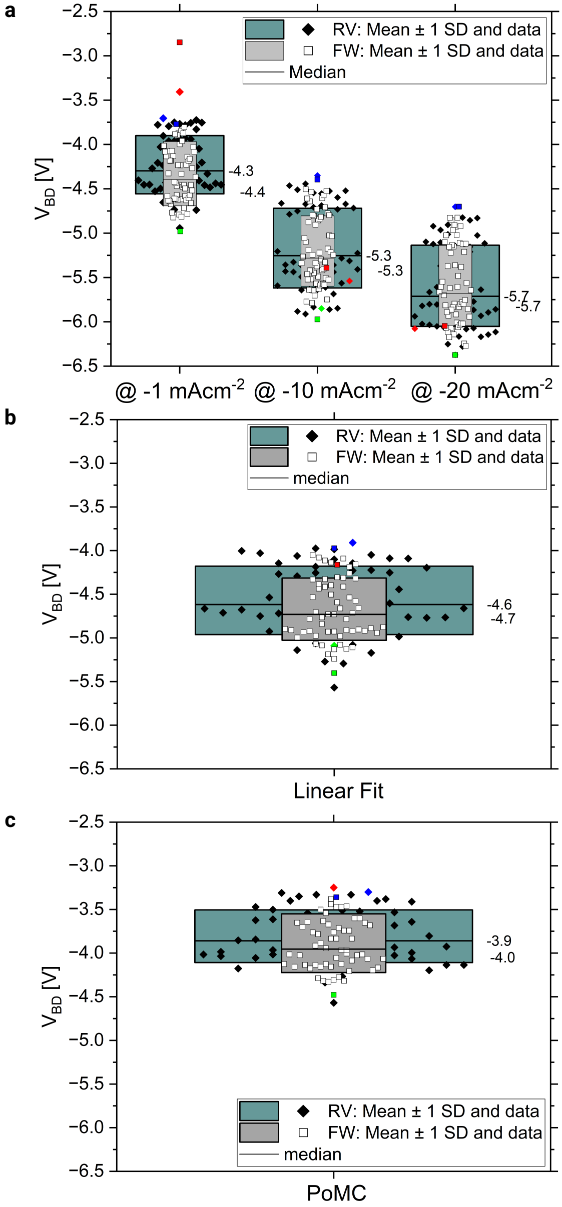

Figure B.3. The breakdown voltages of a batch of 60 PSCs, determined using five different definitions are compared: Three version based on fixed current densities (a), the linear fit method (b), and the method using the PoMC (c). The V_{BD}-values of three cells are colored in red, green and blue in all three sub-figures. The detailed measurement parameters are listed in the main text in Table 4.4.

B.3. Notes

B.3.1. Note 1

Detailed description of the procedure for determining the PoMC:

- Preparation
  - import data
  - calculate current density
  - split curves into reverse and forward sweep
  - remove positive voltage-regime
- Intermediate Step
  - first fitting with exponential fit function
  - calculate first and second derivative
  - calculate curvature
  - find intermediate point of maximum curvature
  - define region around intermediate PoMC
- Final Step
  - second fitting with exponential function (only region around intermediate PoMC)
  - calculate first and second derivative
  - calculate curvature
  - find point of maximum curvature
- Output

B.3.2. Note 2

Fabrication of the batch of perovskite solar cells whose RB-JV measurements were used to compare different methods for determining a V_{BD} in Figure 4.7 of the main text.

Glass substrates with already-patterned (indium-tin oxide) ITO were cleaned by scrubbing with soap water and sonicating in soap water, in de-ionized water, and in 2-propanol (IPA). After a 30-minutes long UV/Ozone treatment, they were brought into a nitrogen-filled glovebox for the further deposition. There, a PTAA (poly-triarylamine) layer was deposited by spin-coating a $2.0\,\mathrm{mg\,mL^{-1}}$ PTAA solution in toluene at 5000 rpm, $3000\,\mathrm{rpm\,s^{-1}}$, for 35 s. Afterwards, the substrates were put onto a hotplate at $100\,°\mathrm{C}$ for 10 minutes for annealing. After a period of 20 minutes of purging the glovebox atmosphere, the perovskite layer was deposited. To that end, a 1.4 M solution of a triple cation, double halide perovskite ($Cs_{0.05}FA_{0.8}MA_{0.15}PbI_{2.7}Br_{0.3}$) in DMF:NMP (9:1) was spin-coated. FA stands for formamidinium, MA for methylammonium, DMF for dimethyl-formamide, and NMP for N-methyl-2-pyrrolidone. The spin-coating settings were 2000 rpm, $200\,\mathrm{rpm\,s^{-1}}$, for $10\,\mathrm{s}$ and then 5000 rpm, $2000\,\mathrm{rpm\,s^{-1}}$ for $30\,\mathrm{s}$. The solution was dropped $5\,\mathrm{s}$ after starting the spinning. $20\,\mathrm{s}$ after the start, a nitrogen pistol at a height of $4\,\mathrm{cm}$ from the substrate was used for gas-quenching. The perovskite layer was annealed immediately after deposition by placing the substrate on a hotplate at $130\,°\mathrm{C}$ for 10 minutes. On the perovskite, C_{60} was deposited via thermal evaporation, a SnO_2-layer (tin-oxide) was added via sALD (spatial atomic layer deposition). After removing the material at the edges of the substrate with a tape, the top electrode was deposited by sputtering ITO. The overlap of bottom and top ITO defined the cell area to be $0.20\,\mathrm{cm^2}$. To improve current collection, gold fingers were evaporated on top.

PTAA was bought from Solaris, PbI_2 from Thermo Fisher Scientific, FAI from Greatcell Solar Materials, $PbBr_2$ from TCI, MABr from Dyenamo, and CsI from Thermo Fisher Scientific.

C

Supporting Information for the impact of the current

C.1. Details about fabrication and layer stack

The layer stack on the glass substrate is listed in Table C.1 with the approximate layer thicknesses. The cell area is $0.16\,\mathrm{cm}^2$. The order of deposition is from the top to the bottom of the table. ITO stands for indium-tin oxide and PTAA for poly(triaryl amine). sALD stands for spatial atomic layer deposition.

Table C.1. The layer stack of the perovskite solar cells used as samples in this work.

Layer material	Thickness [nm]	Deposition process
ITO	180	sputtering
PTAA	10	spin coating
Perovskite	600	spin coating
C_{60}	20	evaporation
SnO_2	45	sALD
ITO	180	sputtering

Glass substrates (3 cm x 3 cm) with patterned ITO are cleaned with soap water, de-ionized water and isopropanol, respectively, by hand and by sonication. After the last cleaning step, they are treated in a UV/ozone oven for 30 min. After transport into an N_2-filled glovebox, a PTAA solution (SigmaAldrich, $2.0\,\mathrm{mgmL^{-1}}$ in Toluene) is deposited via spin-coating (5000 rpm, $3000\,\mathrm{rpms^{-1}}$, 35 s). The samples are annealed for 10 min on a 100 °C hotplate.

A 1.4 M perovskite solution ($Cs_{0.05}MA_{0.15}FA_{0.8}PbI_{2.7}Br_{0.3}$), prepared from PbI_2 (Alfa Aesar), $PbBr_2$ (SigmaAldrich), MABr (greatcell), FAI (TCI) and CsI (SigmaAldrich) in DMF/NMP (9:1), is spin-coated dynamically (first 2000 rpm, $200\,\mathrm{rpms^{-1}}$ for 10 s, then 5000 rpm, $2000\,\mathrm{rpms^{-1}}$ for 30 s) with gas-quenching after 15 s. MA stands for methylammonium and FA for formamidinium. The samples are then placed on a hotplate (130 °C) for 10 min.

A C_{60}-layer is added via evaporation, a SnO_2-layer via spatial ALD and the patterned ITO electrode on top via sputtering. Gold fingers at the edge of the cell areas are deposited via evaporation. The bottom ITO electrode is revealed by removing all layers with a cotton bud and a DMF:chlorobenzene solution (1:6). Lastly, silver paste is applied to the contacting areas at the edges of the glass substrate.

Four cells are fabricated on one substrate. The cells were not packaged.

C.2. Detailed information about the experimental procedure

Every cell passed through the same experimental procedure that consisted of a first characterization step, the degradation step, followed by a second characterization step. Each characterization step included (illuminated) IV measurements, dark IV measurements, dark IV measurements with extended voltage range, and maximum-power-point-tracking. During the degradation step, a constant reverse bias was applied in the dark and the current measured. All measurements were performed in air and at room temperature. During light IV measurements and MPPT, dry air was blown over the cells for cooling. Detailed information is collected in Table C.2.

Table C.2. Detailed information about the measurements of this work.

Measurement	**Measurement tool**	**Additional information:**
IV measurement	Dual light source simulator (WACOM, AM1.5G), Keithley 2400 source meter, illumination mask 0.09 cm^2	forward/reverse sweep: [1.2 V;-0.5 V], step: 0.02 V, scan rate: 0.1 V/s
Dark IV measurement (DIV)	Keithley 2400 source meter	forward/reverse sweep: [1.2 V;-0.5 V], step: 0.02 V, scan rate: 0.1 V/s
Extended dark IV measurement (DIV$_{ext}$)	Autolab PGSTAT30, NOVA 2.1.4	forward/reverse sweep: [1 V;-8 V] with current cut-off at first at 1.75 mA then at 1 mA, step: 0.01 V, scan rate: 0.2 V/s
Maximum-power-point-tracking (MPPT)	Dual light source simulator (WACOM, AM1.5G), Keithley 2400 source meter, illumination mask 0.09 cm^2	Measurement frequency: 0.32 Hz
Degradation step/ reverse bias current measurement	Autolab PGSTAT30, NOVA 2.1.4	Measurement frequency: 4 Hz

C.3. Definition of metrics

We calculate the average reverse bias current density from the reverse bias current $I_{rev}(t)$ that we measure during a degradation step with the duration t_{deg}. A_{cell} is the cell area. Then, the average reverse bias current flowing through the cell is:

$$J_{rev,avg} = \frac{\int_0^t I_{rev}(t)dt}{A_{cell} \cdot t_{deg}} \tag{C.1}$$

We calculate a degradation rate from the PCEs before (PCE_{in}) and after (PCE_{fin}) degradation and the duration of the degradation step t_{deg}:

$$DR = (\frac{PCE_{in} - PCE_{fin}}{PCE_{in}})/t_{deg} \tag{C.2}$$

C.4. The spread of the breakdown voltage

In Figure C.1, the results of RB-JV measurements are shown. There, a significant spread of the V_{BD} is visible.

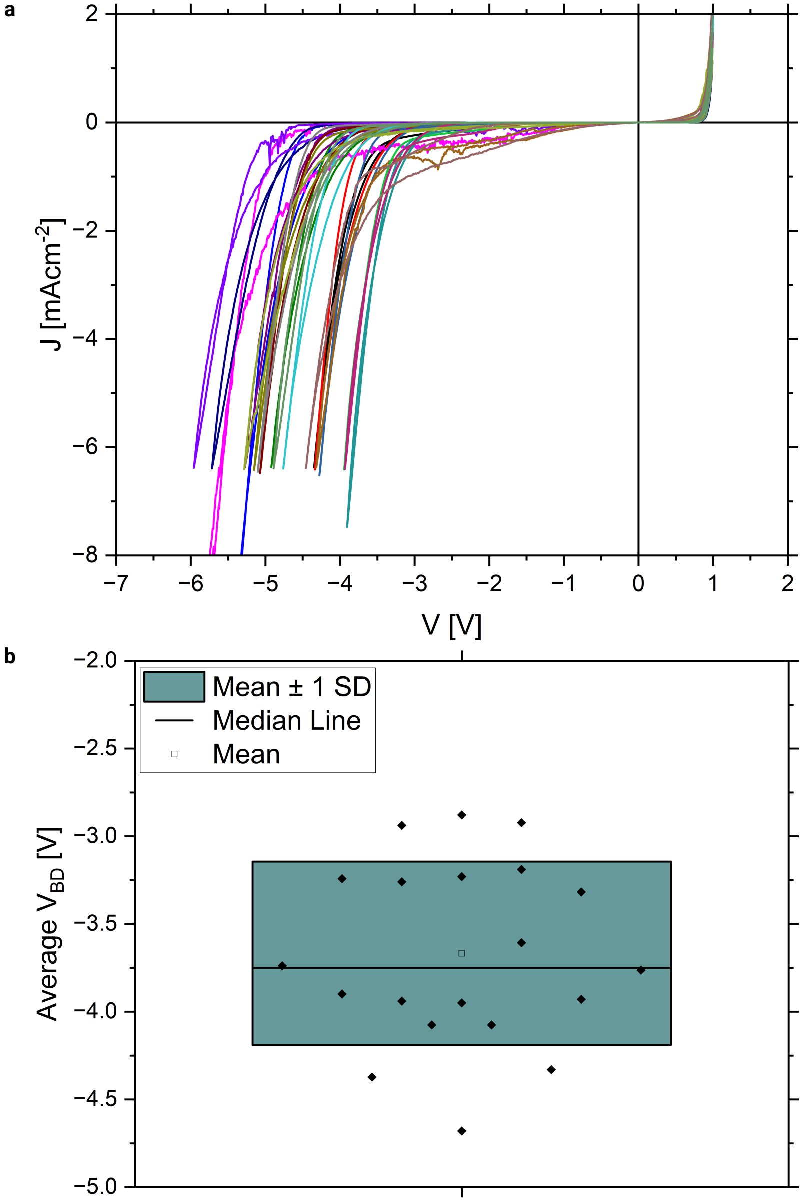

Figure C.1. The results of RB-JV measurements: the RB-JV curves are presented (a). The mean breakdown voltages are shown as box plot with average, median and standard deviation (SD) (b).

C.5. The relation between degradation rate and average current density

The observation that both degradation rate and average reverse bias current show a similar (exponential) dependence on the normalized voltage can be visualized by plotting DR directly against $J_{rev,avg}$. A similar dependence would then lead to a linear dependence of the two metrics on each other. This is visible in Figure C.2. However, due to the nature of the experiment, the data points are largely clustered at small values for $J_{rev,avg}$ where a significant spread is apparent.

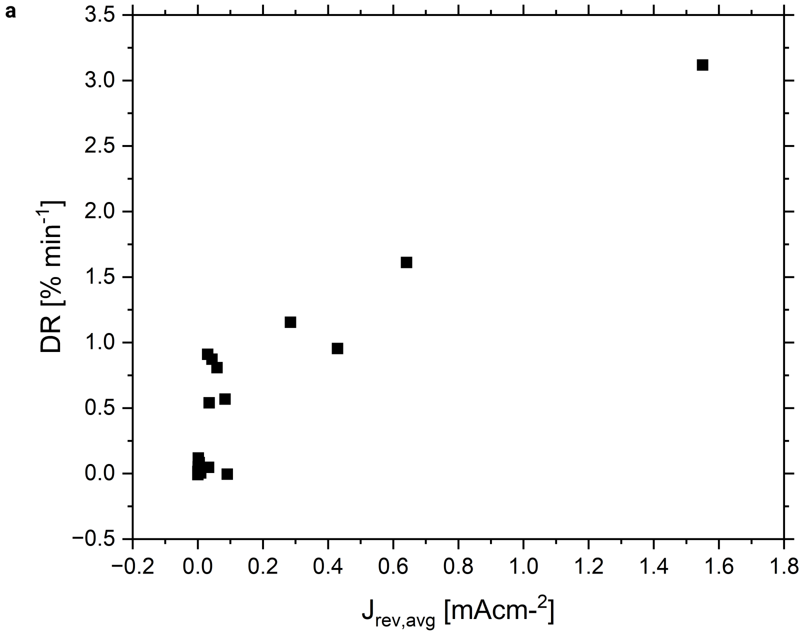

Figure C.2. The degradation rate (DR) is plotted against the average current density ($Jrev, avg$).

D

Supporting Information for the impact of low-intensity illumination

D.1. Device fabrication

Soda-Lime-Glass substrates (3 cm x 3 cm) with patterned indium-tin oxide (ITO) were cleaned by scrubbing with soap water and sonicating in soap water, de-ionized water, and isopropanol. Then, they received a UV/Ozone treatment for $30\,\mathrm{min}$ and were introduced into a nitrogen-filled glovebox.

There, the hole transport layer ($\sim 10\,\mathrm{nm}$) was deposited by spin coating a $2.0\,\mathrm{mg\,mL^{-1}}$ PTAA (SigmaAldrich) solution in toluene at $5000\,\mathrm{rpm}$, $3000\,\mathrm{rpm\,s^{-1}}$ for $35\,\mathrm{s}$. PTAA stands for 'poly(triaryl amine)'. This layer was annealed for $10\,\mathrm{min}$ at $100\,°\mathrm{C}$ on a hotplate.

Next, a 1.4 M solution of a triple cation, double halide perovskite ($\sim 600\,\mathrm{nm}$) $Cs_{0.05}FA_{0.8}MA_{0.15}PbI_{2.7}Br_{0.3}$ with 1 mol-percent RbCl in DMF/NMP (9:1) was deposited by spin coating, at first at $2000\,\mathrm{rpm}$, $200\,\mathrm{rpm\,s^{-1}}$ for $10\,\mathrm{s}$, then at $5000\,\mathrm{rpm}$, $2000\,\mathrm{rpm\,s^{-1}}$ for $30\,\mathrm{s}$ with gas-quenching after $15\,\mathrm{s}$. FA stands for formamidinium and MA for methylammonium. DMF stands for N,N-dimethylformamide and NMP for methylpyrrolidone.

The solution was prepared from PbI_2 from AlfaAesar, $PbBr_2$ from SigmaAldrich, MABr from GreatCell, FAI from TCI, and CsI from SigmaAldrich. This layer was annealed at $130\,°\mathrm{C}$ for $10\,\mathrm{min}$ on a hotplate.

The electron transport layer C_{60} ($\sim 20\,\mathrm{nm}$) was deposited via evaporation, a buffer layer SnO_2 ($\sim 50\,\mathrm{nm}$) via sALD (spatial atomic layer deposition) and the top electrode ITO ($\sim 180\,\mathrm{nm}$) via sputtering. ITO stands for indium-tin oxide.

The overlap of the orthogonal bottom and top (ITO) electrodes defines the cell area as $0.20\,\mathrm{cm^2}$. Lastly, the layers at the edge of the substrates were removed by a tape and a DMF:chlorobenzene (1:6) solution, and gold fingers and contact pads evaporated.

On each substrate, three functioning cells are fabricated.

D.2. Initial characterization

Before any experiments, the solar cells were characterized by JV measurements, dark JV measurements, maximum-power-point tracking (MPPT) and (initial) RB-JV measurements. For the JV measurements and the MPPT, a shading mask was used that defined the active area as $0.09\,\mathrm{cm^2}$. The light source was a dual-light source simulator (WACOM) and the source meter a Keithley 2400. The same source meter was also used for the dark JV-measurements. The voltage sweeps started at $1.2\,\mathrm{V}$, went to $-0.2\,\mathrm{V}$ and back with a step size of $0.02\,\mathrm{V}$ and a scan rate of $0.1\,\mathrm{V\,s^{-1}}$. The MPPT was performed at a measurement frequency of $0.32\,\mathrm{Hz}$. For cooling, dry air was blown over the substrates.

For the (initial) RB-JV measurements, an Autolab PGSTAT30 and the software NOVA 2.1.4 were used. These voltage sweeps began at $1.0\,\mathrm{V}$, and went to $-8.0\,\mathrm{V}$ or to a current cutoff at $-2.0\,\mathrm{mA}$, then back to $1.0\,\mathrm{V}$. The step size was $0.01\,\mathrm{V}$ and the scan rate $0.2\,\mathrm{V\,s^{-1}}$.

D.3. Experiments

Both the RB-JV measurements and the (quasi-)steady state experiments were performed using the Autolab PGSTAT30 and the software NOVA 2.1.4. As light sources, collimated LEDs of Thorlabs were used with the wavelengths 455 nm (blue), 530 nm (green), and 735 nm (far red).

D.4. Figures

After finishing fabrication, the solar cells are characterized by JV measurements under AM1.5G illumination. From the resulting JV curves (see Figure D.2b), solar cell parameters are extracted. These are presented in Figure D.1. We observe that the parameters from reverse (RV) and forward (FW) sweeps are nearly equal. Therefore, our cells can be considered hysteresis-free.

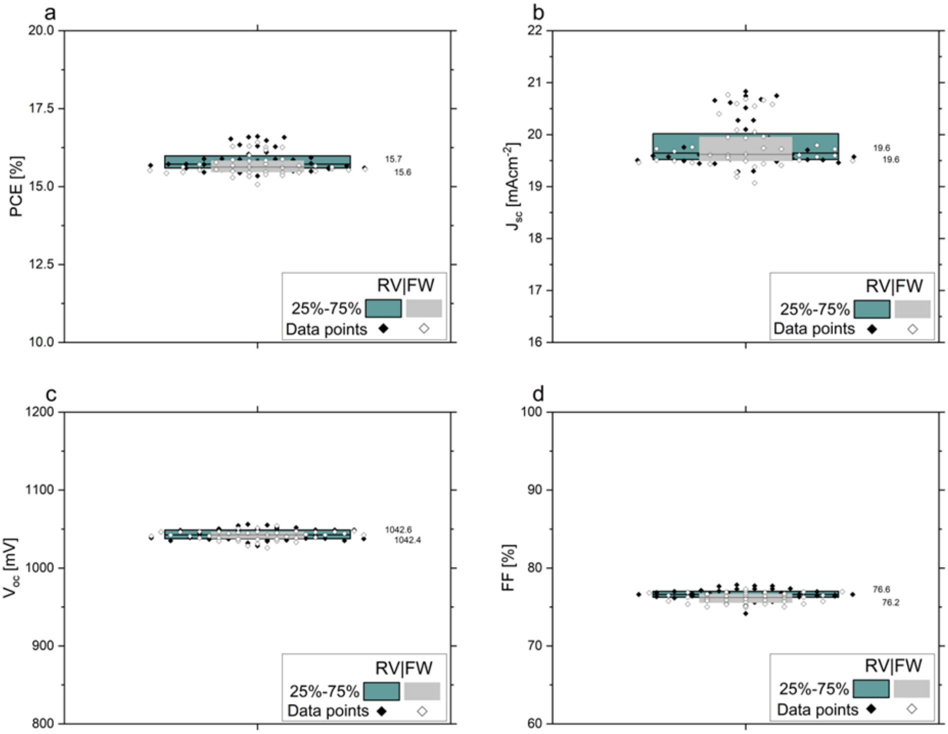

Figure D.1. Results of the initial characterization by JV measurements with a scan rate of about $0.15\,\mathrm{Vs}^{-1}$. Black diamonds correspond to the reverse sweep, empty diamonds to the forward sweep. The green box shows 25 percent to 75 percent of the data points of the reverse sweep, the gray box shows 25 percent to 75 percent of the data points of the forward sweep. To the right of the boxes, the median values are displayed. The power conversion efficiency (PCE) (a), the short circuit current density J_{SC} (b), the open-circuit voltage (V_{OC}) (c), and the fill factor (FF) (d).

On one cell per substrate, we performed maximum-power-point tracking (MPP) for 3 min after the JV measurements. The resulting PCE_{MPP}-curves are displayed in Figure D.2a. We see that their performance is stable under these conditions.

In Figure D.2b, the JV curves of are displayed that were used to calculate the solar cell parameters in Figure D.1.

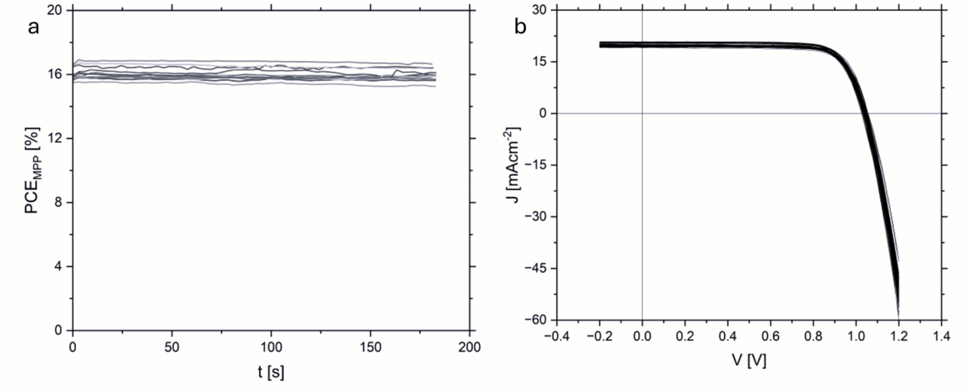

Figure D.2. Additional results of the initial characterization: Rresults of maximum-power-point tracking (MPPT) that was performed on the best cell of each substrate (a). They are rather constant. The JV sweeps that were used to calculate the solar cell parameters shown in Figure D.1 (b). There is no great spread visible.

As final step of the initial characterization, we performed reverse bias (RB-)JV measurements in the dark with a scan rate of $0.2\,\mathrm{Vs^{-1}}$. The results are displayed in Figure D.3 We observe a significant spread of the breakdown voltage. Otherwise, the curves look very similar to each other.

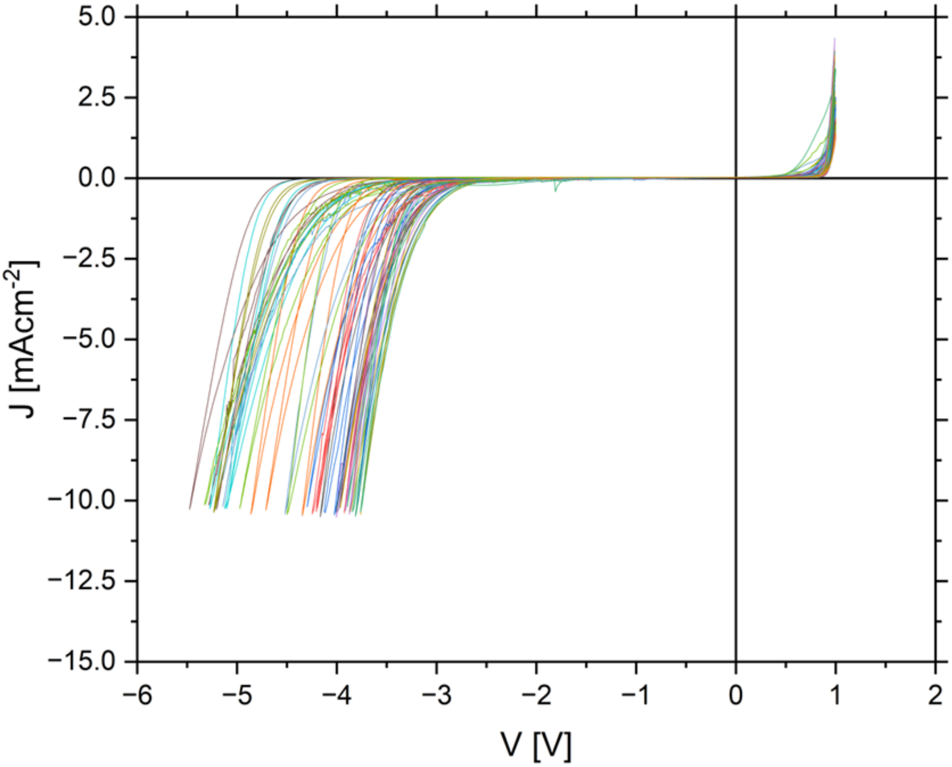

Figure D.3. Additional results of the initial characterization: Initial RB-JV measurements in the dark with a scan rate of $0.2\,\mathrm{Vs^{-1}}$. The voltages sweeps started at $V = 1.0\,\mathrm{V}$, went to a current density cutoff at $-10.0\,\mathrm{mAcm^{-2}}$ and then back up again.

Figure D.4 shows the results of the Voltage Sweep Experiment, i.e. the RB-JV sweeps that were performed alternatingly in the dark and under illumination with a blue LED for various scan rates. Reverse and forward sweeps are split up and shown in different sub-figures (e.g. a and b). As the figures need to be quite large to make the details discernible, Figure D.4 extends over more than one page.

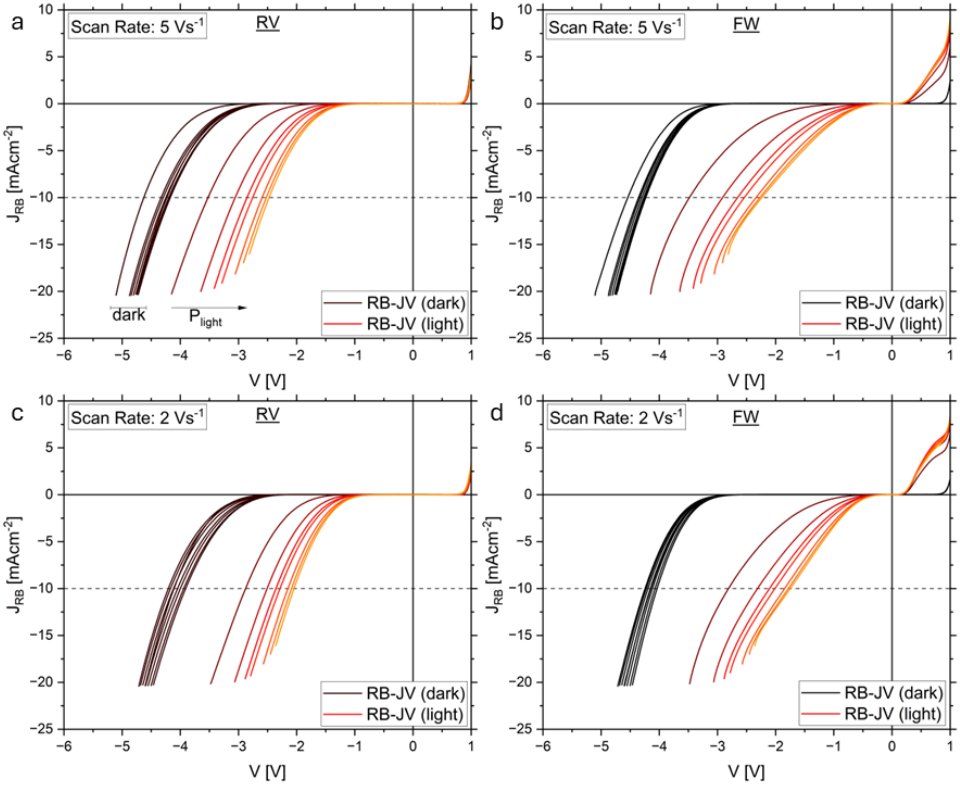

Figure D.4. Results of the Voltage Sweep Experiment: The black curves correspond to the RB-JV measurements in the dark, the red curves to the RB-JV measurements in various intensities of illumination (P_{light} and black arrow) after the correction for the photo-generated current. The lightness of the color corresponds to the the increasing intensity. The results for $5.0\,\mathrm{Vs}^{-1}$ (a, b) and for $2.0\,\mathrm{Vs}^{-1}$ (c, d).

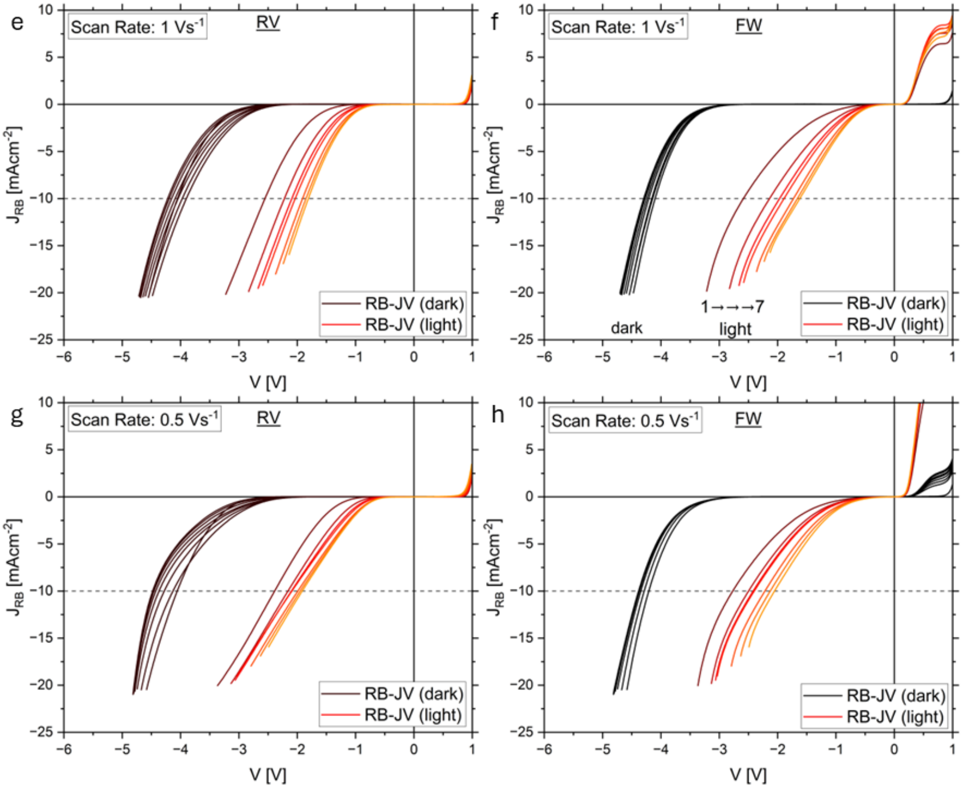

Figure D.4. Results of the Voltage Sweep Experiment: The black curves correspond to the RB-JV measurements in the dark, the red curves to the RB-JV measurements in various intensities of illumination (P_{light} and black arrow) after the correction for the photo-generated current. The lightness of the color corresponds to the the increasing intensity. The results for $1.0\,\mathrm{Vs}^{-1}$ (e, f) and for $0.5\,\mathrm{Vs}^{-1}$ (g, h).

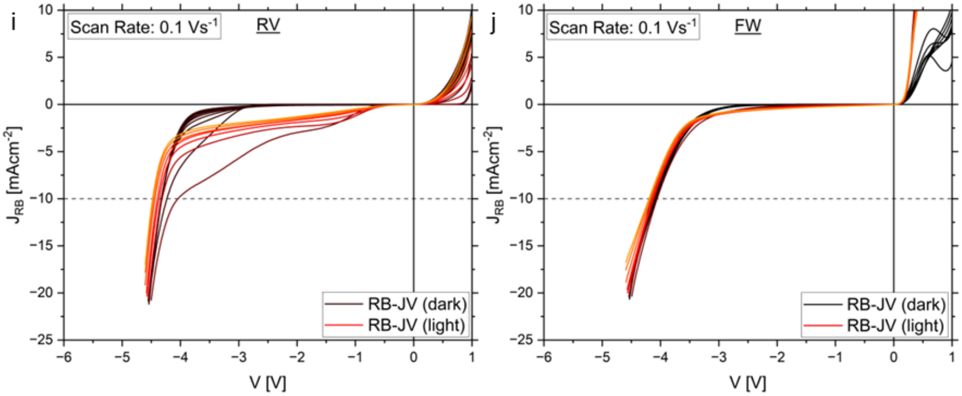

Figure D.4. Results of the Voltage Sweep Experiment: The black curves correspond to the RB-JV measurements in the dark, the red curves to the RB-JV measurements in various intensities of illumination (P_{light} and black arrow) after the correction for the photo-generated current. The lightness of the color corresponds to the the increasing intensity. The results for $0.1\,\mathrm{Vs^{-1}}$ (e, j).

In Figure D.5, the results from Figure D.4 are summarized by showing the breakdown voltage shift ΔV_{BD} as a function of the illumination intensity (expressed as P_{light}). The results from the RV sweeps (left) are separated from the results from the FW sweep (right). Both show qualitatively the same, however.

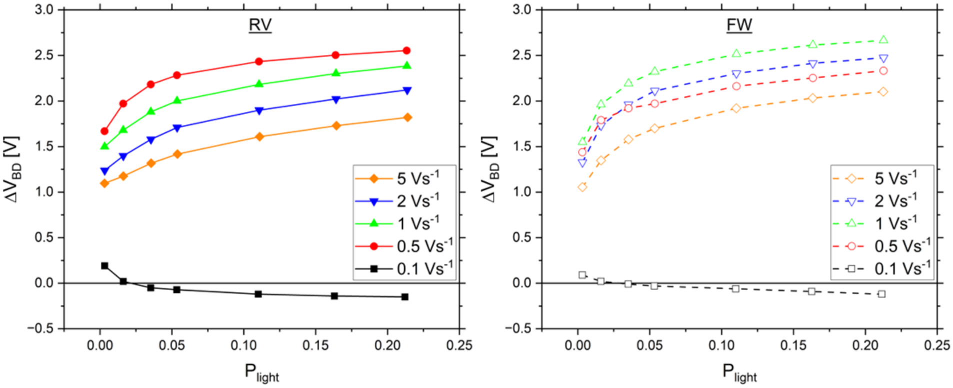

Figure D.5. The summary of the results shown in Figure D.4. The breakdown voltage shifts (the difference between V_{BD} in the dark and under illumination) are displayed as function of the illumination intensity, expressed as P_{light}. The different colors correspond to different voltage scan rates. The results from the RV sweeps (a), and the results from the FW sweeps (b).

Figure D.6 shows the summarized results of the Voltage Sweep Experiment on more solar cells, using a blue LED. The results of the RV sweeps (a, c) are separated from the results of the FW sweeps (b, d). The sub-figures of Figure D.6 are spread over more than one page.

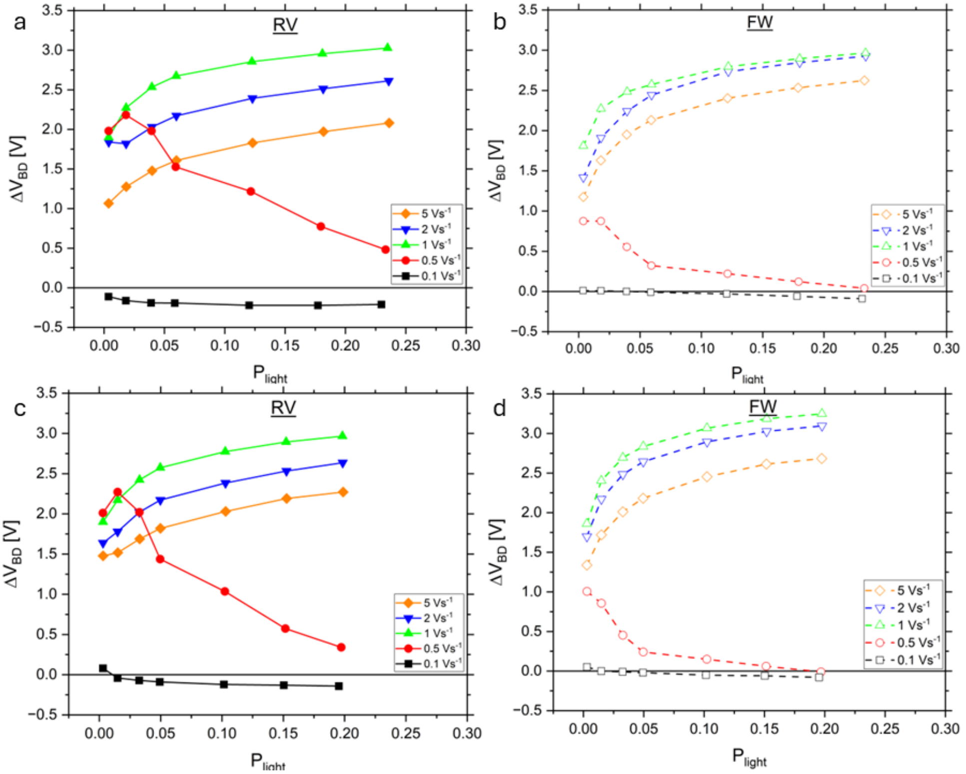

Figure D.6. Additional results from the Initial Experiment with a blue LED on more solar cells, summarized in ΔV_{BD} as function of the illumination intensity which is expressed as P_{light}. The results from the RV sweeps (a, c), the results from the FW sweeps (b, d).

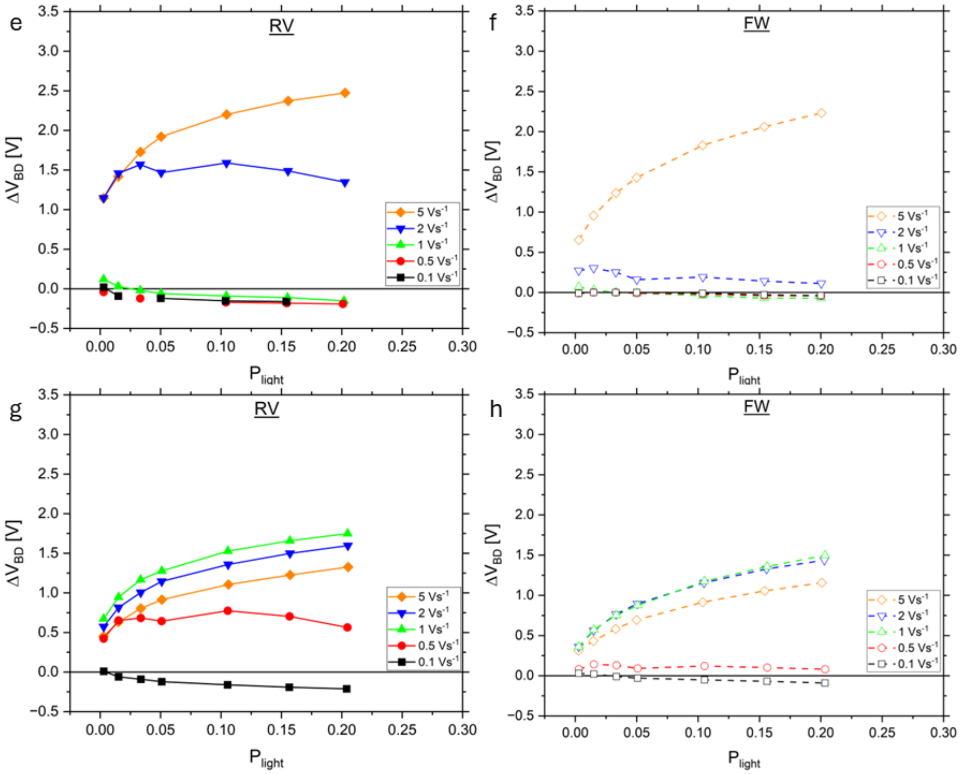

Figure D.6. Additional results from the Initial Experiment with a blue LED on more solar cells, summarized in ΔV_{BD} as function of the illumination intensity which is expressed as P_{light}. The results from the RV sweeps (a, c), and the results from the FW sweeps (b, d).

In Figure D.7, we show the breakdown voltages measured in the dark during an Voltage Sweep Experiment on *one cell*. We observe a spread at every scan rate. This spread is, however, never larger than 0.5 V. Also the impact of the scan rate on the measured V_{BD} is observed to be small.

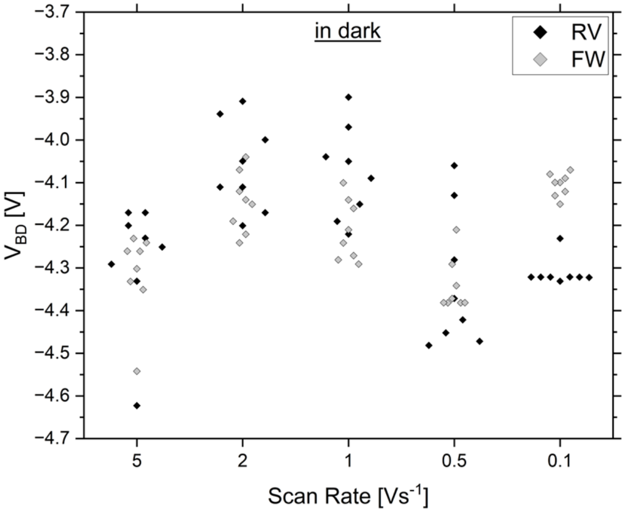

Figure D.7. The breakdown voltages (V_{BD}) as measured in the dark during successive RB-JV-measurements for various voltage scan rates on one cell are displayed. V_{BD} is defined as the voltage where $-10.0\ \text{mAcm}^{-2}$ flows. The black diamonds correspond to the reverse sweep, the gray diamonds to the forward sweep. The spread is never larger than 0.5 V.

Figure D.8 shows the summarized results from Figure D.5 as a semi-logarithmic plot. P_{light} is displayed logarithmically to make a possible logarithmic dependence more visible. On the left, the ΔV_{BD} of the RV sweeps and on the right the ΔV_{BD} of the FW sweeps are plotted.

In both cases and for all scan rates, we observe what might indeed be an apparent linear dependence. That can serve as evidence for a logarithmic dependence of ΔV_{BD} on the illumination intensity.

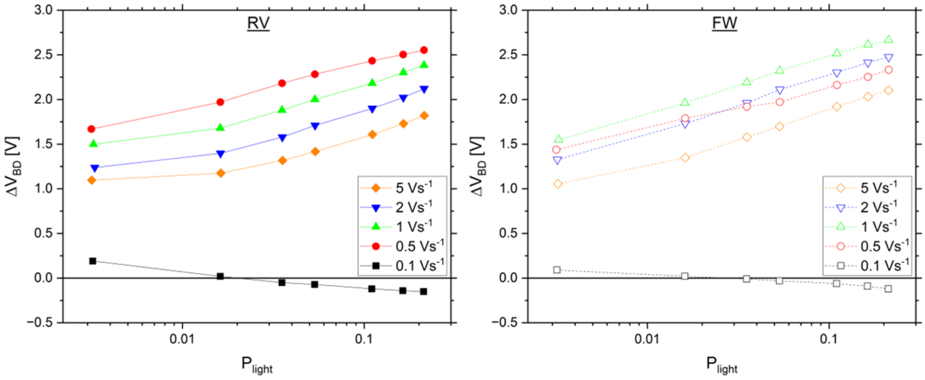

Figure D.8. The results displayed in Figure D.5 are plotted semi-logarithmically. The apparently linear behavior of ΔV_{BD} can serve as hint of a logarithmic dependence. The results from the RV sweeps (a), and from the FW sweeps (b).

In order to estimate the possible impact of a temperature increase due to illumination, we used an infrared (IR) camera to measure the increase of the surface temperature (ΔT). We used a illumination intensity of $P_{light} = 0.25$ and a blue LED. This intensity is among the highest that we used for the voltage sweep experiments and therefore is an extreme case. The results of that experiment are displayed in Figure D.9. All images can be found in the form of a movie in the data archive 4TU.ResearchData (see main text).

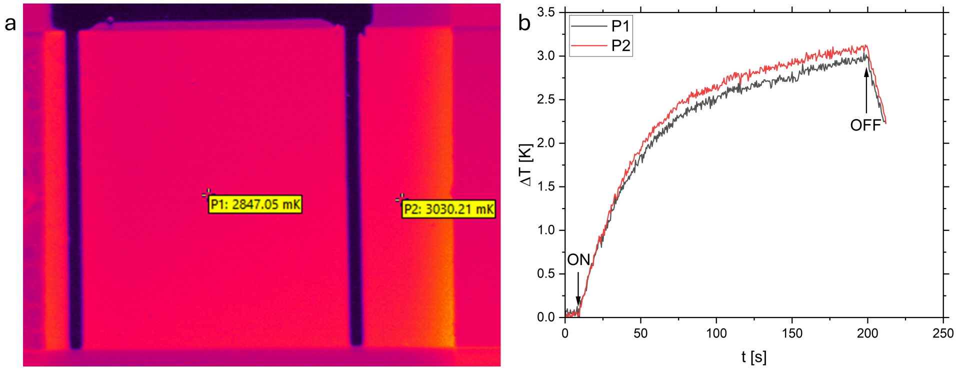

Figure D.9. The temperature increase due to blue illumination with $P_{light} = 0.25$. The cell area with the two points P1 and P2 (a). The temperature increase (ΔT) upon adding illumination for the locations of P1 and P2 (b). The moments where the LED was switched on and switched off are marked with "ON" and "OFF".

Figure D.10 shows how the charge flowing through a solar cell differs depending on the scan rate. The reverse sweeps with scan rate of $0.1\,\mathrm{Vs}^{-1}$ and with $1.0\,\mathrm{Vs}^{-1}$ are plotted against time t. The red areas show the integrals over time which correspond to the charge. The photo-generated current is subtracted by choosing a baseline for the integration.

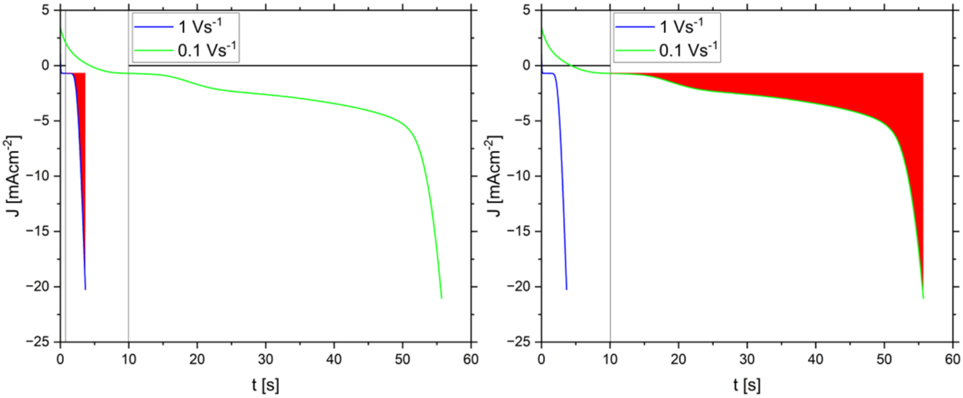

Figure D.10. The current density measured during the reverse voltage sweeps with scan rates of $1.0\,\mathrm{Vs}^{-1}$ (blue) and $0.1\,\mathrm{Vs}^{-1}$ (green) are plotted against time t. The red areas show the integral over time with the photo-generated current density subtracted.

In previous results, it seemed that the wavelength of the illumination (blue, green, or far red) does not have a significant impact on the reverse bias behavior. As we use only blue illumination for the (quasi-) steady state experiments, we want to show that the color does not make a difference here either. So, we used the far red LED as light source for a (quasi-) steady state experiment and present the results in Figure D.11.

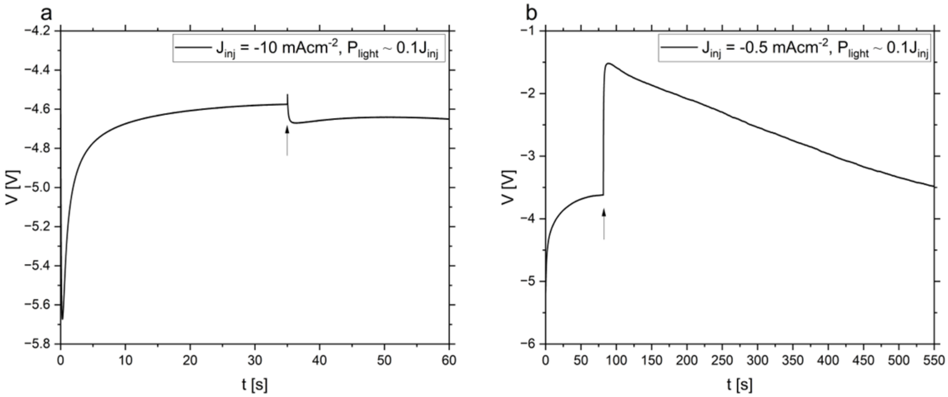

Figure D.11. Results of the (quasi-) steady state experiment using a far red LED. The results of injecting $J_{inj} = -10.0\,\mathrm{mAcm}^{-2}$ (a) and for injecting$J_{inj} = -0.5\,\mathrm{mAcm}^{-2}$ (b) are shown. P_{light} is always chosen so that $P_{light} \sim 0.1 J_{inj}$.

Figure D.12 shows additional results from the (quasi-)steady state experiment with $J_{inj} = -10.0\,\mathrm{mAcm^{-2}}$. P_{light} was chosen such that $P_{light} \sim 0.1 J_{inj}$. The light source was a blue LED. The red arrows show when the illumination was added. Generally, we observe a very limited impact of illumination on the voltage.

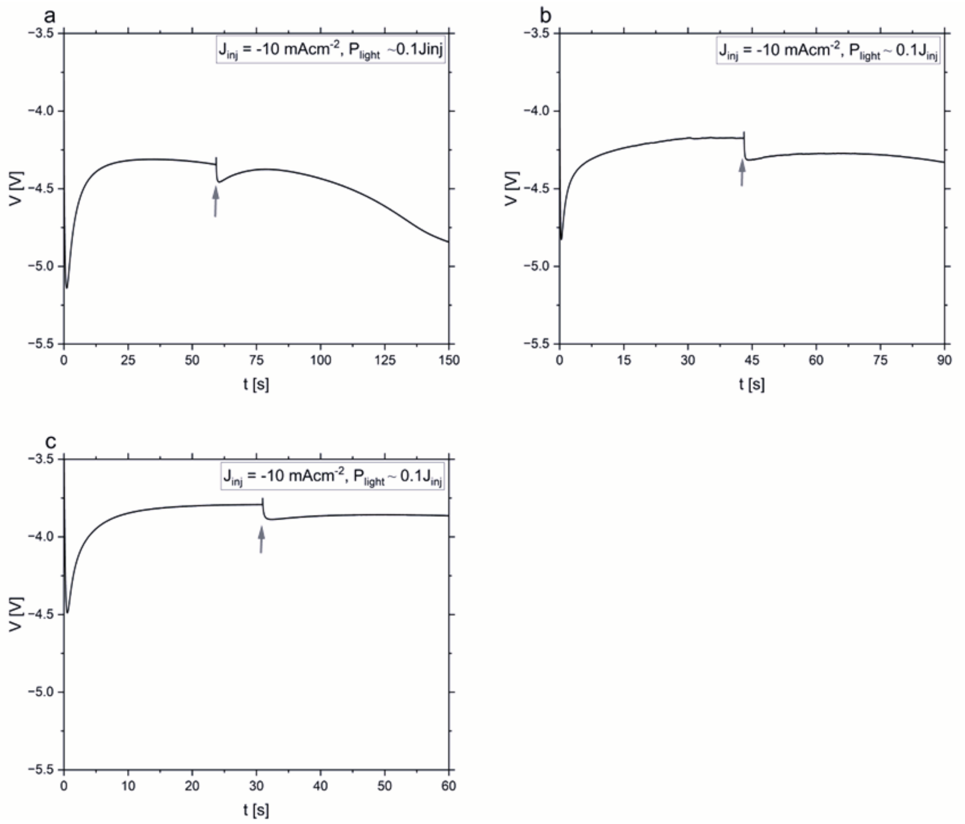

Figure D.12. Additional results of the quasi-steady state experiment on other solar cells. A current density of $-10.0\,\mathrm{mAcm^{-2}}$ was injected. The illumination intensity that was added after stabilization (at the red arrow) was equivalent to $0.1\,\mathrm{J_{inj}}$. As light source, a blue LED was used.

Figure D.13a,b show additional results from the (quasi-)steady state experiment with $J_{inj} = -1.0\,\mathrm{mAcm}^{-2}$. P_{light} was chosen such that $P_{light} \sim 0.1 J_{inj}$. The light source was a blue LED. The red arrows show when the illumination was added.

Figure D.13c shows a result from the (quasi-)steady state experiment with $J_{inj} = -0.5\,\mathrm{mAcm}^{-2}$. P_{light} was chosen such that $P_{light} \sim 0.1 J_{inj}$. This current density was chosen to better align to the pre-breakdown phenomenon in that cell.

Generally, we observe stronger effects of illumination on the voltage at this low current density level than at higher current density levels (as shown in Figure D.12).

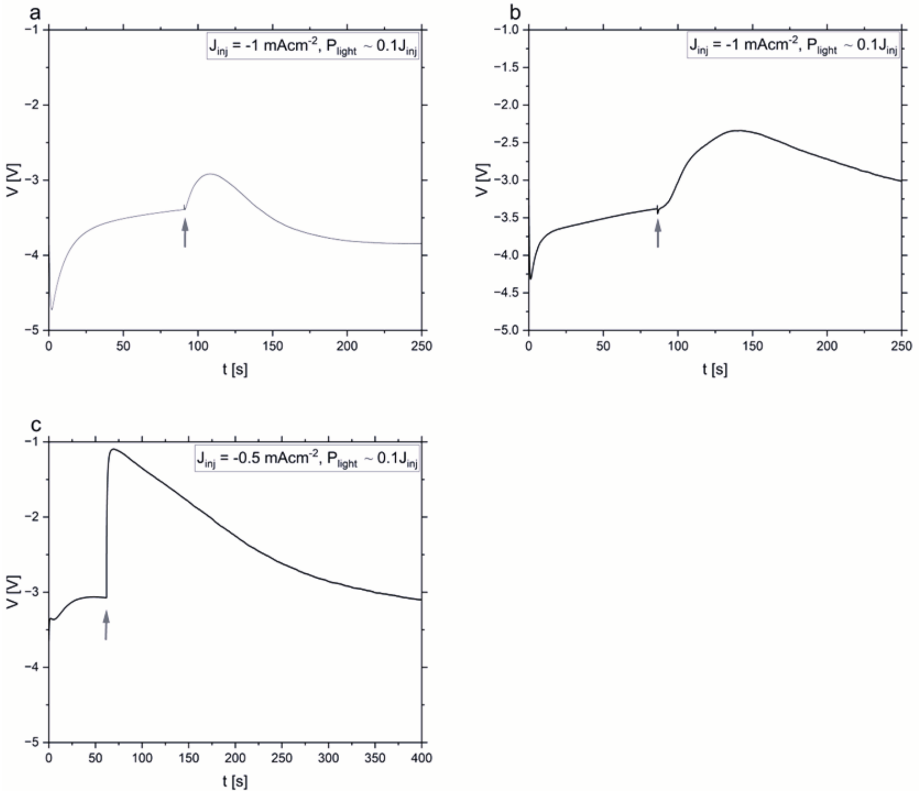

Figure D.13. Additional results of the quasi-steady state experiment on other solar cells. A current density of $-1.0\,\mathrm{mAcm}^{-2}$ (a, b) or $-0.5\,\mathrm{mAcm}^{-2}$ (c) was injected. The illumination intensity that was added after stabilization (at the red arrow) was equivalent to $0.1\,\mathrm{J_{inj}}$. As light source, a blue LED was used.

E

Supporting Information for luminescent imaging using ReBEL

Note 1: Fabrication process

In the following, we will describe the process of fabricating the perovskite solar cell that have been used in this study.

As substrates, we used 3 x 3 cm^2 soda-lime-glass substrate with a thickness of $1.1\,\mathrm{mm}$. The bottom indium-tin oxide (ITO) electrodes ($\approx 150\,\mathrm{nm}$) had already been deposited by full-area sputtering and photo-lithography. Our fabrication procedure begins with cleaning the substrates. To that end, we scrub the substrates (the top side, the edges, and the back side) in a soap solution. The substrates are sonicated for $10\,\mathrm{min}$ in the soap solution. After rinsing with deionized water, they are sonicated for $10\,\mathrm{min}$ in deionized water. Next, they are rinsed with isopropyl alcohol (IPA), and sonicated for $10\,\mathrm{min}$ in IPA. Finally, a UV/Ozone-cleaning step of $30\,\mathrm{min}$ follows.

The substrates are introduced into a glovebox with nitrogen atmosphere where the following spin coating steps follow. We start by depositing the hole transport layer (HTL) ($\approx 10\,\mathrm{nm}$) which is poly(triaryl amine) (PTAA) (Solaris Chem). To that end, we prepare a solution of PTAA in toluene ($2.0\,\mathrm{mg/mL}$). This solution is spin coated dynamically on the cleaned substrates with $5000\,\mathrm{rpm}$, $3000\,\mathrm{rpms}^{-1}$ for $35\,\mathrm{s}$. The solution is dropped about 5 s after the spinning started. Afterwards, all substrates are collected and annealed on a hotplate at $100°$ for $10\,\mathrm{min}$. After a break of $15\,\mathrm{min}$ to allow for the atmosphere in the glovebox to recover, we proceed with the perovskite layer ($\approx 600\,\mathrm{nm}$). The $1.4\,\mathrm{M}$ perovskite solution had been prepared one day prior. It is a triple-cation, double halide perovskite: $Cs_{0.05}FA_{0.8}MA_{0.15}PbI_{2.7}Br_{0.3}$, with FA being formamidinium, MA being methylammonium. This perovskite solution was created by solving PbI_2 (Thermo Fisher), $PbBr_2$ (TCI), MABr (Dyenamo), FAI (greatcell solar), CsI (Thermo Fisher) in DMF/NMP (9:1). DMF is N,N-dimethylformamide and NMP is methylpyrrolidone. This solution was shortly before deposition heated up to $90°$ for

20 min and allowed to cool down over 1 h. It was dynamically spin coated on the substrates with first 2000 rpm, 200 rpms^{-1}, 10 s, then 5000 rpm, 2000 rpms^{-1}, 30 s by dropping the solution 5 s after starting the spinning. 20 s after starting the spinning, a nitrogen pistol was used for gas-quenching for 15 s. The substrates were immediately after deposition put onto a hotplate at 130° for 10 min. Afterwards, the electron transport layer (ETL) C_{60} ($\approx$ 20 nm) was deposited via thermal evaporation. Then, a buffer layer of SnO_2 ($\approx$ 50 nm) was deposited via sALD. Finally, the top electrode of ITO ($\approx$ 180 nm) was deposited via sputtering. The overlap area of the orthogonal bottom and top ITO electrodes is the cell area of 0.20 cm^2. The bottom electrode contacts were revealed by removing all layers except the bottom ITO, using tape and a DMF:chlorobenzene (1:6) solution.

Note 2: Results of the initial characterization

The initial characterization consisted of JV measurements on every cell and maximum-power-point-tracking on one cell from each substrate. The results of the JV measurements are shown in Figure E.1.

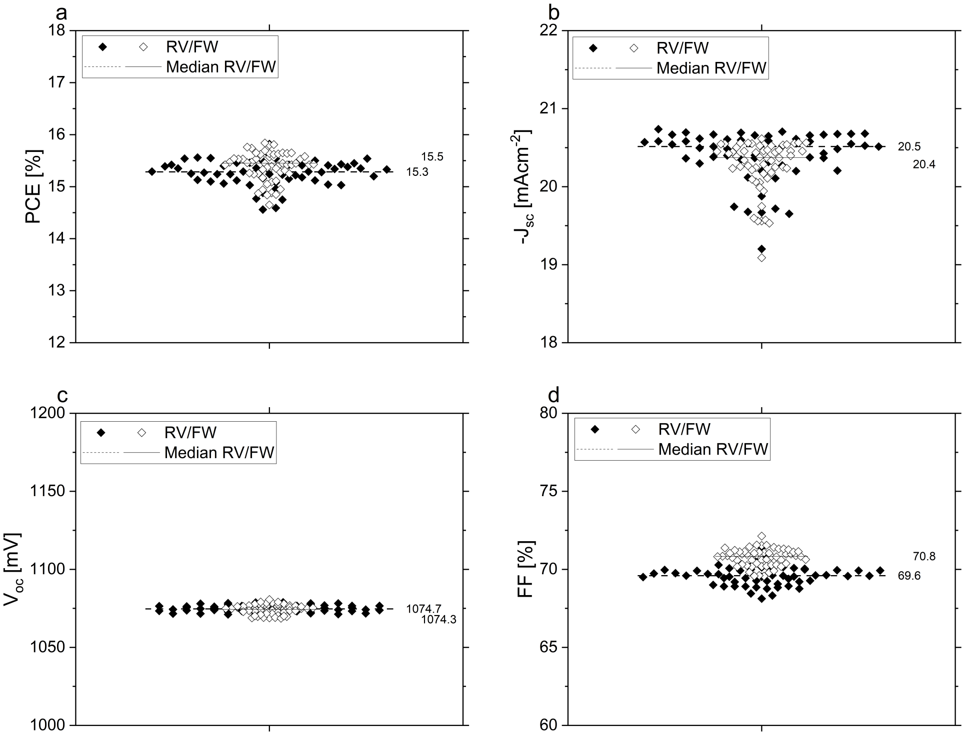

Figure E.1. The results of JV measurements with the PCE (a), the J_{SC} (b), the V_{OC} (c), and the FF (d).

In Figure E.2, the results of MPPT on one cell per substrate are displayed.

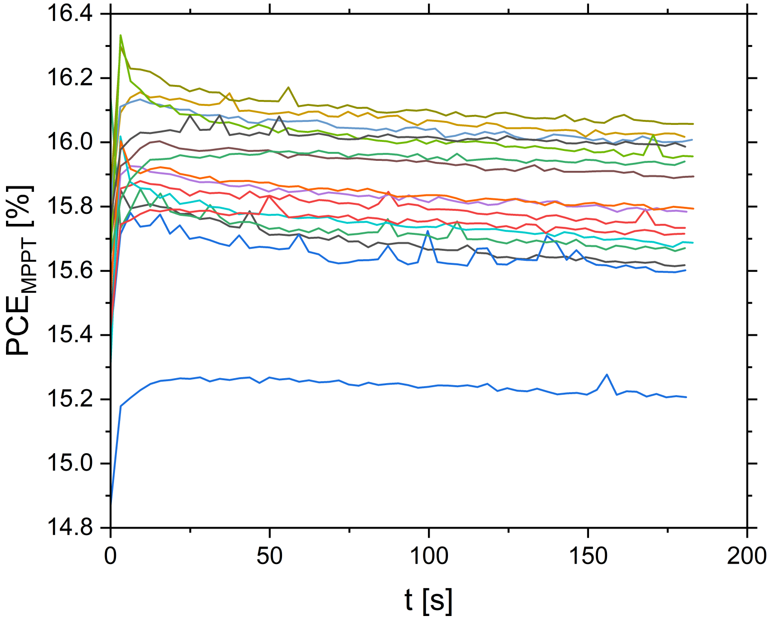

Figure E.2. The results of MPPT.

For ReBEL measurements, we chose cells that showed good efficiencies and did not show any significant spots or other irregularities in electroluminescence. These images can be found in the Supplementary Data.

Note 3: Stabilizing the reverse bias behavior by repeated ReBEL imaging

In the experiment "ReBEL sweep", we repeated the ReBEL image-taking at every RB current level four times. For the analysis, we have only used each fourth image. The reason was that the reverse bias behavior of a perovskite solar cells needs time to stabilize. This is shown in Figure E.3.

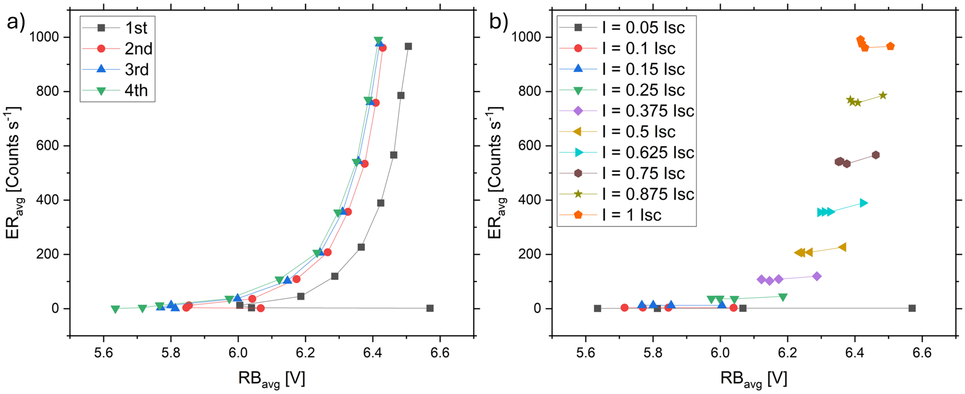

Figure E.3. The impact of repeating the ReBEL image taking: The results of the quantitative analysis on a location in the cell area. The data points are grouped (and colored) according to their affiliation to the first, second, third, or fourth repetition (a). The same data points are grouped according to the RB current level (b).

There, we present the ER_{avg}-values of a small, square location in the cell area. They are plotted linearly against RB_{avg}. Instead of showing only the values from all fourth images, the complete data set is displayed. Figure E.3a and b show the same data points; they are, however, sorted in different groups.

In Figure E.3a, all the first, second, third, and fourth images are grouped together, respectively. We see that all four series show largely the same behavior, but with a voltage shift. A significant voltage difference is visible between the first and the second series. The second and third series are already closer together, and no difference is visible between the third and the fourth series.

Special attention should be devoted to the data points with very small emission rates. There, the differences between the RB_{avg} is largest. Especially one data point at about 6.6 V and its following data points stand out. Despite injecting the same current, the mean RB decreases from about 6.6 V to about 5.6 V. Only the fourth data point of that series fits in with the data points from larger currents. That is the reason why we compare all the fourth images and reverse biases in the main text.

In Figure E.3b, the same data points are displayed, but in different groups. This time, they are sorted by RB current level. We see that the ER_{avg}-values within one group do not change significantly from the first to the fourth image. However, the RB_{avg} does change a lot. It is always significantly higher in the first image, and shifts during the following images to smaller RB_{avg}-values. We also see that especially the differences between the first and the second image is large. Only small additional changes occur between the second and the fourth image. Only at very small RB currents, these changes are even after four images still significant (see red circles, $I = 0.1 I_{sc}$).

This phenomenon is likely related to the slow movements of mobile ions towards the interfaces in the context of the breakdown mechanism. In order to correct for this meta-stable behavior, we have chosen to use only the fourth image of every RB current level. At the fourth repetition, the RB_{avg} seems to be stabilized for most RB current levels.

Note 4: Voltages during ReBEL measurement

During a ReBEL measurement, the voltage is not constant. For that reason, we calculate a mean voltage and use that in the following calculations as RB_{avg}. This is shown in Figure E.4.

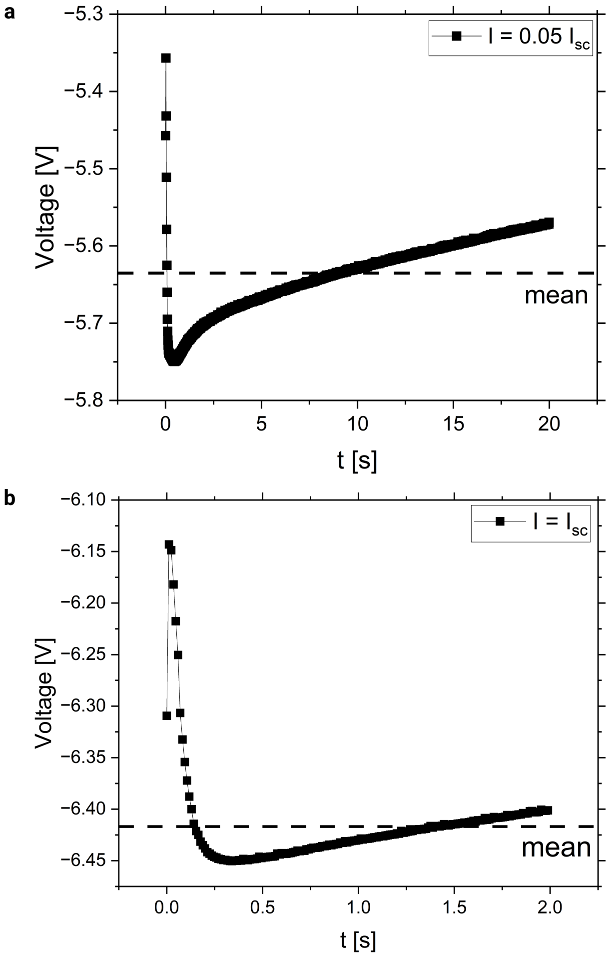

Figure E.4. The voltages logged during ReBEL measurements at a small current (a) and at a large current (b) with the mean voltage that is called RB_{avg} in the following.

Note 5: Spectrally-dependent EL and ReBEL measurements

We used a Renishaw Raman system to make use of its microscopy and its cooled camera. The sample was excited using a Keithley source/measure unit as current source. We measured from 630 nm to 850 nm. For the EL measurement, we accumulated signals for 10 s. For the ReBEL spectrum, we integrated over 100 s in total. The software Wire 3.4 by Renishaw was used to control the system.

In Figure E.5, the raw data, the baseline correction and the resulting spectra are displayed.

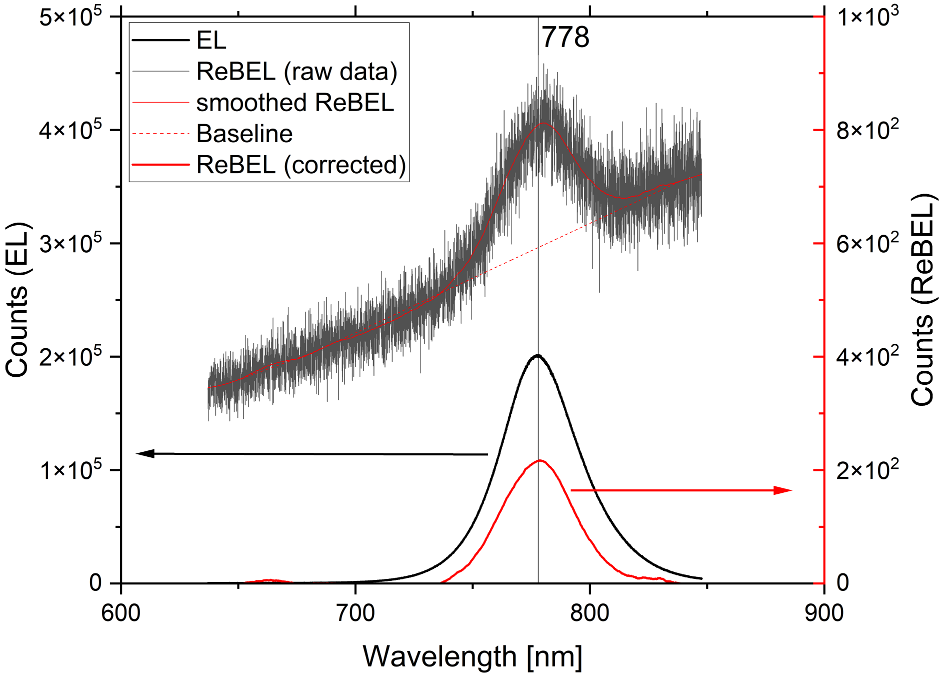

Figure E.5. The EL (thick, black line) and ReBEL (thick, red line) spectrum. The raw data of the ReBEL spectrum is displayed as gray, thin line, the smoothed curve as red, thin, straight line. The baseline that is used for the baseline correction is the red, dashed line.

Note 6: Bright edges in ssIR images

Here, we show that the bright edges, that are visible in some ssIR images, are measurement artifacts. To that end, Figure E.6 shows a series of ssIR images that are taken before the current injection started. The first image is used as baseline and therefore is completely dark. We observe that the edges are in some images barely visible, but in other images very bright or very dark. We conjecture that vibration of the camera, that is caused by the cooling Stirling motor, is responsible for these slight changes.

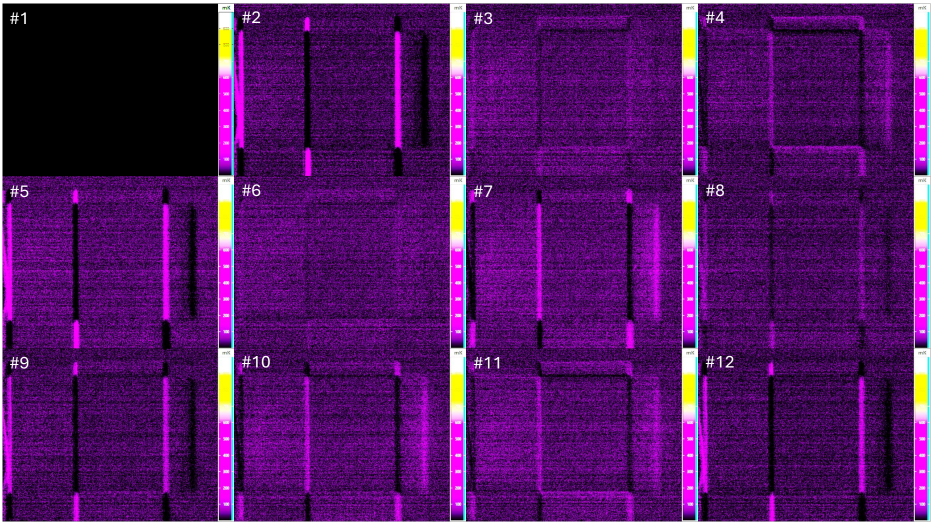

Figure E.6. A series of twelve ssIR images, taken before the current injection started. To make the cell area visible at this size, the brightness of the images was increased.

Note 7: Additional semi-quantitative analysis

In the main text, we showed the semi-quantitative analysis of one example area each for the cell area, the bright edges, and the bright spots. Here, we give additional examples.

Figure E.7 shows the semi-quantitative analysis of several small areas within the cell area. ReBEL images at a small and a large current show the locations of these small areas as blue squares. The graph in Figure E.7c shows the average emission rates and reveals two regimes in the cell area: At the data points with a red background, the cell area has not yet begun lighting up. At voltages with a green background, the cell area has become active. All the points in the cell area behave qualitatively similar. The differences seem to amount largely to a offset in the emission rate.

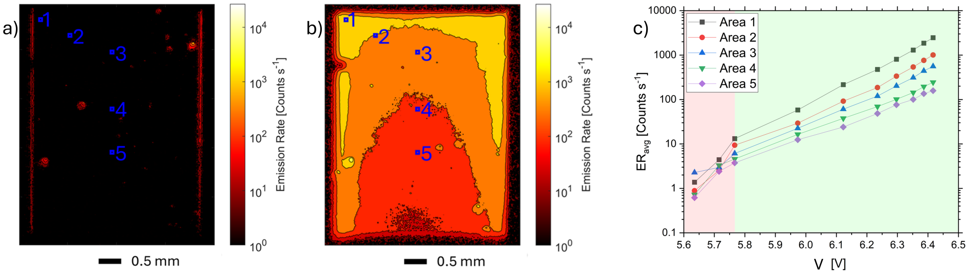

Figure E.7. Five different points in the cell area are marked for semi-quantitative analysis in ReBEL images at a small current (a) and a large current (b). The average emission rates are plotted semi-logarithmically against the reverse bias (c). The background colors mark different regimes.

Figure E.8 shows the semi-quantitative analysis of several different points along the cell edges. The positions of the investigated points are shown in ReBEL images at a small and a large current. Additionally, one point in the cell area is used as comparison. The graph displays the average emission rates semi-logarithmically plotted against the reverse bias. It clearly shows that all points at the edges behave the same way. At small voltages (red background), the edges are bright and turn brighter while the area is yet inactive. When the area begins to light up (green background), the emission rate of the edges saturates. At large reverse biases, the edges are not distinctly visible anymore in the ReBEL images. The emission rates at their former locations are 'pulled along' by the surrounding cell area.

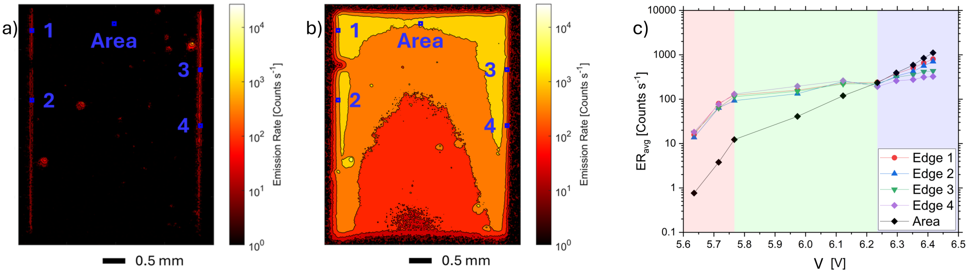

Figure E.8. Four different points at the cell edges are marked for semi-quantitative analysis in ReBEL images at a small current (a) and a large current (b). A point in the cell area is added as comparison. The average emission rates are plotted semi-logarithmically against the reverse bias (c). The background colors mark different regimes.

Figure E.9 shows the semi-quantitative analysis of several bright spots. Their location is shown in ReBEL images at a small and a large current. Additionally, one location in the cell area is used as comparison. The graph shows their average emission rates semi-logarithmically plotted against the reverse bias. It is clearly visible that several different behaviors are present among the bright spots. One commonality is, however, that their emission rates tend to saturate at large reverse biases.

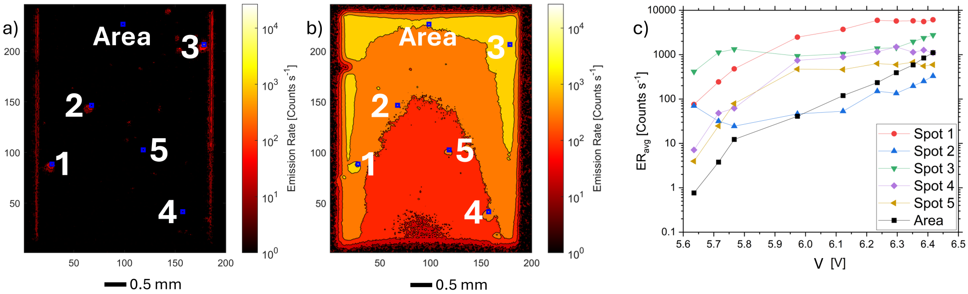

Figure E.9. Five different bright spots are marked for semi-quantitative analysis in ReBEL images at a small current (a) and a large current (b). One point in the cell area is added as comparison. The average emission rates are plotted semi-logarithmically against the reverse bias (c).

Note 8: Profilometry results

Two different bottom ITO electrodes were tested in regards to their effect on the bright edges in ReBEL images. Profilometry was used to investigate the edge of the ITO stripes. Figure E.10 shows the results. In Figure E.10a, the edge of the standard ITO is shown, in Figure E.10b, the edge of rounded ITO. We see that the standard ITO shows a very sharp, step-like edge while the rounded ITO displays a rounded edge. The green and red vertical bars were are markers for the calculation of the layer thickness.

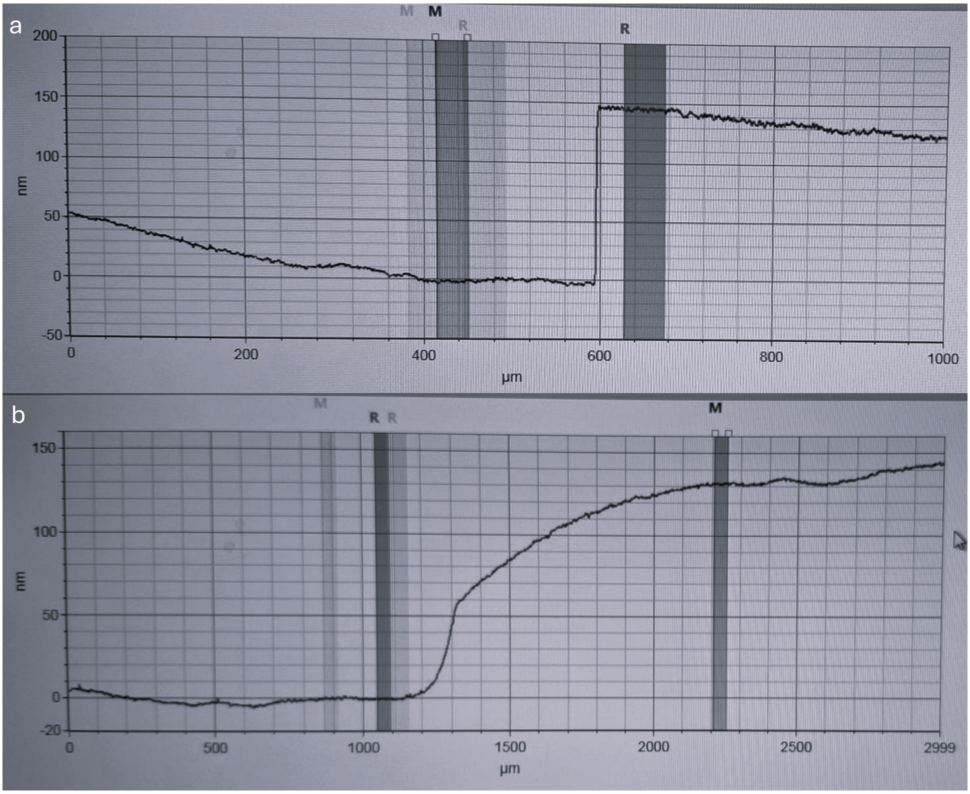

Figure E.10. Results of profilometry measurements on full-area ITO, patterned via photolithography ITO electrodes (a) and ITO electrodes that have been sputtered through a mask (b).

Acknowledgments

This thesis began with a quote from J.R.R. Tolkien's The Lord of the Rings, and so it shall end:

"*It's over; it's done!*", said Frodo Baggins after the one ring had finally met its maker in the fiery hell of Mount Doom.

To compare the last four years of my life to the quest of Frodo and Sam from Rivendell into Mordor would be ludicrous, and comparing the attention of my supervisors to the ever-searching Eye of Sauron even more so. After a closer look, the only commonality lies in the feeling of accomplishment, of having completed something, a feeling of 'a job well done'. This is a feeling I would like to share with you who have accompanied me on my journey (like Sam), supervised me and tried to ease my journey from afar (like Gandalf), and everyone with roles in between.

First, I would like to thank the two institutions that have accommodated me and enabled the PhD project. The collaboration between the TU Delft and TNO has revealed perspectives to me that would otherwise have stayed invisible. The two organizations were represented by Olindo, whose support as my promotor was invaluable, and the successive TNO research managers of the department I was part of: André Schilt, Jan Hoegee, and especially Carlijn Vernooij. Thank you for your consideration of my 'special' position and your backing that allowed me to complete my PhD successfully.

I would also like to thank Luana, my co-promotor. You brought perovskite-specific knowledge and experience to the table and a way with the written word that I learned a lot from.

Then, there is Arthur, my other promotor from the TU Delft. I still remember our first in-person meetings: On the "interview day" in Eindhoven, we had a lunch break together where I talked so much that it caused you to be late to your following meeting. Then, when I first visited the TU Delft, you were the one who welcomed me. These nicely summarize what I would like to thank you for: On the one hand, there is, of course, the bird's eye perspective that you provided, combined with the background in semiconductor physics that you brought to the table. On the other hand, the conversations I had with you during our meetings were always pleasant experiences and within your comments I could feel your interest in my success and well-being. That is what I am most thankful for.

Finally, I would like to thank Mirjam. We met and got to know each other during my semi-internship while a certain pandemic held Europe in its grip. Your guidance and feedback during that time were part of what motivated me to start a PhD. Later, you were my contact person within TNO and the driving force behind the project: Without you, I probably would never have come here. During the PhD itself, your

Laissez-Faire approach gave me ample room for growth and to find my own way into the sometimes confusing topic of reverse bias degradation. At the same time, you were always on hand to help me when I needed something, be that in communication, contacting other experts or discussing my work and my worries. Last but not least, you also guided me out of the rabbit holes that I sometimes fell into and made me realize that, to really understand measurement results, you have to write a paper about them. Without you, both my PhD and myself would be different than what they are now. In my opinion, both have turned out to be quite acceptable and for that I thank you!

Despite not being part of my official supervisory team, yet at least similarly important to the success of the project, Klaas was heavily involved in my work as well. As my spiritual predecessor in research on reverse bias stability, as a PhD researcher that finished his project about two years before me, and just as an incredibly knowledgeable colleague, your help was crucial. When half-baked ideas asked to be bounced off someone else, when characterization equipment was not cooperative or needed additional capabilities, or when I just wanted to complain about perovskites, you were always up for a coffee. I also remember the countless walking lunch breaks that led us around the lake on the High Tech Campus, immersed in conversation about everything and anything. I learned a lot from you, be it the finer art of soldering, repairing setups, the electrical engineer's perspective on solar cells or the "Brabantse kwartiertje". It was a pleasure working with you and I am deeply thankful for your support. Without you, my PhD would have been a very different one, as well.

Of course, enjoying life beyond the work on the PhD is also important. Therefore, I would also like to thank my TNO colleague Johannes for the memorable zombie-filled evenings. On the TU Delft side, I want to thank first and foremost my good friends: Thank you, Haoxu, Yingwen, and Jin. I will remember our countless lunch breaks, our many dinners, the card games and movies, and one memorable dumpling-making Chinese New Year celebration. Most of all, I cherish our conversations and discussions about all and sundry.

Furthermore, there are my office mates and neighbors at the TU Delft: Govind, Federica, Sreejith, Katarina and Yi. I did not visit the office often, but when I was present, it was pleasant to work beside you. Then, there is Paul with whom I had several inspiring conversations about defects in perovskites. I also want to thank all the other members of the PVMD group, including our technicians, especially Stefaan, and our (former) secretaries, especially Mark who helped me a lot.

On the TNO side, I want to thank my team leads Sjoerd, Valerio, and Ilker. Additionally, there are many other TNO colleagues with whom I remember working together, eating together, or just working alongside: Johan, Anne, Giulia, Denise, Aldo, Marcel, Harri, Mehrdad, Ryley, Felipe, Manvika, Rémi, Zohair, Baris, Thomas, Corné, Dorrit, Casper, Suzanne, Radha, Hero, Monique, Drishya, Joris, Markos, Subhadra, Wiljan, Anuja, Lincy, Felipe, and Nitish, and my interns Nils, Nadia, and Maxime. Be it fabrication, characterization, simply small-talk, informative conversations, advice about life, or advice for restaurants in Milano, for each of you there is something I would like to thank you for.

Last but not least, there is my own family to mention that helped and supported me countless times: Thank you Rebecca, Yuri, Leah, Johannes, Miriam, Lothar, Jakob, Deborah, Benjamin, Fridolin, Mama, and Papa.

With that, this thesis has reached its end and I would like to close with the words of Bilbo Baggins:

"The Road goes ever on and on
Down from the door where it began.
Now far ahead the Road has gone,
And I must follow, if I can,
Pursuing it with eager feet,
Until it joins some larger way
Where many paths and errands meet.
And whither then? I cannot say."

Curriculum Vitæ

Jonathan Antonio Henzel

Jonathan was born on 24 January 1997 in Berlin, Germany.

From 2016 onward, he pursued his Bachelor studies at the Julius-Maximilians-University of Würzburg, Germany. His chosen degree's course was "Funktionswerkstoffe" (roughly: "Functional Materials") which provided a broad scientific foundation, covering physics, organic chemistry, material science, electrical engineering, and biochemistry. During his studies, Jonathan served an internship at the Fraunhofer ISC in Würzburg. He wrote his Bachelor thesis within the Department of Experimental Physics on the use of X-Ray fluorescence for the investigation of organic crystals.

Afterwards, Jonathan continued with his Master studies at the same university, focusing on semiconductor technology and physics. During his Master program, an internship at TNO under the supervision of Dr. Mirjam Theelen was arranged but was canceled due to the advent of the COVID-19 pandemic. Instead, he conducted several months of literature work on the indoor and outdoor degradation testing of CIGS solar cells and modules. Jonathan completed his Master of Science degree by writing his thesis on radiative recombination in perovskite solar cells in the Department of Experimental Physics of the Julius-Maximilians-University of Würzburg, Germany.

Following his university education, Jonathan continued his scientific career with a PhD at the Department for Solar Technology & Application at TNO, Netherlands, with Delft University of Technology serving as academic partner. To pursue this work, he moved to the Eindhoven area in the Netherlands. The overarching topic of his research was the reverse bias stability and behavior of perovskite solar cells. The work from 2022 to 2026 resulted in this thesis.

List of Publications

Peer-reviewed publications

Henzel, J., Bakker, K., Najafi, M., Zardetto, V., Veenstra, S., Isabella, O., Mazzarella, L., Weeber, A., & Theelen, M. (2023). Impact of the Current on Reverse Bias Degradation of Perovskite Solar Cells. ACS Applied Energy Materials, 6(22), 11429–11432. DOI: 10.1021/acsaem.3c02273

Henzel, J., Bakker, K., Veenstra, S., Isabella, O., Mazzarella, L., Weeber, A., & Theelen, M. (2025). The impact of low-intensity illumination on the reverse bias behavior of perovskite solar cells. Journal of Materials Chemistry A, 13(37), 31755–31769. DOI: 10.1039/D5TA04100G

Henzel, J., Bakker, K., Veenstra, S., Isabella, O., Mazzarella, L., Weeber, A., & Theelen, M. (2026). Determining the Reverse Bias Breakdown Voltage of Perovskite Solar Cells. Solar RRL, 10(3), e202500875. DOI: 10.1002/solr.202500875

Henzel, J., Bakker, K., Veenstra, S., Isabella, O., Mazzarella, L., Weeber, A., & Theelen, M. (2026). Luminescent Imaging of the Reverse Bias Behavior of Perovskite Solar Cells using ReBEL. submitted to Small Science.

Aninat, R., Bakker, K., **Henzel, J.**, Zardetto, V., Dogan, I., Gevaerts, V., Veenstra, S., & Theelen, M. (2025). Mapping the Partial Shading Degradation in a Monolithically Integrated Perovskite Module. Progress in Photovoltaics: Research and Applications, 1–9. DOI: 10.1002/pip.3881

Conference contributions:

Henzel, J., Bakker, K., Veenstra, S., Isabella, O., Mazzarella, L., Weeber, A., & Theelen, M. (2022). Degradation of Perovskite Solar Cells under Small Reverse Biases. ISOS-13 Conference, Sonderborg, Denmark. Poster Presentation.

Henzel, J., Bakker, K., Veenstra, S., Isabella, O., Mazzarella, L., Weeber, A., & Theelen, M. (2023). Where does the current flow? - Spatial Inhomogeneity of the Reverse Bias Current and its Impact on Degradation. PSCO Conference, Oxford, UK. Poster Presentation.

Henzel, J., Bakker, K., Veenstra, S., Isabella, O., Mazzarella, L., Weeber, A., & Theelen, M. (2024). Reverse Bias under Illumination - Transient vs. Steady State. ISOS-15 Conference, Berlin, Germany. Oral Presentation.